Fluid Dynamic Assessments of Spiral Flow Induced by Vascular Grafts

Efstratios Kokkalis

A thesis submitted for the degree of Doctor of Philosophy

The University of Dundee

November 2014

Contents

List of figures

List of tables

Acronyms and abbreviations

AV	Arteriovenous
BMF	Blood mimicking fluid
CAD	Computer-aided design
CFD	Computational fluid dynamics
CT	Computed tomography
DICOM	Digital imaging and communications in medicine
ePTFE	Expanded polytetrafluoroethylene
IEC	International Electrotechnical Commission
MRI	Magnetic resonance imaging
PAD	Peripheral arterial disease
PRF	Pulse repetition frequency
PV	Peripheral vascular
PVA-c	Polyvinyl alcohol cryogel
STL	stereolithography
TMM	Tissue mimicking material
WSS	Wall shear stress
2D	Two-dimensional
3D	Three-dimensional

Nomenclature

A	Area	$[\mathrm{m}^2]$
α	Attenuation coefficient	$[\mathrm{m}^{-1}]$
c	Sound velocity	$[\mathrm{m} \cdot \mathrm{s}^{-1}]$
D	Diameter	$[\mathrm{m}]$
f	Frequency	$[\mathrm{Hz}]$
H	Helicity	$[\mathrm{m}^4 \cdot \mathrm{s}^{-2}]$
H_k	Kinetic helicity	$[\mathrm{m} \cdot \mathrm{s}^{-2}]$
L	Length	$[\mathrm{m}]$
p	Pressure	$[\mathrm{Pa}]$
Q	Flow rate	$[\mathrm{m}^3 \cdot \mathrm{s}^{-1}]$
R	Acoustic reflection coefficient	$[\mathrm{m}]$
r	Radius	$[\mathrm{m}]$
Re	Reynolds number	
u, v, w	Cartesian velocity components	
V	Volume	$[\mathrm{m}^3]$
x, y, z	Cartesian coordinates	
z	Acoustic impedance	$[\mathrm{kg} \cdot \mathrm{s}^{-1} \cdot \mathrm{m}^{-2}]$

Γ	Circulation of a vortex	$[\mathrm{m}^2 \cdot \mathrm{s}^1]$
$\bar{\Gamma}$	Mean circulation	$[\mathrm{m}^2 \cdot \mathrm{s}^1]$
δ	Boundary layer thickness	$[\mathrm{m}]$
ΔP	Pressure drop	$[\mathrm{Pa}]$
μ	Dynamic viscosity	$[\mathrm{Pa} \cdot \mathrm{s}]$
v	Kinematic viscosity	$[\mathrm{m}^2 \cdot \mathrm{s}^{-1}]$
ρ	Density	$[\mathrm{kg} \cdot \mathrm{m}^{-3}]$
υ	Velocity	$[\mathrm{m} \cdot \mathrm{s}^{-1}]$
ω	Vorticity	$[\mathrm{s}^{-1}]$
$\bar{}$, $\langle\ \rangle$	Mean value symbol	
$\wedge$	Normalised value symbol	

Acknowledgements

I would like to thank my first supervisor Graeme Houston for giving me the opportunity to conduct this research and for his advice and support, particularly from a clinical perspective. I sincerely acknowledge my second supervisor George Corner for his guidance and input during this work and ensuring I had access to appropriate facilities.

I would like to express my gratitude to my external supervisor from the University of Edinburgh, Peter Hoskins, for his excellent supervision and support since he joined the project. In addition, for providing essential hardware and software and introducing me to researchers whose input was valuable to this study.

Thanks are due to the fellow students and staff of the Institute of Cardiovascular Research and the Institute for Medical Science and Technology for providing a friendly and helpful environment during the last three and half years. In particular, I would like to thank Shona Matthew for proofreading the thesis, Peter Stonebridge for clinical advice on spiral flow and vascular grafts, Anthony Doull for support with MATLAB and Suzanne Duce for providing access to AMIRA and guidance using the software. Special thanks to my friends and colleagues Deirdre Cassidy, Fiona Adams, Martin Rube, Stuart Coleman and Naveed Akbar for their support and for making my time in Scotland enjoyable.

I want to thank Andrew Cookson and Spencer Sherwin from King's College London and Imperial College London respectively, for advice in the area of fluid dynamics. In addition, thanks to Prashant Valluri from the University of Edinburgh for providing access to ANSYS CFX, guidance for computational simulations and a friendly working environment in summer 2013. Thanks also to Pedro Saenz for his support with ANSYS CFX during my stay in Edinburgh. Another person who provided useful information about the computational simulations is Michael Walsh from the University of Limerick and I would like to thank him.

Thanks to Duncan Kirkcaldy, Duncan Martin, Ian Rutherford and Patrick Carena from the Medical Physics and Institute for Medical Science and Technology workshops for their technical assistance.

Furthermore, I want to acknowledge Scot Dundas, Glen Gardner, Joanna Barlow and Dawn Barrie from the Clinical Research Centre CT unit and Stephen Gandy from the Clinical Research Centre MRI unit for scanning the vascular-graft models.

Thanks to the Scottish Universities Physics Alliance INSPIRE programme (supported by the Scottish Funding Council) and the Vascular Flow Technologies Ltd. for our successful collaboration and for funding this project. Finally, I would like to thanks the Scottish Imaging Network (SINAPSE) for their support throughout my studies.

Declaration of originality

I hereby declare that I am the author of this thesis; that, unless otherwise stated, all references cited have been by myself; that the work of which the thesis is a record has been done by myself except due acknowledgement is made in the text and that it has not been previously accepted for a higher degree.

Efstratios Kokkalis

Supervisor’s declaration

This is to certify that Efstratios Kokkalis has done this research under my supervision and that I have read this thesis. Also, to certify that he has fulfilled the conditions of Ordinance 39 and relevant Regulations of the University of Dundee, so that he is qualified to submit for the Degree of Doctor of Philosophy.

Prof J Graeme Houston

Abstract

Peripheral vascular grafts are used for the treatment of peripheral arterial disease and arteriovenous grafts for vascular access in end stage renal disease. The development of neo-intimal hyperplasia and thrombosis in the distal anastomosis remains the main reason for occlusion in that region. The local haemodynamics produced by a graft in the host vessel is believed to significantly affect endothelial function. Single spiral flow is a normal feature in medium and large sized vessels and it is induced by the anatomical structure and physiological function of the cardiovascular system. Grafts designed to generate a single spiral flow in the distal anastomosis have been introduced in clinical practice and are known as spiral grafts. In this work, spiral peripheral vascular and arteriovenous grafts were compared with conventional grafts using ultrasound and computational methods to identify their haemodynamic differences.

Vascular-graft flow phantoms were developed to house the grafts in different surgical configurations. Mimicking components, with appropriate acoustic properties, were chosen to minimise ultrasound beam refraction and distortion. A dual-beam two-dimensional vector Doppler technique was developed to visualise and quantify vortical structures downstream of each graft outflow in the cross-flow direction. Vorticity mapping and measurements of circulation were acquired based on the vector Doppler data. The flow within the vascular-graft models was simulated with computed tomography based image-guided modelling for further understanding of secondary flow motions and comparison with the experimental results. The computational assessments provided a three-dimensional velocity field in the lumen of the models allowing a range of fluid dynamic parameters to be predicted.

Single- or double-spiral flow patterns consisting of a dominant and a smaller vortex were detected in the outflow of the spiral grafts. A double- triple- or tetra-spiral flow pattern was found in the outflow of the conventional graft, depending on model configuration and Reynolds number. These multiple-spiral patterns were associated with increased flow stagnation, separation and instability, which are known to be detrimental for endothelial behaviour. Increased in-plane mixing and wall shear stress,

which are considered atheroprotective in normal vessels, were found in the outflow of the spiral devices. The results from the experimental approach were in agreement with those from the computational approach.

This study applied ultrasound and computational methods to vascular-graft phantoms in order to characterise the flow field induced by spiral and conventional peripheral vascular and arteriovenous grafts. The results suggest that spiral grafts are associated with advanced local haemodynamics that may protect endothelial function and thereby may prevent their outflow anastomosis from neo-intimal hyperplasia and thrombosis. Consequently this work supports the hypothesis that spiral grafts may decrease outflow stenosis and hence improve patency rates in patients.

Chapter 1

Introduction

1.1 Spiral flow in vessels

In the past few decades it has been well established that that blood flow in medium and large size vessels is spiral, which means that the blood velocity vectors are not parallel to the vessel wall. The existence of secondary flow motions in vessels is related to both the physiological function and anatomical structure of the cardiovascular system.

1.1.1 Heart

The heart is a remarkable structure that displays a helical, transmural and overlapping pattern of the myocardial fibres. The fascinating architecture of myocardium has been studied since the 17th century (Kocica et al. 2006). During the last couple of decades it has been showed that the helical structure of heart anatomy is related with its function, resulting in a twisting motion during systole and early diastole (Buckberg 2002). Jung et al. (2006) presented imaging evidences that the heart operates as a spiral-compressive pump, where the wall follows a helical descent motion rather than a direct linear motion to the centre (Figure 1.1). The twisting motion during contraction and early dilation generates a spiral blood pattern in the ascending aorta, that may provide more efficient cardiac emptying and reduce the myocardium effort (Stonebridge 2011).

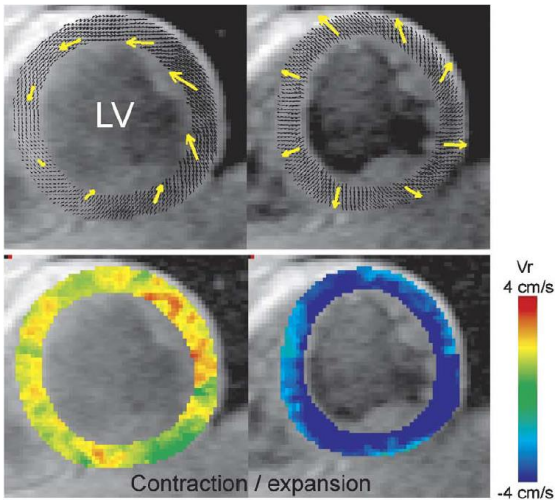

Figure 1.1: Systolic and diastolic wall motion of the left ventricle detected with MRI; *Vr* = radial velocity (Jung et al. 2006, with permission of Oxford University Press).

The anatomy and function of the heart do not only generate spiral flow but also form vortices in its champers. There is an increased interest in the analysis of left ventricular vortical structures during diastolic filling. It is believed that the normal vortex pattern minimises the fluid energy dissipation and optimises myocardial efficiency and left ventricular emptying. Vortices in left ventricles have been illustrated with velocity vector and vorticity maps using particle image velocimetry (Cimino et al. 2012; Hong et al. 2008) and ultrasound (Garcia et al. 2010; Mehregan et al. 2014; Uejima et al. 2010).

1.1.2 Aorta

The existence of helical flow in the ascending aorta was detected in 1987 by Segadal and Matre with a transluminal Doppler ultrasound probe. Three years later Frazin et al. (1990) used colour Doppler ultrasound to show single rotational flow in an aortic arch model and human descending thoracic aorta. The velocity vector followed the right hand rule during systole and showed opposite components of rotation during diastole. Later on they confirmed their results in the abdominal aorta beyond the renal arteries and noted that the helical velocity is at least 25% of axial velocity in the aortic arch and descending aorta (Frazin et al. 1996).

The centre of rotation of the single spiral flow is located at the centre of the ascending aorta as shown with vector Doppler ultrasound (Tanaka et al. 2010). This is believed to

support the bloods passage through the aortic arch and aiding the dispersion of wall shear stress (WSS) in the aortic wall. Vector Doppler has also been used to detect spiral flow in the abdominal aorta and measure its rotational frequency (Pedersen et al. 2011).

The development of phase contrast MRI verified right-handed helical flow in the aortic arch and abdominal aorta of healthy volunteers during systole and showed a second retrograde rotational flow along the inner wall at end systole (Houston et al. 2003, 2004; Kilner et al. 1993; Markl et al. 2005). Harloff et al. (2010) concluded that this retrograde secondary flow motion in aortas with plaque in the descending section is a source of cerebral embolism.

1.1.3 Peripheral arteries

The study of secondary flow motions in peripheral arteries was initiated in vascular models. Ku and Giddens (1983) constructed a realistic carotid bifurcation and presented secondary flow patterns and flow separation in the internal carotid artery. They showed low WSS and flow stagnation in the outer wall of the internal carotid artery, where atheromatous plaques were seen in human carotid specimens. This was later confirmed by Karino et al. (1987) along with various secondary flow phenomena, when they studied flow in glass and vascular models of peripheral arteries and aortic branches. Pedley (1980) displayed single and double spirals in small diameter tubes as a result of bifurcation and curvature. The double spiral patterns were associated with flow separation (two rotating cells) and flow stagnation points (Figure 1.2).

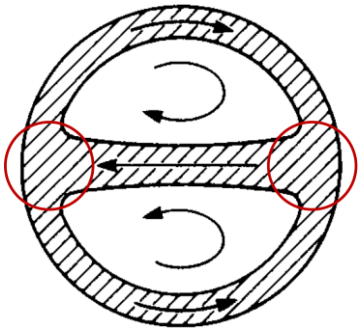

Figure 1.2: Double spiral at the cross-section view of a tube. The shaded regions correspond to viscous boundary layers and the red circles indicate flow stagnation points (reproduced with permission of Cambridge University Press, from Pedley 1980).

In 1991 Stonebridge and Brophy were the first to concluded that flow in arteries is spiral in nature, by directly visualising spiral flow in peripheral arteries of the lower extremities using angioscopy. The presence of single spiral flow in the common femoral artery was confirmed by Hoskins et al. (1994) with colour Doppler and vector Doppler imaging. Using the same methodology Stonebridge et al. (1996) reported single spiral flow in both lower limbs, while Pedersen et al. (2011) applied a different vector Doppler approach to measure the angular frequency of rotational flow in common iliac arteries. Rotating asymmetric axial velocity profiles in peripheral arteries were also found with two-dimensional (2D) phase contrast MRI in the iliac and carotid arteries (Caro et al. 1996). In 2009, Harloff et al. presented spiral flow in the internal carotid artery using 4D phase contrast MRI. Rotational patterns distal from the carotid bifurcation have been also detected with colour and vector Doppler ultrasound (Pedersen et al. 2011; Picot et al. 1993; Udesen et al. 2007).

1.1.4 Veins

Single helical blood patterns have been detected in veins of the upper extremities after the creation of an arteriovenous (AV) fistula (Marie et al. 2014) and in the portal vein using colour Doppler (Rosenthal et al. 1995). These studies highlighted that veins can act as peripheral generators of single spiral flow and support the belief that vortical structures play an important role in the cardiovascular system. The exact mechanism underlying these findings in veins is not known.

1.1.5 Progression of spiral flow in vessels

A number of researchers have pointed out that single spiral flow is propagating in the arterial system due to the multi-planar curvature, tapering and branching geometry of the arterial tree (Caro et al. 1996; Frazin et al. 1996; Stonebridge et al. 1996). Numerical simulations in aortic arch models showed that a curved but planar arch would exhibit a typical Dean flow with two symmetric helical structures, indicating the importance of aortic torsion (Liu et al. 2009, 2010). Stonebridge and Brophy (1991) detected spiral folds on the arterial walls of 51 out of 75 arteries examined downstream from the aortic

bifurcation. Such anatomical folds may play a significant role in the propagation of single spiral flow.

It can be postulated that single rotational flow in veins is supported by the geometry of the venous tree (multi-planarity, tapering, branching), anatomical folds on venous walls and functional factors such as the venous valves.

1.1.6 Clinical correlation of spiral flow

Frazin et al. (1996) speculated that the tangential component of velocity imported by single spiral flow affects the wall shear forces and endothelial cell alignment and may play an important role in plaque deposition, organ perfusion, dissection formation and flow separation in aortic branches. Recent numerical studies support the hypothesis that the aortic single spiral flow may enhance oxygen flux to the arterial wall and benefit the oxygen transport. Moreover, it may suppress the luminal surface concentration polarisation of low-density lipoproteins, which is involved in the localisation of atherogenesis (Liu et al. 2009, 2010). The conclusion that single spiral flow reduces the uptake of low-density lipoproteins in arteries was also presented in an *ex-vivo* study using segments of rabbit thoracic aorta (Ding et al. 2010).

The helical velocity of a single spiral flow may be an important stabilising factor of WSS magnitude and dispersion and therefore may have a beneficial effect on the mechanisms of endothelial damage and repair (Caro et al. 1996; Frazin et al. 1996; Stonebridge et al. 1996). Caro et al. (2005) demonstrated that a single helical blood pattern may lead to uniform WSS and inhibit flow stagnation, separation and instability, thus protecting vessels from neo-intimal hyperplasia and thrombosis.

Parabolic flow has been compared with single spiral flow in stenosed straight tube models. The single spiral was associated with a significant reduction of both turbulent kinetic energy and capability to preserve a coherent pattern downstream of the stenosis, suggesting flow stabilisation even in stenosed vessels (Paul and Larman 2009; Stonebridge et al. 2004). Chen et al. (2009) demonstrated that a single helical flow within a stented region reduced the size of disturbed flow zones, increased the average WSS and lowered the oscillatory shear index, which may suppress the development of

restenosis after stent implantation. Zhan et al. (2010) presented experimental data that proved single spiral flow decreased the adhesion of platelets in a test tube in comparison to parabolic flow. They concluded that a single spiral may indeed decrease the risk of acute thrombus formation.

Single spiral flow is accepted as a normal feature of blood circulation at least in a part of the cardiovascular system. Many authors have hypothesised its atheroprotective nature and presented numerical (Doorly and Sherwin 2009), experimental (Zhan et al. 2010), animal (Caro et al. 2005; Ding et al. 2010; Jahrome et al. 2011) and nonrandomised clinical evidence (Stonebridge et al. 2012). Houston et al. (2003, 2004) associated the lack of aortic spiral flow with carotid atheromatous disease and short-term renal function deterioration in patients with renal arterial stenosis. However, there is still a need for long-term randomised clinical data to characterise the relationship of flow patterns against the development of arterial disease in order to prove the exact correlation between single spiral flow and atheromatous plagues (Stonebridge 2011).

1.2 Peripheral arterial disease

Peripheral arterial disease (PAD) refers to stenoses in arteries due to development of atherosclerotic plaques. Technically, the definition of PAD includes problems within the extracranial carotid circulation, the upper and lower extremities, the mesenteric and the renal circulation; however, it is commonly used as a manifestation of atherosclerosis in the lower extremities and the aortic bifurcation (Kanjwal et al. 2004; Ouriel 2001).

Ischaemic heart disease is the leading cause of mortality worldwide, closely followed by cerebrovascular disease (World Health Organization 2014). PAD is recognised as an independent risk factor for both myocardial and cerebrovascular events (Abdulhannan et al. 2012; Belch et al. 2003; Peach et al. 2012).

1.2.1 Epidemiology

PAD affects primarily the superficial femoral and popliteal arteries and secondarily the aortic bifurcation and iliac arteries. It can be either symptomatic or asymptomatic, with

most patients found to be symptom-free. In symptomatic cases PAD can degrade the quality of life and lead to major disabilities. The most common symptom is intermittent claudication during ambulation. The pain from intermittent claudication is generally located distal to the stenosed region. Approximately 25% of patients with intermittent claudication deteriorate resulting in rest pain and tissue loss, known as critical limb ischemia. Untreated critical limb ischemia can lead to ulceration, gangrene and eventually amputation (Abdulhannan et al. 2012; Norgren et al. 2007; Ouriel 2001; Peach et al. 2012).

1.2.2 Pathophysiology and risk factors

PAD is the result of any disease that can lead to stenosis, of which atherosclerosis is the main aetiology. Atherosclerosis is a complex disease that involves endothelial dysfunction, platelet activation that leads in thrombosis, abnormal proliferation of vascular smooth muscle, oxidative stress, lipid disturbances, metabolism and genetic factors (Abdulhannan et al., 2012; Ouriel, 2001; Peach et al., 2012).

PAD usually develops in arterial bifurcations due to complicated blood flow patterns that affect the gradient of WSS in the lumen. It is believed that low and oscillatory WSS are related to endothelial dysfunction and consequently atherosclerosis (Figure 1.3) (Abdulhannan et al. 2012; C. Caro 2009; Malek et al. 1999).

The risk of atherosclerosis is increased with age. Stenosis formation generally commences in the teenage years due to endothelial dysfunction. With time the stenosis may progress to advanced lesions and thrombosis. The disease affects more males than females. Other risk factors are smoking, diabetes mellitus, hypertension, dyslipidemia, hyperhomocysteinaemia, and chronic renal insufficiency (Abdulhannan et al. 2012; Norgren et al. 2007; Ouriel 2001; Peach et al. 2012).

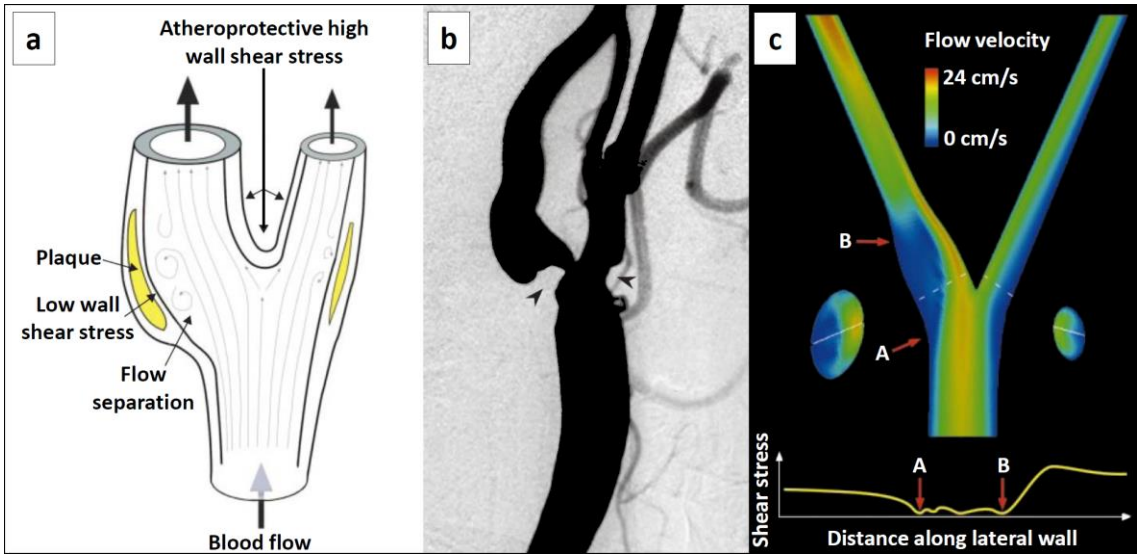

Figure 1.3: (a) Schematic illustration of carotid bifurcation and atherosclerosis in the outer walls. (b) Arteriogram of the carotid bifurcation in a patient who experienced a cerebrovascular event. Arterial stenosis is seen at the outer walls of the bifurcation in both the internal and external carotid arteries (arrowhead). (c) Velocity map in a carotid bifurcation at the end-systole using computational fluid dynamics. Low velocities associated with low wall shear stress can be seen at the outer walls of the bifurcation (reproduced with permission of the American Medical Association, from Malek et al., 1999)

1.2.3 Treatment of peripheral arterial disease

The symptoms of PAD can be intense and result in rest pain, tissue loss and nonhealing ulcers that may interfere with patient lifestyle or leave the patient incapacitated. In such cases revascularisation is required. This is possible either with an endovascular procedure or with open surgery. The type of revascularisation procedure selected for each patient relies on the balance between the risk of the intervention and the expected durability of the improvement. Generally, progressed cases require an open surgery.

In infrainguinal surgical revascularisation a bypass graft is used, which can be either a prosthetic conduit or an autogenous vein. An autogenous vein is associated with higher primary and secondary patency rates in both above- and below-knee applications (Figure 1.4). However, it is not always available and a prosthetic peripheral vascular (PV) graft is required. The primary patency rate refers to the number of functional grafts without revision procedures in comparison to the total number of implantations. The secondary patency expresses the number of functional grafts that followed revision

procedures to restore patency after occlusion in comparison to the total number of implantations (Diehm et al. 2007; Tricht et al. 2005).

Infrainguinal revascularisation is conducted with end-to-side anastomoses, which means that the ends of the graft are connected at the side of an artery, bypassing the stenosed region (Norgren et al. 2007; Ouriel 2001; Peach et al. 2012).

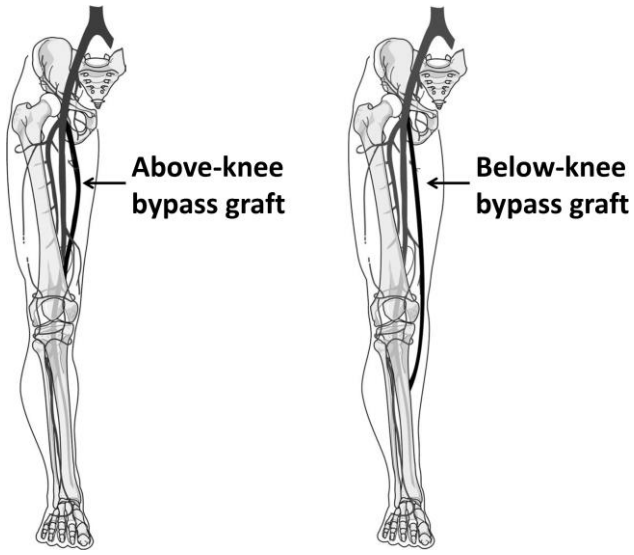

Figure 1.4: Above- and below-knee surgical configuration of a bypass graft (republished with permission of ELSEVIER, from Norgren et al. 2007).

1.3 End stage renal disease

Patient with end stage renal disease requiring haemodialysis need a reliable vascular access. In patients where renal recovery is possible, a temporary catheter is positioned in the jugular or femoral vein. If renal failure is enduring a permanent vascular access needs to be constructed using the patient vessels. The most common approaches for permanent vascular access are with the autogenous AV fistula and the prosthetic AV graft. With both techniques blood flow is diverted from an artery to a vein. For a fistula an artery is connected directly to a vein whilst with a graft, prosthetic tubing is used to connect the vessels as shown in Figure 1.5. In both cases the vein is subjected in increased flow rates, which makes it to grow larger and stronger. During dialysis the blood leaves the body and travels through an extracorporeal circuit and dialyser before returning to the venous circulation. The vascular access allows large amounts of blood

to flow continuously in the venous system in a short period of time ensuring adequate dialysis clearance (Tricht et al. 2005).

1.3.1 Permanent vascular access techniques

An autogenous AV fistula is considered the first choice for permanent vascular access in 90% of patients in Europe, because fistulas are associated with higher patency rates and better long term results than a graft. Moreover, the surgery for an AV graft is more demanding and is associated with greater morbidity. In contrast, in the USA there are more AV graft applications than AV fistulas; although with the introduction of the 'Fistula First Breakthrough Initiative' there is an attempt to reverse this practice. An AV fistula may fail to mature or it may not be feasible in patients with unsuitable or unavailable vessels, mainly due to exhausted superficial veins from previous AV fistulas, aging and diabetes. In these cases an AV graft is implanted (Akoh 2009; Gessaroli and Massini, 2012; Rayner et al. 2004; Tricht et al. 2005).

A vascular access can be placed in the upper or lower extremities. Applications in the upper extremities are preferable because they are associated with less complications and higher patency rates. In a review on AV prosthetic grafts Akoh (2009) reported one and two year cumulative patency rates in the arm 59 - 90% and 47 - 85% and in the thigh 41 - 68% and 26 - 43% respectively.

If possible, the most distal available location is used so as to preserve the more proximal locations for future accesses in case of failure of the first access (Akoh 2009; Gessaroli and Massini 2012). An AV graft can be placed in a loop or straight surgical configuration as shown in Figure 1.5. The loop configuration yields greater patency rates and is considered the first option (Akoh 2009; Brown and Mitchell 2014).

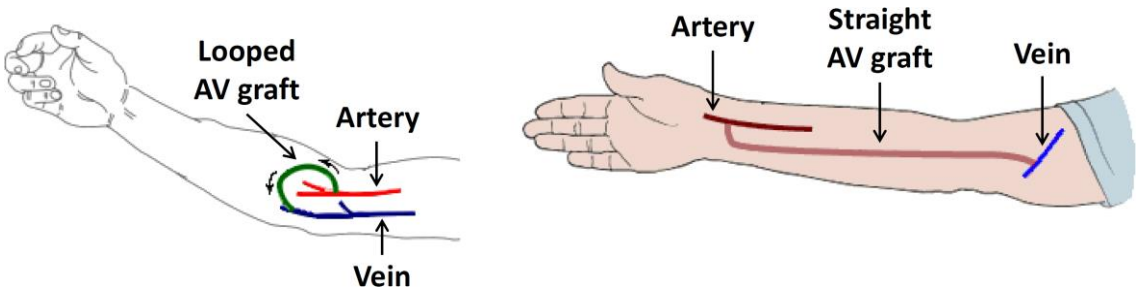

Figure 1.5: Looped (left) and straight (right) AV graft surgical configurations.

1.4 Implications of vascular prosthetic grafts

A vessel is arranged in three layers; the intima, media and adventitia from the lumen to the perivascular soft tissue respectively. The intima is thinnest consisting of a single layer of endothelial cells and a basement connective membrane. The media is the thickest layer and is composed of vascular smooth muscle cells. The adventitia consists of collagen and elastin and acts as the extracellular matrix providing structural and biochemical support. The intima-media and media-adventitia interfaces are separated with a dense elastic membrane known as the internal and external elastic lamina respectively (Tortora and Derrickson 2006).

In implanted vessels, neo-intimal hyperplasia occurs when the vascular smooth muscle cells migrate to the intima layer, proliferate and deposit an extracellular matrix. With time this is progresses to an advanced atherosclerotic lesion, which contains necrotic lipids covered by fibrous connective tissue causing a stenosis in the lumen that restricts the blood flow. The fibrous cap of the lesion may also thin and rupture releasing lipids and causing thrombus formation. A thrombus is a blood clot that can either block the stenosed region or flow downstream in the blood circulation (Abdulhannan et al. 2012; Hammer 2008).

The patency rates of PV and AV prosthetic grafts remain a challenge because of the development of neo-intimal hyperplasia and thrombosis at the anastomoses, which can lead to occlusion. In the AV applications midgraft stenosis is also possible due to in-growth fibrous tissue through multiple puncture holes (Haruguchi and Teraoka 2003; Mickley 2004). Neo-intimal hyperplasia and thrombosis occurs predominantly at the

heel, toe and floor of the distal anastomosis or outflow of a prosthetic graft. The heel and toe are located at the suture line between the graft and the vessel. The floor, which is also known as bed, is situated at the wall opposite from the anastomosis (Figure 1.6). Disease formation at the suture line is attributed to three main factors; material mismatch between the vessel and the prosthetic graft, surgical trauma to the endothelium and vessel wall during graft implantation and abnormal haemodynamics around the anastomosis. Disease formation at the floor of the junction is believed to be entirely associated with the abnormal flow patterns, which are induced as the blood impinges from the graft to the host artery (Gessaroli and Massini 2012; Mickley 2004; Walsh et al. 2003). Formation of stenosis related to haemodynamics is also possible downstream of the outflow anastomosis in both PV and AV prosthetic grafts (Doelman et al. 2005; Houston et al. 2007; P.A. Stonebridge et al. 1997).

The haemodynamics in an AV graft is particularly important because the vein is subjected in abnormal pressure and flow rate. For instance a normal venous pressure in the arm is about 20 mmHg, whilst after an AV graft implantation it changes to 60 - 120 mmHg after an AV graft implantation (Tricht et al. 2005).

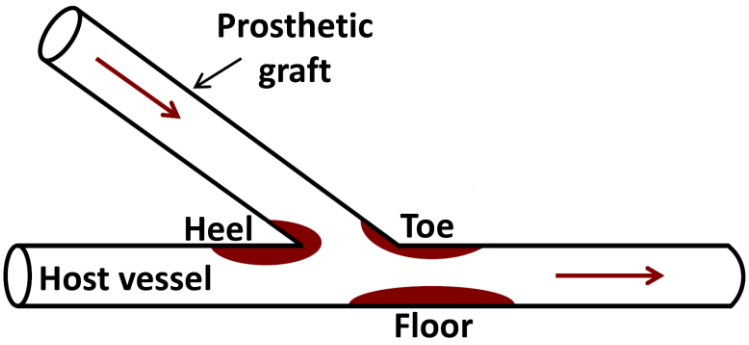

Figure 1.6: End-to-side outflow anastomosis of a prosthetic graft and stenosis at the heel, toe and floor.

Vascular geometry affects the blood flow profile. The development of stenosis obstructs the blood circulation and clearly affects further its flow pattern. On the other hand, the traction (i.e. force per unit area) exerted on the vascular walls by the blood affects the function of the endothelial cells. This mechanism shows a mutual interaction between vascular biology and haemodynamics, which is not yet fully understood. This interaction is believed to have a strong impact on the patency of a graft because the

anastomoses alters the local haemodynamics and the distribution of WSS downstream from grafted region (Doorly and Sherwin 2009; Haruguchi and Teraoka 2003; Papaharilaou et al. 2002).

1.4.1 Improvement of prosthetic grafts

There are two leading strategies aimed at improving prosthetic graft patency rates by preventing neo-intimal hyperplasia and thrombosis in the distal anastomosis; anticoagulation and flow modification. In the first case the graft is bonded with an anticoagulant such as heparin (Daenens et al. 2009). In the second case the design of the graft is modified to try and introduce physiologic single spiral flow as a way of stabilising the flow profile to reduce disturbances (Caro et al. 2005; Huijbregts et al. 2007; Jahrome et al. 2011; Stonebridge 2012). Both approaches have shown promising results.

An early nonrandomised clinical study on a PV spiral graft demonstrated primary patency rate of 81% for above-the-knee and 57.3% for below-the-knee bypasses at 30 months follow up. The respective secondary patency rates were 81% and 64% (Stonebridge et al. 2012). At the time of the publication, the above-the-knee results were better or similar to other PV prosthetic graft studies. The below-the-knee results compared well with other reported studies except for a nonrandomised heparin-bonded graft study, where the primary patency rate at one year was reported to be 81% (Daenens et al. 2009).

It has been proposed that in the future prosthetic grafts could combine the flow modification and pharmacologic strategy (Stonebridge et al. 2012).

1.5 Ultrasound flow imaging

The first medical ultrasound images were bi-stable (black and white) and published in early 1950s. Grey scale imaging was introduced in the 1970s, providing a more detailed display of tissue structures. In the mid-1970s real-time scanning systems were developed, which enabled visualisation of moving structures and reduced the

examination time. The ongoing development of Doppler ultrasound over many years allowed the technique to be used for the detection of blood flow in vessels by the 1980s (Gibbs et al. 2009). Nowadays Doppler ultrasound methods are widely used in clinical diagnosis and research, for example to visualise and quantify blood flow in order to access the cardiovascular system.

1.5.1 B-mode imaging

Bright-mode, more commonly known as B-mode imaging, is a cross-sectional view of tissues and organ boundaries within the body. The source of ultrasound or transducer emits short pulses of ultrasound into the patient. As the pulses travel into the body, they are reflected at tissue boundaries because different media have different density and compressibility and so different acoustic impedance. The pulses are also scattered from small tissue structures whose dimensions are similar to or less than a wavelength and whose acoustic impedances are different. Both reflection and scattering generate echoes. Some of these echoes return back to the transducer where they are detected. The produced signal is used to form the image. The brightness of the image at each point is related to the amplitude of the returned echo. The closer an echo source is to the transducer and the higher the amplitude of the echo, the brightest the corresponding spot in a B-mode line is (Martin, 2010; McDicken & Anderson, 2011).

A 2D B-mode image is formed from 100 or more B-mode lines. Each line in the image is generated by a pulse-echo sequence. This sequence includes the transmission of a pulse and the consequent returned echoes from interfaces and scatterers positioned in different depths into the body. The depth of the source of an echo is calculated based on the known speed of sound in soft tissue (usually 1540 $m \cdot s^{-1}$) and the time difference between emission and reception (Martin, 2010; McDicken & Anderson, 2011).

1.5.2 Doppler ultrasound imaging

The Doppler effect describes the relationship between the frequency of a sound wave transmitted by a source (f_t) and the frequency of a sound wave received by an observer (f_r). If the source and the observer are stationary the frequency of the transmitted sound is same to that of the received sound ($f_r = f_t$). If the source is moving toward the

observer as it transmits the sound wave, the wavefronts traveling towards the observer are closely packed, and the frequency of the received wave that the observer witnesses is higher than the transmitted ($f_r > f_t$). If the source is moving away from the observer as it transmits the sound wave, the wavefronts traveling towards the observer are spread out, and the frequency of the wave received by the observer will be lower than that emitted ($f_r < f_t$). The potential difference between the transmitted and received frequency is known as Doppler shift frequency (f_d) and is proportional to the relative velocity between the observer and the source.

Doppler ultrasound employs the Doppler effect to measure the change in the frequency of the transmitted ultrasound wave as it is scattered by the moving blood, which acts like a source. Generally the transducer is held relatively stationary and the ultrasound waves strike the blood as shown in Figure 1.7. When the blood is stationary the frequency of the received ultrasound wave is same with that transmitted by the transducer (Figure 1.7a). When the blood is moving towards the probe the frequency of the received ultrasound wave is greater than that transmitted by the probe and vice versa occurs when the blood is moving away from the transducer (Figure 1.7b, Figure 1.7c).

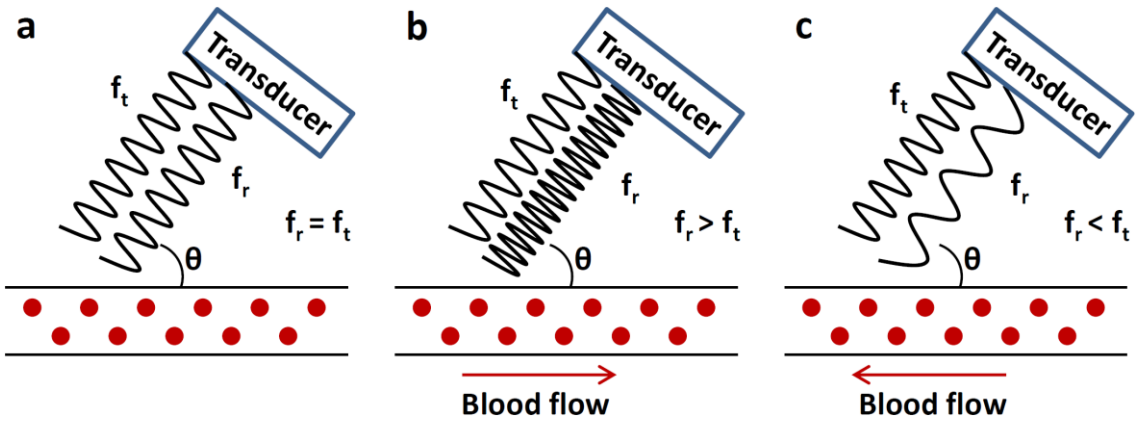

Figure 1.7: The Doppler effect in ultrasound imaging. (a) The transducer and the blood are stationary; the transmitted ultrasound frequency (f_t) is equal to the received (f_r). (b) The transducer is stationary and the blood is moving toward it; the transmitted ultrasound frequency (f_t) is less than the received (f_r). (c) The transducer is stationary and blood is moving away from it; the transmitted ultrasound frequency (f_t) is greater than the received (f_r). Theta (θ) is the angle between the ultrasound beam and the direction of the blood flow.

The detected Doppler frequency shift (f_d) is mathematically expressed in Equation 1.1, where f_r is the received frequency, f_t the transmitted frequency, υ the velocity of the blood, c the speed of the ultrasound wave in soft tissue and θ the angle between the Doppler ultrasound beam and the direction of the blood or angle of insonation (Figure 1.7).

$$f_d = f_r - f_t = \frac{2f_t \upsilon cos\theta}{c} \quad \textbf{1.1}$$

Equation 1.1 shows that the Doppler frequency shift is directly proportional to blood flow velocity. In other words, the greater the flow velocity the larger the Doppler shift. If the value of f_d is known then the blood flow velocity can be calculated with rearrangement of Equation 1.1.

$$\upsilon = \frac{f_d c}{2f_t cos\theta} \quad \textbf{1.2}$$

The angle of insonation depends on the orientation of the probe in relation to the scanning vessel. For $\theta = 0°$, $\cos\theta = 1$ and for $\theta = 90°$, $\cos\theta = 0$. Therefore, the smaller the angle between the ultrasound beam and a blood vessel, the higher the Doppler frequency shift. The produced signal is very small when the angle of insonation approaches 90°. It can be seen that the most desirable situation occurs when the ultrasound beam is aligned parallel to the targeted vessel, which is rarely possible in clinical practice. The general rule is that angles less than 60° provide relatively reliable Doppler frequency shifts.

Diagnostic ultrasound Doppler techniques can be categorised as either non-imaging or imaging. The non-imaging Doppler techniques are based on continuous-wave systems. The imaging Doppler techniques are based on pulsed-wave systems and the main types are colour flow and spectral Doppler, both of which are presented in conjunction with B-mode imaging (Gibbs et al. 2009; Hoskins 2010; Maulik 2005; McDicken and Anderson 2011).

Colour Doppler imaging

A *colour box* is positioned in the region of interest on the B-mode image (Figure 1.8). The size and position of this colour box can be adjusted. The colour flow image is created by ultrasound pulses that are typically three to four times longer than those used for B-mode imaging. The elements of the transducer are rapidly switched between B-mode and colour Doppler imaging to produce a combined simultaneous image, which is known as *duplex imaging*.

Hundreds of scan lines are used in the region of the colour box. Each line is divided into a column of small sample volumes. The mean Doppler frequency shift is calculated for each of these sample volumes, using 10 or more pulse-echo sequences for increased reliability. When the received frequencies are greater than the transmitted frequency, the mean Doppler frequency is positive and when the received frequencies are smaller, the mean Doppler frequency is negative. Typically, red shades are used for positive Doppler shifted signals or flow traveling towards the transducer and blue shades for negative Doppler shifted signals or flow travelling away from the transducer. A vertical *colour scale* bar is displayed to the side of the B-mode image and relates the (commonly used) red and blue shades with mean Doppler frequency shifts or corresponding flow velocities (Figure 1.8). Typically, the higher the velocity values the brighter the assigned colour shade (Gibbs et al. 2009; Hoskins 2010; McDicken and Anderson 2011).

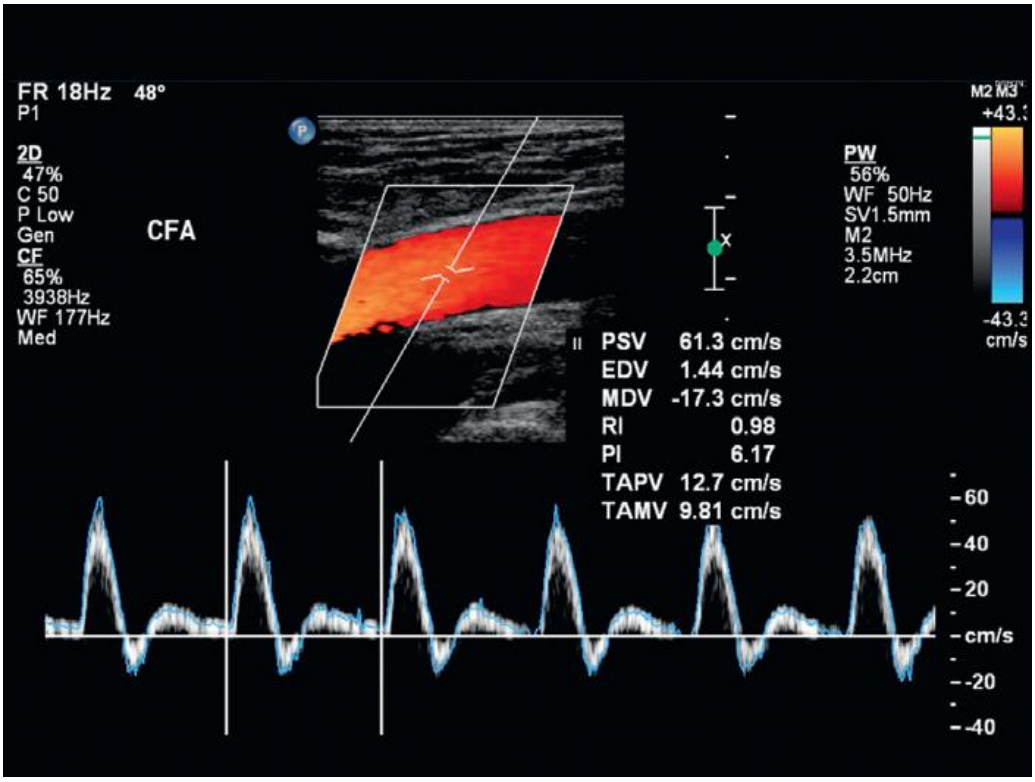

Figure 1.8: Triplex ultrasound imaging of a common femoral artery. The colour box required for colour Doppler imaging, and the sample volume and single Doppler beam axis of the spectral Doppler imaging are superimposed onto the B-mode image. The velocity shift-time plot, which is extracted from the spectral sampling volume, is displayed at the bottom. Quantitative parameters such as peak systolic velocity (PSV), end-diastolic velocity (EDV), minimum diastolic velocity (MDV), resistance index (RI), pulsatile index (PI), time-averaged peak velocity (TAPV) and time-averaged mean velocity (TAMV) can be calculated in contemporary systems (republished with permission of ELSEVIER, from Deane and Goss 2011).

Demodulation and high-pass filtering

The Doppler frequency shift produced by a moving target is a very small fraction of the transmitted frequency. For example, if a 5 MHz frequency is transmitted (f_t) from a target moving with speed 1 $m \cdot s^{-1}$ and the insonation angle is 0°, the resulting Doppler shifted signal (f_d) is 6.5 kHz (see Equation 1.1). Assuming that the direction of the moving target is toward the transducer then the received frequency (f_r) is 5.0065 MHz. The extraction of Doppler frequency shift from the received frequency is applied by the ultrasound system and is called *demodulation* (Figure 1.9).

The received signal from the colour box region includes signal from moving blood, which has high frequency and low amplitude, and signal from stationary and slow

moving tissue which has low frequency and high amplitude. The noise from stationary and slow moving tissue is known as *clutter* signal and is commonly removed with a *cut-off filter*. This high pass filter removes the frequencies below a specific threshold. An unfortunate consequence of this technique is the loss of Doppler frequency shifts from slowly moving blood (Figure 1.9) (Hoskins 2010).

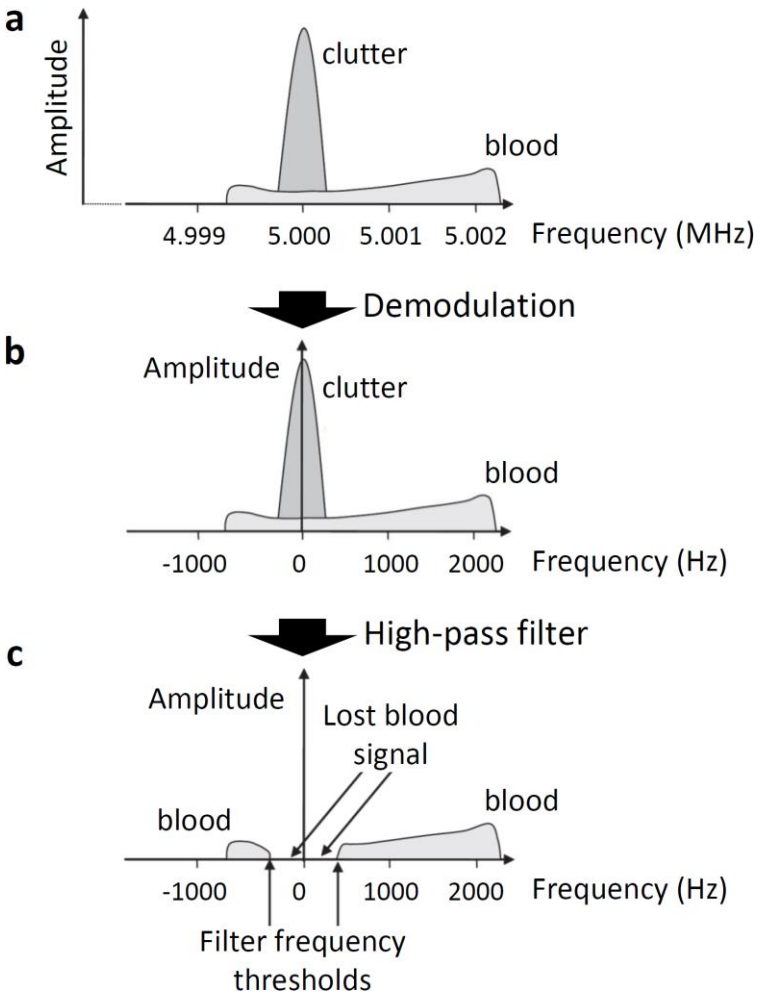

Figure 1.9: Demodulation and high-pass filtering of received Doppler signal. (a) Received Doppler signal from a vascular region consists from low amplitude signal from moving blood and high amplitude clutter signal from stationary and slowly moving tissue. (b) Demodulation removes the high frequency transmitted ultrasound signal leaving the Doppler shifted ultrasound signal. (c) The high-pass filter removes the high amplitude clutter signal (reproduced with permission of Cambridge University Press, from Hoskins 2010).

Aliasing

Blood flow in a vessel consists of low velocity flow near the wall and high velocity flow in the centre. As a result there is a range of Doppler frequency shifts along a

Doppler scan line so thousands of pulses are required for their detection. The frequency or sampling rate of these pulses is known as pulse repetition frequency (PRF) and can be adjusted by the colour scale control. If the PRF is too low the estimated Doppler shifted signal will be incorrect. This phenomenon is known as *aliasing* and is explained in Figure 1.10. A Doppler signal is shown in Figure 1.10a. This signal is correctly sampled in Figure 1.10b where the PRF is high and the number of samples is sufficient. In Figure 1.10c the signal is sampled at just two samples per cycle. This is known as the *Nyquist limit,* as reducing the sampling rate below this would result in an insufficient and incorrect calculation of Doppler shifted frequency as shown in Figure 1.10d. The Nyquist limit mathematically expresses that the maximum Doppler frequency shift (f_d) that can be detected is equal to half the PRF.

$$f_d = \frac{PRF}{2} \qquad \textbf{1.3}$$

When aliasing occurs, the colours in the image *wrap around* and the maximum colour of one direction is displayed instead as the maximum colour of the opposite direction (Gibbs et al. 2009; Hoskins 2010).

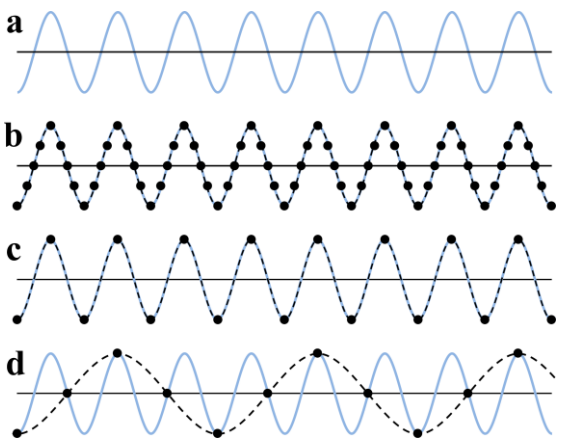

Figure 1.10: Aliasing. (a) Returned Doppler signal (f_d). (b) The returned Doppler signal is correctly detected because PRF > f_d/2. (c) The returned Doppler signal is just sampled sufficiently with two samples per cycle; PRF = f_d/2. (d) There are less than two samples per cycle and the detection of the returned Doppler signal is incorrect; PRF < f_d/2.

Spectral Doppler

Spectral Doppler allows the evaluation of blood flow in a very small sample volume. The sample volume lies across a single Doppler beam axis and is positioned in the

region of interest within a vessel. The sample volume and single Doppler beam axis are superimposed onto the B-mode image. The colour Doppler can also be part of the assessment and this technique is known as *triplex imaging* (Figure 1.8). The information from the sample volume is displayed as a frequency- or velocity-shift versus time plot. The vertical distance from the baseline corresponds to Doppler frequency or velocity shift and the greyscale of the plot indicates the amplitude of the detected signal (Gibbs et al. 2009; Hoskins 2010).

1.5.3 Vector Doppler

Conventional colour Doppler imaging is limited to displaying the direction and magnitude of velocity along the transmitted ultrasound beam and is dependent on the angle between the transducer and the vessel. This angle dependence is very restrictive because most vessels run relatively parallel to the skin and so the dominant velocity component of blood follows the same direction. To some extent, this is reduced by tilting the Doppler beam (electronically) and the probe, but there is always significant remaining angle dependence between the ultrasound beam and the flow; for instance at an angle of 60° a velocity of 1 $m \cdot s^{-1}$ is displayed as 0.5 $m \cdot s^{-1}$. The angle dependence is also affected by secondary flow phenomena in vessels. These phenomena are particularly intense in bifurcations (Karino et al. 1987; Udesen et al. 2007), stenoses (Blake et al. 2009; Hoskins 1997), graft anastomoses (Doorly and Sherwin 2009) and the heart (Cimino et al. 2012; Uejima et al. 2010). The velocity vector of blood flow is further affected by pulsatile cardiac pumping. Therefore colour flow imaging is not reliable for quantification and diagnosis based on velocity magnitude. Moreover, its limitation to detect only one component of the velocity direction (toward or away from the transducer) reduces its ability to characterise vortical structures, where at least two components of the velocity vector are required.

Spectral Doppler is more reliable than colour Doppler for the measurement of velocity magnitude in a small volume, because the Doppler beam can be steered electronically and positioned parallel to the vessel wall. Although it is still subjected to increased errors in regions of complicated flow patterns and non-straight vascular geometries

where alignment of the beam with the wall vessel is not feasible (Evans 2011; Hoskins 2010; Hoskins 2011).

Angle dependence was recognised as a problem for investigating blood flow at the advent of Doppler ultrasound. The first proposed methods to obtain angle independent flow velocity focused on small sample volumes using multiple cross beams to determine the velocity from different directions (Fox and Gardiner 1988; Fox 1978). Later on Fei et al. (1994), Hoskins et al. (1994) and Maniatis et al. (1994) applied cross beam approaches in colour Doppler scan planes to produce vector Doppler maps. Vector Doppler imaging does not only remove the angle dependence but also depicts the vortical structures in the scan plane. More recently, different novel techniques have been proposed showing results of real-time vector Doppler imaging (Garcia et al. 2010; Jensen and Munk 1998; Ohtsuki and Tanaka 2006). The vector Doppler technique by Jensen and Munk (1998) was the first to be integrated in a commercial system (Hansen 2011; Pedersen et al. 2011; Pedersen et al. 2012) (Figure 1.11). Vector Doppler provides two components of velocity in the scan plane allowing further fluid dynamic parameters to be extracted. For instance, Mehregan et al. (2014) applied a core vorticity technique to quantify left ventricular vortices.

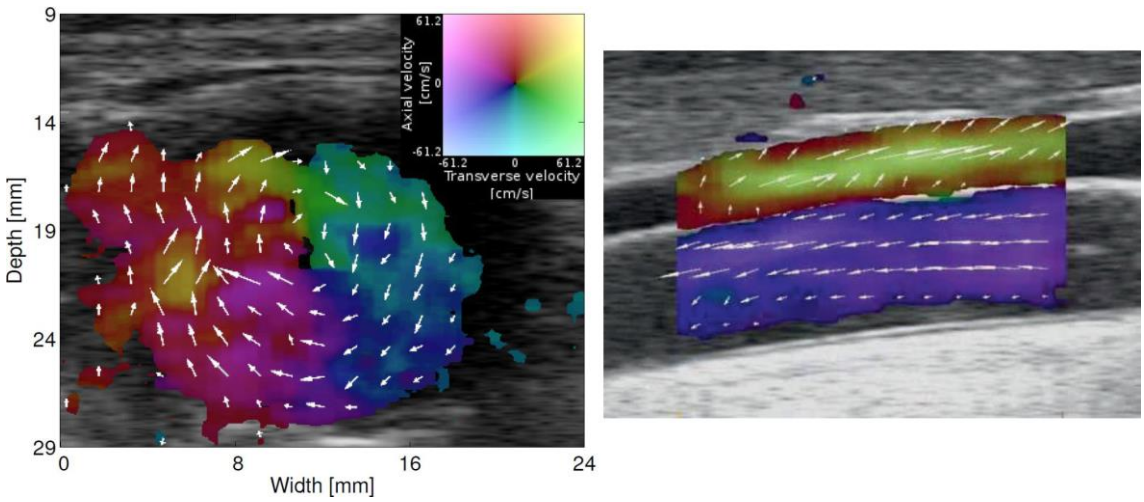

Figure 1.11: Clinical examples of real-time vector Doppler imaging. Left: Transverse view of the abdominal aorta showing secondary flow motion; the colours of the vector Doppler mapping are explained in the upper right corner (republished from Pedersen et al. 2011, © 2011 IEEE). Right: Longitudinal view of the common carotid artery (top) and jugular vein (bottom) illustrating bidirectional blood flow (republished with permission of Springer, from Hansen et al. 2011).

1.6 Flow phantoms and fluid mechanics

A flow phantom is an attempt to simulate the flow of blood in the cardiovascular system. It consists of tissue mimicking material (TMM), blood mimicking fluid (BMF), vessel mimicking tubing and a pump which circulates the BMF. The schematic diagram of a flow phantom is shown in Figure 1.12.

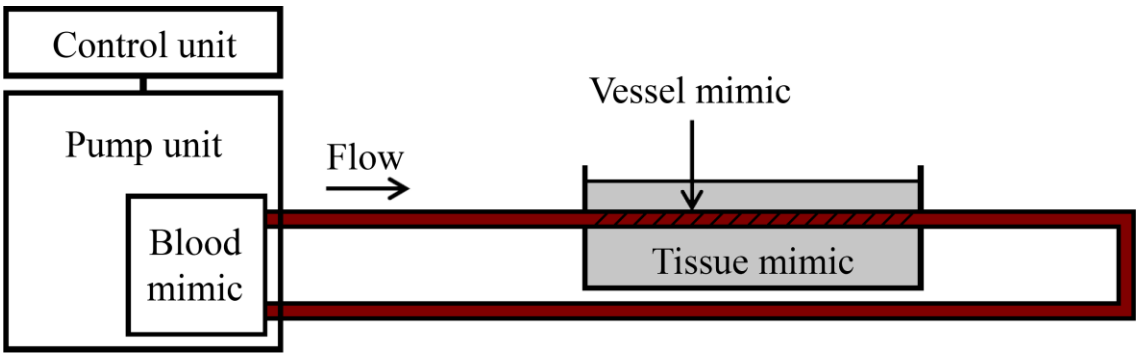

Figure 1.12: Schematic diagram of a flow phantom.

A variety of pumps have been used to develop ultrasound flow phantoms including piston, gear, roller and centrifugal. These systems can produce constant and physiologic pulsatile waveforms.

The quality of flow phantoms for ultrasound imaging is critically dependent on the physical properties of the mimicking components that the acoustic wave passes through. Three important parameters related to the transmission of ultrasound are the speed of sound, attenuation and density. Different mimicking materials with different speed of sound can cause refraction of the ultrasound wave at their boundaries resulting in displacement of the structures in an image and miscalculation of parameters like velocity. The product of density and speed of sound of a material defines its acoustic impedance. The reflection of the ultrasound beam at the interface of two mimicking components is highly related to the difference in their impedance. An increased attenuation coefficient of a mimicking component causes extended absorption of the ultrasound and restricts its propagation. The development of BMF is particularly demanding because parameters such as the size, density and concentration of the scattering particles affect the BMF backscatter properties, while viscosity affects its

rheological properties. The elastic modulus of tissue and vessel mimics affects their stiffness and can be very important on pulsatile flow studies. In general, the physical parameters of human tissues are used as reference in the development of ultrasound flow phantoms (Hoskins 1994, 2007, 2008; Martin and Ramnarine 2010).

A flow phantom enables assessments which can be practically and ethically very difficult in patients. Physiologic (King et al. 2011; Meagher et al. 2007), stenosed (Blake et al. 2009; Hoskins 1997; Poepping et al. 2004) or implanted vessel phantoms can be designed for ultrasound applications.

1.6.1 Viscosity

Viscosity, or more precisely dynamic viscosity, describes the resistance of a fluid to deformation by shear forces. In a flow through a pipe, this resistance is due to frictional forces between the particles of the fluid and between the wall boundary and the fluid. Thus the velocity v of the fluid is zero at the wall boundary and increases with the distance y from the wall as it is presented in Figure 1.13.

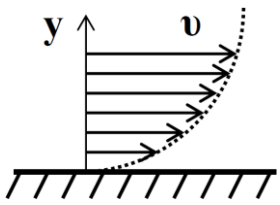

Figure 1.13: The velocity in a pipe is zero at the wall boundary and is increased with distance.

The spatial gradient of velocity or variation of velocity with distance (dv/dy) is known as shear rate. Dynamic viscosity μ is defined as the ratio of the shear stress τ to shear rate.

$$\mu = \frac{\tau}{dv/dy} \qquad \textbf{1.4}$$

The SI unit of dynamic viscosity is pascal-second (Pa·s = N·s/m^2 = kg/m·s).

The viscosity of a fluid depends on the relationship between the shear stress and shear rate (Figure 1.14). A fluid with a linear relationship between shear stress and shear rate

is known as a Newtonian fluid. The viscosity of a Newtonian fluid is constant (e.g. water). A fluid with a nonlinear relationship between shear stress and shear rate is known as a non-Newtonian fluid. Non-Newtonian fluids can be separated to:

- Bingham plastic. A yield stress is required before flow starts (e.g. toothpaste).
- Shear thinning. The viscosity decreases with increasing shear rate (e.g. blood).
- Shear thickening. The viscosity increases with increasing shear rate (e.g. cornstarch solutions)

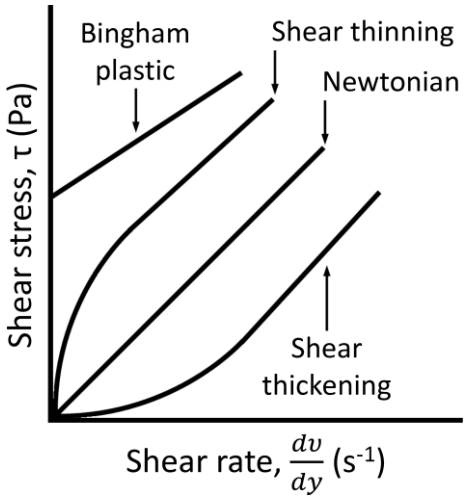

Figure 1.14: Shear stress – shear rate behaviour for Bingham plastic, shear thinning, shear thickening and Newtonian fluids.

Dynamic viscosity of a fluid is often expressed over its density ρ and this quantity is called kinematic viscosity v.

$$v = \frac{\mu}{\rho} \qquad \textbf{1.5}$$

The SI unit of kinematic viscosity is $m^2 \cdot s^{-1}$ (Morrison 2013).

Blood viscosity doesn't only decrease in a nonlinear way with increasing shear rate but it also depends on haematocrit and fibrinogen content (Slager et al. 2005). In experimental and computational applications blood is commonly assumed to be a Newtonian fluid with viscosity in the range of 3.4 - 4 mPa·s (Hoskins 2008; Marshall et al. 2004).

1.6.2 Reynolds number

The Reynolds number *Re* of a fluid is a dimensionless parameter, which is defined as the ratio of inertial to viscous forces. For the flow in a pipe it is expressed by Equation 1.6.

$$Re = \frac{\rho \bar{v} D}{\mu} = \frac{\bar{v} D}{\nu} \quad \textbf{1.6}$$

where ρ is the fluid density, $\bar{v}$ the mean axial velocity, D the pipe diameter (m), μ the dynamics viscosity and ν the kinematic viscosity.

The Reynolds number of a fluid is related to its flow state. When Reynolds number is less than 2100 the flow is considered laminar and when it is greater than 4000 the flow is considered turbulent. With laminar flow fluid elements follow parallel paths, whilst with turbulent flow they follow time varying erratic paths. Reynolds numbers between 2100 and 4000 are related to transition states where the fluid may be subjected to intermittent periods of turbulent and laminar flow (Morrison 2013).

1.6.3 Inlet length

The geometry of a pipe affects the three-dimensional (3D) flow profile in it. Steady flow through a straight pipe produces a flat velocity profile at the pipe entrance because of the minimal forces of viscosity. Beyond a certain distance known as the *inlet length*, the velocity profile becomes parabolic and remains unchanged. A formula for the inlet length L is expressed by Equation 1.7 and applies in both steady and pulsatile flow.

$$L = 0.04\, D\, Re \quad \textbf{1.7}$$

where D is the inner diameter of the pipe and *Re* is the Reynolds number (McDonald 1960; Nichols and O'Rourke 2005). It is general practice in flow phantoms to take into consideration the inlet length prior to the region of interest. This verifies a stable velocity or time-varying velocity profile and standardises the setup (Hoskins 2008).

1.7 Computational fluid dynamics in vascular models

It is well accepted that blood flow influences the endothelial behaviour and can be a source of atherosclerosis and neo-intimal hyperplasia (Caro 2009; Malek et al. 1999). Imaging techniques are widely used in diagnosis of vascular disease but they can only detect a small fraction of useful physical information. They are mainly focused on the geometry and structure of the vessels but they remain limited on the characterisation of the 3D blood flow field. The detailed 3D analysis of blood flow is possible with computational fluid dynamics (CFD) (Hoskins and Hardman 2009).

CFD uses numerical methods and algorithms to solve and analyse a flow field such as that of blood within the vascular system. Initially, the geometry of the examined region is required and can be obtained either by computer-aided design (CAD) or by using an imaging modality. In the second approach the vascular region of interest is scanned and the geometry of the lumen is extracted. The method is known as *image-guided modelling* and is considered preferable because it is based on physical and not idealised geometries. The volume of the lumen is discretised in small cells creating a computational volume mesh. Solving the viscous forces near the wall boundary is demanding and for this reason the size of the cells is commonly decreased moving outwards from the centreline of the volume mesh to its perimeter. The physical properties of the flow are specified in the inlet and outlet boundaries of the mesh and the flow field is solved based on the Navier-Stokes governing equations of flow. These are the principle of conservation of momentum and the continuity equitation, which for a steady-state flow of an incompressible, Newtonian, homogeneous fluid are defined by Equation 1.8 and 1.9 respectively.

$$\rho(v \cdot \nabla)v = -\nabla p + \mu\nabla^2 v \qquad \textbf{1.8}$$

$$\nabla \cdot v = 0 \qquad \textbf{1.9}$$

where ρ is the density, v the velocity, p the pressure and μ the dynamic viscosity (Grigioni et al. 2005).

There is an increased interest for CFD applications in the cardiovascular system. Ideally such CFD simulations need to be validated with experimental data (ISO 5840:2005).

1.8 Aims of thesis

The literature review introduces spiral flow in vessels and explains that single spiral flow is a physiologic characteristic of blood circulation that may protect a vessel from stenosis. Based on this hypothesis modified spiral prosthetic graft designs have been proposed for the introduction of a single spiral in their outflow as a way of improving patency rates. Promising results from computational, animal and particularly clinical studies have motivated this thesis in a bid to assess spiral and conventional prosthetic grafts for PV and AV applications. The aims of this thesis are:

- To determine the ability of PV and AV spiral grafts to introduce a single spiral flow;
- To compare the flow patterns induced by spiral grafts with those induced by conventional devices;
- To detect fluid dynamic parameters associated with advanced haemodynamics in order to explain the mechanisms of spiral flow grafts that lead to improved patency rates in clinical practice;

1.9 Thesis outline

This thesis can be separated in two parts. The experimental, which is described in chapters 2, 3 and 4, and the computational, which is described in chapters 5 and 6.

Chapter 2 describes the development and validation of ultrasound flow phantoms and 2D vector Doppler and vorticity imaging using conventional ultrasound.

Chapter 3 describes the development of in-house vascular-graft phantoms for the experimental testing of spiral and conventional PV grafts. It then goes on to compare the flow patterns induced by both types of grafts using vector Doppler and vorticity maps and applying quantitative assessments.

Chapter 4 contains the development of in-house vascular-graft phantoms for the experimental analysis of spiral and non-spiral AV grafts. Vector Doppler and vorticity

mapping is utilised to visualise the flow phenomena induced by both types of prostheses and to quantify their flow profile.

In chapter 5, the experimental PV models were subjected to computational comparisons. The results of this study were validated with the results from chapter 3. CFD provided information of the 3D flow field and thus apart from the visualisation of secondary flow motions using velocity and vorticity, it allowed the extraction of several quantitative parameters for comparison.

In chapter 6 the ultrasound AV flow phantoms were subjected to computational comparisons. The experimental data from chapter 4 was used to validate the numerical approach. Secondary flow motions and a number of quantitative parameters were compared in the outflow of the spiral and control graft.

Chapter 7 discusses aspects that apply to both the experimental and computational work of chapters 2 – 6.

Chapter 8 concludes this thesis and provides suggestions for future work related to this research.

Chapter 2

Two-dimensional ultrasound and flow quantification in vascular phantoms

2.1 Introduction

The evolving understanding of the role of local haemodynamics in endothelial function and the proliferation of vascular smooth muscle (Caro 2009; Malek et al. 2013; Slager et al. 2005a, 2005b), serves to increase the interest for more detailed velocity profiles and fluid dynamic assessments. Vector Doppler imaging has been proposed to reduce the angle dependence error of Doppler ultrasound and to provide 2D flow maps, which are particularly useful for the assessment of secondary flow motions. Vector Doppler imaging can be applied to both clinical and experimental studies and allows the application of fluid mechanic quantities such as vorticity and circulation. Hence, vector Doppler and extracted quantities can provide a further insight of vortical structures in the cardiovascular system (Siggers and Waters 2005, 2008).

This chapter focuses on the validation of the methodology that is applied in both chapters 3 and 4. The overall design of the applied ultrasound flow phantoms and properties of the utilised mimicking components are described. The development of 2D velocity and vorticity maps from conventional colour flow ultrasound is presented, as well as their validation using numerical and experimental techniques.

2.2 Ultrasound flow phantoms

2.2.1 Materials and methods

PV and AV prosthetic grafts, suitable for clinical applications, were housed in flow phantoms for experimental ultrasound imaging assessments. The outflow or distal end of both types of grafts was connected to in-house polyvinyl alcohol cryogel (PVA-c) vessel mimic tubing, with an end-to-side anastomosis. These PV and AV vascular-graft models were placed in an in-house acrylic tank of dimensions 485×180×60 mm (L×W×D) under the required geometry. The geometry of these vascular-graft models are not in the scope of this chapter and are described in detail in chapter 3 for the PV models and in chapter 4 for the AV models.

A range of holes were available in the sidewalls of the tank to facilitate the connection of each vascular-graft model with a flow pump. The outflow of the pump was connected with the inflow of the tank and the outflow of the tank with the inflow of the pump using polyvinyl chloride (PVC) tubing. Straight, rigid 60 mm long PVC screw connectors supported these connections. The inner diameter of all flow components was 6 mm. An overview of the flow phantom setup is shown in Figure 2.1.

The acrylic tank was filled with a liquid medium glycerol based TMM, covering the vascular-graft model. Its composition by volume was 9% glycerol (J.M. Loveridge Ltd, Andover, UK) and 91% distilled water. Blood was simulated with the *model 707* (ATS Laboratories, Bridgeport, CT, USA) BMF. Air bubbles in the BMF circulation is a common problem of flow phantom assessments. For ultrasound applications this can significantly affect the image quality. The absence of bubbles was verified before data collection with spectral Doppler. Air bubbles appear as spikes in a Doppler waveform.

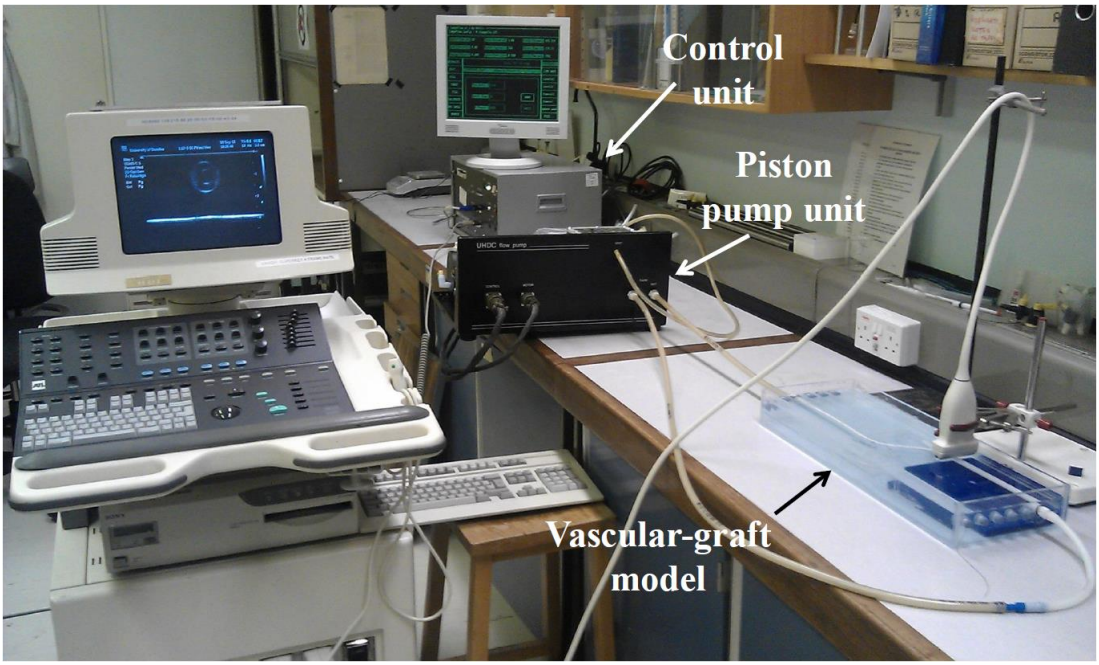

Figure 2.1: Flow phantom setup and ultrasound system.

Flow pump

The flow pump was a UHDC computer controlled piston system (Shelley Medical Imaging Technologies, London, ON, Canada). The manufacturer claims a steady cycle-to-cycle reproducibility with standard deviation of less than 1% for constant flow rates up to 35 $mL \cdot s^{-1}$. The outflow of the pump was tested for the flow rates applied in this work (4, 6, 8, 10 and 12 $mL \cdot s^{-1}$) to verify accuracy and consistency. A measuring cylinder with 1 mL accuracy was used. The pump running period was 10 s and all measurements were repeated three times.

In-house vessel mimic tubing

A 15% PVA (PVAGELS, Marquette, MI, USA) and 0.46% benzalkonium chloride concentration by weight were added to distilled water and boiled for four to five hours under high pressure, creating a gel like material known as PVA-c. The benzalkonium chloride antibacterial agent was added to increase the lifetime of the vessel mimic tubing (King et al. 2011).

A stainless steel mould was designed and manufactured to create the vessel mimic tubing using PVA-c. This mould consisted of a 6 mm diameter rod centred within a

13 mm inner diameter tube. A PVC flange was positioned at each end of the mould to keep the rod centred (Figure 2.2). The rod was lubricated with silicone grease to aid the vessel mimic removal at the end of the moulding process. A see-through injection port was bored at one end of the tube for injection of the PVA-c (Dineley et al. 2006).

The PVA-c was injected into the mould using a syringe and the mould was left to stand upright for 12-15 hours to allow air bubbles to settle. The mould was subjected to six continuous freeze-thaw cycles at ± 20 °C to reach the required velocity properties for ultrasound and to increase the elasticity thus providing a durable vessel mimic. The freeze period was 10 hours and the thaw 12 hours. The vessel mimic was removed from the mould and stored in a container filled with water in a fridge. This prevented dehydration and increased its lifetime.

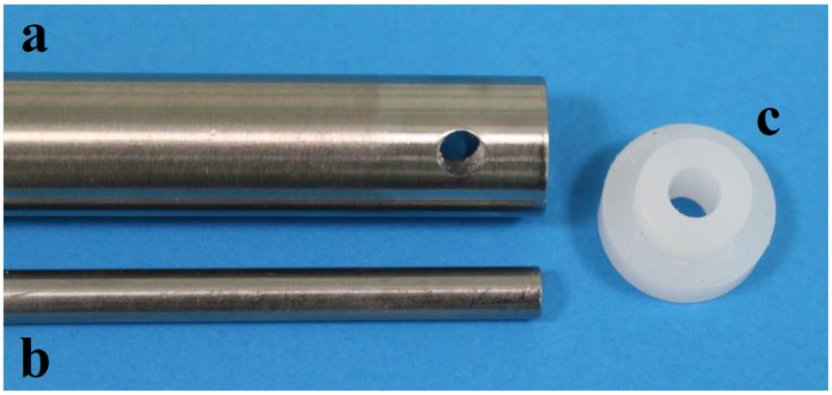

Figure 2.2: One end of the vessel mimic mould. (a) Stainless-steel tube where the see-through injection port can be seen. (b) Stainless-steel rod. (c) Plastic flange (republished with permission of ELSEVIER, from Kokkalis et al. 2013).

Physical properties of phantom mimicking components

The blood, tissue and vessel mimicking components were chosen to have similar acoustic properties to each other that matched those from relevant human tissues. Differences in the propagation speeds of these components would cause refraction of the ultrasound beam, resulting in distortion of the detected Doppler frequency shifts (Hoskins 1994, 2007, 2008).

The acoustic properties and density of the BMF are provided from the manufacturer (ATS 2011), while those of the TMM are available from previous studies (Hoskins 1994, 2008). These properties are summarised in Table 2.1. They were within the

specifications of the International Electrotechnical Commission (IEC), presented in Table 2.2 (IEC 2001), providing the appropriate acoustic match.

Table 2.1: Physical properties of applied blood and tissue mimicking components.

	Material	Density ($kg\ m^{-3}$)	Velocity ($m\ s^{-1}$)	Attenuation ($dB\ cm^{-1}\ MHz^{-1}$)	Reference (year)
BMF	n/a	1040 ± 10	1571 ± 15	< 0.1	Manufacturer
TMM	Glycerol	1023	1539	–	Hoskins (1994, 2008)

Table 2.2: The International Electrotechnical Commission specifications for blood and tissue mimic.

	Density ($kg\ m^{-3}$)	Velocity ($m\ s^{-1}$)	Attenuation (f $dB\ cm^{-1}\ MHz^{-1}$)
Blood mimic	1050 ± 40	1570 ± 30	< 0.1
Tissue mimic	n/a	1540 ± 15	0.5 ± 0.05

where f the acoustic-working frequency

The viscosity of the utilised BMF was 1.7 mPa·s at room temperature. The IEC recommendation for viscosity is 4 ± 0.4 mPa·s (IEC 2001). Viscosity does not have a significant effect on the ultrasound beam propagation but affects the rheological properties of the fluid.

To calculate the density of the vessel mimic, the weight of a sample was measured with a laboratory precision scale and divided over its volume, which was measured with a graduated measuring cylinder.

The speed of sound and attenuation of the vessel mimic were detected with an ultrasound characterisation setup. A transmission and a reception transducer (Sonatest, Milton Keynes, UK) operating at 4.8 MHz, were aligned facing each other and positioned in the centre of a tank. A PVA-c sample moulded in a rectangular box of dimensions 60×50×45 mm (L×W×D) was positioned centrally between the transducers. The tank was filled with degassed water and measurements started after two hours to allow the setup to reach thermal equilibrium with the room temperature (21 °C). A signal generator (DSOX3024A, Agilent Technologies, Santa Clara, CA, USA) was used

to excite the ultrasound pulses and an oscilloscope (MSO7104A, Agilent Technologies, Santa Clara, CA, USA) to monitor both the transmitted and received signals. Measurements were undertaken at three time points, first without the sample in place and then with the sample in place. A schematic diagram is shown in Figure 2.3.

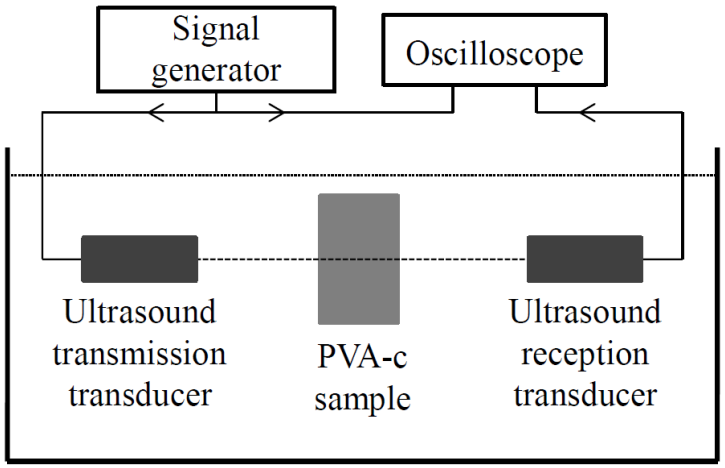

Figure 2.3: Ultrasound characterisation setup.

The speed of sound in the sample (c_s) was deduced from Equation 2.1

$$c_s = \left(\frac{1}{c_w} - \frac{\Delta_t}{\Delta_x}\right)^{-1} \quad \textbf{2.1}$$

where c_w is the speed of sound in water, Δ_t is the temporal shift between the pulse transit times with and without the sample and Δ_x the thickness of the sample (Zell et al. 2007).

The attenuation coefficient of the sample (α_s) was calculated using Equation 2.2.

$$\alpha_s = \alpha_w - \frac{1}{\Delta x}[\ln A_s - \ln A_w - 2\ln(1-R)] \quad \textbf{2.2}$$

where α_w is the attenuation coefficient of water, Δx the thickness of the sample, A_s the amplitude of the received ultrasound pulse with the sample in position, A_w the amplitude of the received ultrasound pulse without the sample in position and R the acoustic reflection coefficient at the interface between the water and the sample.

The attenuation coefficient of water was calculated using Equation 2.3.

$$\alpha_w = 2.5 \times 10^{-4} f^2 \quad \textbf{2.3}$$

where the attenuation coefficient has units of cm^{-1} and the frequency f of MHz (Zell et al. 2007).

The acoustic reflection coefficient depends on the difference between the acoustic impedance of the water and the sample as shown in Equation 2.4.

$$R = \frac{z_s - z_w}{z_s + z_w} \quad \textbf{2.4}$$

where z_s and z_w represent the acoustic impedance of the sample and the water medium respectively. The impedance of each material is given by Equation 2.5.

$$z = \rho c \quad \textbf{2.5}$$

where ρ is the density and c the velocity of sound in the medium. The attenuation conversion factor from cm^{-1} to $dB\ cm^{-1}$ is 8.686 (Spirou et al. 2005; Zell et al. 2007).

2.2.2 Results

Measurements from the accuracy and consistency testing of the flow pump system are shown in Table 2.3.

Table 2.3: Testing of flow pump accuracy.

Flow rate (mL s^{-1})	Duration (s)	Run 1 (mL s^{-1})	Run 2 (mL s^{-1})	Run 3 (mL s^{-1})	Mean (± S.D.) (mL s^{-1})	Precision (% ± S.D.)
4	10	41	40.5	39	40±1	-0.4±2.6
6	10	58	60	59.5	59.2±1	-1.4±1.7
8	10	78	78	79.5	78.5±0.9	-1.9±1
10	10	98	103	102.5	101.2±2.8	1.2±2.8
12	10	124	118	123.5	121.8±3.3	1.5±2.8

An example of the vessel mimic tubing is shown in Figure 2.4a. Its inner diameter was measured with b-mode ultrasound in the cross section and found to be 5.4 mm (Figure 2.4b).

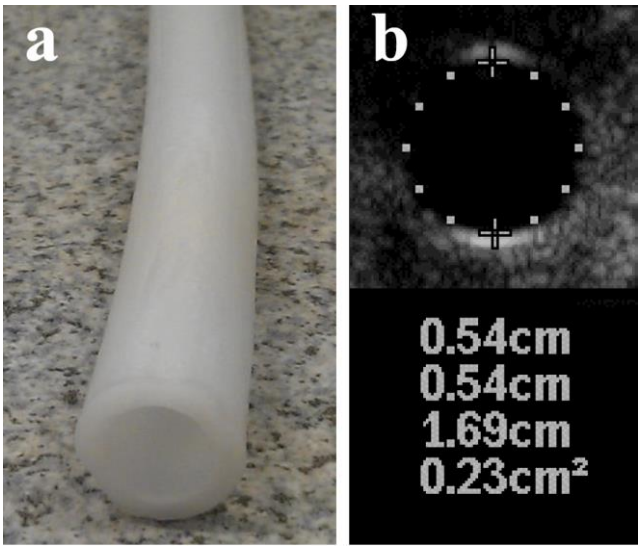

Figure 2.4: (a) PVA-c vessel mimic tubing. (b) B-mode cross-section image of the tube and measurement of its inner diameter (0.54 cm).

The acoustic properties of the vessel mimicking material (VMM) are presented in Table 2.4.

Table 2.4: Physical properties of the vessel mimicking material.

	Material	Density ($kg\ m^{-3}$)	Velocity ($m\ s^{-1}$)	Attenuation ($dB\ cm^{-1}\ MHz^{-1}$)
VMM	PVA-c	1025	1537 ± 3.7	0.14 ± 0.001 (at 4.8 MHz)

2.2.3 Discussion

The outflow of the pump was found to be reliable with precision of more than 4% (Table 2.3). The small errors were possibly associated with the interaction between the control unit and the operator.

The inner diameter of the vessel mimic tubing was measured 5.4 mm, although the stainless steel rod of the vessel mimic tubing mould was 6 mm. This difference was due

to shrinkage of the PVA-c when it was removed from the rod and was most likely related to the freeze-thaw moulding process.

The sound velocity of the applied PVA-c was close to that of the TMM and BMF minimizing the possibility of beam refraction in their interfaces. King et al. (2011) reported in their validation study of recipes for PVA-c anatomical vessels, that the optimum recipe had a velocity of 1538 ± 5 m·s^{-1}. The velocity of sound in normal human arterial wall tissue has been measured between 1492 and 1534 m·s^{-1} by Greenleaf et al. (1974). Duck (1990) has reported velocities in the human aorta of between 1560 and 1660 m·s^{-1} and in large bovine blood vessels of between 1559 and 1575 m·s^{-1}.

There are no IEC specifications for VMMs. The main requirement during this study was for the PVA-c vessel mimic to withstand peak physiologic flow rates similar to that observed in the upper and lower limps, exhibit the flexibility to facilitate the construction of vascular-graft models and match the velocity of the BMF and liquid medium TMM. Previous PVA-c vessel mimic studies have shown that the elastic modulus of PVA-c reaches a plateau after 5-7 freeze-thaw cycles (Chu & Rutt 1997; Dineley et al. 2006; King et al. 2011). Dineley et al. (2006) found the elasticity upper limit of 330 ± 21 kPa for a 15% PVA-c concentration after 7 cycles and King et al. (2011) quoted 160 kPa for a 10% PVA-c concentration after 5 cycles. In this study 6 cycles were applied to assure increased elasticity. The elastic properties of physiologic arteries vary greatly with age, body size and their site in circulation. More specifically, the Young's modulus at a physiologic pressure (100 mm Hg) varies from few hundred kPa to more than 2000 kPa (Caro et al. 2012).

Blood is commonly assumed to be a Newtonian fluid with viscosity in the region of 3.4 – 4 mPa·s. The decreased viscosity of the applied BMF can affect the secondary flow motions within the vascular graft model. This is examined in chapter 5.

2.2.4 Conclusions

A flow phantom setup for the testing of vascular-graft models and the development of in-house produced PVA-c vessel mimic tubing were presented. The acoustic properties

of this vessel mimic were measured. The appropriate matching of these properties with those of the utilised blood and tissue mimics was shown. This was important to this study as it minimised beam refractions in material interfaces and distortions of the recorded ultrasound data.

2.3 Spiral flow methodology

2.3.1 Detection of spiral flow using ultrasound

Spiral flow patterns can generally be detected in blood vessels and flow phantoms with colour flow ultrasound in a scan plane transverse to the flow direction; ideally in both the anteroposterior and right to left directions. The vortical structures appear in the image as red-blue areas or splits representing flow toward and away from the transducer (Frazin et al. 1990; Hoskins et al. 1994; Stonebridge et al. 1996). The number or red-blue splits in a scan plane is dependent on the number of vortices in it. For instance a single spiral appears as a single red-blue split with a dark band in the border dividing them. This border corresponds to velocities below the colour high-pass filter level. Examples of single- double- and four-spiral patterns detected with colour Doppler in a flow phantom are shown in Figure 2.5.

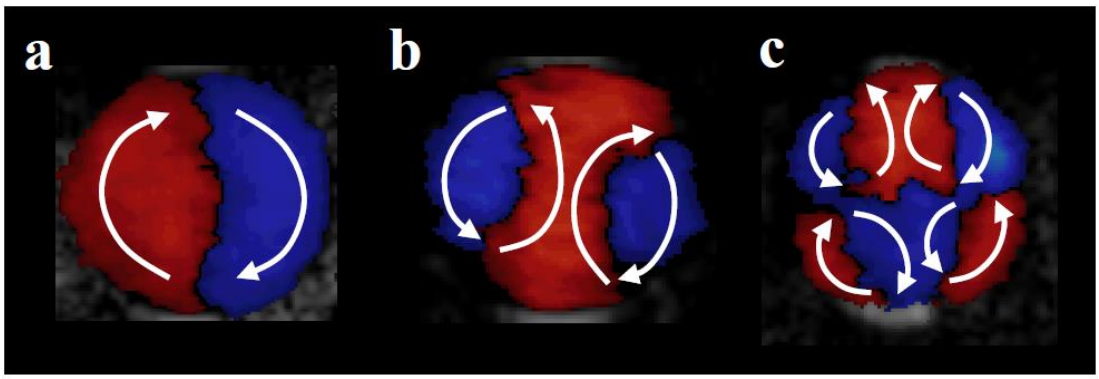

Figure 2.5: Spiral flow patterns detected with colour Doppler ultrasound in a flow phantom. (a) Single-spiral. (b) Double-spiral. (c) Four-spiral.

2.3.2 Two-dimensional vector Doppler ultrasound

Vector Doppler ultrasound provides a more reliable and clear presentation of spiral flow in blood vessels and flow phantoms than conventional colour Doppler. The vector Doppler technique, which is described below, was originally proposed by Hoskins et al. (1994). Colour Doppler data are acquired from two different steered beam-target angles in relation to the linear transducer transmission. The beams from the left and right apertures need to overlap in the region of interest. Assuming that the scan plane is parallel to the *x*-*y* plane of the Cartesian coordinate system, a 2D velocity vector, v_{xy}, can be calculated at each point in the region of interest by triangulation of the velocity information, v_L and v_R, which is recorded from the left and right apertures respectively (Figure 2.6).

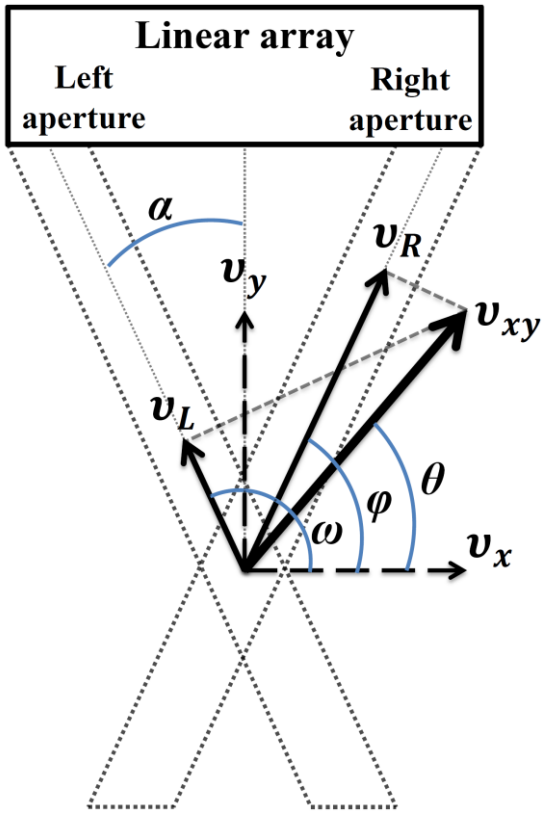

Figure 2.6: Schematic diagram of dual-beam vector Doppler.

The horizontal (v_x) and vertical (v_y) components of velocity vector v_{xy} can be obtained by compounding the velocities v_L and v_R.

$$v_x = \frac{v_L - v_R}{-2sin\alpha} \quad \textbf{2.6}$$

$$v_y = \frac{v_L + v_R}{2cos\alpha} \quad \textbf{2.7}$$

Then the magnitude, v_{xy}, and direction, θ, of the velocity vector can be calculated with Equations 2.8 and 2.9.

$$v_{xy} = \sqrt{v_x^2 + v_y^2} \quad \textbf{2.8}$$

$$\theta = atan\frac{v_y}{v_x} \quad \textbf{2.9}$$

Explanation of vector Doppler equations

It is know that:

$$\cos(180 - \varphi - \theta) = cos[180 - (\varphi + \theta)] = -\cos(\varphi + \theta) \quad \textbf{2.10}$$

$$\cos(\varphi - \theta) = cos\varphi cos\theta + sin\varphi sin\theta \quad \textbf{2.11}$$

$$\cos(\varphi + \theta) = cos\varphi cos\theta - sin\varphi sin\theta \quad \textbf{2.12}$$

Also from Figure 2.6:

$$\upsilon_x = v_{xy}\cos\theta \; and \; v_y = v_{xy}sin\theta \quad \textbf{2.13}$$

$$\upsilon_L = v_{xy}cos(180 - \varphi - \theta) \quad \textbf{2.14}$$

$$\upsilon_R = v_{xy}cos(\varphi - \theta) \quad \textbf{2.15}$$

Using Equation 2.10-2.15 accordingly and providing that $\alpha = 20°$ and $\varphi = 70°$, Equation 2.6 and Equation2.7 are proved as:

$$\begin{aligned} v_L - v_R &= v_{xy}cos(180 - \varphi - \theta) - v_{xy}cos(\varphi - \theta) \\ &= v_{xy}[-\cos(\varphi + \theta) - \cos(\varphi - \theta)] \\ &= v_{xy}(-cos\varphi cos\theta + sin\varphi sin\theta - cos\varphi cos\theta - sin\varphi sin\theta) \\ &= -2v_{xy}cos\varphi cos\theta = -2cos\varphi v_x = -2sin\alpha v_x \end{aligned} \quad \textbf{2.16}$$

$$\begin{aligned} v_L + v_R &= v_{xy}cos(180 - \varphi - \theta) + v_{xy}cos(\varphi - \theta) \\ &= v_{xy}[-\cos(\varphi + \theta) + \cos(\varphi - \theta)] \\ &= v_{xy}(-cos\varphi cos\theta + sin\varphi sin\theta + cos\varphi cos\theta + sin\varphi sin\theta) \\ &= 2v_{xy}sin\varphi sin\theta = 2sin\varphi v_y = 2cos\alpha v_y \end{aligned} \quad \textbf{2.17}$$

Based on Figure 2.6, Equation 2.18 is extracted as:

$$tan\theta = \frac{v_y}{v_x} \leftrightarrow \theta = atan\frac{v_y}{v_x} \quad \textbf{2.18}$$

2.3.3 Vorticity and circulation

Vorticity and circulation are flow characterisation parameters of fluid dynamics. They can be calculated when at least two components of velocity are known.

Vorticity

Vorticity $\vec{\omega}$ is a vector, or more precisely a *pseudo-vector*, which is defined as the curl of the fluid velocity field.

$$\vec{\omega} = \nabla \times \vec{v} \quad \textbf{2.19}$$

where $\vec{v}$ is the 3D velocity vector and ∇ the del operator.

For a 2D flow map parallel to the *x*-*y* plane, it is the axial component of the vorticity vector, ω_z, in which we are interested. This is defined as

$$\omega_z\hat{\mathrm{k}} = \left(\frac{\partial v_y}{\partial x} - \frac{\partial v_x}{\partial y}\right)\hat{\mathrm{k}} \quad \textbf{2.20}$$

where v_x and v_y are the components of the velocity vector $\vec{v}$ and $\hat{k}$ is the unit vector in the axial direction. In this case the vorticity vector is always perpendicular to the plane of the flow or parallel to axis *z* (Morrison 2013; Tritton 2007). The velocity components v_x and v_y of a 2D flow field can be calculated using the vector Doppler technique described in section 2.3.2 (Figure 2.6, page 40) and vorticity maps can be created based on colour flow ultrasound as discussed later in this thesis (chapters 3 and 4).

The relationship between the rotational motion of an element and the direction of the vorticity vector is described by the right-hand rule. The unit of vorticity is radians per second and because the radian is dimensionless, it can be defined as s^{-1} (Morrison 2013). The vorticity vector of a fluid particle is taken as twice its angular velocity (Wu et al. 2006).

Vorticity shows the spinning motions of elements in a fluid as a result of applied shearing and compression forces. An element of fluid may be considered to be translating (moving with no rotation) and rotating (rotating but with no translation). Vorticity only applies to the rotational component, so that a fluid element, which is translating but not rotating, has zero vorticity.

Circulation

Circulation, Γ, is the line integral around any arbitrary closed curve *C* of the velocity field $\vec{v}$ in a fluid. If *dl* is a unit element of curve *C* then this line integral is defined by the first part of Equation 2.21. If *S* is the surface which has the closed curve *C* as boundary and *dS* is a unit element of this surface, then from Stoke's theorem it can be seen that circulation is also equal to the integral of vorticity $\vec{\omega}$ in this area, as shown in Equation 2.21.

$$\Gamma_c = \oint_c \vec{v} \cdot dl = \int_s \vec{\omega} \cdot dS \qquad \textbf{2.21}$$

Circulation and vorticity are intimately related. Circulation is the product of length and velocity or area and vorticity. The unit of circulation is length squared over time ($m^2 \cdot s^{-1}$). This parameter allows quantification of the total strength of a vortex in a specific area (Morrison, 2013; Tritton, 2007).

In the rest of the thesis vorticity refers to axial vorticity, ω_z.

2.3.4 Ultrasound acquisition and processing

The spiral flow ultrasound data was recorded using a clinical ATL HDI 5000 scanner (ATL Ultrasound, Bothell, WA, USA) with a linear array transducer (L21-5) (Figure 2.1). The data was transferred to a workstation for off-line analysis using an in-house

suite of programs in MATLAB R2012a (The MathWorks, Natick, MA, USA). These programs were based on a previously written MATLAB toolbox known as XIFtoolbox v0.4.3 (Blake 2006) (freely available from the MATLAB File Exchange), which is able to read the raw HDI 5000 cine files (.XIF file format).

2.4 Testing the vector Doppler technique and vorticity using synthetic data

2.4.1 Materials and methods

Two characteristic vortical types were numerically simulated in the cross-flow view of a tube using MATLAB R2012a. For these simulations, steered velocity information was calculated to mimic the left and right steered Doppler velocities v_L and v_R (see Figure 2.6). It was assumed that the steering angles of these velocities were equal to minus and plus 20° respectively in relation to the linear transmission ($\alpha = 20°$ and $\varphi = 70°$ in Figure 2.6). The velocity information obtained was used to test the vector Doppler and vorticity equations (Equation 2.6 - 2.8 and 2.20 respectively).

The first vortical type was a counter-clockwise *rigid-body rotational flow pattern*. In such a flow type the particles translate in circular paths with speed proportional to their distance from the centre. At the same time they rotate around their axes at a constant rate due to the shear forces between adjacent trajectories. This flow is expected to have a steady positive vorticity (following the right-hand rule) due to the constant rate of self-rotation (Morrison 2013).

The second vortical type was a counter-clockwise pattern where the particles moved with a speed inversely proportional to their distance from the centre. As a result of this the shear forces keep the particles in a steady orientation so that they do not rotate around their axes. In other words the particles translate in a circular pattern but they do not rotate. The vorticity is zero and the flow pattern is known as *irrotational* (Morrison 2013).

These two flow types were chosen to test the vector Doppler and vorticity algorithms because of their characteristic vorticity flow patterns.

2.4.2 Results

Figure 2.7 illustrates the velocity direction, velocity magnitude and vorticity maps for the constructed rigid-body and irrotational counter-clockwise flow patterns. In the velocity direction maps, the length of the vectors is proportional to the magnitude of the velocity and the colour distribution represents the displacement of the velocity vector from 0° to 360°. In the velocity magnitude maps, the colour distribution represents the magnitude of the velocity. Vorticity maps correspond to axial vorticity, ω_Z, where positive regions are associated with counter-clockwise rotation. In all maps darkest blue and darkest red symbolise the lower and upper limits of the values measured.

These maps show that the particles translate with a speed proportional to their distance from the centre for the rigid-body flow pattern and inversely proportional to their distance from the centre for the irrotational flow pattern. The rotating nature of each case is presented with the vorticity maps, where constant positive vorticity is shown for the rigid-body flow and zero for the irrotational flow. The existence of vorticity in the centre of the latter case is the result of zero velocity in the centre.

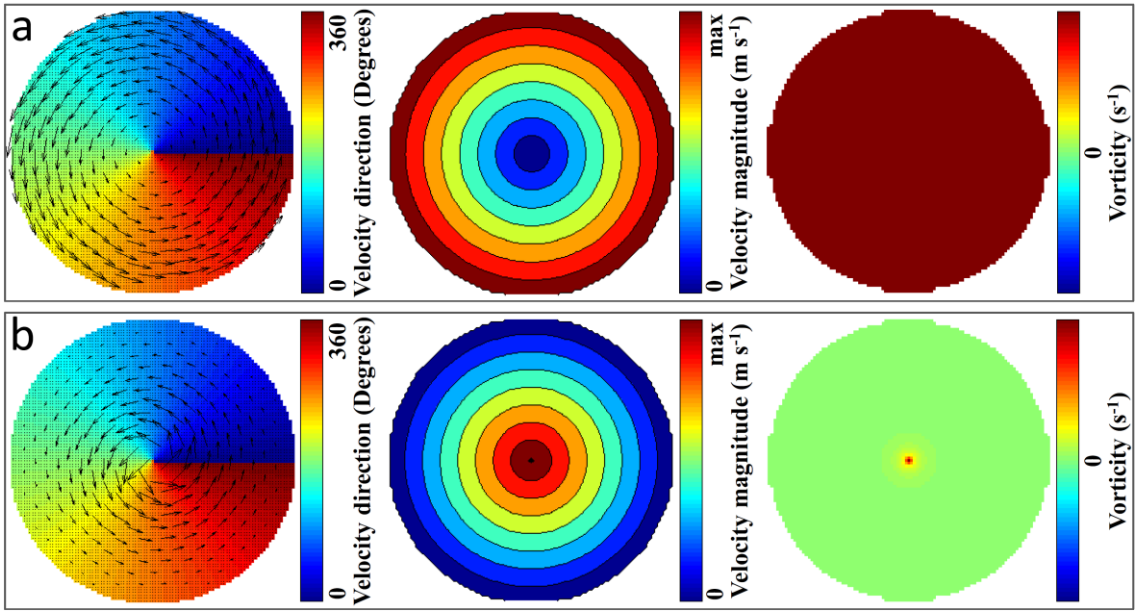

Figure 2.7: Numerical simulation of two characteristic counter-clockwise single spiral patterns using the vector Doppler and vorticity equations. (a) Rigid-body rotational flow pattern. (b) Irrotational flow pattern. Velocity direction, velocity magnitude and vorticity maps can be seen in both cases from left to right.

2.4.3 Discussion

The characteristics of both vortical patterns in Figure 2.7 were clearly illustrated verifying the vector Doppler and vorticity algorithms. The vorticity of the fluid elements in each example was associated with shearing processes. These processes are further explained in the schematic diagram of Figure 2.8. The black arrows represent the magnitude of velocity in each trajectory and two particles are illustrated at three different times (t_1, t_2, t_3). The blue and red arrows in the centre of the first and second particle respectively, indicate their direction in space as they move in circular counter-clockwise paths.

Figure 2.8a shows a rigid-body vortex similar to that presented in Figure 2.7a. The proportional increase of translational velocity with distance from the centre of rotation creates shear forces between adjacent trajectories. These forces cause both particles to rotate about their own axis at a speed that ensures the same side of each particle always points outwards and their vorticity remains constant. Figure 2.8b illustrates an irrotational vortex similar to that presented in Figure 2.7b. In this example the translational velocity decreases proportionally from the centre. The shearing forces in

this case are such that the orientation of both particles remains steady with time (moving with no rotation) and their vorticity remains zero.

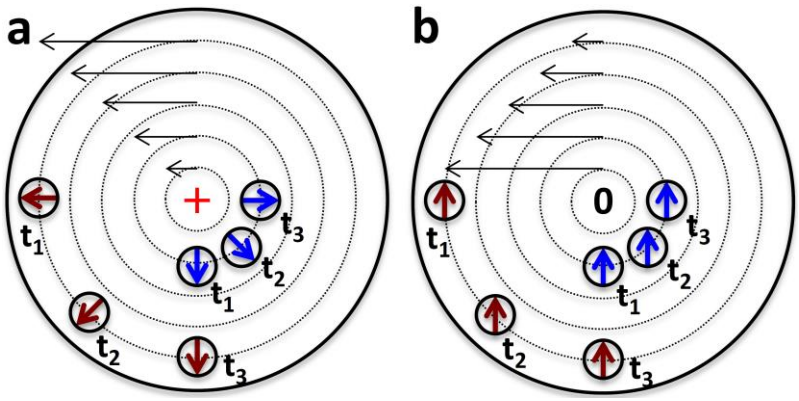

Figure 2.8: Schematic diagrams of particles translating in: (a) Rigid-body rotational flow pattern; (b) Irrotational flow pattern.

In the cross-flow view of a physiological single spiral flow, like that observed in medium or large size vessels, the speed of flow of particles reaches a maximum in the region between the centre of the vessel and the vessel wall (Stonebridge et al. 1996). The vorticity of such a vortex is explained in Figure 2.9. The translational velocity of the vortex is increased from the centre of the spiral to the third trajectory. This spins the first particle counter-clockwise resulting in a positive vorticity. After the third trajectory the translational velocity is decreased due to the non-slip boundary condition resulting in zero velocity relative to the wall. The inverse shear forces that are applied to the second particle spin it clockwise resulting in an opposite vorticity in relation to the first particle. Thus the vorticity of this single vortex appears to change direction near to the wall (Figure 2.9). This example will help the understanding of vorticity maps from vascular flow phantoms, which are presented in the next chapters.

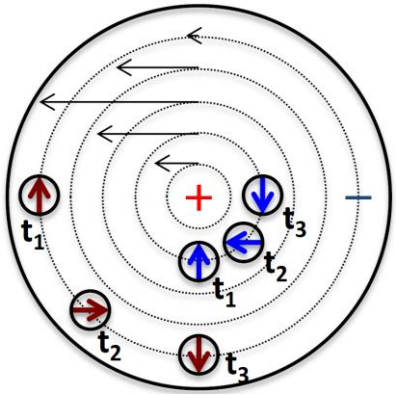

Figure 2.9: Schematic diagram of a physiological single spiral flow. The first particle spins around its own axis in a counter-clockwise direction resulting in positive vorticity and the second particle spins clockwise resulting in negative vorticity. The plus and minus signs indicate the direction of vorticity.

2.4.4 Summary

Two characteristic examples of spiral flow were numerically simulated. These examples were reconstructed in such a way that allowed the application and verification of the vector Doppler and vorticity algorithms. The simulated vortical types were a rigid-body rotational flow pattern and an irrotational counter-clockwise flow pattern. A detailed explanation of the relationship between vorticity and shear processes in a 2D flow field was presented.

2.5 Testing the vector Doppler technique using a rotating phantom

2.5.1 Materials and methods

In order to measure the accuracy of the vector Doppler technique, a target of known velocity and vorticity was required. This project focused on spiral flow phenomena in medium size vessels and therefore it was desirable to simulate a rotating flow rather than a parabolic flow. Ideally this would be a spiral flow phantom with known velocity magnitude, direction and vorticity in the vector Doppler cross-flow imaging plane. This would be extremely challenging due to the complicated 3D nature of flow, so instead a

rotating phantom was used. The phantom was composed of an agar-based tissue-mimicking material (TMM), which was manufactured by Yang et al. (2013). This TMM recipe was developed for use with clinical ultrasound scanners (Teirlinck et al. 1998) and is commonly used for quality assurance testing and research (Hoskins 2008). Its physical properties (Table 2.5) correlate well with that of human tissue and are within the IEC specifications (Table 2.2).

Table 2.5: Physical properties of agar-based tissue-mimicking material.

	Material	Density ($kg\ m^{-3}$)	Velocity ($m\ s^{-1}$)	Attenuation ($dB\ cm^{-1}\ MHz^{-1}$)	Reference (year)
TMM	Agar	n/a	1551	0.53 (at 6 MHz)	Teirlinck et al. (1998)
TMM	Glycerol	1023	1539	–	Hoskins (1994, 2008)

The TMM phantom was cylindrical with 6 mm diameter, matching the diameter of the flow phantom setup described in section 2.2 (page 31). A string phantom (BBS Medical Electronics, Stockholm, Sweden) was modified to rotate the cylindrical TMM. The TMM was moulded on a drive wheel, which was specifically manufactured to support it. The drive wheel was attached to the motor of the string phantom as shown in Figure 2.10.

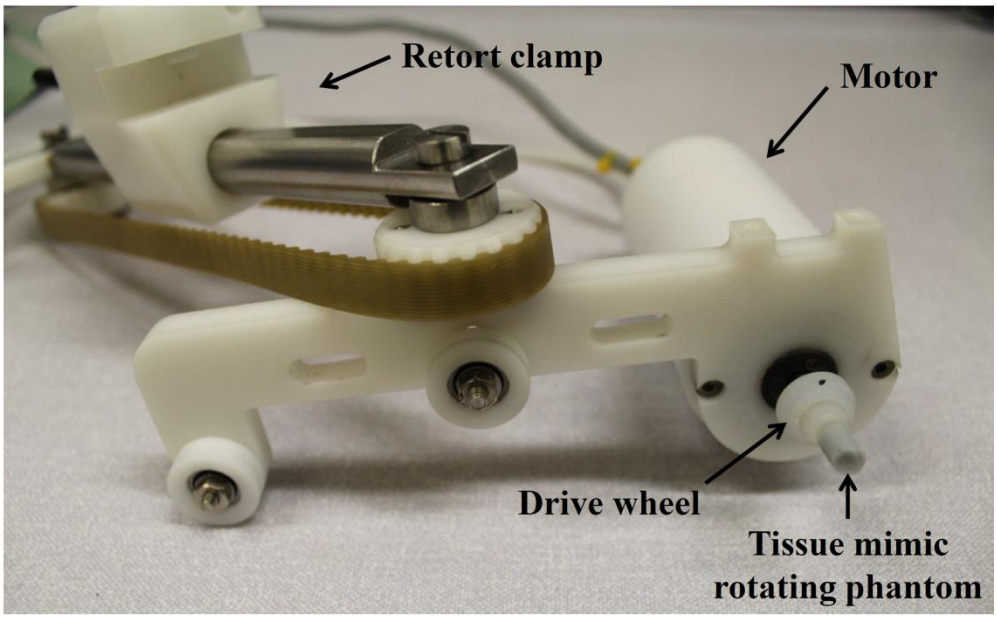

Figure 2.10: The rotating tissue-mimicking material phantom.

The motor with the agar based TMM phantom was submerged in a tank filled with the previously described liquid glycerol based TMM (9% glycerol and 91% distilled water by volume). Similar speed of sound between the agar based and glycerol based TMMs minimised ultrasound beam distortion at their interface (Table 2.5). The motor was held with a retort clamp and driven by a controller (BBS Medical Electronics, Stockholm, Sweden) from which the rotational speed could be adjusted. The transducer was positioned over the rotating phantom at a distance of 4-5 mm from the agar based TMM surface and held steady with a retort stand clamp in a plane perpendicular to the axis of rotation. An acoustic absorber pad (F28, Precision Acoustics, Dorchester UK) was placed at the bottom of the tank to minimize ultrasound beam reflections. Colour Doppler cine-loops, composed of 115 frames each, were acquired from the left and right steered projections (±20° in relation to the linear transmission) filling the memory buffer of the scanner. These cine-loops were sent to a workstation for post-processing. The colour box was kept as small as possible to increase the frame rate. The line-density was set to *C* yielding maximum colour line density or velocity information every 0.2 mm in the data file. More colour Doppler settings are listed in Table 2.6.

Table 2.6: Colour Doppler settings of the HDI 5000 scanner in this study.

Setting	Value
Persistence	Low
Sensitivity	Medium
Smoothing	Low
Dynamic motion differentiation	Off
Wall filter	Low

Each cine-loop was averaged to reduce noise from colour speckle and small localised variations, resulting in one velocity information array for each projection. The centres of these arrays were matched by applying a central gravity registration algorithm to verify that there was no lateral displacement between the two steered beams. Two-dimensional estimated velocity magnitude, velocity direction and vorticity maps were reconstructed using the vector Doppler algorithm.

The motor controller was unable to provide a completely accurate reading of the rotational speed that would allow the true linear velocity of the rotating phantom to be calculated. Therefore a video technique was applied. After the ultrasound recording, and without switching off the controller, the motor with the rotating phantom was positioned across from a camera and a 50 frames per second video was acquired. The video was watched frame by frame and the true period of rotation was detected by using a black dot as a reference point at the edge of the drive wheel. The true linear velocity, $V_{(true)}$, was defined as

$$V_{(true)} = \frac{\pi D}{T} \qquad \textbf{2.22}$$

where D was the diameter of the TMM and T the period of rotation (Yang et al. 2013).

The true rotational speed was set at 207 r min^{-1} (rotations per minute) producing a true linear velocity at 6 mm diameter of 0.065 $m{\cdot}s^{-1}$. Stonebridge et al. (1996) have reported a peak systolic tangential or perpendicular velocity (transverse to the blood flow direction) of approximately 0.06 $m{\cdot}s^{-1}$ in the common femoral artery of healthy volunteers.

The true velocity vector (direction and magnitude) and vorticity of the rotating phantom were simulated for comparison with the estimated data. A slightly off-centre rotation of the TMM phantom resulted in large variations of the estimated velocity at its perimeter. In order to avoid this error, a comparison was performed within a circle of diameter equal to 86% of the rotating phantom. The velocity magnitude error, V_{err}, velocity direction error, θ_{err}, and vorticity error, $\omega_{z\,err}$, were defined for each pixel of the estimated velocity and vorticity maps using Equation 2.23, 2.24 and 2.25 respectively.

$$V_{err}(\%) = \left(\frac{Estimated\ velocity\ magnitude}{True\ velocity\ magnitude} - 1\right) \times 100 \qquad \textbf{2.23}$$

$$\theta_{\ err}(degrees) = Estimated\ velocity\ direction - True\ velocity\ direction \qquad \textbf{2.24}$$

$$\omega_{z\,err}(\%) = \left(\frac{Estimated\ vorticity\ magnitude}{True\ vorticity\ magnitude} - 1\right) \times 100 \qquad \textbf{2.25}$$

Parametric flow maps were made based on the velocity magnitude, velocity direction and vorticity error.

2.5.2 Results and discussion

In this section the results and discussion are presented together. This is because the analysis for some of the initial results is discussed and reanalysed using a different approach.

A grey scale image of the rotating phantom, with a 6 mm diameter coloured circle superimposed on its perimeter, is shown in Figure 2.11a. Colour Doppler images from the left and right transducer apertures are illustrated in Figure 2.11b-c. In both images, there is a dark band in the border between the two colour encoded rotating regions (red and blue areas). This line corresponded to velocities below the high-pass frequency filter. This cut-off filter was kept as low as physically possible without inducing aliasing artefacts, to decrease the size of the dark band and increase the accuracy of vector Doppler measurements in this region. Peak velocities can be seen as bright blue and bright red hues.

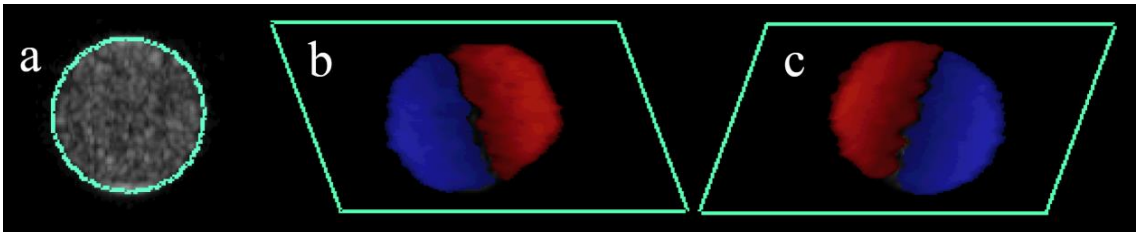

Figure 2.11: (a) B-mode image of the rotating phantom. (b) Colour Doppler image from the left aperture of the transducer. (c) Colour Doppler image from the right aperture of the transducer.

Figure 2.12a shows the estimated velocity direction, velocity magnitude and vorticity map from the rotating phantom and Figure 2.12b the respective maps from the true data for comparison. The description of the vectors and colour distribution in velocity direction and magnitude maps are same as that of Figure 2.7 (page 46). In the vorticity maps (ω_Z), the negative sign of vorticity indicates clockwise rotation, where the darkest blue and lightest blue shades symbolises the lower and upper limits of the values measured. A single spiral clockwise rotation in a rigid-body like pattern is illustrated for both of the estimated and true data. Accurate velocity direction distribution, uniform velocity magnitude distribution (from zero in the centre to peak at the perimeter) and constant negative vorticity is shown for the true data. For the estimated data, errors are seen in the distribution of velocity magnitude and vorticity maps. These errors are primarily associated with regions of velocity under the colour cut-off filter. These are the regions at and around the dark band in Figure 2.11b-c, where velocity magnitude was underestimated. In the velocity direction map of the estimated data, only limited errors can be seen.

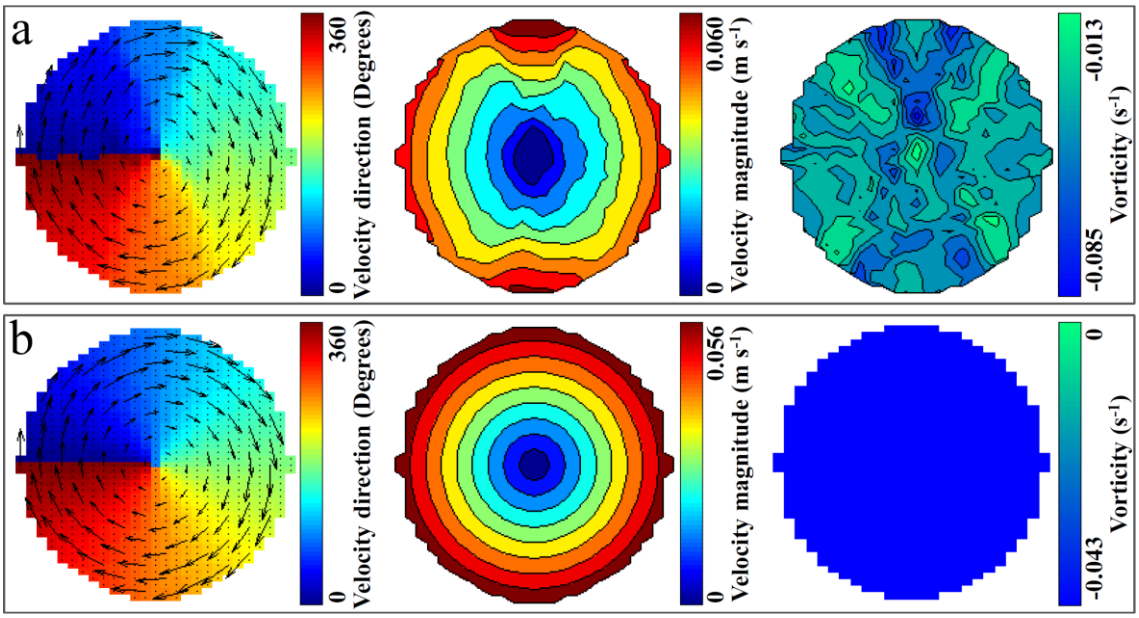

Figure 2.12: (a) Estimated velocity direction, velocity magnitude and vorticity map based on the vector Doppler algorithm. (b) Respective true maps from constructed data.

Vector Doppler errors were calculated using Equations 2.23, 2.24 and 2.25. A positive error indicated overestimation of the estimated value in relation to the true value and a negative error indicated underestimation of the estimated value in relation to the true value. Parametric images of these errors are presented in Figure 2.13. Absolute values of the errors were used to increase the contrast and clarification of the image. The parallel black lines enclose the regions where the frequency shifts lay under the cut-off filter. Each parametric image was analysed based on the regions of Figure 2.14. In regions labelled 1, both the left and right colour flow images were above the cut-off filter, in regions labelled 2, one of the colour flow images was under the cut-off filter and in region 3 both were under the cut-off filter.

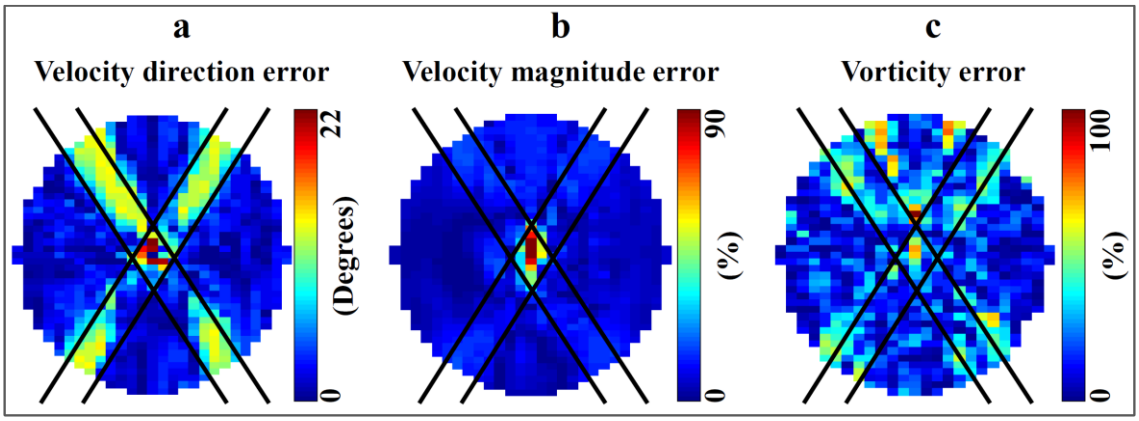

Figure 2.13: Parametric images of the vector Doppler imaging errors. (a) Velocity direction error (Degrees). (b) Velocity magnitude error (%). (c) Vorticity error (%).

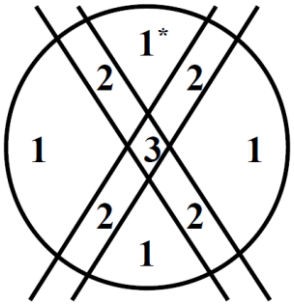

Figure 2.14: Each parametric map was segmented in these three regions for error analysis in relation to the Doppler cut-off filter.

The mean error and standard deviation of each region are shown in Table 2.7. The accuracy of velocity vector detection was improved when the estimated Doppler frequencies were above the cut-off filter for both beam projections (regions 1). In the four regions labelled 1, the highest error was found in the upper most region which is marked with an asterisk, as can be observed in the parametric velocity magnitude Figure 2.13b. In general the errors in the upper and lower regions labelled 1 were associated with overestimation, whilst the lateral regions labelled 1 with underestimation. In regions labelled 2, the vector Doppler technique accurately detected the velocity angle but there was an increased underestimation of velocity magnitude. This is because the velocities in one of the steered beams were under the high pass filter. In region 3, all target velocities were low and the returned ultrasound signal had frequencies below the cut-off filter for both projections, explaining the significant errors found in this region.

The mean vorticity error was low in all regions but the standard deviation of this mean was high. From Figure 2.13c it can be seen that the increased errors are located in the boundaries between one region and another.

Table 2.7: Errors of the rotating phantom 2D velocity field.

Region	Mean direction error θerr (degrees)	Mean magnitude error *Verr* (%)	Mean vorticity error $\omega_{z\,err}$ (%)
1	-1.4 ± 6.5	-1.7 ± 8.9	-6.9 ± 22.9
2	-1.3 ± 13.2	-8.6 ± 13.4	-1.3 ± 26.3
3	-5.0 ± 11.7	-37.9 ± 27.0	-4.3 ± 37.0

Vorticity is considered the kinematic representation of the shearing and compressing processes in a flow field. The true rigid-body rotational data had constant vorticity due to the smooth transition, or steady velocity increment, from zero in the centre to peak velocity at the perimeter (see section 2.4.3, page 46).

In the estimated data, the variations in velocity transition from zero (centre) to maximum (perimeter), resulted in variations of vorticity. From the parametric vorticity maps (Figure 2.13c) it can be observed that the peak vorticity errors lie under and around the black boundaries separating regions 1-3. Such locations are associated with transitions between areas of relatively different scales of velocity. Vorticity is significantly affected in these transition zones because there is an abrupt change in velocity increment from point to point. In a previous paragraph in this section it was described that regions labelled 2 were generally related to velocity underestimation and region 1^* with velocity overestimation. This is the reason that the peak vorticity errors are located at the boundaries between region 1^* and the contiguous regions labelled 2. The low mean and increased standard deviation values of vorticity error in Table 2.7, are explained by the fact that the peak vorticity errors are located at the boundaries between one region and another. Therefore, it was considered appropriate to relocate the regions of vorticity analysis based on these transition zones to areas with velocities under the cut-off filter, as shown in Figure 2.15.

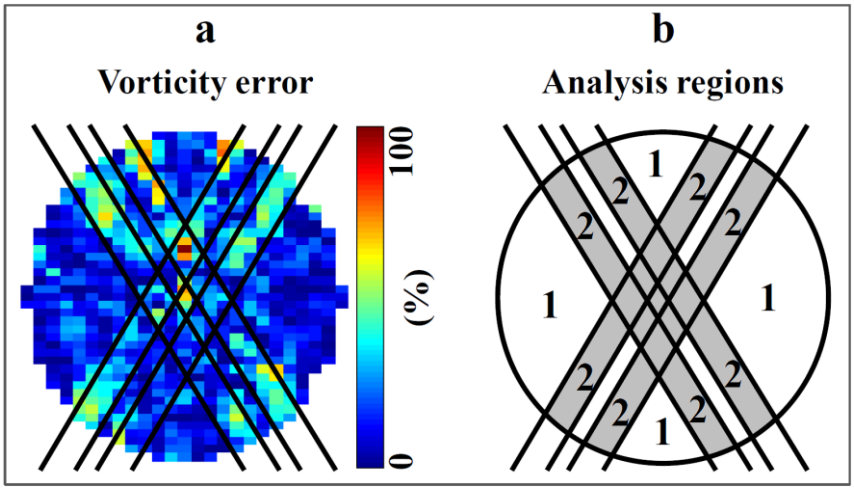

Figure 2.15: Relocated analysis regions of the vorticity parametric image.

For this vorticity analysis the image was separated into two regions instead of three. Parts of regions 1 now appear between the newly positioned regions 2. Table 2.8 demonstrates the mean errors in these relocated regions. The errors were now decreased in regions 1 and increased in regions 2, in relation to the original regions 1 and 2, as was expected. This suggests that defining the regions based on the transition zones of areas of relatively different scales of velocity, was indeed more accurate.

Table 2.8: Errors of vorticity measurements based on the relocated regions of analysis.

Region	Mean vorticity error $\omega_{z\,err}$ (%)
1	-5.7 ± 14.7
2	-3.9 ± 27.5

Hoskins et al. (1994) analysed the velocity errors of the same vector Doppler technique using a rotating phantom consisting of a cylinder of reticulated foam. The diameter of this phantom was 15.5 mm and the rotational speed 250 r min^{-1} which is similar to that applied in this study. The setup and error analysis performed in this study were similar in order to enable comparison. Hoskins et al. (1994) results are presented in Table 2.9.

Table 2.9: Vector Doppler technique errors as they were presented by Hoskins et al. (1994).

Region	Mean direction error *θerr* (degrees)	Mean magnitude error *Verr* (%)
1	-1.4 ± 7.0	-1.9 ± 9.6
2	-0.0 ± 13.0	-2.6 ± 29
3	–	-100 ± 0

There was increased agreement in both velocity direction and magnitude errors in regions 1. In regions 2 there was increased agreement in velocity direction errors. The velocity magnitude error in Hoskins et al. (1994) was about three times lower but the standard deviation was about 55% higher. Therefore, the results in this work showed better precision. In region 3 the estimated velocity provided by Hoskins et al. (1994) was zero resulting in 100% error. The differences between Hoskins et al. (1994) errors and the errors found in this study for regions 2 and 3 may be associated with the different ultrasound scanners and the materials used for the rotating phantom.

The rotating phantom analysis was based on a flow pattern with zero velocity in the centre and maximum velocity at the perimeter. In this case the underestimation of velocity in the centre using the described dual-beam technique may not significantly affect the detection of the overall flow phenomena. This is because the magnitude of velocity in the centre is much lower than that throughout the rest of the cross-flow area and therefore the error could be assumed to be negligible. We expect that the impact of the limited velocity detection at the centre would be worse in a pattern with peak velocities in it as such an underestimation could affect the overall characterisation of flow phenomena in a cross-section plane.

2.5.3 Conclusions

The accuracy of 2D velocity and vorticity maps based on the applied dual-beam vector Doppler technique was tested with a rotating phantom spinning at known velocities.

Errors in the acquired velocity vectors were low in regions where the mean (non-aliased) Doppler frequencies were above the cut-off colour filter for both oblique projections. Errors, especially in velocity magnitude, were increased in regions where the mean Doppler frequencies were under the cut-off filter for at least one of the two

oblique beams. These velocity errors were in good agreement with Hoskins et al. (1994).

Vorticity mapping was also possible with vector Doppler imaging. However, there were localised areas of increased errors, which needed to be taken into consideration. The accuracy of vorticity mapping was decreased in regions of transition between areas with mean Doppler frequencies above the high-pass filter for both beams and areas with mean frequencies below the high-pass filter for at least one of the beams.

Chapter 3

Secondary flow motions in the outflow of peripheral vascular prosthetic grafts

3.1 Introduction

The development of neo-intimal hyperplasia in the distal end-to-side anastomosis of a PV graft results in stenosis and eventually outflow occlusion of the device. The nature of local haemodynamics is an important factor in the formation of neo-intimal hyperplasia due to the interaction with endothelial behaviour. However, the exact mechanism of this interaction is not fully understood (Doorly et al. 2002; Doorly and Sherwin 2009; O'Brien et al. 2005; O'Callaghan et al. 2006; Walsh et al. 2003).

PV grafts that are manufactured to reintroduce physiologic single spiral flow into their distal anastomosis have been proposed as a way of restricting disturbed haemodynamics (Stonebridge 2011; Zhang et al. 2008). A graft of this nature has recently been introduced into clinical practice (Stonebridge et al. 2012). The aim of this chapter is to describe and compare the vortical structures in the outflow of spiral and control, conventional PV grafts. Identical vascular-graft models were manufactured for both types of grafts and each was tested in the flow phantom setup previously described (section 2.2, page 31). Two-dimensional velocity and vorticity maps were developed for flow visualisation and the peak velocity and circulation were compared for flow quantification.

3.2 Material and methods

3.2.1 Peripheral vascular grafts

The flow modified spiral graft, known as *Spiral Laminar Flow*^{TM} PV graft and the control, non-spiral graft were made of expanded polytetrafluoroethylene (ePTFE) with a 6 mm inner diameter (Vascular Flow Technologies Ltd, Dundee, UK). The former device was externally modified with a bio-durable medical grade polyurethane ridge, which formed an internal spiral inducer segment and a 3D helix shape at its distal end (Figure 3.1a). This inducer provided an internal ridged cross section and non-planar geometry designed to establish a single spiral outflow pattern. The control device was a standard PV graft with smooth lumen surface (Vascular Flow Technologies Ltd, Dundee, UK).

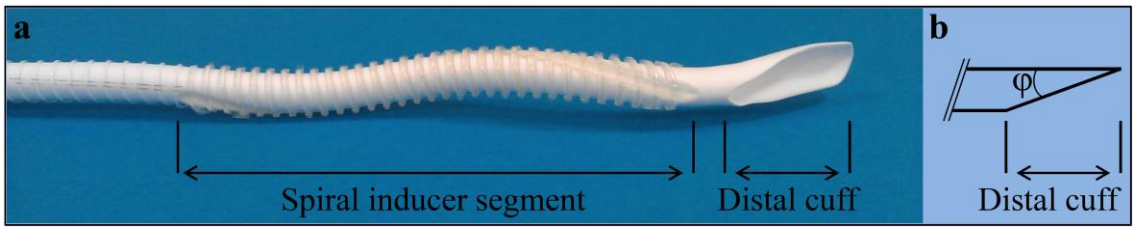

Figure 3.1: (a) Distal end of a 6 mm inner diameter peripheral vascular spiral graft. (b) Side-view diagram of the distal cuff; angle $\varphi = 15°$ (republished with permission of ELSEVIER, from Kokkalis et al. 2013).

3.2.2 Vascular-graft model

The distal cuffs of the spiral and control grafts were trimmed at 15° (Figure 3.1b) and connected to a PVA-c vessel mimic with an end-to-side anastomosis. The connection was made with superglue and reinforced with epoxy adhesive. A PV graft with a PVA-c arterial mimic, referred to in this thesis as a vascular-graft model, was developed for both the spiral and control grafts. Each model was housed in an acrylic tank and connected in the flow rig circulation (section 2.2, page 31).

The proximal end of the vessel mimic was blocked so that the blood mimic was forced to flow downstream. The vessel mimic length between the anastomosis and its distal end was 150 mm. Both models were subjected to four different graft-vessel mimic

angles θ to mimic different vascular surgical implantation geometries, as shown in Figure 3.2. Specifically the angle θ was applied at 20°, 40°, 60° and 80° for both PV graft models using a gauge protractor. In this way the connection between the cuff of the graft and the vessel mimic remained consistent for both the spiral and control models, in order to avoid variations from the connection point under the four applied angles θ.

Overall four pairs of vascular-graft models were compared. Each pair consisted of a spiral and a control model at the same angle θ. Figure 3.2 presents the geometry of the models as well as the heel, toe and floor of the end-to-side anastomosis (How et al. 2006; Maniatis et al. 1994). During the study the temperature in the vascular-graft tank was monitored with a mercury thermometer and maintained at 21 ± 1°C using ice bags to ensure that acoustic properties were correctly maintained (Hoskins 1999).

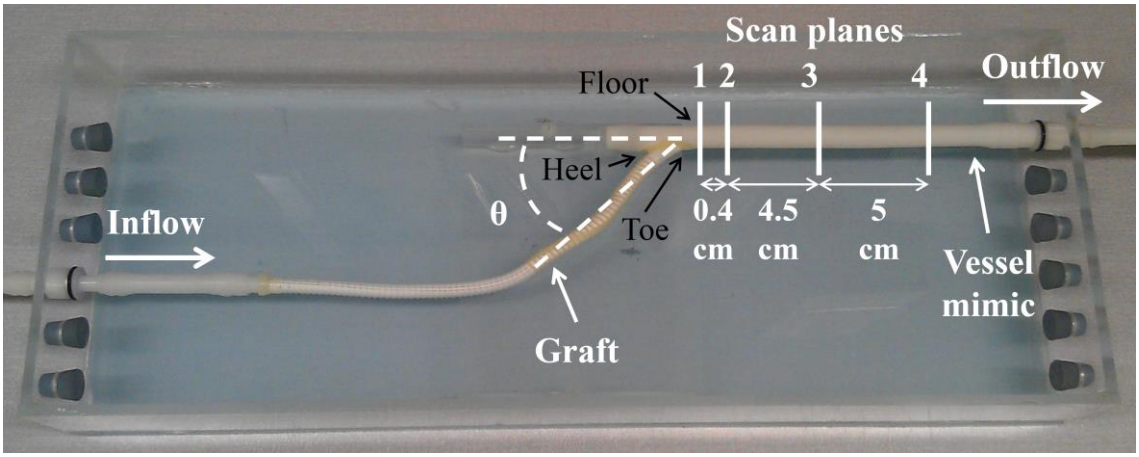

Figure 3.2: Peripheral vascular-graft model using a spiral graft. Data were collected at scan planes 1 to 4. Scan plane 1 was positioned 0.1 cm distally from the graft outflow. Angle θ was applied at 20°, 40°, 60° and 80°. The control graft model was setup in an identical way (republished with permission of ELSEVIER, from Kokkalis et al. 2013).

The flow profile in a phantom is influenced by the tubing geometry. The pump system, flow rig tubing and vascular-graft models were positioned at the same height in order to create a planar design and standardise the flow conditions. An exception to the planarity of these models was the spiral flow inducer segment of the PV spiral graft. The value of the inlet length (section 1.6.3, page 26) was calculated based on the peak applied flow rate and taken into consideration in the length of the tubing between the pump outflow

and the inlet of each vascular-graft model. In this way the flow pattern proximal to the graft inlet was standardised.

3.2.3 Data acquisition

Colour flow data was collected from the four pairs of vascular-graft models at 0.1, 0.5, 5 and 10 cm (Figure 3.2, scan planes 1-4) distal to the graft outflow, to examine the progression of vortical structures. Proximal outflow (scan planes 1-2) is clinically associated with neo-intimal hyperplasia and distal outflow (scan planes 3-4) with PAD progression downstream (Stonebridge et al. 1997). The scan planes were transverse to the flow in both anteroposterior and right to left directions to allow rotational patterns to be detected.

Steady flow rates of 240, 360, 480, 600 and 720 mL·min^{-1}, corresponding to Reynolds numbers of 570, 850, 1140, 1420 and 1700 respectively, were applied. These Reynolds number were calculated based on the mean axial velocity, $\bar{v}$, the inner diameter D of the vessel mimic and the kinematic viscosity ν of the blood mimic (Equation 1.6). The mean axial velocity, $\bar{v}$, was determined using Equation 3.1.

$$\bar{v} = \frac{Q}{A} \qquad \textbf{3.1}$$

where Q is the flow rate and A the area of the tube. A similar approach was previously used to calculate the Reynolds number based on flow rate in a flow phantom (Sherwin et al. 2000).

The transducer was kept steady in the scan planes using a retort clamp, which was adjusted in a micromanipulator to accomplish relatively accurate displacements. The micromanipulator was accurate to 0.5 mm and had three degrees of freedom (Figure 3.3). The distance between the surface of the vessel mimic and the transducer was 4-5 mm. An acoustic absorber pad (F28, Precision Acoustics, Dorchester UK) was placed under the vessel mimic to prevent ultrasound beam reflections.

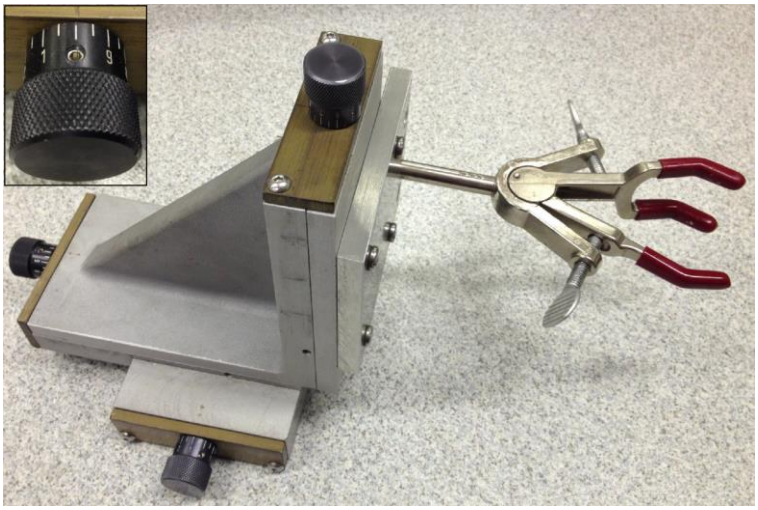

Figure 3.3: Micromanipulator.

The colour box was kept small to increase the frame rate. The line-density was set to *C* yielding maximum colour line density or velocity information every 0.2 mm in the data file. Other colour Doppler settings are listed in Table 3.1.

Table 3.1: Colour Doppler settings of the scanner in the peripheral vascular graft study.

Setting	Value
Persistence	Low
Sensitivity	High
Smoothing	Low
Dynamic motion differentiation	Off
Wall filter	Low

In each scan plane two cine-loops were acquired; one with the ultrasound beam steered at +20° and the other with the ultrasound beam steered at -20° relative to the linear transmission. The cine-loops consisted of 115 frames each, which was the capacity of the scanner memory buffer. All measurements were repeated three times to verify repeatability. Each time the transducer was repositioned. Off-line post processing was undertaken using MATLAB R2012a.

Each cine-loop was averaged to reduce noise from colour speckle and small variations in the flow pattern over time, creating one array of velocity information for each projection. The centres of these arrays were aligned applying a central gravity registration algorithm, to confirm that there was no lateral displacement between the

two steered beams. The vector Doppler and vorticity algorithms were executed and 2D velocity direction, velocity magnitude and vorticity maps were reconstructed.

3.2.4 Data analysis

Peak velocity comparison

The angle independent peak tangential velocity was detected in each scanning location for each of the applied flow rates. These measurements were normalised to the mean axial velocity, $\overline{v}$, (see Equation 3.1) as shown in Equation 3.2 and a comparison between the spiral and control graft models was applied.

$$\hat{v} = \frac{v}{\overline{v}} \qquad \textbf{3.2}$$

where, $\hat{v}$, the normalised velocity. The flow rate Q in the calculation of mean velocity $\overline{v}$ was equal to the average of the five applied flow rates.

Detection and comparison of circulation

The peak velocity comparison provides an indication of the velocity range but it has the limitation that it is based on a single point. In contrast, circulation is a parameter that quantifies the total 2D cross-flow vortical field and can be calculated from axial vorticity maps.

A vorticity map was generated for each 2D velocity data set. Vorticity is the kinematic representation of the shearing and compressing processes in a flow field. It can appear to change direction in the case of counter rotating vortices and it can also appear to change direction in the case of a single vortex, as was described in detail in section 2.4.3, page 46. The compression of a water based fluid like the BMF applied requires significant pressure. Therefore, vorticity in this flow phantom is most possible associated with the shearing process of fluid elements.

The total circulation in each vorticity map was computed based on both positive and negative areas of vorticity. Figure 3.4 shows examples of 2D vector Doppler velocity and vorticity maps for a single- and for a four-spiral pattern in the cross-flow direction.

In the velocity maps, the colour distribution and arrow size relate to the magnitude of the velocity vector, while the direction of the arrows relates to the direction of the velocity vector. In vorticity maps, values change from positive to negative and this is represented through a colour scale ranging from dark red to dark blue respectively. The boundaries of zero vorticity between the areas of positive and negative vorticity, are represented by a thick black contour line. In each spiral structure the regions of positive (Figure 3.4b,d) and negative vorticities (Figure 3.4a,c) were separated. Then in each example of spiral pattern the regions of positive and negative vorticity were integrated over their areas, and their absolute values were summed giving the total circulation. This was applied to all scan planes and flow parameters for each of the four pairs of phantoms, to compare the outflow of the spiral and non-spiral grafts.

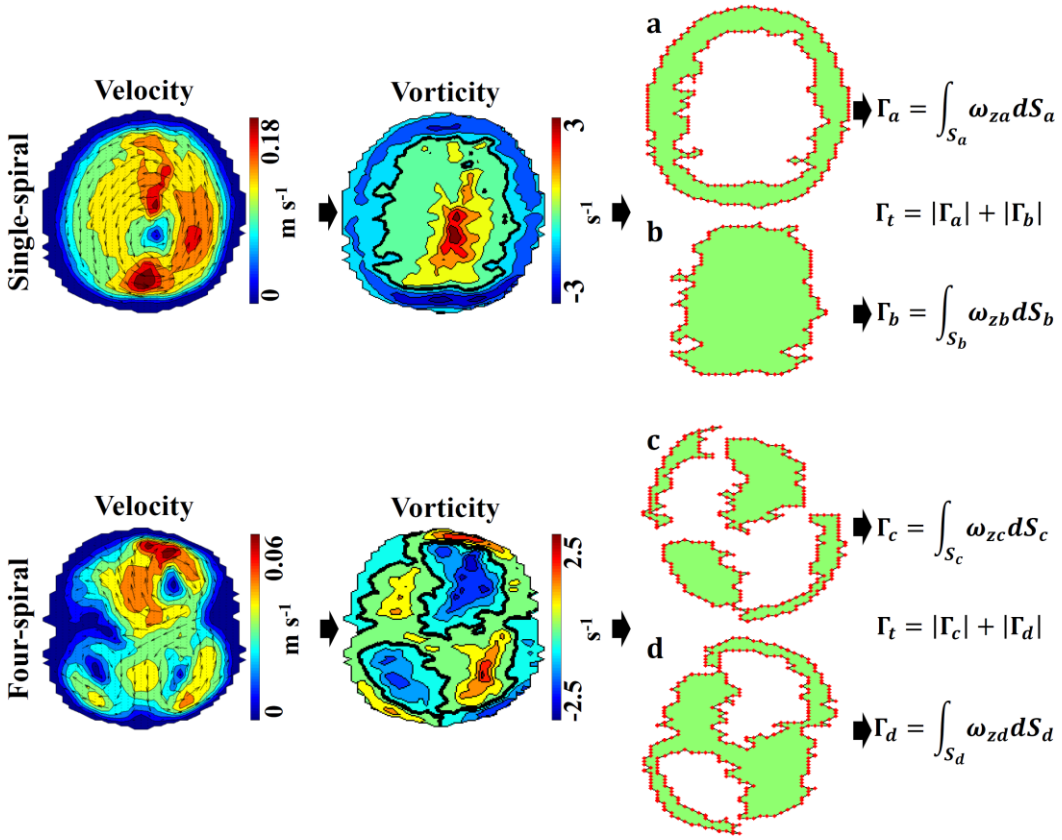

Figure 3.4: Examples of the calculation of circulation Γ in a single- and a four-spiral pattern. In each example the regions of positive and negative axial vorticities were separated, integrated over their areas and their absolute values were summed to provide the total circulation Γ_t; ω_z is the axial vorticity, S the area and dS a unit element within the area. The boundary between the positive and negative vorticity is represented by a thick black contour line.

Each circulation value, Γ, was normalised to the total mean circulation, $\overline{\Gamma}$, for the 20°, 40°, 60° and 80° pair of phantoms using Equation 3.3.

$$\hat{\Gamma} = \frac{\Gamma}{\overline{\overline{\Gamma}}} \quad \textbf{3.3}$$

where $\hat{\Gamma}$ is the normalised circulation.

Statistical analysis

The differences in measures of peak velocity and circulation between the spiral and control models were examined using an unpaired, two-tailed student's t-test; p values < 0.05 were considered statistically significant, p values ≤ 0.01 highly significant and p values ≤ 0.001 very highly significant. The statistical tests were performed with SPSS Version 21 (SPSS Inc., Chicago, IL, USA).

3.3 Results

3.3.1 Vector Doppler and vorticity imaging

An initial observation of vortical structures in the cross-flow direction was accomplished using Colour Doppler ultrasound. Two-dimensional velocity and vorticity maps were developed based on vector Doppler imaging and are illustrated in Figure 3.5 - Figure 3.8. These figures represent the four scan planes from the proximal (scan plane 1 at 0.1 cm) to the distal (scan plane 4 at 10 cm) outflow of the models with angle θ equal to 40° (Figure 3.2). In each of these figures, spiral and control graft outflow mapping is included for the minimum, middle and maximum Reynolds number, 570, 1140 and 1700 respectively. The orientation of the maps is such that the left and right sides are the toe and floor wall sides of the vessel mimic respectively, and the top and bottom are the anterior and posterior wall sides respectively (see Figure 3.2). Velocity direction maps are shown in the first row for each graft, velocity magnitude in the second and vorticity in the third. The colour distribution in the velocity direction maps represents the displacement of the velocity vector from 0° to 360° and the length of the vectors is proportional to the magnitude of the velocity. Vorticity maps correspond to

axial vorticity, ω_Z, where positive regions are associated with counter-clockwise rotation and negative regions with clockwise rotation. The boundaries of zero vorticity between the areas of positive and negative vorticity are represented by a thick black contour line. In all maps the darkest blue and darkest red symbolise the lower and upper limits of the values measured.

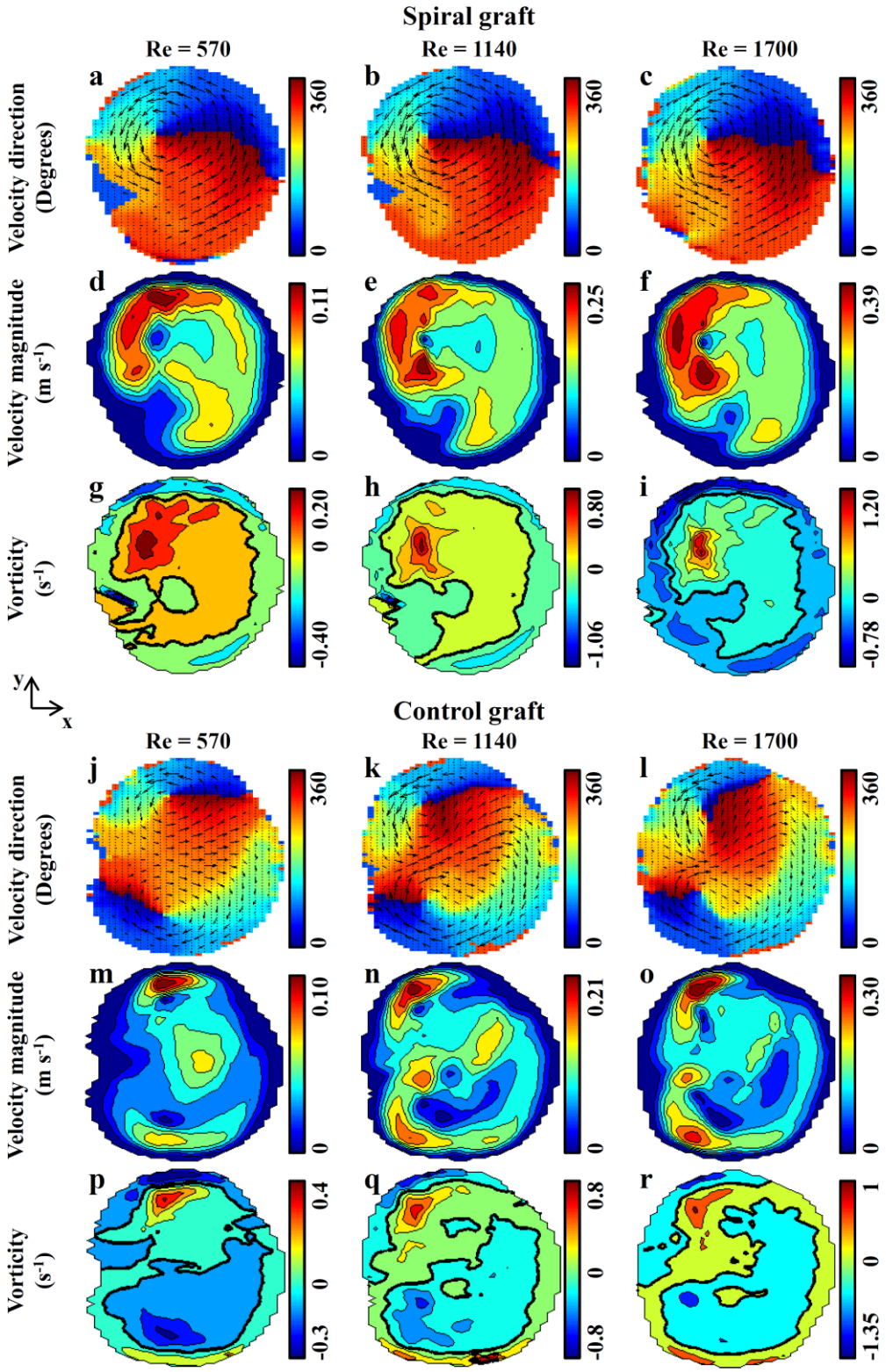

Figure 3.5: Presents the flow maps for the spiral and control PV models; scan plane 1, anastomotic angle θ = 40°. The first and forth rows illustrate in-plane velocity direction, the second and fifth rows illustrate in-plane velocity magnitude and the third and sixth rows illustrate axial vorticity ω_z. The boundaries of zero vorticity are represented by a thick black contour line. The orientation of each map in relation to the anastomotic locations is: left side = toe and right side = floor.

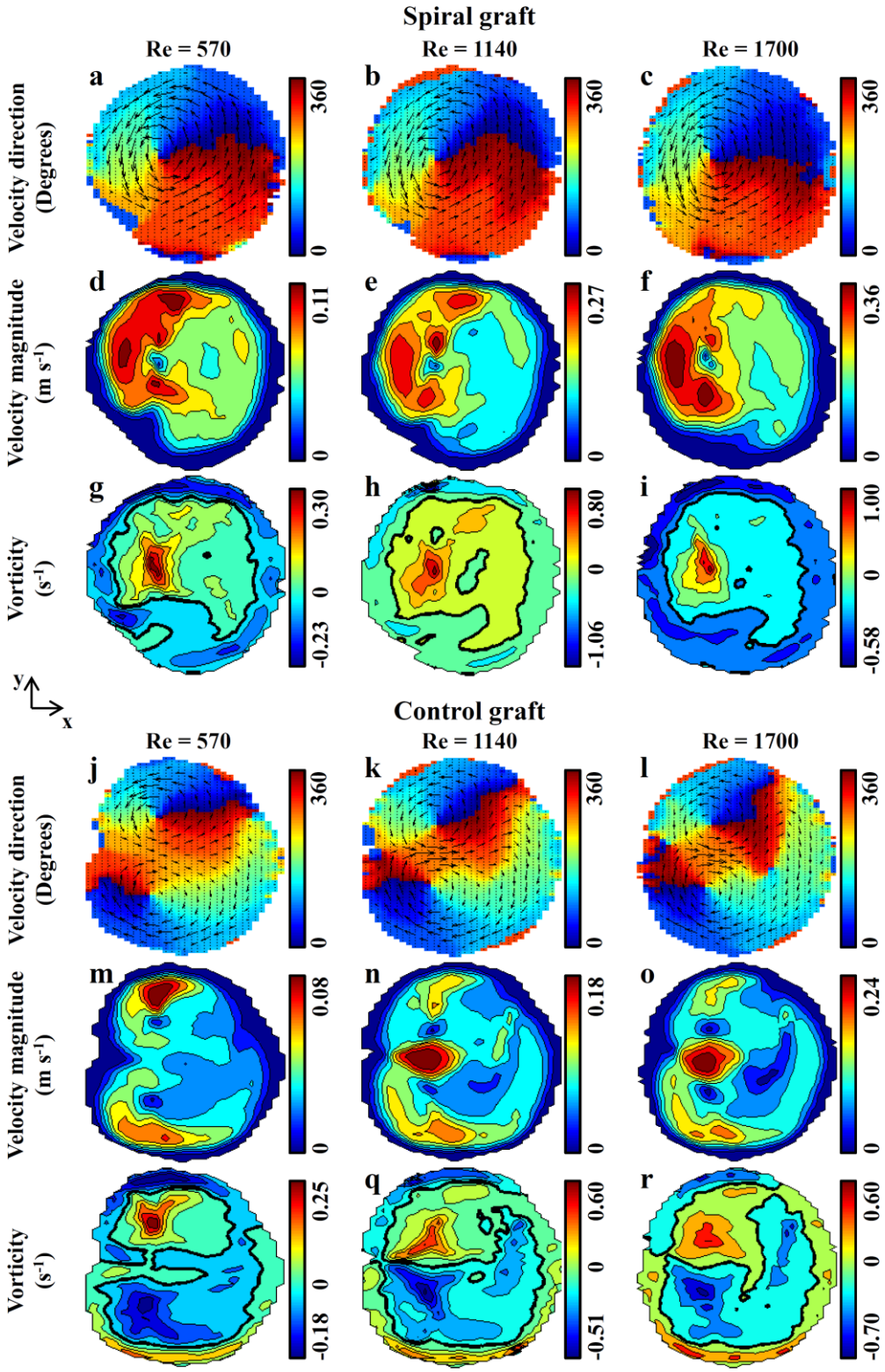

Figure 3.6: Presents the flow maps for the spiral and control PV models; scan plane 2, anastomotic angle θ = 40°. The first and forth rows illustrate in-plane velocity direction, the second and fifth rows illustrate in-plane velocity magnitude and the third and sixth rows illustrate axial vorticity ω_z. The boundaries of zero vorticity are represented by a thick black contour line. The orientation of each map in relation to the anastomotic locations is: left side = toe and right side = floor.

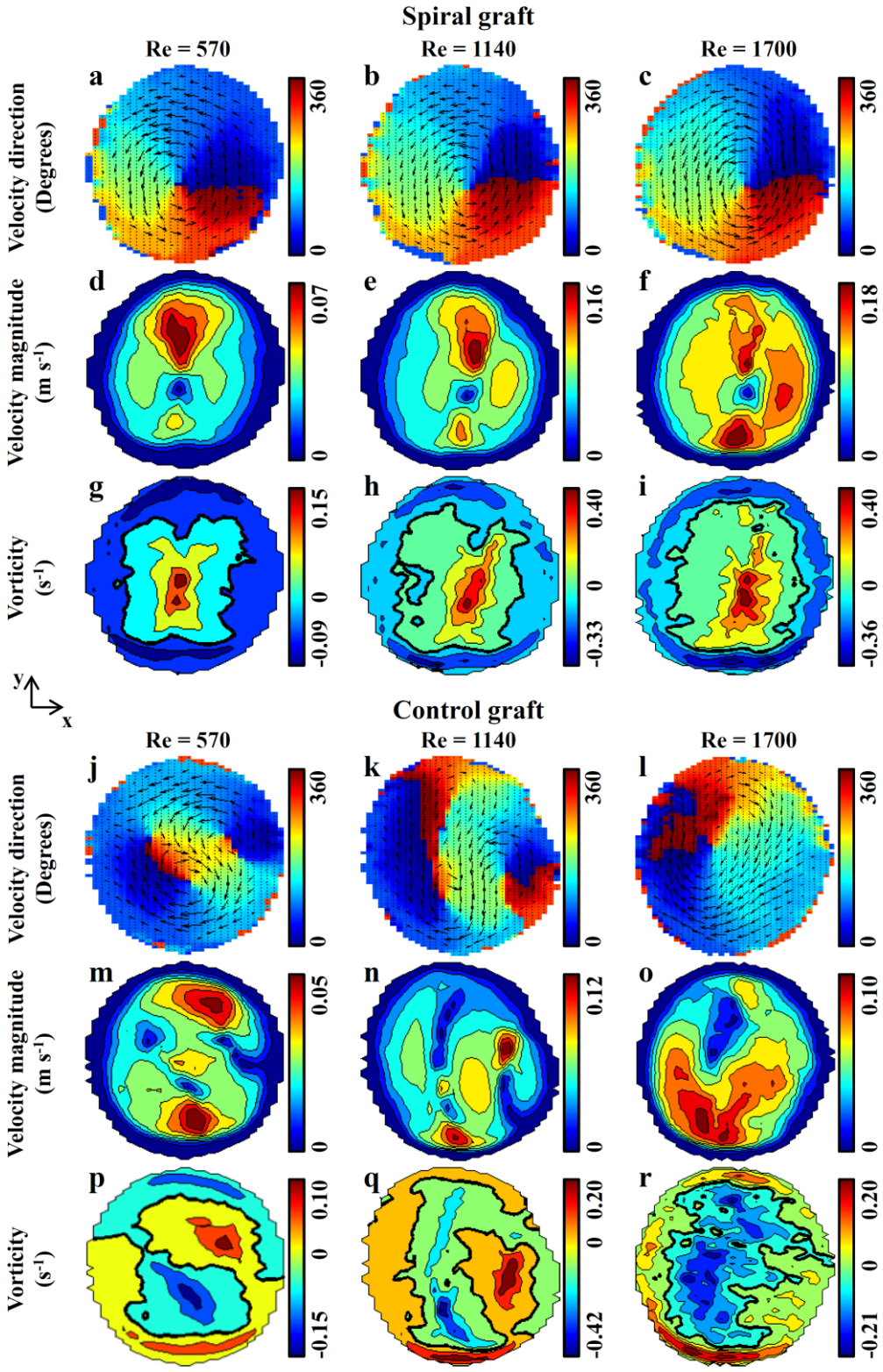

Figure 3.7: Presents the flow maps for the spiral and control PV models; scan plane 3, anastomotic angle $\theta = 40°$. The first and forth rows illustrate in-plane velocity direction, the second and fifth rows illustrate in-plane velocity magnitude and the third and sixth rows illustrate axial vorticity ω_z. The boundaries of zero vorticity are represented by a thick black contour line. The orientation of each map in relation to the anastomotic locations is: left side = toe and right side = floor.

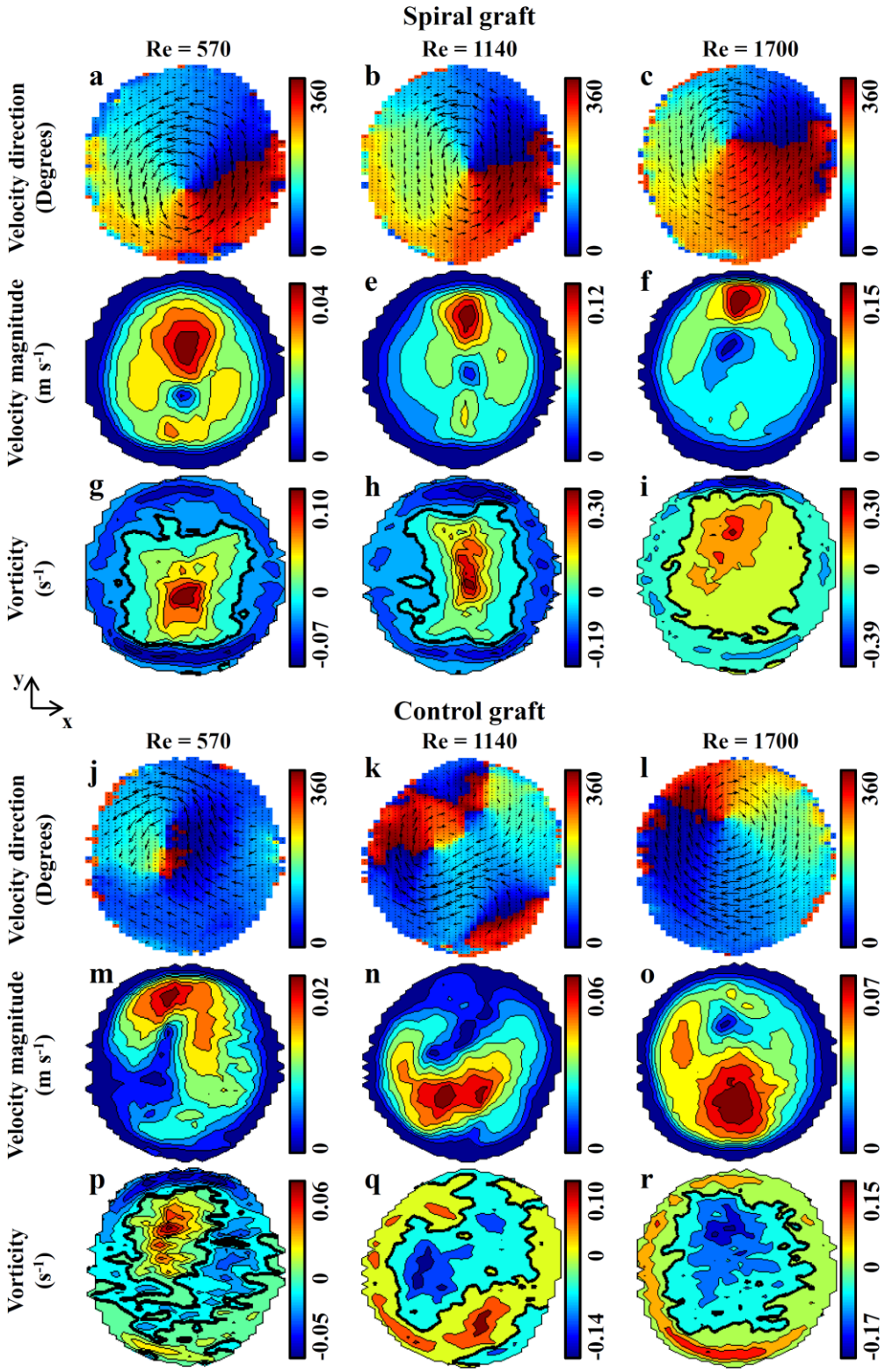

Figure 3.8: Presents the flow maps for the spiral and control PV models; scan plane 4, anastomotic angle $\theta = 40°$. The first and forth rows illustrate in-plane velocity direction, the second and fifth rows illustrate in-plane velocity magnitude and the third and sixth rows illustrate axial vorticity ω_z. The boundaries of zero vorticity are represented by a thick black contour line. The orientation of each map in relation to the anastomotic locations is: left side = toe and right side = floor.

The main finding from the proximal velocity maps (Figure 3.5a-f) of the spiral device was a dominant single vortex. The centre of this vortex was positioned near to the toe side of the anastomosis. There was a flow disturbance in the region between the toe and posterior (bottom) side, which was potentially associated with a second small spiral. This may explain the appearance of a second centre of low velocities in the magnitude map for Reynolds number 1700. In scan plane 2 (Figure 3.6a-f), a single-spiral occupied almost the whole area and the flow disturbance was barely seen. A single-spiral flow was observed in distal scan planes 3 and 4 (Figure 3.7a-f and Figure 3.8a-f respectively), showing a relatively uniform near-wall gradient of velocity. When moving from the proximal to the distal outflow, the centre of the spiral re-positioned to the centre of the lumen.

The velocity maps of the control graft in scan planes 1 and 2 (Figure 3.5j-o and Figure 3.6j-o) showed a symmetric double-spiral pattern, known as Dean flow, for low Reynolds numbers and a triple-spiral pattern for increasing Reynolds numbers. In scan plane 3 (Figure 3.7j-o) the flow patterns were unstable with two main spirals and potentially a third smaller spiral for Reynolds number 570, triple-spiral for 1140 and disturbed single-spiral for 1700. In scan plane 4 (Figure 3.8j-o) there was a weak double-spiral flow pattern for Reynolds number 570, showing that the secondary flow phenomena were declined, a double- or triple-spiral for 1140 and a single-spiral for 1700.

The core of each vortex is clearly illustrated in vorticity maps showing a perfect match with the velocity direction and magnitude maps. Each vortex was associated with regions of counter rotation near the wall.

3.3.2 In-plane velocity

Figure 3.9 - Figure 3.12 present a comparison of normalised peak in-plane or tangential velocity between spiral and control grafts for the four pairs of phantoms (anastomosis angle θ = 20°-80°) and for all applied Reynolds numbers. For the 20°, 40° and 60° models (Figure 3.9, Figure 3.10, Figure 3.11), the spiral graft produced higher peak velocities under all applied conditions, and the difference was almost always significantly higher from scan plane 2 and beyond. The difference was not clear for the

80° model (Figure 3.12). More specifically, in scan plane 1 the peak velocity for low Reynolds numbers was higher for the control device whilst for high Reynolds numbers, it was higher for the spiral device. In scan planes 2 and 3, the velocity was higher for the spiral graft, with the exception of Reynolds number 850 in scan plane 2. However, the standard deviations overlapped in most cases. In scan plane 4 the difference reached significance for the spiral graft with three of the applied Reynolds numbers, showing stronger downstream propagation of spiral flow.

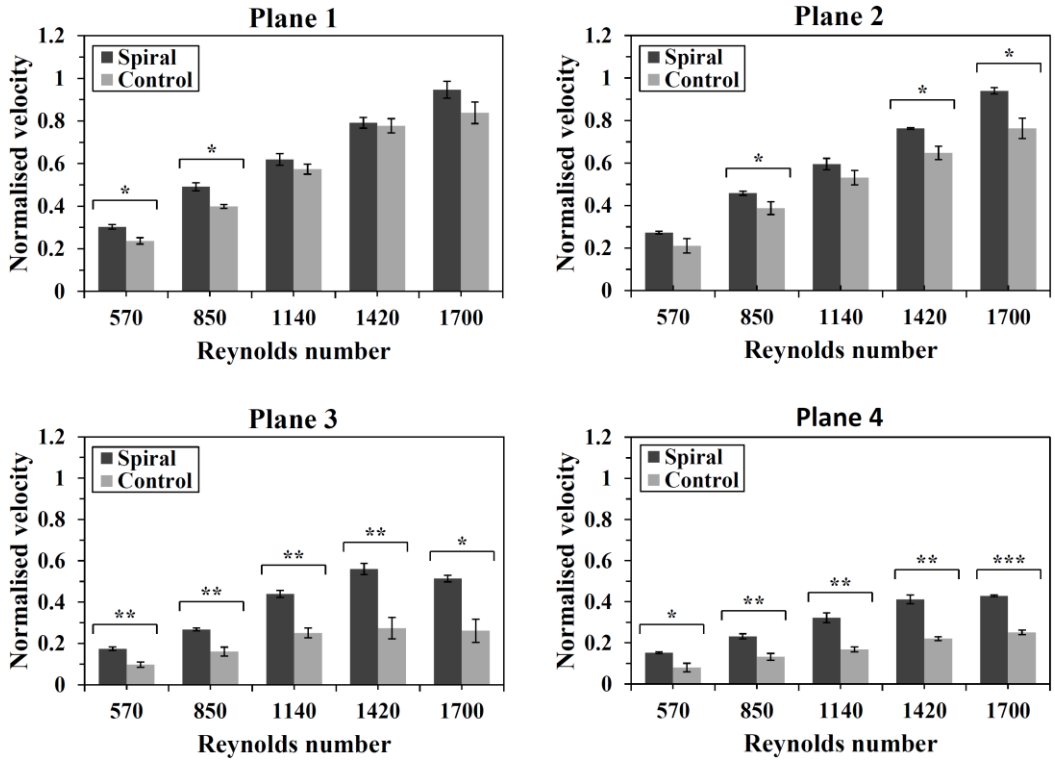

Figure 3.9: Progression of peak in-plane velocity at scan planes 1 to 4 of the spiral and control models for angle $\theta = 20°$; * $p < 0.05$, ** $p \leq 0.01$, *** $p \leq 0.001$.

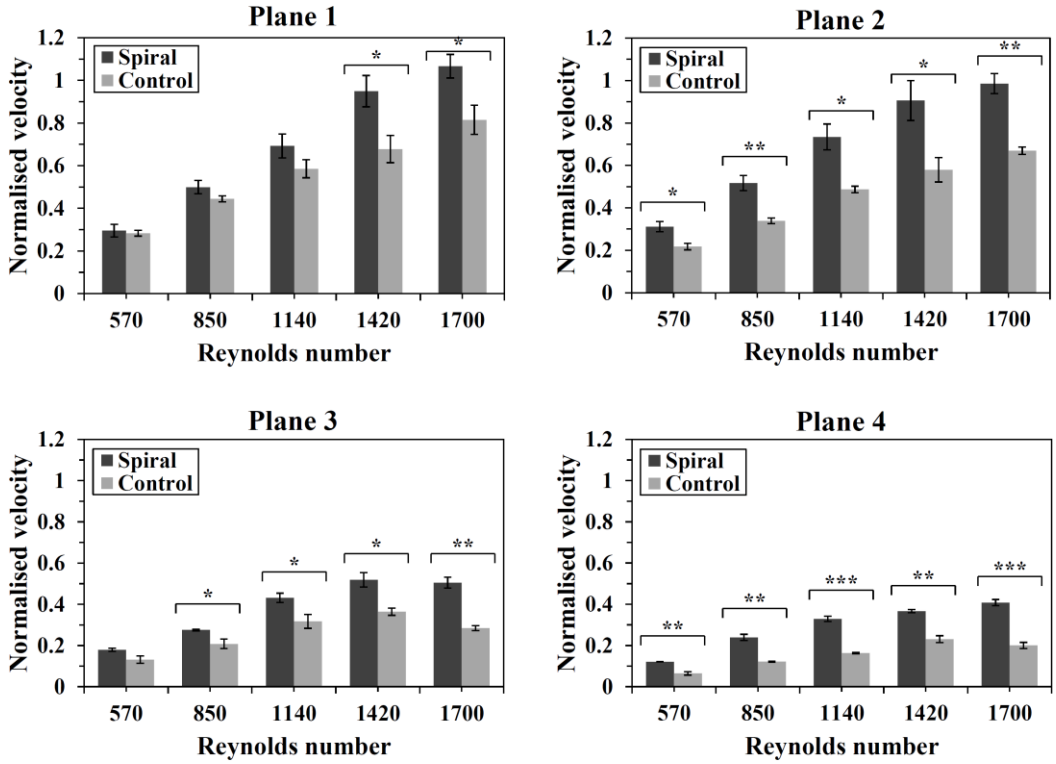

Figure 3.10: Progression of peak in-plane velocity at scan planes 1 to 4 of the spiral and control models for angle $\theta = 40°$; * $p < 0.05$, ** $p \leq 0.01$, *** $p \leq 0.001$.

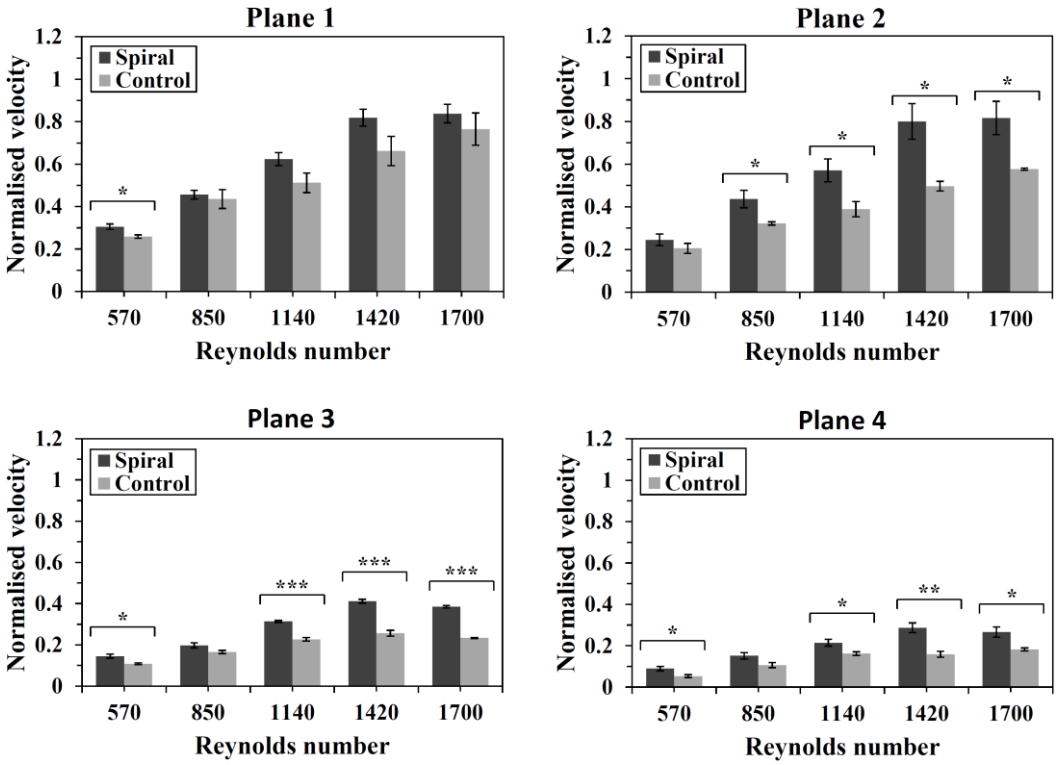

Figure 3.11: Progression of peak in-plane velocity at scan planes 1 to 4 of the spiral and control models for angle $\theta = 60°$; * $p < 0.05$, ** $p \leq 0.01$, *** $p \leq 0.001$.

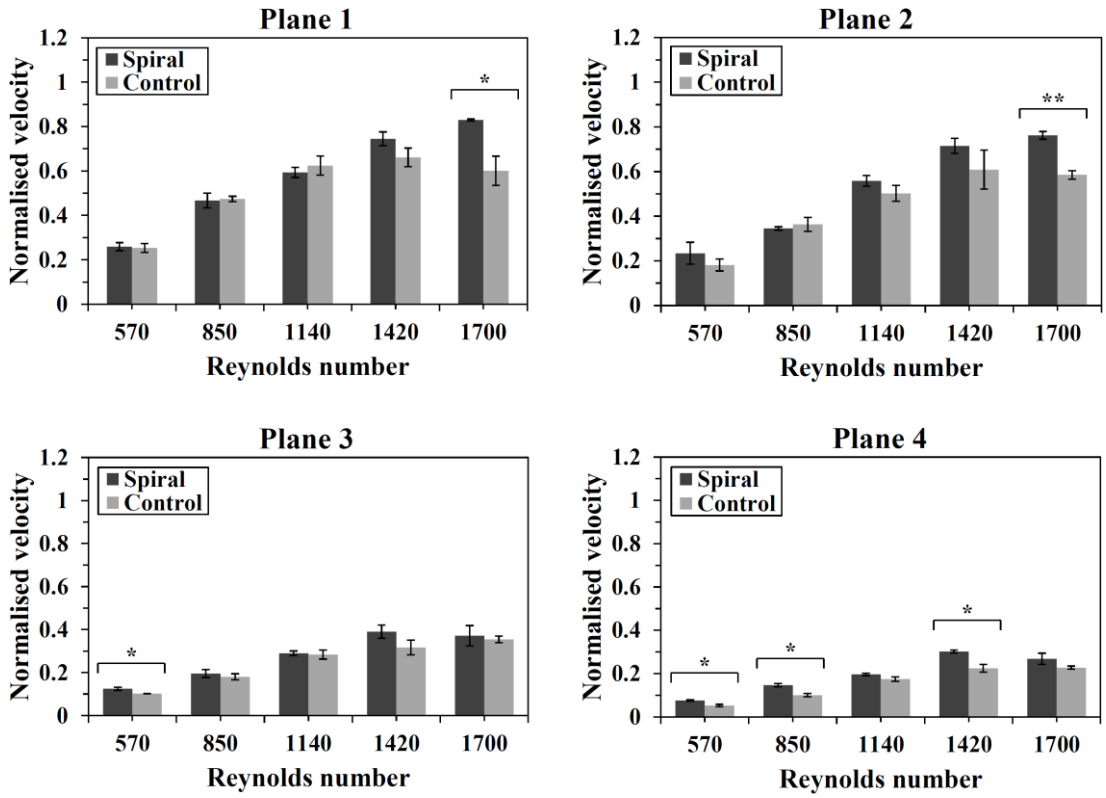

Figure 3.12: Progression of peak in-plane velocity at scan planes 1 to 4 of the spiral and control models for angle $\theta = 80°$; * $p < 0.05$, ** $p \leq 0.01$, *** $p \leq 0.001$.

3.3.3 Circulation

Figure 3.13 - Figure 3.16 show a comparison of circulation for the 20°**,** 40°**,** 60° and 80° models respectively. For anastomosis angles up to 60°**,** circulation was consistently higher for the spiral graft. For the 20° models (Figure 3.13) the difference almost always reached significance. For the 40° models (Figure 3.14) the difference reached significance from scan plane 2 and beyond and for the 60° models (Figure 3.15) from scan plane 3 and beyond. For the 80° models (Figure 3.16) no clear difference was found in scan planes 1 to 3. In scan plane 4 circulation was significantly higher for the spiral prosthesis.

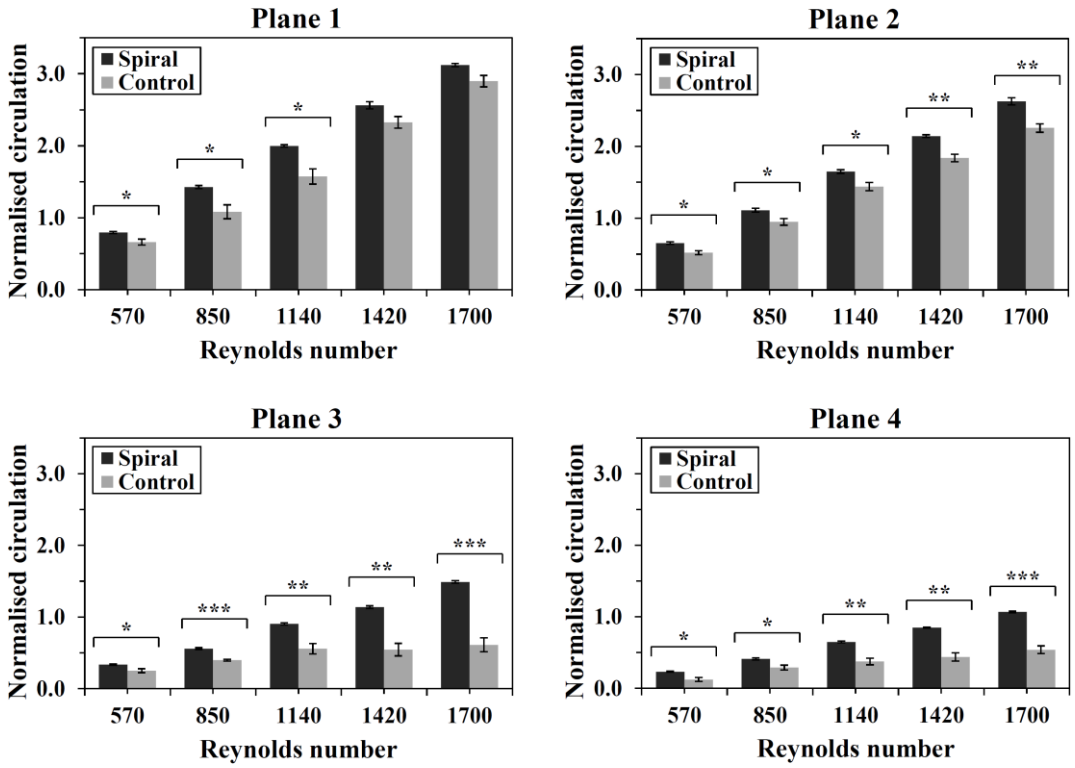

Figure 3.13: Progression of circulation at scan planes 1 to 4 of the spiral and control models for angle $\theta = 20°$; * $p < 0.05$, ** $p \leq 0.01$, *** $p \leq 0.001$.

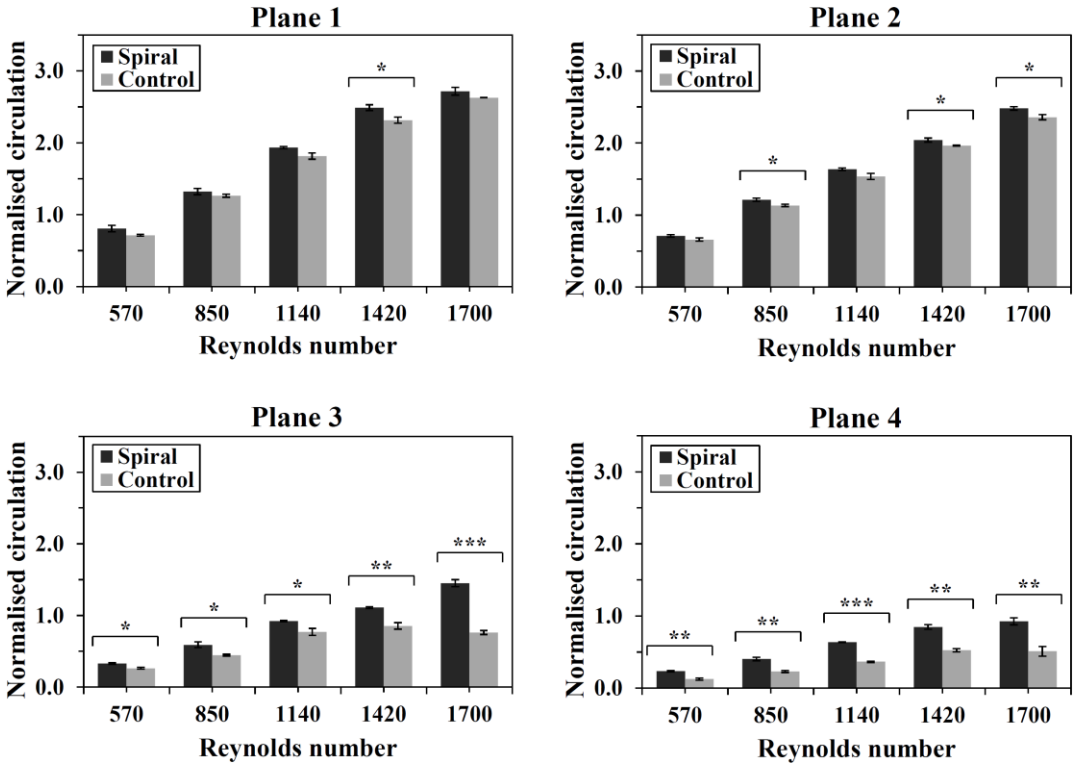

Figure 3.14: Progression of circulation at scan planes 1 to 4 of the spiral and control models for angle $\theta = 40°$; * $p < 0.05$, ** $p \leq 0.01$, *** $p \leq 0.001$.

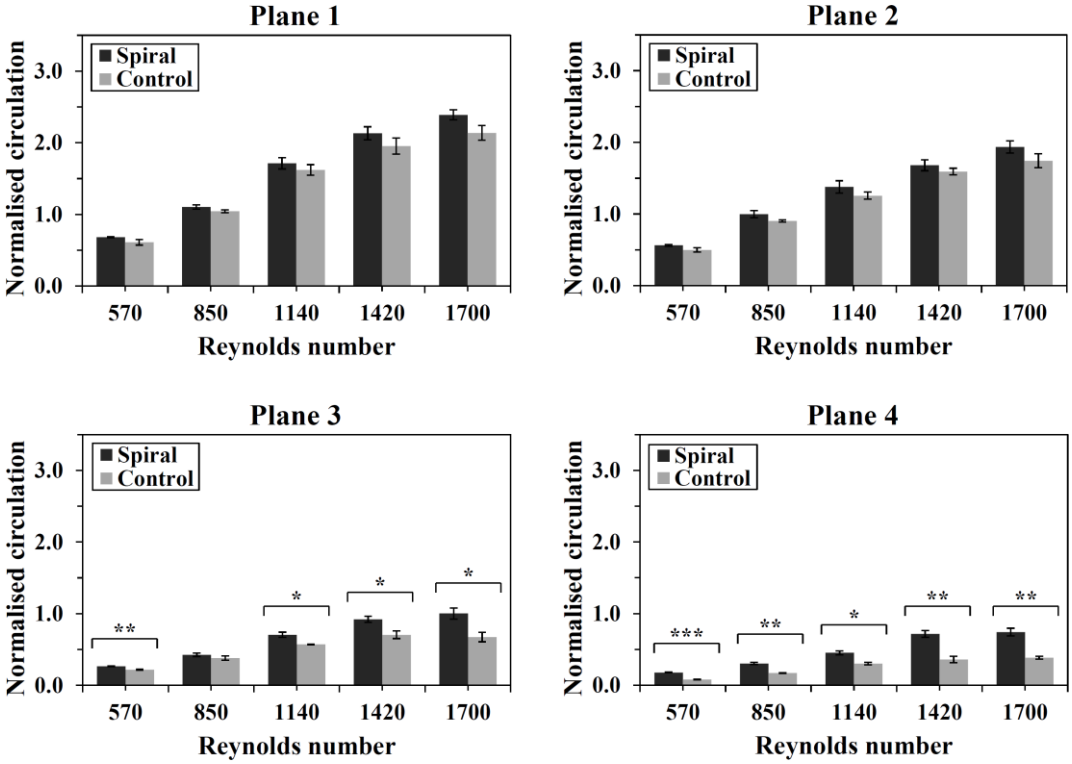

Figure 3.15: Progression of circulation at scan planes 1 to 4 of the spiral and control models for angle $\theta = 60°$; * $p < 0.05$, ** $p \leq 0.01$, *** $p \leq 0.001$.

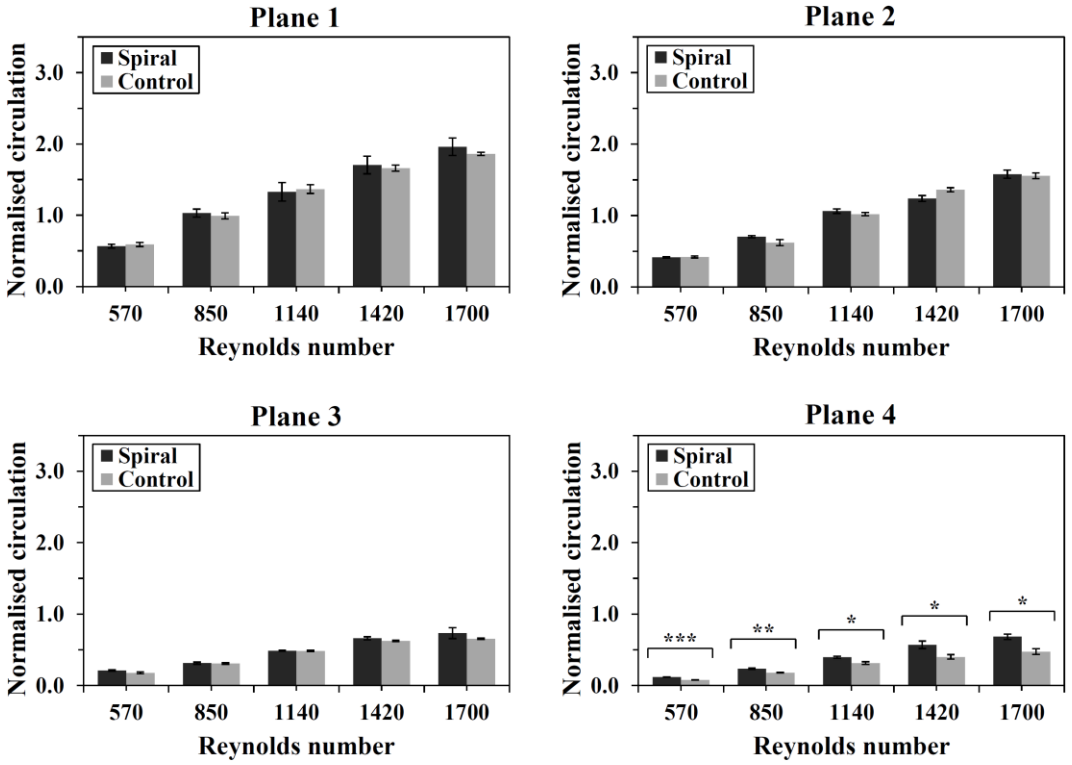

Figure 3.16: Progression of circulation at scan planes 1 to 4 of the spiral and control models for angle $\theta = 80°$; * $p < 0.05$, ** $p \leq 0.01$, *** $p \leq 0.001$.

3.4 Discussion

The rotational patterns from the proximal scan planes 1 and 2 of the control vascular-graft model demonstrated Dean flow for Reynolds number 570, which suggested a plane of symmetry about the model centreline (Figure 3.5jmp, Figure 3.6jmp). This plane would pass from the floor and toe wall sides and would bisect the cylindrical volume of the vessel mimic. Solutions of a similar nature have been presented by other researchers (Doorly and Sherwin 2009; Sherwin et al. 2000). The number of spiral cells in scan planes 1 and 2 increased from two to three for Reynolds numbers of 1140 and above. In the distal scan planes 3 and 4 of the control vascular-graft model, the spiral cells varied in number from one to three in a nonspecific way (e.g. in scan plane 3 or Figure 3.7 there were two or three spirals for Re = 570, three spirals for Re = 1140 and one spiral for Re = 1700). These results implied flow separation and instability in the outflow of the control, planar graft. The velocity magnitude maps presented a non-uniform near-wall distribution of the velocity field and cross-flow stagnation points (Sherwin et al. 2000), near to the wall where adjacent vortexes were mixed (Figure 3.17b). In the first two scan planes such points appeared in the toe and the upper floor wall side, locations which are commonly associated with neo-intimal hyperplasia (Doorly et al. 2002; Sherwin et al. 2000; Walsh et al. 2003). In the last two scan planes stagnation points did not appear in steady locations as the flow pattern was unstable.

In contrast, the rotational patterns in each scan plane of the spiral, non-planar graft had relatively steady profile, showing flow stability even at peak Reynolds numbers. From scan plane 2 and beyond the flow pattern was that of a single-spiral with uniform near-wall velocity distribution, showing flow coherence without cross-flow stagnation points. Stagnation points appear in scan plane 1 in the region between the toe and posterior (bottom) wall side where a flow disturbance was detected (Figure 3.17a). Results that support the introduction of flow stability and coherence from single-spiral flow have been presented in previous studies (Stonebridge et al. 2004). Stonebridge and Brophy (1991) hypothesised that single-spiral flow may exert a beneficial effect on the mechanism of endothelial damage and repair. This hypothesis was later supported by Caro et al. (2005) who demonstrated that a single vortex may inhibit blood stagnation, separation and instability.

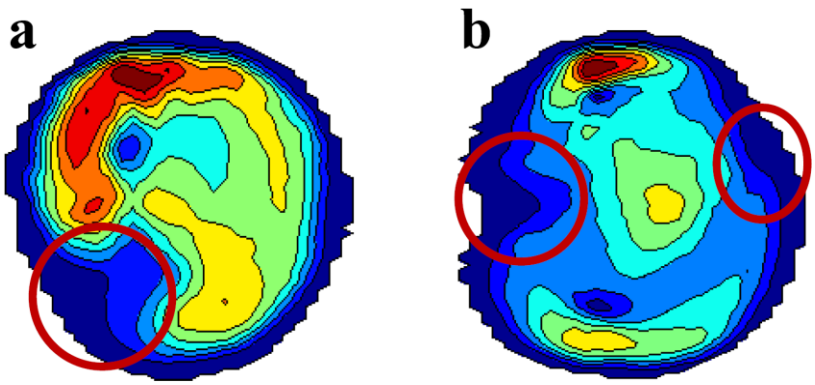

Figure 3.17: Stagnation points in vector Doppler velocity magnitude maps. (a) Spiral graft (from Figure 3.5d). (b) Control graft (from Figure 3.5m).

Comparisons of peak in-plane velocity and circulation in Figure 3.9 – Figure 3.16, demonstrated increased values for the spiral graft. This quantitative evaluation indicated increased in-plane mixing for the spiral device. In-plane mixing has been proposed as a mechanism for protecting anastomotic regions from neo-intimal hyperplasia and thrombosis (Caro et al. 2005). The difference in these values increases in significance when moving from the proximal to distal scan planes. The level of significance also increased with increasing Reynolds number, especially in the distal scan planes. The increase of anastomosis angle θ had a clearly negative impact on the strength of vortical structures induced by the spiral graft. More specifically in the 20° angle models the differences in both velocity and circulation reached significance from scan plane 1 and beyond, whilst in the 80° angle models only differences in scan plane 4 reached significance. Moreover, the magnitude of the circulation values generally decreased with increasing connection angle θ.

The last three paragraphs describe a relation between single helical flow and advanced local haemodynamics that may protect endothelial function and prevent the abnormal proliferation of vascular smooth muscles. Such a mechanism would inhibit the formation of atheromatous plaque and could be an explanation for the improved clinical results of the spiral PV graft presented by Stonebridge et al. (2012).

Each vortex revealed counter vorticity regions near the wall. This was the result of no-slip boundary conditions relative to the wall. Taking as an example a single vortex, the counter vorticity appears in the whole circumference because of the inverse shearing

forces of the fluid particles relative to the wall where the velocity was decreased. Solutions of this nature have been previously reported in other studies (Cookson et al. 2009; Yamamoto et al. 2002; Zabielski and Mestel 1998). The interested reader can refer to section 2.4.3 (page 46) for additional information.

As the PV anastomosis in clinical practice is commonly around 45°, the colour maps presented were those of the 40° pair of phantoms. Models of 45° anastomosis are widely investigated in computational studies (Doorly et al. 2002; Ethier et al. 2000; O'Callaghan et al. 2006; Walsh et al. 2003).

The velocity and vorticity maps from the 20°, 60° and 80° spiral graft models were very similar to those presented for the 40° model in all the examined scan planes. However, the maps from the 80° spiral graft model had a less uniform distribution of velocity gradient and more disturbed spirals when compared to the maps from lower angles, especially in the proximal graft outflow.

The velocity and vorticity maps from the 20°, 60° and 80° control graft models were very similar to those presented for the 40° model in the proximal scan planes. In the distal scan planes there was a variation of one to three spirals, as presented in Figure 3.7 and Figure 3.8, but there was no specific relationship between the number of spirals and the angle of anastomosis and Reynolds numbers. In some cases of scan plane 4 and Reynolds number 570, it was very difficult to detect a specific flow pattern suggesting dissipation of vortical structures. This may be a transitional region from vortical to parabolic flow. Also the single spiral, which was detected in some cases at the distal scan planes, may imply a natural characteristic of multiple-spiral flows coalescing before they dissipate.

The description of flow maps from the 20°, 60° and 80° pairs of phantoms correlates well with the quantitative analysis in Figure 3.9 - Figure 3.16. There were increased quantitative differences in the flow patterns of the distal scan planes, a region where the spiral graft revealed a uniform single-spiral and the non-spiral graft an unstable, weak flow profile. The decreased quantitative differences in the proximal outflow of the 80° spiral and non-spiral models may be linked with the less uniform distribution of velocity, and more disturbed spirals, in the proximal outflow of the spiral graft. Velocity

maps from the 60° vascular-graft models are presented in Appendix A for comparison (reproduced from Kokkalis et al. 2013).

The arterial flow rate in the lower proximities varies from high peak values to retrospective flow during the cardiac cycle, resulting in a large range of Reynolds numbers. For instance, a normal distal superficial femoral artery has an average diameter of 0.54 ± 0.11 cm and peak systolic velocity of 94 ± 14 $cm \cdot s^{-1}$ (Armstrong and Bandyk 2010). If we assume blood is a Newtonian fluid with kinematic viscosity, ν, 3.5×10^{-6} $m^2 \cdot s^{-1}$ (or 3.5 cSt), the Reynolds number can reach 1700. In this study the applied Reynolds numbers were between 570 and 1700 to enable the detection of vortical structures at a range of physiologic values. It has been noted that pulsatile flow can play an important role in blood mixing (Caro et al. 2005; Cookson et al. 2009).

The vascular-graft models were manufactured assuming that the host vessel mimic was blocked proximal from the graft-vessel mimic anastomosis. However, there are clinical cases where the bypassed region is not totally occluded. In such cases a bi-directional run-off is detected in the graft outflow (Fisher et al. 2004). We would expect that this would have an impact on the secondary flow motions detected in the outflow of PV prosthetic grafts.

3.5 Conclusions

Ultrasound flow phantoms were developed for the comparison of a spiral, non-planar and a non-spiral, planar bypass PV graft. The grafts were positioned in four surgically valid configuration geometries. Two-dimensional velocity and vorticity maps were generated in the cross-flow direction of the phantoms based on conventional colour Doppler ultrasound. The vortical structures induced with these devices were compared from their proximal outflow up to 10 cm downstream the flow direction.

In general, the vortical maps revealed a single-spiral flow for the spiral prosthesis and a double- or triple-spiral flow for the non-spiral prosthesis. The single spiral induced stability and coherence in the outflow profile. The multiple-spiral maps were associated with increased stagnation points, flow separation and instability. Enhanced peak in-

plane velocity and total circulation were detected in the outflow of the spiral device in comparison to the control, indicating increased in-plane mixing.

These results support the hypothesis that a PV graft able to generate a single helical flow pattern, may inhibit the development of neo-intimal hyperplasia and blood thrombosis in its proximal outflow and hence the development of PAD downstream in the arterial circulation. In clinical practice this would lead in improved patency rates.

Chapter 4

Secondary flow motions in the outflow of arteriovenous prosthetic grafts

4.1 Introduction

The vein walls connected to an AV graft outflow are subjected to abnormally high flow rates. The implantation of an AV graft introduces disturbed flow patterns creating an adverse flow environment in the host vein. It is believed that these disturbances in haemodynamics affect the endothelial function triggering irregular tissue growth (Haruguchi and Teraoka 2003; Papaharilaou et al. 2002).

It has been postulated that a stabilised and uniform flow profile, such as that of a single spiral pattern, can protect the vein from stenosis. A novel AV spiral graft has been introduced in clinical practice and an initial pilot clinical study (Inston and Hofmann 2013) and previous animal study (Jahrome et al. 2011) have shown encouraging results. These results motivated this investigation into the haemodynamics induced by this spiral AV graft.

The aim of this chapter was to describe and compare the secondary flow motions in the outflow of both the spiral and a conventional AV prosthetic graft. Identical vascular-graft models were manufactured for both types of prostheses and both were tested in a phantom setup, previously described (section 2.2, page 31). Vector Doppler and vorticity imaging was used for flow visualisation and the peak in-plane velocity and circulation were measured for flow quantification.

4.2 Materials and methods

4.2.1 Arteriovenous access grafts

The spiral graft, which is known as *Spiral Laminar Flow*^{TM} AV graft, and the control non-spiral graft were made of ePTFE and had a 6 mm inner diameter (Vascular Flow Technologies Ltd, Dundee, UK). At the distal end of the spiral device, injection moulded medical grade polyurethane formed a spiral inducer segment (Figure 4.1a). This inducer created an internal ridged cross sectional and non-planar geometry to deliver a single spiral in its outflow. The control device was a conventional AV graft without a spiral inducer (Vascular Flow Technologies Ltd, Dundee, UK).

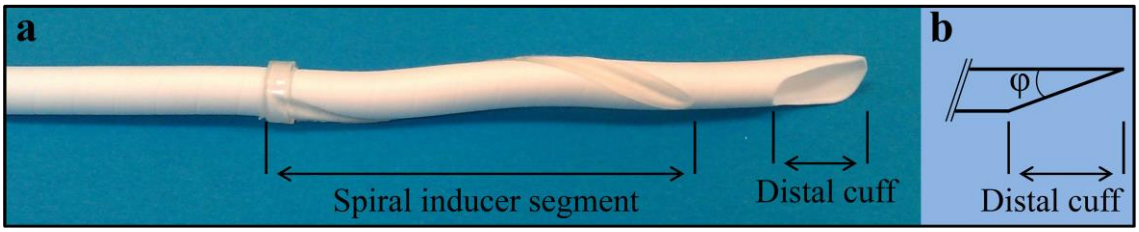

Figure 4.1: (a) Distal end of a 6 mm inner diameter arteriovenous spiral graft. (b) Side view diagram of the distal cuff with cut-off angle φ = 15°.

4.2.2 Vascular-graft model

The inflow of both the spiral and control grafts was connected to C-Flex® tubing (Cole-Parmer, London, UK) used to mimic the arterial vessel. The distal cuffs of the grafts were trimmed to 15° (Figure 4.1b) and connected to PVA-c venous mimics. Both the inflow and outflow connections were positioned in end-to-side configurations using superglue and reinforced with epoxy adhesive. The spiral and control AV grafts, connected to the arterial C-Flex® and the venous PVA-c mimic, are referred to in this thesis as spiral and control vascular-graft models. Each model was housed in an acrylic tank and connected to the previously described flow rig (section 2.2, page 31).

Two pairs of vascular-graft models were created. One pair simulated the looped surgical configuration and the other the straight surgical configuration (Figure 4.2), (Akoh 2009; Brown and Mitchell 2014). Each pair consisted of a spiral graft model and a non-spiral graft model positioned in identical geometries. The proximal end of the looped grafts

was cut at 15° whilst the proximal end of the straight grafts was cut at 90°. The distal cuff of all grafts was trimmed at 15° (Fig. 1b). A consultant vascular surgeon verified the quality and similarity of the models with that found in clinical practice. The distal end of the arterial mimic and proximal end of venous mimic were blocked so as to force the blood mimic to pass through the grafted region and venous flow direction. Figure 4.2 illustrates the overall geometry of the models and the heel, toe and floor of the end-to-side distal anastomosis (Haruguchi and Teraoka 2003; Tricht et al. 2005). During the study the temperature in the vascular-graft tank was monitored with a mercury thermometer and maintained at 21 ± 1°C using ice bags to ensure the acoustic properties were correctly maintained (Hoskins 1999).

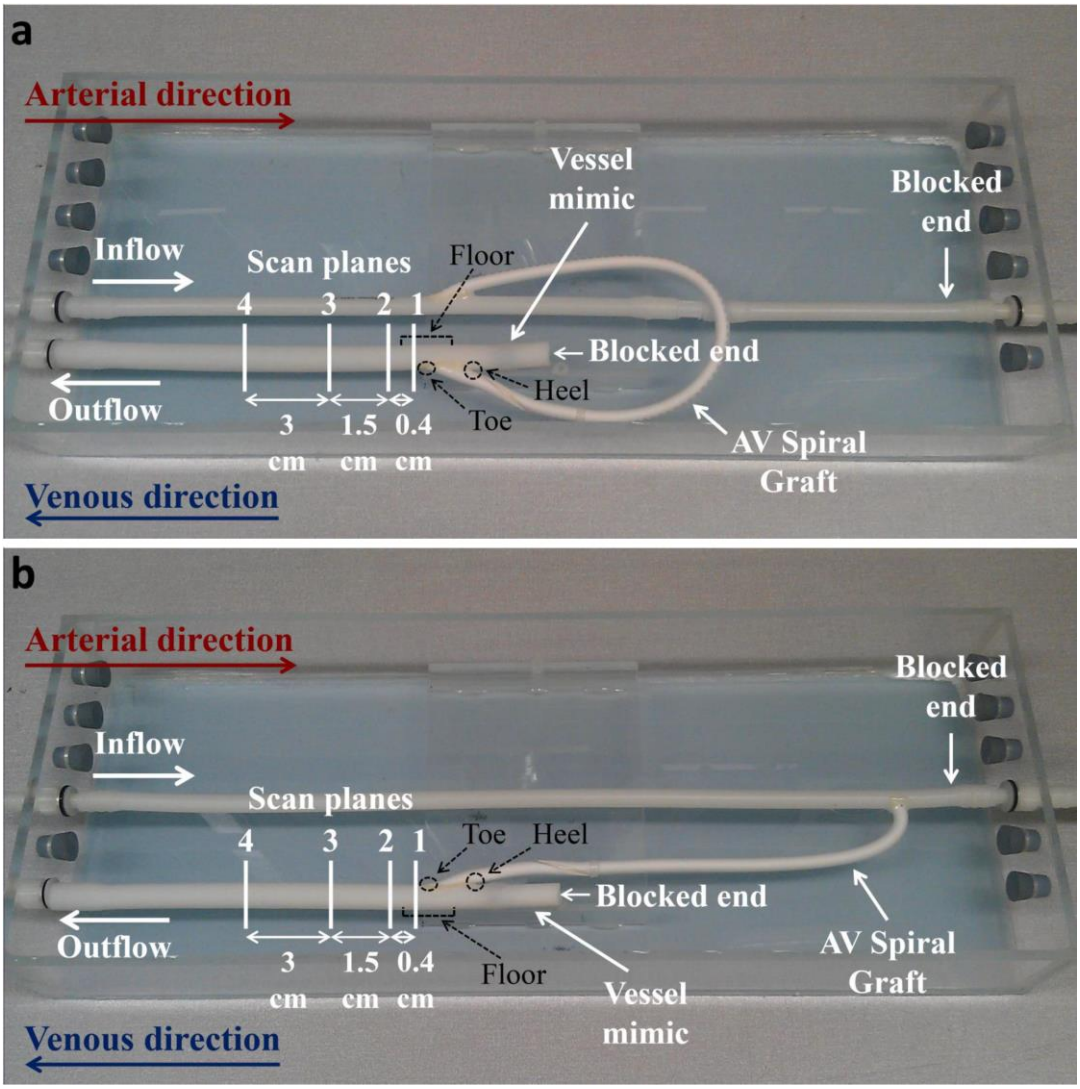

Figure 4.2: (a) Looped configuration AV spiral graft model. (b) Straight configuration AV spiral graft model. The respective control models were identical. Data was collected at scan planes 1 to 4. Scan plane 1 was positioned 0.1 cm distal from the graft outflow.

The 3-D flow profile in a fluid circuit is strongly influenced by the tubing geometry. The pump, flow rig tubing and vascular-graft models were positioned at the same height to create a planar flow design and to standardise the flow conditions. An exception to the planarity of these models was the spiral flow inducer segment of the AV spiral grafts. The value of the inlet length (section 1.6.3, page 26) was calculated as in the previous chapter (Equation 1.6) and taken into consideration in the length of the tubing between the pump outflow and the inlet of each vascular-graft model.

4.2.3 Data acquisition

It is known that an AV graft introduces abnormal haemodynamics linked with stenosis, primarily in the outflow anastomosis and the first 2-5 cm distal from it (Haruguchi and Teraoka 2003), but also downstream in the host vein (Doelman et al. 2005). Therefore, colour Doppler cine-loops were recorded for both pairs of phantoms at 0.1, 0.5, 2, 5 and 10 cm distal from the graft outflow, to study the development of vortical structures (Figure 4.2a,b, scan planes 1-4). These scan planes were transverse to the flow in both anteroposterior and right to left directions to detect vortical structures.

Clinically, flow rates under 600 $mL \cdot min^{-1}$ in the outflow AV graft anastomosis are linked with thrombosis and the minimum requirement for adequate dialysis clearance is 300 $mL \cdot min^{-1}$ (Akoh 2009). Hence, constant flow rates of 240, 360, 480, 600 and 720 $mL \cdot min^{-1}$, corresponding to Reynolds numbers of 570, 850, 1140, 1420 and 1700 respectively, were applied in the models. These Reynolds numbers were calculated as explained in section 3.2.3 (page 63).

The transducer was kept steady in the scan planes with a retort clamp, which was adjusted in a micromanipulator to accomplish relatively accurate displacements. The micromanipulator had three degrees of freedom and was accurate to 0.5 mm (Figure 3.3). The distance between the surfaces of the venous mimic and the transducer was 4-5 mm. An acoustic absorber pad (F28, Precision Acoustics, Dorchester UK) was placed under the vessel mimic to prevent ultrasound beam reflections.

The colour box was kept small to increase the frame rate. The line-density was set to *C* yielding the maximum colour line density or velocity information every 0.2 mm in the data file. More colour Doppler settings are listed in Table 3.1.

Table 4.1: Colour Doppler settings of the scanner in the peripheral vascular graft study.

Setting	Value
Persistence	Low
Sensitivity	High
Smoothing	Low
Dynamic motion differentiation	Off
Wall filter	Low

In each scan plane two cine-loops were acquired; one with the ultrasound beam steered at +20° and the other with the ultrasound beam steered at -20° relative to the linear transmission. The cine-loops consisted of 115 frames each, which was the capacity of the scanner memory buffer. All measurements were repeated three times to verify repeatability. Each time the transducer was repositioned. Off-line post processing was undertaken using MATLAB R2012a.

Each cine-loop was averaged to reduce noise from colour speckle and small variations in the flow pattern over time, creating one array of velocity information for each projection. The centres of these arrays were aligned applying a central gravity registration algorithm, to confirm that there was no lateral displacement between the two steered beams. The vector Doppler and vorticity algorithms were executed and 2D velocity direction, velocity magnitude and vorticity maps were reconstructed.

4.2.4 Data selection criteria

A significant flow pattern variation was observed from frame to frame in the 10 cm scan plane for the non-spiral models, for all applied flow rates. Moreover, for low flow rates the in-plane tangential velocity signal was weak and the Doppler frequency shift low. Reduced PRF and increased colour gain were tried to allow the detection of these weak secondary flow motions, but the clutter signal induced from the venous and tissue mimic regions prevented this. These observations for the control models at low flow rates may suggest dissipation of rotational structures in the cross-flow of plane 4. On the

contrary, a clear and steady flow pattern was detected at the same scanning location and flow parameters for the spiral graft models. The 10 cm scan plane was excluded from the study due to a lack of satisfactory returned Doppler signal and flow stability from the control models.

4.2.5 Data analysis

Comparison of peak in-plane velocity

The angle independent peak cross-flow velocity was detected in each scanning location under all applied flow parameters. These measurements were normalised to the mean axial velocity, $\overline{v}$, as it was described in Equation 3.2 (page 65).

Comparison of circulation

A vorticity map was generated for each 2D velocity data set. The flow in these maps was quantified with circulation. The contiguous regions of positive and negative vorticity were integrated over their areas and their absolute values were summed to calculate the total circulation. This was applied to the entire AV graft models datasets. The mean circulation of the spiral and non-spiral loop configuration models was used to normalise each of their circulation values, Γ, as shown in Equation 3.3 (page 67). The same method was applied to the spiral and non-spiral straight models. The corresponding circulation values between the two types of grafts were compared.

Statistical analysis

The differences in measures of peak velocity and circulation between the spiral and control models were examined as described in chapter 3, section ‘Statistical analysis’, page 67.

4.3 Results

4.3.1 Vector Doppler and vorticity imaging

Colour Doppler ultrasound was used for an initial observation of the vortical structures in the cross-flow view. Two-dimensional velocity and vorticity maps were developed based on vector Doppler imaging as illustrated in Figure 4.3 - Figure 4.6. These figures represent the four scan planes from the proximal (scan plane 1 at 0.1 cm) to the distal (scan plane 4 at 5 cm) outflow of the looped configuration models (Figure 4.2a). In each of these figures, spiral and control graft outflow mapping is included for the minimum, middle and maximum Reynolds number, 570, 1140 and 1700 respectively. The orientation of the maps is such that the left and right sides are the floor and toe wall sides of the vessel mimic respectively, and the top and bottom are the anterior and posterior wall sides respectively (Figure 4.2a). Velocity direction maps are shown in the first row for each graft, velocity magnitude in the second and vorticity in the third. The colour distribution in the velocity direction maps represents the displacement of the velocity vector from 0° to 360° and the length of the vectors is proportional to the magnitude of the velocity. Vorticity maps correspond to axial vorticity, ω_z, where positive regions are associated with counter-clockwise rotation and negative regions with clockwise rotation. The boundaries of zero vorticity between the areas of positive and negative vorticity are represented by a thick black contour line. In all maps the darkest blue and darkest red symbolise the lower and upper limits of the values measured.

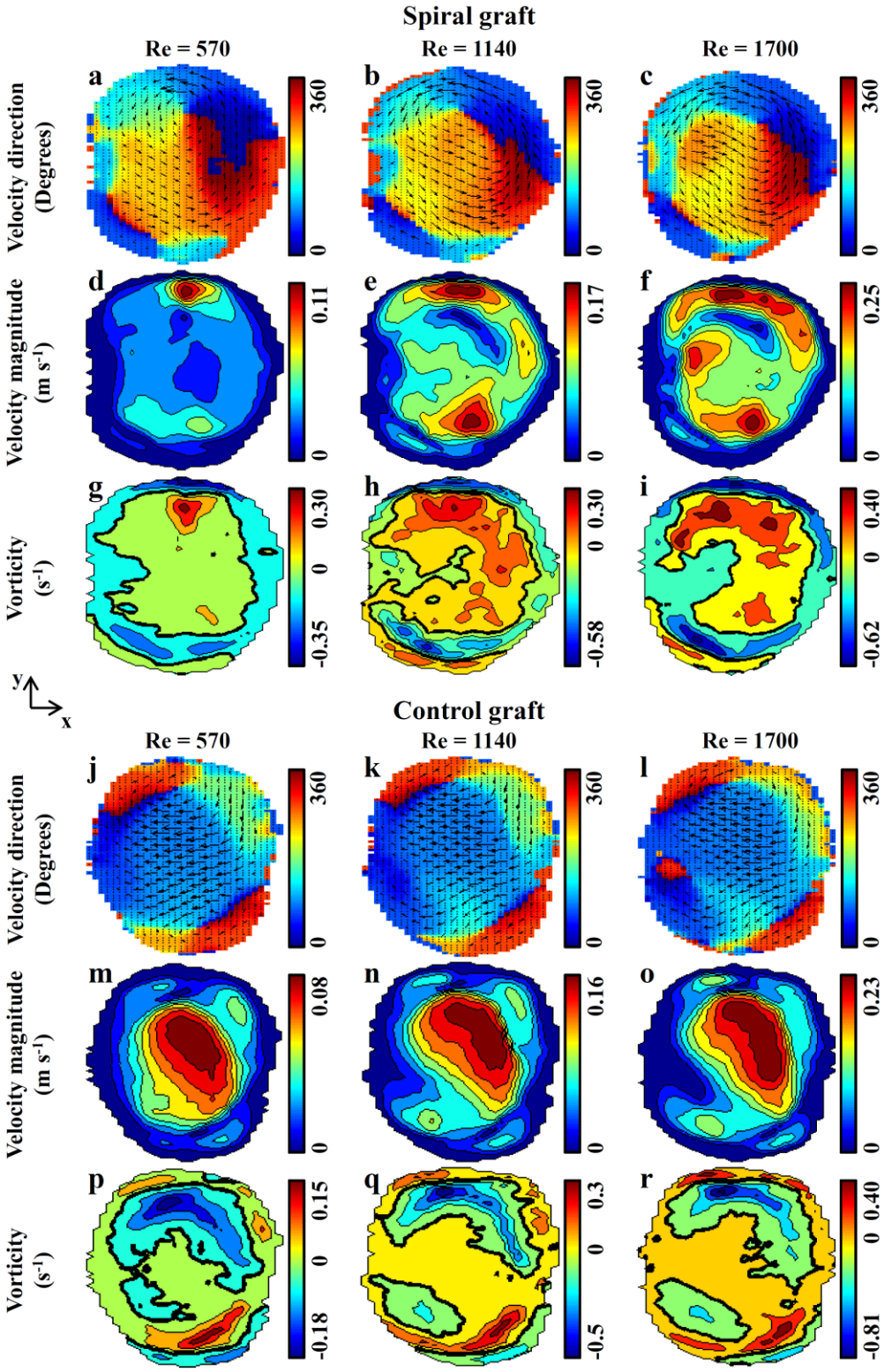

Figure 4.3: Presents the flow maps for the spiral and control looped AV models, for scan plane 1. The first and forth rows illustrate in-plane velocity direction, the second and fifth rows illustrate in-plane velocity magnitude and the third and sixth rows illustrate axial vorticity ω_z. The boundaries of zero vorticity are represented by a thick black contour line. The orientation of each map in relation to the anastomotic locations is: left side = floor and right side = toe.

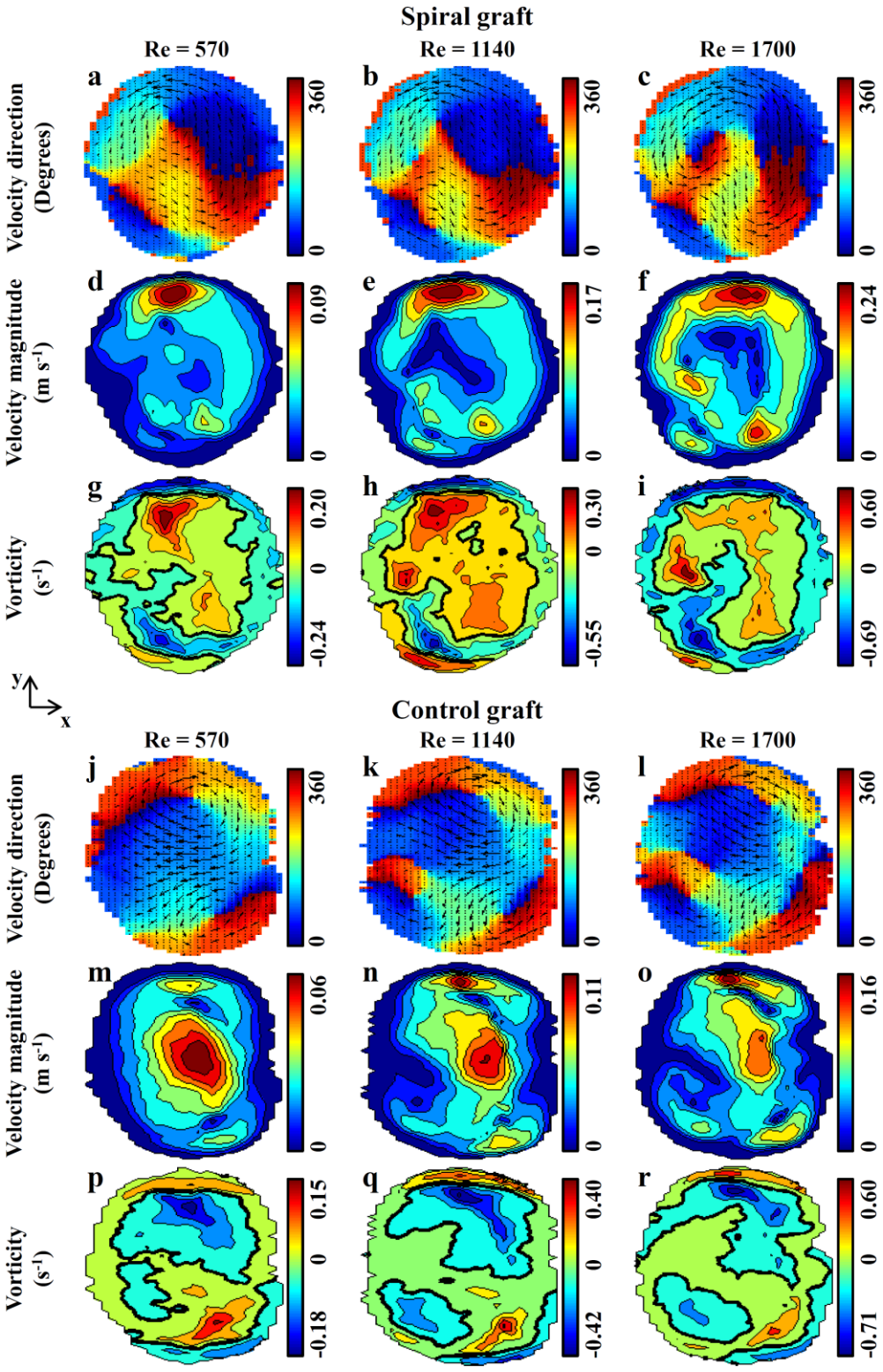

Figure 4.4: Presents the flow maps for the spiral and control looped AV models, for scan plane 2. The first and forth rows illustrate in-plane velocity direction, the second and fifth rows illustrate in-plane velocity magnitude and the third and sixth rows illustrate axial vorticity ω_z. The boundaries of zero vorticity are represented by a thick black contour line. The orientation of each map in relation to the anastomotic locations is: left side = floor and right side = toe.

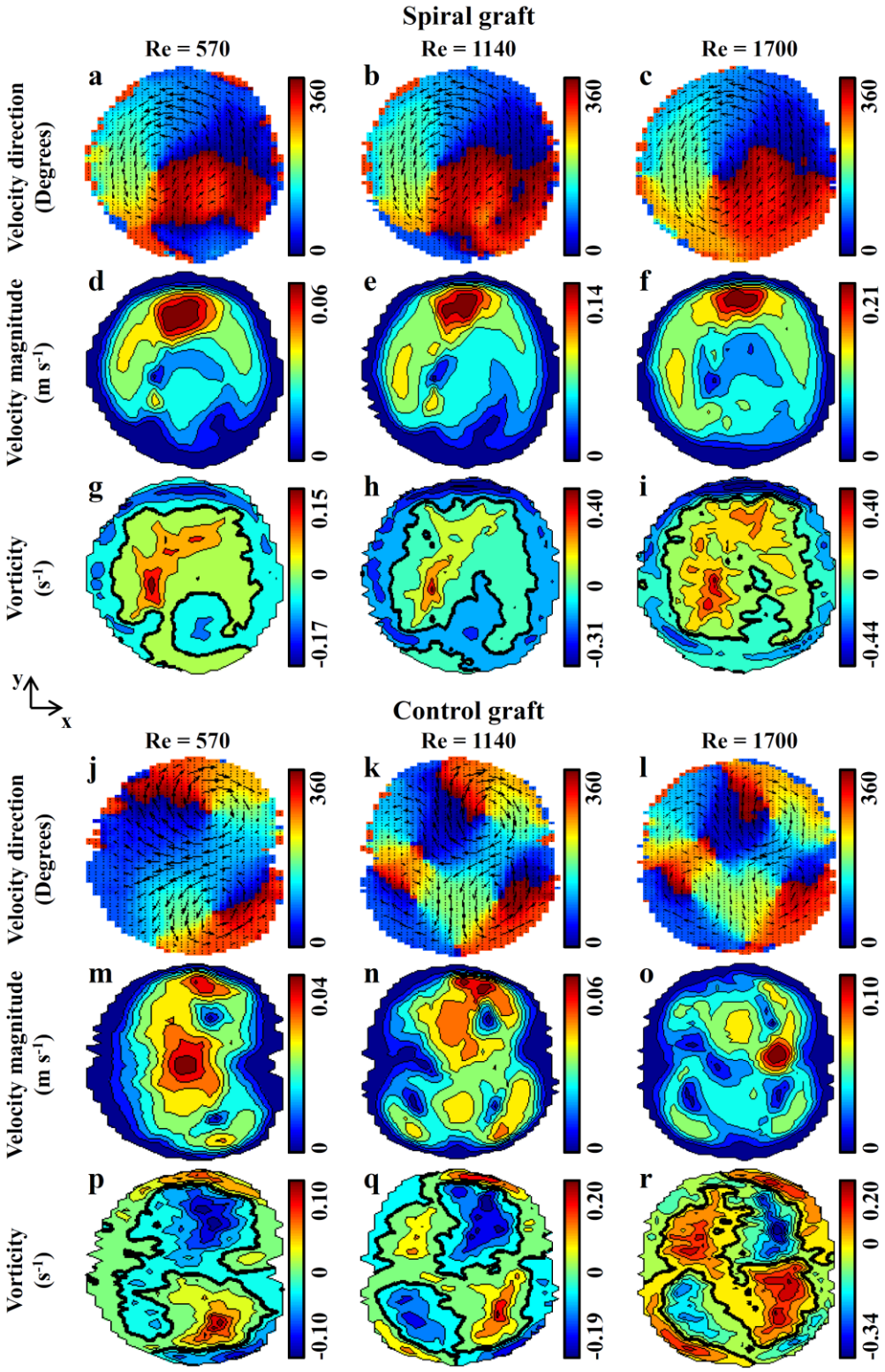

Figure 4.5: Presents the flow maps for the spiral and control looped AV models, for scan plane 3. The first and forth rows illustrate in-plane velocity direction, the second and fifth rows illustrate in-plane velocity magnitude and the third and sixth rows illustrate axial vorticity ω_z. The boundaries of zero vorticity are represented by a thick black contour line. The orientation of each map in relation to the anastomotic locations is: left side = floor and right side = toe.

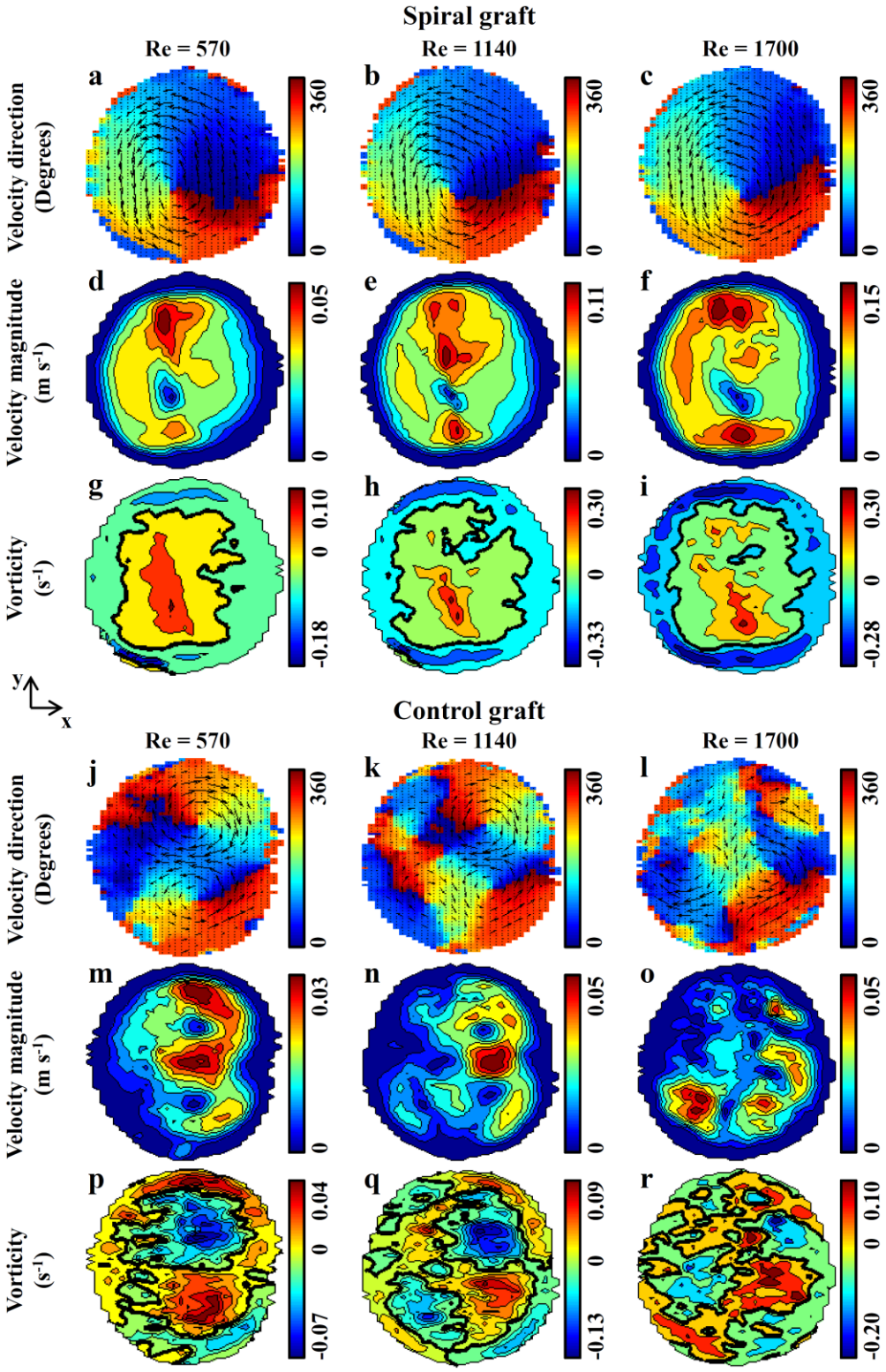

Figure 4.6: Presents the flow maps for the spiral and control looped AV models, for scan plane 4. The first and forth rows illustrate in-plane velocity direction, the second and fifth rows illustrate in-plane velocity magnitude and the third and sixth rows illustrate axial vorticity ω_z. The boundaries of zero vorticity are represented by a thick black contour line. The orientation of each map in relation to the anastomotic locations is: left side = floor and right side = toe.

In scan plane 1 the flow maps revealed a double-spiral flow pattern for both grafts (Figure 4.3). In the case of the spiral graft, this double-spiral was composed of a dominant spiral at the anterior side (top) and a smaller spiral at the posterior side (bottom). The double-spiral induced by the control graft had the profile of a Dean flow pattern. In scan plane 2 (Figure 4.4), the flow patterns created by the spiral graft were similar to those observed in Figure 4.3, whereas the flow created by the control graft in this plane was that of a three- and a four-spiral pattern for Reynolds numbers 1140 and 1700 respectively. In scan plane 3 the spirals produced by the spiral graft began to coalesce for low Reynolds numbers and this process was completed for the peak Reynolds number (Figure 4.5a-i). For the non-spiral graft Dean flow was observed at a Reynolds number of 570 and a four-spiral pattern at Reynolds numbers 1140 and 1700 (Figure 4.5j-r). In scan plane 4, the spiral device produced a uniform single vortex for all Reynolds numbers (Figure 4.6a-i), whereas the control graft produced Dean flow for Reynolds number 570, a four-spiral pattern for 1140 and a disturbed pattern for 1700 (Figure 4.6j-r).

The rotating characteristics of flow particles were illustrated with vorticity mapping. There was a clear correlation between the core of vortices in the velocity and vorticity maps. Regions of counter vorticity were observed near the walls for each vortex.

4.3.2 In-plane velocity

Figure 4.7 and Figure 4.8 present a comparison of peak in-plane or tangential velocity for the looped and straight configuration respectively. The velocity was consistently higher for the spiral prosthesis in both geometries, with the exception of plane 1 for the straight models at Reynolds number 1420. The differences found in peak velocity for the looped models reached significance for all planes with the exception of plane 1, Reynolds numbers 1140 and 1700. In terms of the straight models, differences reached significance in planes 2 and 4 and also in plane 3 for Reynolds numbers 570, 850 and 1420.

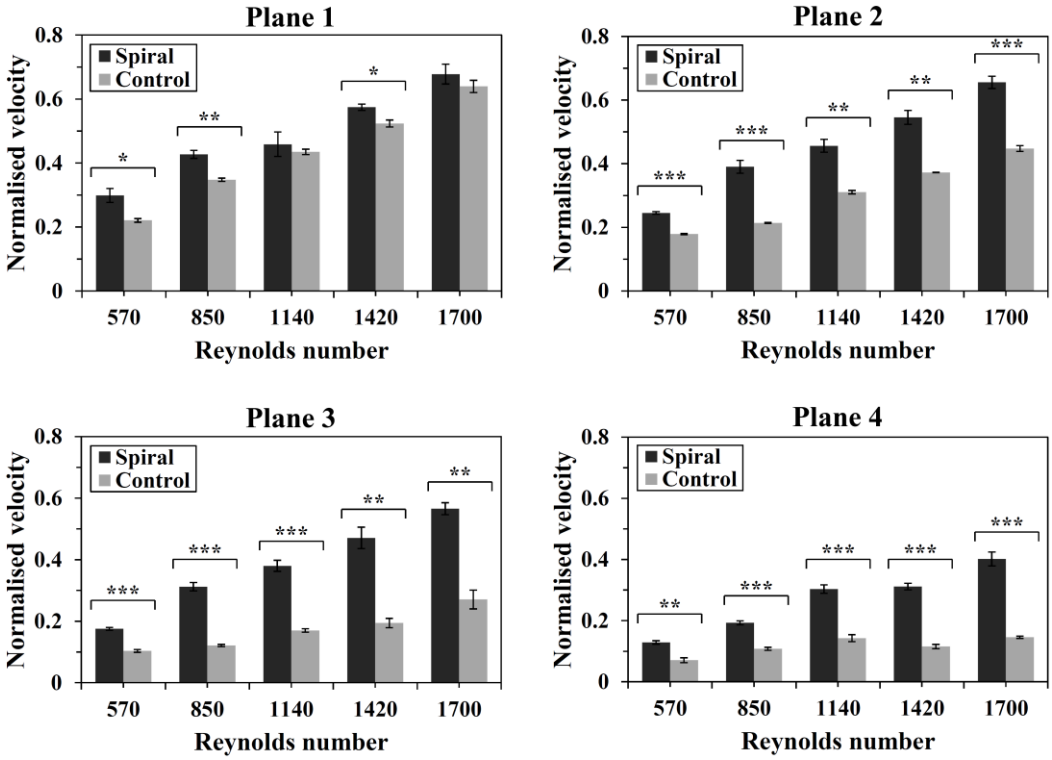

Figure 4.7: Progression of peak in-plane velocity at scan planes 1 to 4 for the spiral and control looped models; * $p < 0.05$, ** $p \leq 0.01$, *** $p \leq 0.001$.

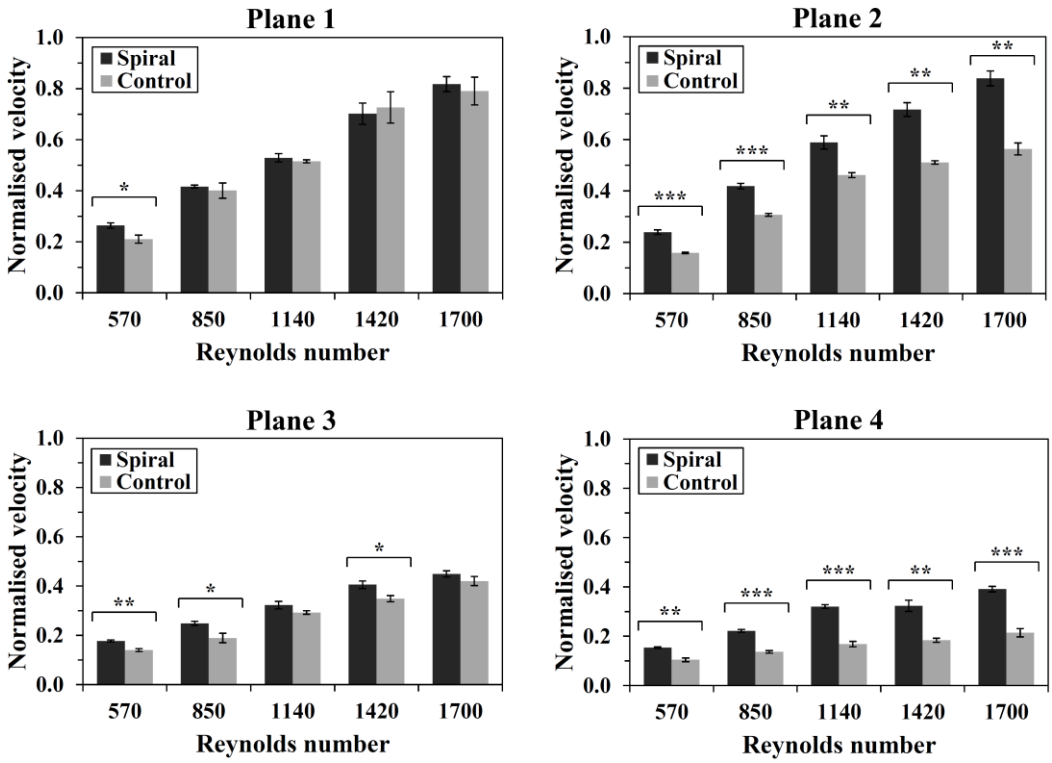

Figure 4.8: Progression of peak in-plane velocity at scan planes 1 to 4 for the spiral and control straight models; * $p < 0.05$, ** $p \leq 0.01$, *** $p \leq 0.001$.

4.3.3 Circulation

Figure 4.9 and Figure 4.10 show the comparison of circulation for the looped and straight geometry respectively. Circulation was constantly higher for the spiral device except for plane 1, Reynolds number 850 and 1140, Figure 4.10. This difference reached significance for the looped models, with the exception of plane 1, Reynolds number 1140. In the straight surgical configuration the differences reached significance from plane 2 onwards.

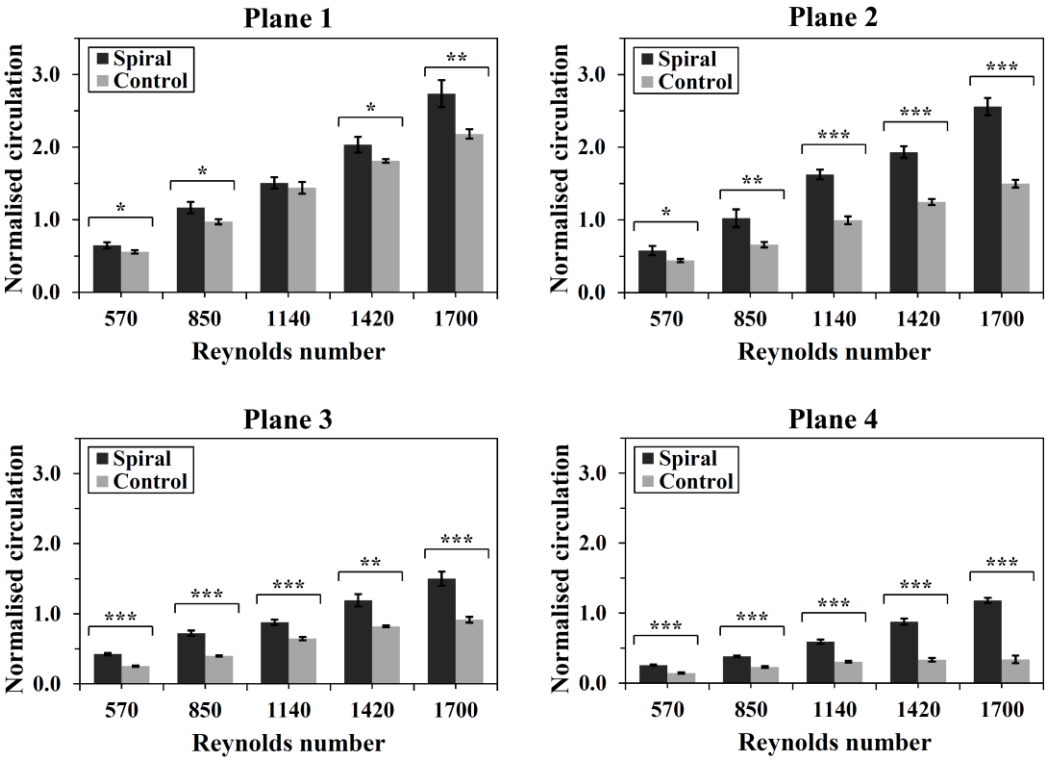

Figure 4.9: Progression of circulation at scan planes 1 to 4 for the spiral and control looped models; * $p < 0.05$, ** $p \leq 0.01$, *** $p \leq 0.001$.

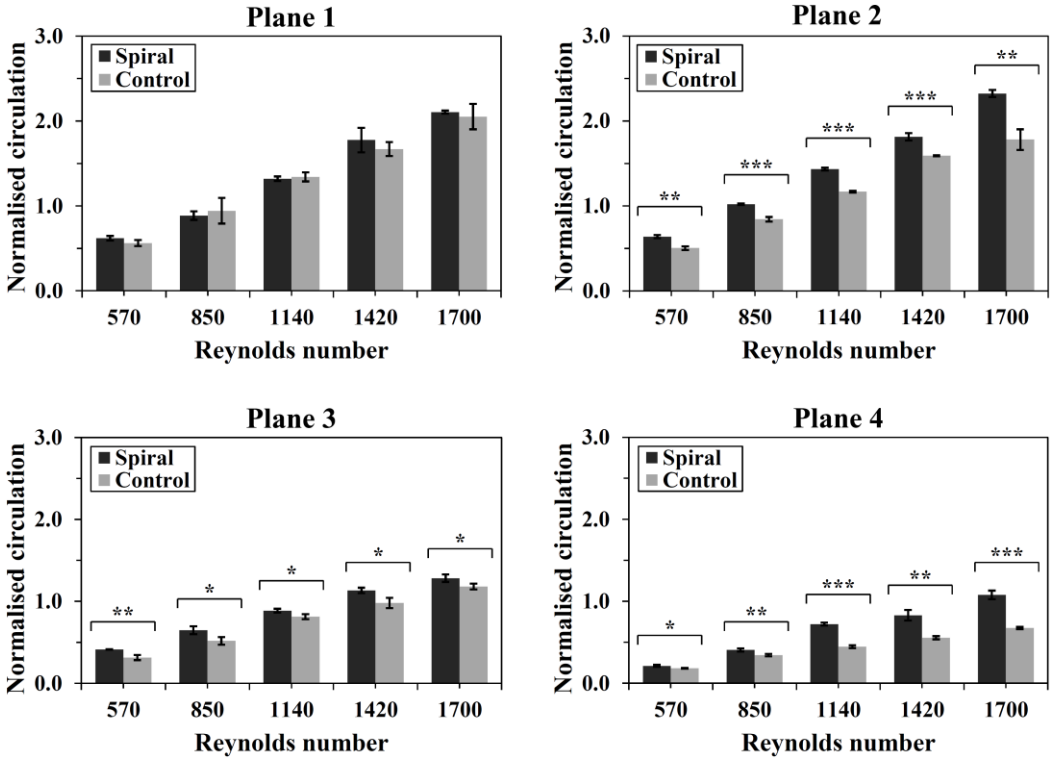

Figure 4.10: Progression of circulation at scan planes 1 to 4 for the spiral and control straight models; * $p < 0.05$, ** $p \leq 0.01$, *** $p \leq 0.001$.

4.4 Discussion

The rotational patterns in each scan plane of the spiral graft had relatively steady profiles, suggesting stable flow even with increasing Reynolds numbers. The second smaller spiral that was observed in the posterior side of planes 1 and 2 (Figure 4.3 and Figure 4.4) was associated with cross-flow stagnation points in the floor and posterior walls. The spirals started to coalesce in plane 3 (Figure 4.5a-i) creating stagnation points in the posterior sidewall particularly for low Reynolds numbers. The formation of uniform bulk rotation in scan plane 4, induced coherence in the flow profile without stagnation points (Figure 4.6a-i).

The rotational patterns within the control graft-venous mimic model demonstrated a constant Dean flow for Reynolds number 570, which suggested a plane of symmetry about the model centreline (Figure 4.3jmp - Figure 4.6jmp). This plane would pass from the floor and toe wall sides and would bisect the cylindrical vessel mimic. The number of recirculation cells from plane 2 and beyond was increased from two to four as the

Reynolds number was increased. At peak Reynolds numbers, in scan plane 4, the flow pattern had a disturbed or chaotic profile (Figure 4.6lor). The number of recirculation cells demonstrated flow separation in the outflow of the control, planar graft. This variation of spirals in each scan plane revealed flow instabilities in the outflow of the device. The velocity magnitude maps presented cross-flow stagnation points in the wall sides of the floor and toe in almost all maps. Such points were also seen in a number of anteroposterior locations. The interest in such observations in the floor and toe side of the anastomoses is increased due to their clinical relation to neo-intimal hyperplasia (Haruguchi and Teraoka 2003; Tricht et al. 2005; Walsh et al. 2003).

Comparisons of peak in-plane perpendicular velocity and circulation demonstrated increased values for the spiral grafts. The level of significance in these comparisons was increased with increasing distance from the anastomosis. There was a match in the ranking and level of significance between the peak velocity and circulation comparisons in each pair of phantoms. These quantitative evaluations showed increased in-plane mixing in the outflow of AV spiral grafts. Caro et al. (2005) postulated that in-plane mixing in vessels may inhibit the development of neo-intimal hyperplasia and thrombosis.

Moreover, in the previously discussed excluded scan plane (10 cm distal the anastomosis) a single spiral was found for each of the five Reynolds numbers applied to the spiral graft, whilst in comparison the colour flow information from the control device was weak and temporarily disturbed (see section 4.2.4, page 88). This supports the theory that a spiral graft is capable of developing a stable and uniform flow profile downstream of the anastomosis, which may protect endothelial function. The absence of a steady, detectable flow pattern with the non-spiral graft may indicate a dissipation of vortical structures downstream of the anastomosis.

In the vorticity maps, the core of each vortex was seen along with regions of counter rotation near the wall. This counter rotating vorticity was the result of opposite shearing forces of the fluid particles near the wall, where the velocity was decreased due to the no-slip wall boundary conditions. Solutions of this nature have also been reported by other researchers (Cookson et al. 2009; Yamamoto et al. 2002; Zabielski and Mestel 1998).

The velocity and vorticity maps of the straight configuration spiral graft showed a double-spiral flow pattern in the proximal scan planes 1 and 2. This was composed of a dominant vortex and a second smaller vortex near the anterior wall. In scan plane 3 the second spiral was observed for low Reynolds numbers but was coalesced with the main vortex for high Reynolds numbers. A single spiral with uniform near-wall velocity gradient was found in scan plane 4. The double-spiral velocity magnitude maps revealed one to two cross-flow stagnation points each, in the near-wall regions where adjacent vortices were mixed.

The flow maps of the straight configuration conventional graft showed three helices in the proximal scan planes 1 and 2. These helices were merged to two in scan plane 3, before they coalesce into one disturbed spiral in the distal scan plane 4. The velocity magnitude map of this single-spiral had a non-uniform distribution of velocity, showing near-wall areas of low velocity. Two to three stagnation points were seen for the three-spiral patterns and one to two for the double-spiral patterns.

In general, the maps from the straight configuration models showed less stagnation points for the spiral than the control prosthesis. The flow separation phenomena were more intense in the outflow of the control graft. The spiral, non-planar graft was capable of producing a uniform, stabilised single-spiral downstream to the flow circulation, even in the cancelled scan plane 10 cm distal of the anastomosis.

In this study it was assumed that the arterial mimic was blocked in the distal end and the venous mimic was blocked proximal from the anastomosis, in relation to the blood mimic flow direction (Figure 4.2). In other words, if these were clinical cases there would be no blood circulation through these vessels to the hand. Clinically there is some flow through both blocked locations. The magnitude of this second flow in the venous anastomosis is very low in comparison to that from the vascular access graft. However, it is possible that it may have an impact on the secondary flow motions of the graft outflow.

Recently Marie et al. (2014) presented a study on flow patterns in newly formed AVFs in patients. They reported that the existence of single helical flow in the non-operated arterial segment proximal from the anastomosis was a predictor of successful AVF

maturation. This pattern was converted into a chaotic flow in the anastomosis, but in many cases the non-operated distal venous segment acted as a peripheral generator of single spiral flow. This supports the idea that an AV graft capable of introducing a single helix may increase patency rates.

4.5 Conclusions

A spiral, non-planar and a control, planar AV graft were housed in an ultrasound flow phantom to compare the vortical structures in their outflow. A dual-beam colour Doppler approach was used to produce 2D velocity and vorticity maps in the cross-flow direction. The comparison was applied within the first 10 cm of the grafts outflow. The grafts were tested under two common surgical configurations.

Two vortices were found in the proximal outflow of the spiral graft and one vortex in its distal outflow, for both applied surgical configurations. A variation increasing from two to four vortices was detected in the outflow of the control graft in the looped configuration whereas vortices decreased from three to one in the straight configuration, looking from the proximal to distal outflow. The spiral graft stabilised the flow pattern, particularly in the distal outflow, where a coherent flow profile was observed. More cross-flow stagnation points were found in the outflow of the control graft. The range of multiple-spiral patterns in the outflow of the control graft indicated instability and increased flow separation. The quantitative comparison of peak in-plane velocity and total circulation demonstrated increased magnitudes for the spiral product showing enhanced in-plane mixing.

These results verified that the geometry of an AV graft can significantly affect the flow profile. In clinical practice a spiral graft may break the symmetric flow observed in end-to-side vascular anastomosis, decrease the cross-flow stagnation points and develop a more uniform near-wall velocity gradient. These may have a beneficial impact on the pathophysiology of the host vein protecting it from neo-intimal hyperplasia and thrombosis.

Chapter 5

Computational assessments of peripheral vascular prosthetic grafts

5.1 Introduction

The four pairs of PV vascular-graft models that were compared in chapter 3 of this thesis were subjected to CFD simulations. The computational mesh of their lumen was acquired based on 3D CT imaging and segmentation. Velocity, vorticity and circulation assessments were conducted with the same approach as in chapter 3 to allow for comparison. The CFD analysis provided the three components of velocity field within the whole lumen of the PV vascular-graft models. This allowed direct predictions of WSS in the floor and toe wall sides, for deeper understanding of the effect of haemodynamics in the outflow of PV spiral and non-spiral grafts. Moreover, important parameters such as pressure drop and helicity were analysed. The aim of this chapter is to present the methodology and results from CFD applications on the PV vascular-graft models, which were experimentally tested in chapter 3.

5.2 Methods

5.2.1 Imaging of PV vascular-graft models

The geometry of the PV vascular-graft models were extracted using 3D imaging, to ensure that the CFD simulations were as close as possible to the flow phantom

simulations. The resolution limits of both clinical MRI and CT were tested as spatial resolution is an important parameter for reproducing the geometry of the lumen of the models. The smallest feature in the PV vascular-graft models was that of the spiral inducer segment of the spiral graft. Hence, the spiral graft model was used as the testing subject for MRI and CT to determine which imaging modality would be chosen for segmentation. The model was positioned in the tank which was used during the experimental study, to maintain an identical geometry and to facilitate the scanning (see Figure 3.2, page 62).

Magnetic resonance imaging

Magnetic resonance imaging (MRI) relies on the detection of radio frequency signals emitted by excited hydrogen atoms in the test subject. Hence, the tank was filled with enough water to cover the vascular-graft model. A 3 Tesla MRI scanner (MAGNETOM TRIO, SEIMENS, Erlangen, Germany) and a T1 3D MP-RAGE (magnetisation prepared – rapid gradient echo) sequence was used. Body and spine matrix array coils were positioned around the tank. The applied parameters were repetition time (TR) 1570 ms, echo time (TE) 3.26 ms, inversion time (TI) 900 ms, flip angle 9°, slice thickness 0.35 mm, averages 5 and sequence bandwidth 199 Mz/pixel. The matrix was 512×447 and field of view (FOV) 180×180 mm, which resulted in isotropic resolution of 0.35×0.40 mm^2. These parameters were chosen to increase the spatial resolution. Images were acquired in the coronal plane and image acquisition lasted 25 min.

The detection and resolution of the spiral ridge was very poor, so imaging was repeated with the lumen of the model filled with a gadolinium based contrast agent solution to increase the signal intensity within it.

Computed tomography

The same vascular-graft model, free of water and gadolinium solution, was scanned with computed tomography (CT) (Biograph mCT, SIEMENS, Erlangen, Germany). As CT uses x-rays there was no need for a liquid media within the lumen and the tank of the model. The slice thickness was 0.6 mm with an increment of 0.3 mm to increase the resolution in scanning direction (*z* axis of a *xyz* Cartesian system). In this way adjacent

slices were overlapped ensuring a smooth transition from one slice to another. The FOV was 170 × 170 mm and the detectors spiral pitch was 0.7 mm. The in-plane image resolution was 512 × 512 pixels and each pixel represented an area of 0.33 × 0.33 mm^2. The acquisition time was approximately 10 s.

5.2.2 Segmentation and surface rendering

The application of CFD requires the extraction of the geometry of the lumen from each model. The digital imaging and communications in medicine (DICOM) files from MRI and CT were transferred to a workstation for offline processing. The geometry of each lumen was determined by segmenting and then surface rendering the region of interest from the DICOM files with Amira (FEI Visualization Sciences Group, Bordeaux, France and Zuse Institute Berlin, Berlin, Germany). Amira is a four dimensional software for data visualisation, processing and analysis.

In the acquired DICOM images each pixel corresponded to a specific intensity value. The grey scale distribution of the images was based on these intensities. Pixels from the same structure (e.g. graft wall, vascular-graft lumen, vessel mimic wall) had similar intensities. The 3D segmentation of each vascular-graft model was based on the selection of the appropriate intensity threshold, which retained only the pixels from the required structure. During segmentation, the objective was to extract an accurate geometry of the lumen of the model with good resolution of the spiral ridge and a diameter as close as possible to the real one.

Figure 5.1 illustrates an example obtained using MRI. Three different views of the PV spiral vascular-graft model are presented. In this MRI test only a part of the vessel mimic has been scanned to reduce the acquisition time. Even so the acquisition time was 25 min, because of the high resolution scanning parameters. High intensities corresponded to bright grey-scale shades and low intensities to dark grey-scale shades (Figure 5.1). The wall of the graft was a region of low intensities due to an absence of hydrogen atoms. Therefore the segmentation between the internal surface of the graft and its lumen required the choice of a low intensity threshold to correctly define their boundary and provide a sharp spiral inducer ridge.

The signal intensity difference between the lumen and the PVA-c vessel mimic was very low. Amira was unable to segment the PVA-c inner wall from the lumen because of the intensity similitude. Different intensity thresholds were tried, even at the expense of low quality in the shape of the spiral inducer ridge and reduced lumen diameter, but the software was still unable to detect a uniform boundary between the PVA-c inner wall and its lumen. The purple boundary lines in the three plane views of Figure 5.1 are part of the segmentation process. From the coronal view can be seen that this line correctly defines the boundary between the graft and the lumen, but erroneously defines the boundary between the PVA-c and the surrounding media instead of the boundary between the PVA-c and the lumen.

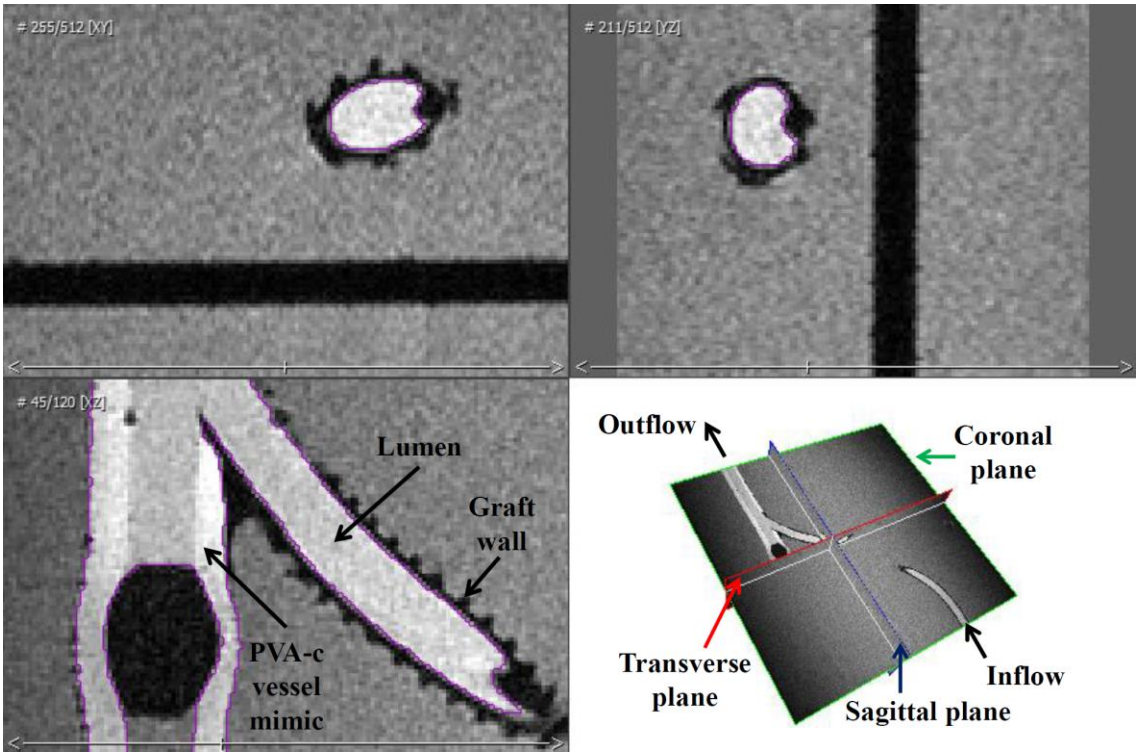

Figure 5.1: MRI images from the PV spiral vascular-graft model. Top left: transverse plane; top right: sagittal plane; bottom left: coronal plane. The ridged cross sectional internal geometry of the spiral graft can be seen in the transverse and sagittal views. The purple line in the inside wall of the graft and outside wall of the vessel mimic defines the segmentation boundary.

An example of the extracted geometry based on MRI data is presented in Figure 5.2. The inside wall geometry rendering of the graft and the undesirable outside wall

geometry rendering of the vessel mimic are shown, resulting in an incorrect geometry of the lumen of the vascular-graft model.

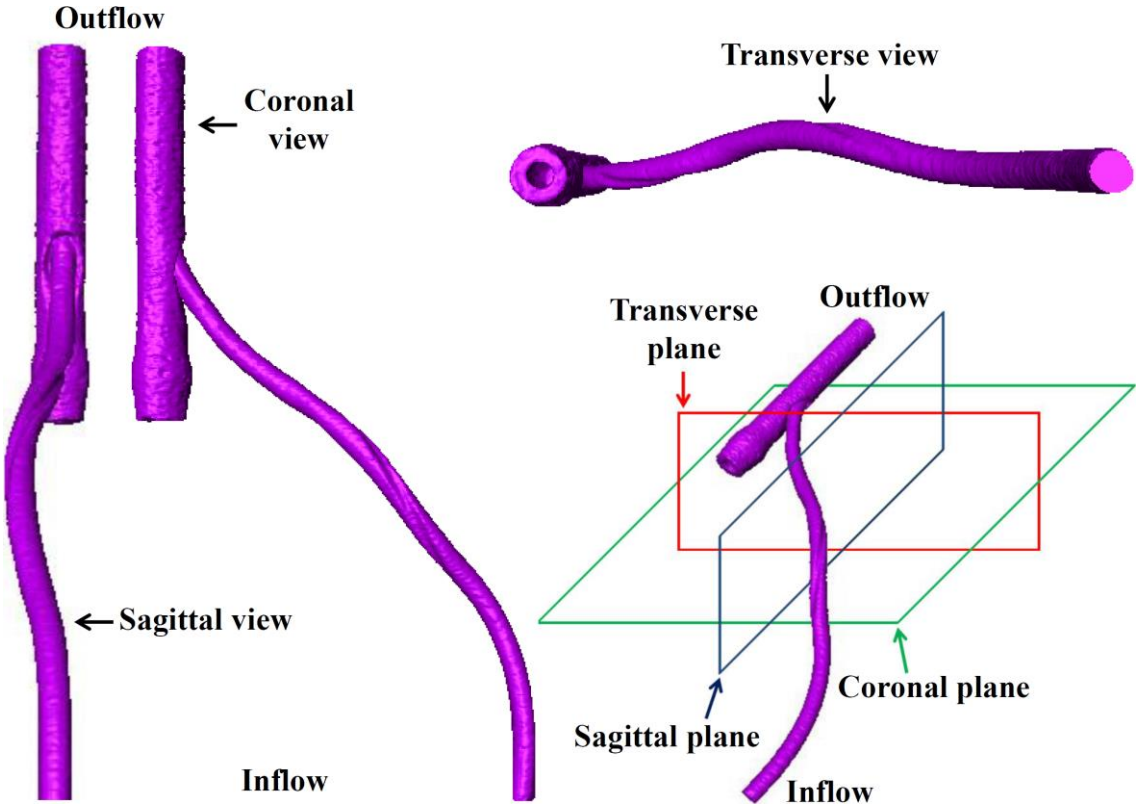

Figure 5.2: Segmented geometry based on the MRI data. In the grafted region the geometry of the lumen of the graft including the groove from the spiral ridge is presented. In the vessel mimic region segmentation was based on the outside instead of the inside wall boundary.

Figure 5.3 shows an example from the CT scanning. The transverse, sagittal and coronal view of the PV spiral vascular-graft model is shown. High intensities corresponded to bright grey-scale shades and low intensities to dark grey-scale shades. The lack of any material within the vascular-graft model increased the intensity difference between the lumen and the wall. Thus there was no difficulty in defining the boundary of the lumen, which is shown with a green line in Figure 5.3. The criterion for the chosen segmentation intensity threshold was to match the diameter of the extracted lumen geometry with the actual lumen diameter as closely as possible. The same intensity threshold was chosen for both the spiral and non-spiral models.

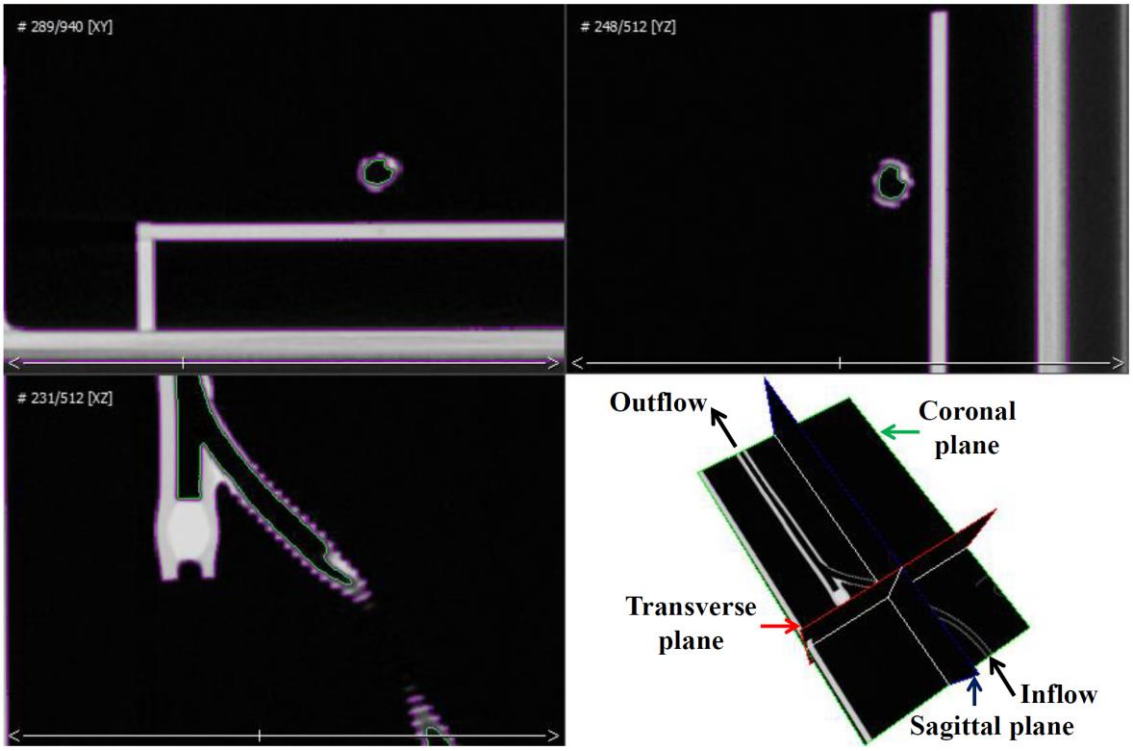

Figure 5.3: CT images from the PV spiral vascular-graft model. Top left: transverse plane; top right: sagittal plane; bottom left: coronal plane. The ridged cross sectional internal geometry of the spiral graft can be seen in the transverse and sagittal views. The green line in the lumen defines the segmentation boundary.

Figure 5.4 provides an example of the extracted lumen geometry from the PV spiral vascular-graft model based on CT imaging. The sagittal, coronal and transverse views are presented.

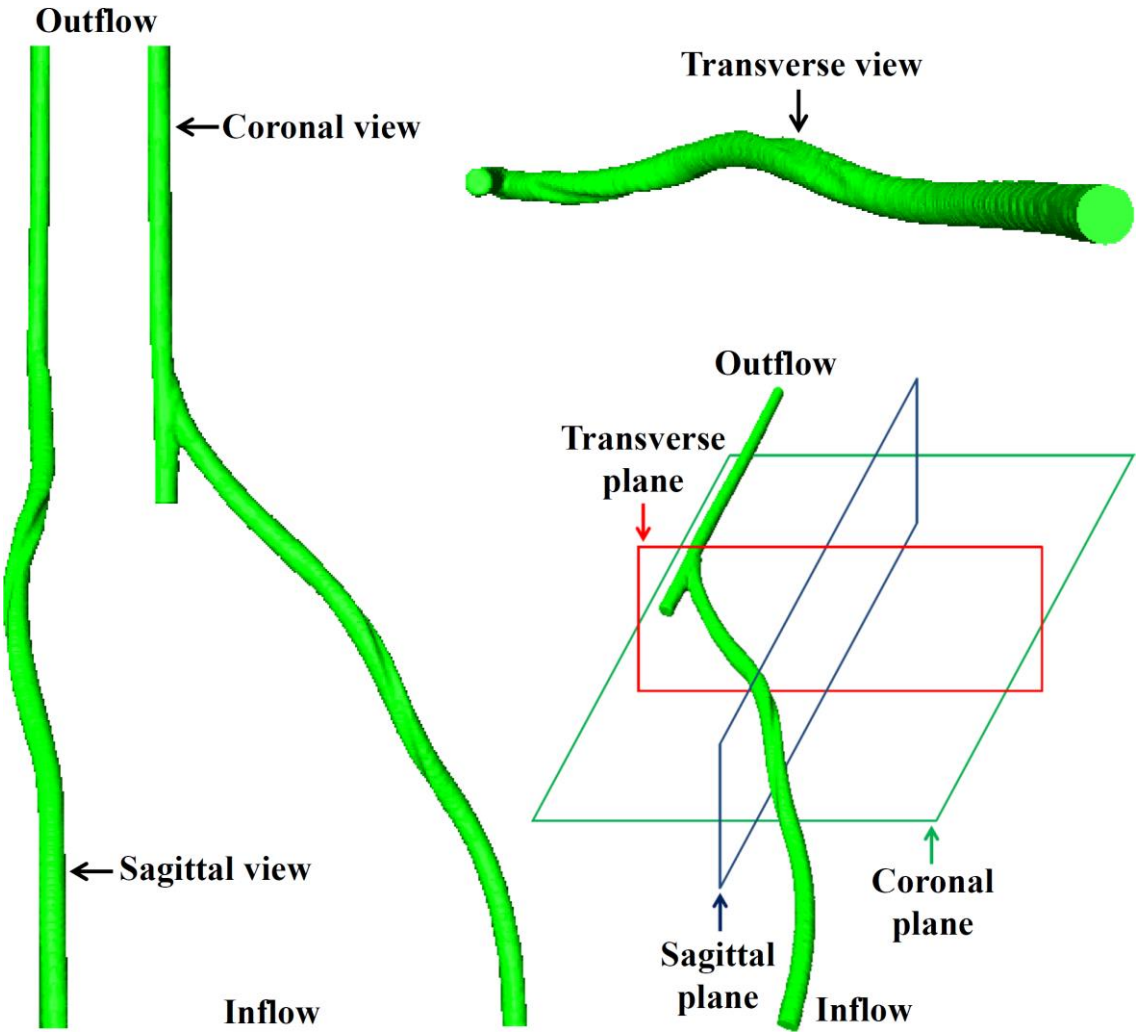

Figure 5.4: Extracted lumen geometry from the PV spiral vascular-graft model based on CT imaging data. The groove of the spiral ridge can be seen at the distal end of the graft.

CT was chosen as the optimal imaging modality, because the isotropic resolution of CT was higher than that of MRI and the segmentation of the CT data was straight forward and relatively accurate, whilst MRI data could not be segmented correctly. In addition, the CT acquisition time (approximately 10 s) was much shorter than that of the MRI (25 min for partial length of the vascular-graft model). This provided a further advantage to CT because all models could be scanned within an acceptable time frame. Eight models were imaged in total, four for the spiral and four for the non-spiral graft models to enable simulation of the four applied angles of the anastomosis.

Segmentation is based on intensity differences from pixel to pixel and the extracted geometry appears like numerous small triangular surfaces connected to each other, known as surface mesh (Figure 5.5). The normal to the three points of each triangle dictate its orientation. A surface mesh defines a boundary which in this work is that of a vascular-graft lumen. It is common that the original surface mesh has a zigzag shape as shown in Figure 5.5a, therefore smoothing is required. The smoothing tools in Amira are based on averaging the height of adjacent surface element. Increased smoothing in the spiral graft had detrimental effects on the groove from the spiral ridge and decreased the diameter of the geometry (Figure 5.5c). Limited smoothing was applied to provide a surface free of sharp zigzag edges with the minimum degradation of the groove from the spiral ridge as shown in Figure 5.5b.

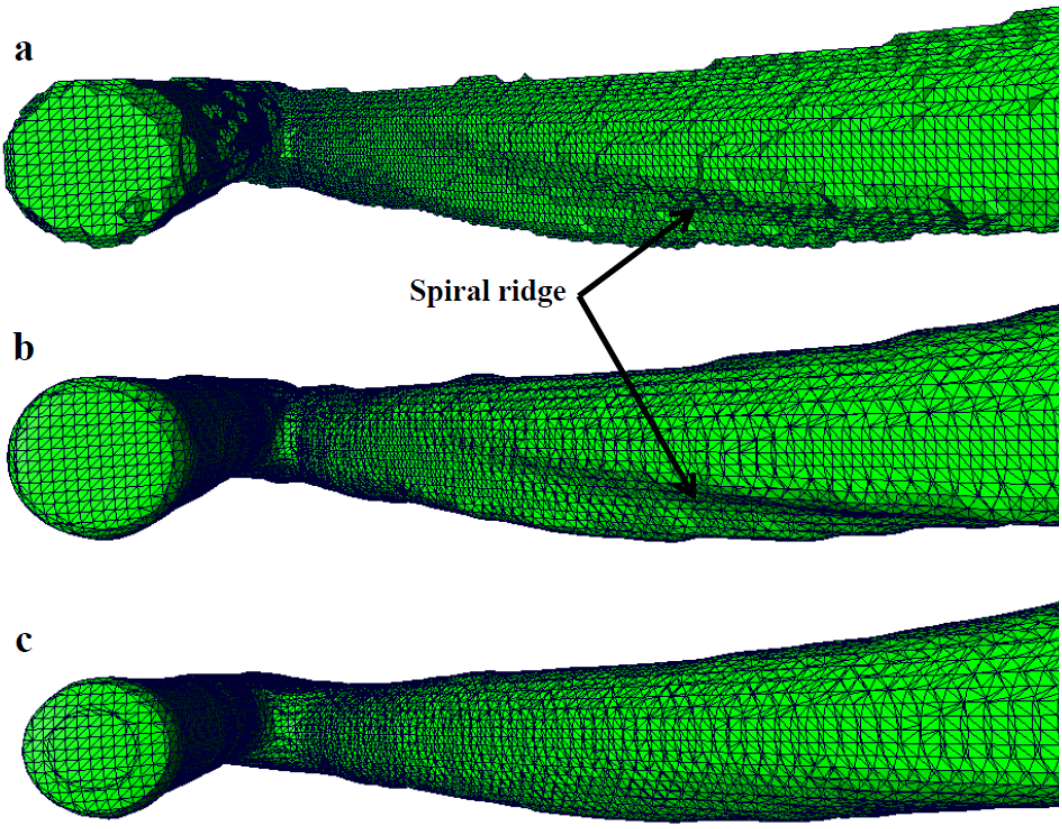

Figure 5.5: A transverse view of the spiral vascular-graft geometry anastomosis, including the end of the groove from the spiral ridge. (a) No smoothing applied. (b) Limited smoothing; this was applied in the models of this study. (c) Increased smoothing; the diameter of the extracted geometry has been decreased and the groove from the spiral ridge has been vanished.

The surface mesh from each vascular-graft model was saved as a triangulated mesh file in stereolithography (.STL) format. This file format is commonly utilised to define 3D surfaces in CAD and rapid prototyping and can be loaded in most CFD programs.

5.2.3 Volume mesh

The simulations were conducted with the commercially available package ANSYS CFX 14.0 (Canonsburg, PA, USA). A computational volume mesh was produced for each vascular-graft lumen and the flow was solved in a discretised manner.

Each STL file was imported into ICEM CFX (ANSYS) for volume mesh generation. The volume mesh consisted of 3D tetrahedral cells in the centre and prismatic cells in the fluid boundary layer at the vascular-graft wall (ANSYS 2011). To ensure a fine near wall flow simulation, ten layers of prismatic cells were applied (Cheng et al. 2010; Cheng et al. 2013). Mesh independence tests were conducted for the 60° PV vascular-graft models to determine the optimum number of mesh elements. The number of elements needs to be adequate to provide reliable results but not excessive so as to keep a reasonable computational execution time. The independence tests were conducted using the maximum applied Reynolds number (Tan et al. 2008). The results of the difference in the value of maximum velocity and maximum WSS are provided in Table 5.1 for the spiral model and Table 5.2 for the non-spiral model. The chosen volume mesh was number 3 in both cases. The criteria for the optimum volume mesh was to have less than 4% difference in maximum velocity and maximum WSS from the previous and proceeding volume mesh (Cheng et al. 2010; Wood et al. 2006). The flow of a fluid can be well resolved using a low density mesh in terms of velocity profiles. Nevertheless, an accurate velocity field does not imply accurate calculation of higher order computed quantities such as WSS, which is more dependent on mesh refinement and need to be examined in mesh independence tests (Morris et al. 2005; Prakash and Ethier 2001).

Table 5.1: Mesh independence test results from the comparison of maximum WSS and maximum velocity between different meshes of the spiral PV model.

Mesh number	Elements	Nodes	Maximum velocity (m s^{-1})	Difference (%)	Maximum WSS (Pa)	Difference (%)
1	1168498	454688	0.575		4.345	
				0.352		15.070
2	1925974	696480	0.573		5.116	
				0.461		0.160
3	2560528	890162	0.570		5.108	
				0.394		2.789
4	3219003	1078630	0.572		5.254	

Table 5.2: Mesh independence test results from the comparison of maximum WSS and maximum velocity between different meshes of the non-spiral PV model.

Mesh number	Elements	Nodes	Maximum velocity (m s^{-1})	Difference (%)	Maximum WSS (Pa)	Difference (%)
1	1231334	474290	0.532		4.903	
				0.496		15.987
2	2017908	724140	0.534		5.836	
				0.243		3.970
3	2670008	920872	0.536		6.078	
				0.141		2.921
4	3426333	1139978	0.536		5.910	

Figure 5.6 presents cross-section views of the volume meshes in the outflow of the spiral and non-spiral models. The mesh numbers 1 – 4 in Figure 5.6 corresponds to the mesh numbers 1 – 4 in Table 5.1 and Table 5.2. During the mesh optimisation, the only parameters that were changed from one volume mesh to a finer volume mesh were the minimum and maximum size of elements, although their ratio was kept steady (minimum size / maximum size = 0.6) (ANSYS 2011). That means that for any increase in the number of elements in a volume mesh, the minimum and maximum size of elements were decreased proportionally, resulting in proportional decrease of all mesh elements as shown in Figure 5.6. The smallest elements were always the cells in the first prismatic layer at the wall boundary and the biggest elements were the tetrahedral cells in the core of the volume mesh.

Mesh numbers 1, 2, 3 and 4 from the spiral model had identical parameters with mesh numbers 1, 2, 3 and 4 from the control model respectively, thus allowing their computational comparison (Table 5.1, Table 5.2 and Figure 5.6). The chosen mesh parameters (mesh number 3) were also applied in the 20°, 40° and 80° vascular-graft models. Each volume mesh was smoothed using a conservative approach to ensure a smooth transition between the elements and then tested for integrity.

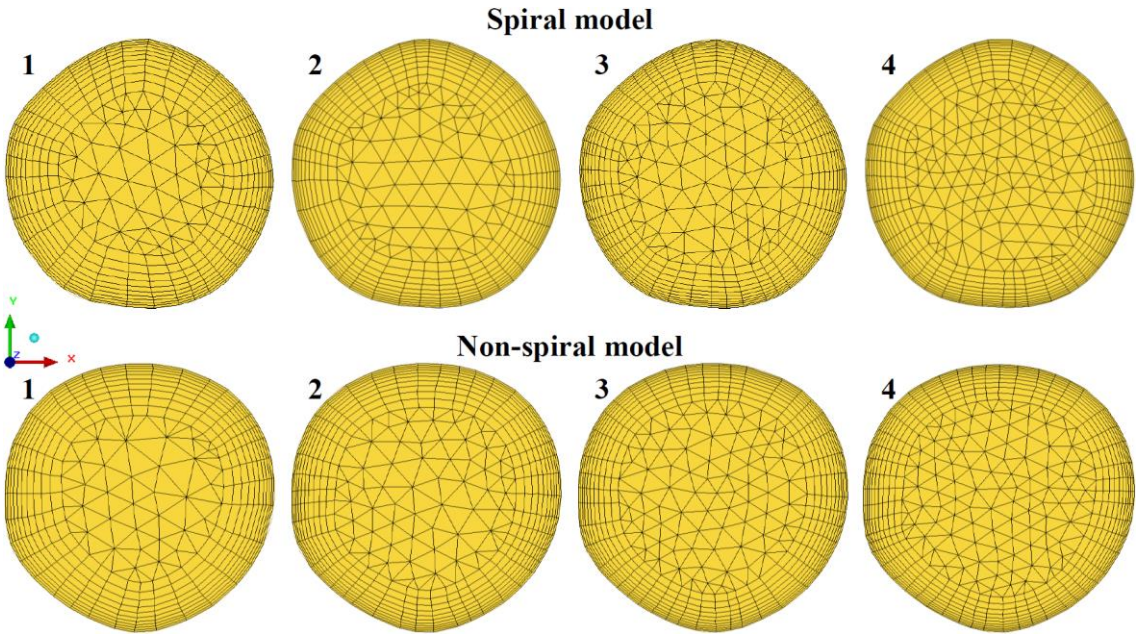

Figure 5.6: Cross-section view of the volume mesh in the outflow of the spiral and non-spiral model. Mesh numbers 1 – 4 correspond to the mesh numbers 1 – 4 in Table 5.1, Table 5.2.

5.2.4 Wall boundary layer thickness

The ability of a volume mesh to provide a reliable velocity profile at the wall boundary characterises the quality of the mesh. Therefore, the wall boundary layer thickness was tested in the 60° vascular-graft models that were used as testing objects in the mesh independence tests. The region of interest in the CFD PV study was the vessel mimic distal from the graft outflow, as for the experimental assessments (chapter 3). For the boundary layer thickness calculation the origin of the flow was assumed to be immediately after the outflow anastomosis where the flow had to readapt itself. This origin was the cross-flow plane at 0 mm of Figure 5.7a. The boundary layer thickness

was tested in the cross-flow plane 4 mm distal from the assumed origin of flow (Figure 5.7a).

The theoretical value of the boundary layer thickness was calculated using Equation 5.1 where δ is the boundary layer thickness, r the radius of the vessel mimic and Δ a quantity determined by Equation 5.2 (Bird 2002). In Equation 5.2, v is the kinematic viscosity, z the distance of the examined cross-section location from the origin (4 mm distal the anastomosis) and $\langle v_z \rangle$ the average axial velocity at this location. These equations are applied a short distance (in relation to the total length) from the entrance of a pipe.

$$\delta = \Delta \cdot r \tag{5.1}$$

$$\frac{vz}{\langle v_z \rangle R^2} = \frac{1}{10}\left[7\Delta + 48\ln\left(1 - \frac{1}{3}\Delta\right) + \frac{27\Delta}{3 - \Delta}\right] \tag{5.2}$$

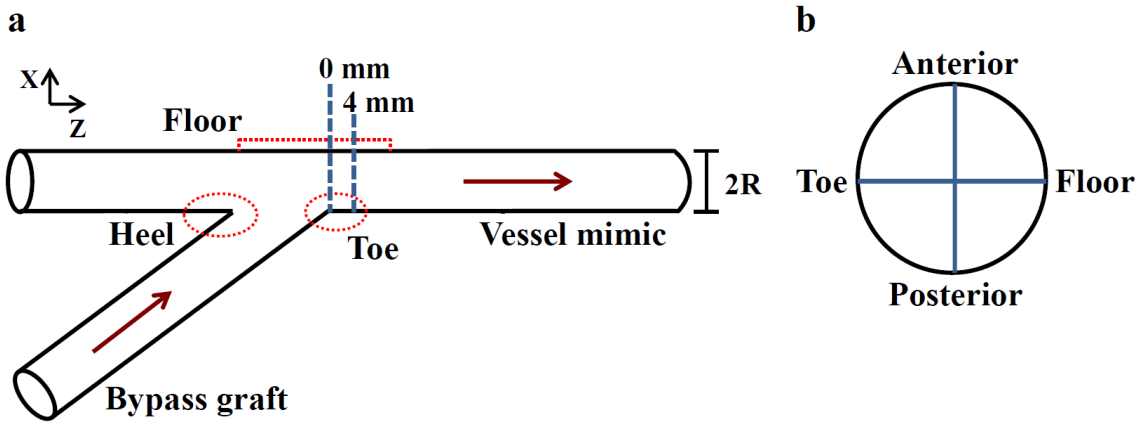

Figure 5.7: (a) Schematic diagram of bypass graph outflow anastomosis. (b) Cross-section view of the vessel mimic downstream of the anastomosis; the perpendicular lines present the locations where the axial velocity profiles were extracted for boundary layer thickness assessments.

The theoretical wall boundary layer thickness was 0.677 mm for the spiral model and 0.687 mm for the non-spiral model. Axial velocity profiles were extracted from the toe-floor and anterior-posterior perpendicular lines, which are shown in Figure 5.7b. This diagram is a cross-flow view of the vessel-mimic. The extracted axial velocity profiles are presented in Figure 5.8 for the spiral and Figure 5.9 for the control non-spiral model.

The agreement between the theoretical wall boundary layer thicknesses and those presented in Figure 5.8 and Figure 5.9, verifies the ability of the volume meshes to solve the flow field within the vascular-graft models.

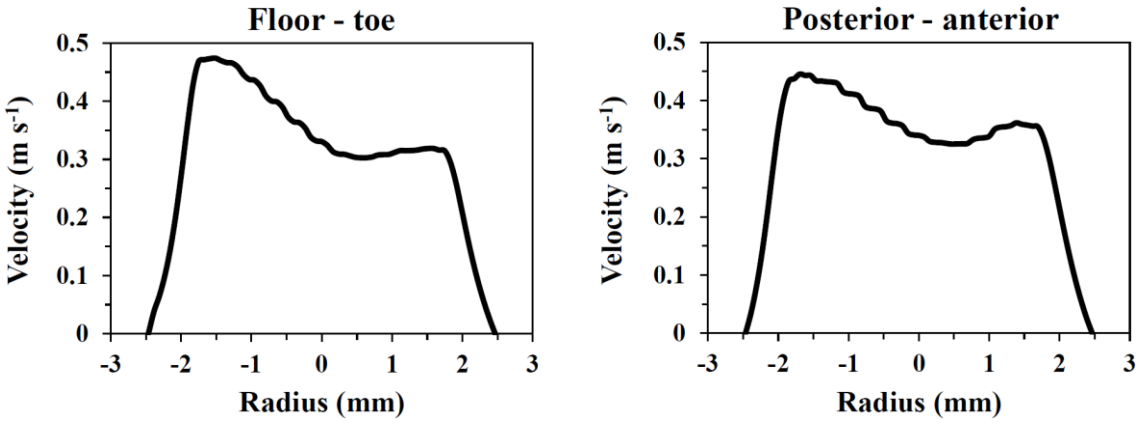

Figure 5.8: Axial velocity profiles from the spiral model in the cross-flow view 4 mm distal from the graft outflow as shown in Figure 5.7a. The left profile is from the diametric line between the floor and toe wall sides of the vessel mimic; the right profile is from the diametric line between the posterior and anterior wall sides of the vessel mimic (Figure 5.7b).

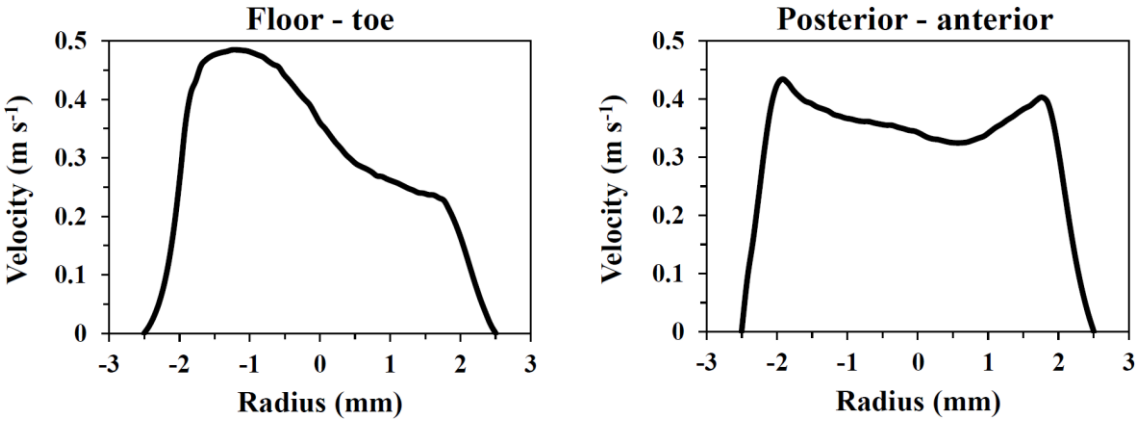

Figure 5.9: Axial velocity profiles from the control model in the cross-flow view 4 mm distal from the graft outflow as shown in Figure 5.7a. The left profile is from the diametric line between the floor and toe wall sides of the vessel mimic; the right profile is from the diametric line between the posterior and anterior wall sides of the vessel mimic (Figure 5.7b).

5.2.5 Model properties and boundary conditions

The physical parameters of the required simulations were defined with the CFX-pre module of ANSYS CFX 14.0. The approach taken was to simulate the experimental flow

parameters which were applied in the spiral and control vascular-graft models in chapter 3. The simulated blood was assumed to be a homogeneous, Newtonian and incompressible fluid, which is a valid and common assumption in medium and large size vessels (Kim et al. 2008; Morris et al. 2005; Wood et al. 2006). Its density was 1040 kg m^{-3} and dynamic viscosity 1.7 mPa·s to match that of the properties of the BMF applied in the flow phantom. The walls of the graft and vessel mimic were considered to be rigid with a no-slip condition for zero velocity at the walls. The flow was assumed to be steady and laminar. A Hagen-Poiseuille parabolic profile was applied at the inlet of the grafts for flow rates 240 and 360 mL·min^{-1}. The flow rate was steady throughout the whole length of each model. The Navier-Stokes governing equations (principle of continuity equation and momentum conservation) of flow were solved with the CFX-solver module of ANSYS CFX 14.0.

Viscosity correction

In order to detect the impact of low viscosity in spiral flow patterns and provide quantitative comparisons between the spiral and non-spiral models, dynamic viscosity was corrected from 1.7 mPa·s to 3.5 mPa·s. The remaining model properties and boundary conditions during this validation substudy remained steady. The simulations with the corrected dynamic viscosity were applied in the 40° vascular-graft models.

The volume mesh independence tests were applied only for the original dynamic viscosity of 1.7 mPa·s. The mesh requirements are inversely proportional to viscosity. Moreover, the mesh had to be same between the simulations of different viscosity to allow comparison.

5.2.6 Analysis of results

The applied flow rates of 240 and 360 mL·min^{-1} produced average Reynolds numbers of 620 ± 3.5 and 935 ± 10.4 respectively within the vessel mimic section. Each average was based on three different cross-section areas of the vessel mimic segment (at 0, 5, 10 cm downstream from the anastomosis) for the four pairs of models. Small variations in diameter and axial velocity of these areas resulted in small differences of the Reynolds number.

The flow patterns were examined in cross-flow planes 1, 2, 3 and 4, which were located at 0.1, 0.5, 5 and 10 cm distal from the graft outflow of each vascular-graft model. These were the same locations as those examined in the experimental study (chapter 3). Thus the computational data could be compared with that from the experimental. In these cross-flow planes of the spiral and control PV models, the in-plane velocity, axial velocity and vorticity maps were extracted and the peak in-plane velocity and total circulation were calculated. The total circulation of each plane was the sum of the absolute circulation from the negative and positive areas of vorticity, as described in the section 'Detection and comparison of circulation', page 65.

Wall shear stress

The WSS was detected at the centreline of the floor and toe wall sides of all PV models, as demonstrated in Figure 5.10. This included a region proximal to the graft outflow anastomosis (-10 to 20 mm for the floor and 0 to 20 mm for the toe centreline), which is clinically related to neo-intimal hyperplasia and thrombosis, and a region distal from the graft outflow anastomosis (100 to 120 mm for both the floor and toe centrelines), which is clinically related to progression of the PAD (Stonebridge 1997). Regions from the spiral models were compared with the corresponding regions from the control models. A similar approach to detect WSS in the outflow of PV grafts has been presented by other researchers (Keynton et al. 2001; O'Brien et al. 2005; O'Callaghan et al. 2006; Walsh et al. 2003).

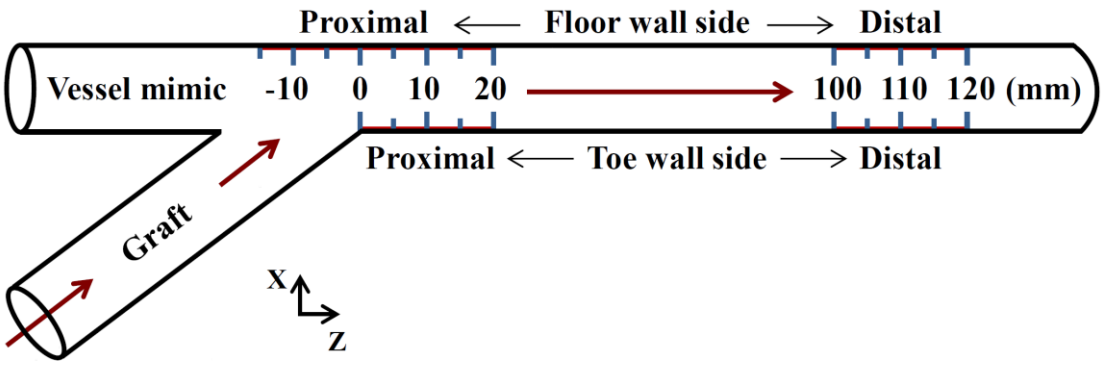

Figure 5.10: Regions of the floor and toe wall centrelines downstream from a PV graft outflow where WSS was examined.

Pressure drop

The pressure drops within the spiral and non-spiral PV models were detected and compared. Specifically, they were detected from the inlet of the grafts to the distal side of their vessel mimic segments in cross-flow plane 4 (10 cm distal from the anastomosis). The length of the grafted region was not identical for the spiral and non-spiral grafts, because of the 3D helical shape in the spiral inducer segment of the spiral device. Hence, it was considered appropriate to calculate the pressure drop in relation to the length of the examined region as shown in Equation 5.3.

$$\frac{\Delta P}{L} = \frac{P_{out}^{avg} - P_{in}^{avg}}{L} \quad \textbf{5.3}$$

where ΔP was the pressure drop, P_{out}^{avg} was the average pressure in the outlet of the examined region, P_{in}^{avg} was the average pressure in its inlet and L the length from location P_{in}^{avg} to P_{out}^{avg}.

Helicity

The density per unit volume of kinetic helicity H_k is expressed as

$$H_k = \vec{v} \cdot (\nabla \times \vec{v}) \quad \textbf{5.4}$$

where $\vec{v}$ is the velocity vector at each point of the fluid domain and $\nabla \times \vec{v}$ is the vorticity field $\vec{\omega}$ of the flow (see Equation 2.19). If V is a volume of a flow field and dV an element of this volume, helicity H is defined as the volumetric integral of kinetic helicity.

$$H = \int_V \vec{v} \cdot (\nabla \times \vec{v}) \cdot dV \quad \textbf{5.5}$$

From Equation 5.5 it can be derived that the unit of helicity is metres to fourth power over seconds squared ($m^4 \cdot s^{-2}$).

Helicity is known to have a great influence on the stability and evolution of both laminar and turbulent flow. Equation 5.4 shows that helicity is maximal when the velocity and vorticity vectors lie along the same direction and zero when the velocity

and vorticity vectors lie in orthogonal directions. For instance in a 2D velocity field the vorticity vector is always perpendicular to velocity and consequently helicity is zero ($\vec{v} \cdot \vec{\omega} = 0$) (Belian et al. 1998; Grigioni et al. 2005; Morbiducci et al. 2007).

The strength of helical phenomena in the outflow of the PV grafts was quantified with helicity (Gallo et al. 2012; Grigioni et al. 2005; Hardman et al. 2013; Morbiducci et al. 2007; Zhan et al. 2010). The testing region of helicity included the vessel mimic volume from cross-flow plane 0 (0 mm) to cross-flow plane 4 (100 mm) (Figure 5.10).

5.3 Results

If *x*, *y*, *z* are the Cartesian coordinates with *z* parallel to the direction of flow and *u*, *v*, *w* the corresponding Cartesian velocity components, then in-plane velocity in this chapter is defined by the *v* and *u* velocity components. This is the same with the tangential or in-plane velocity v_{xy} in the experimental chapters.

In the flow maps the orientation is such that the left and right sides are the toe and floor wall sides of the vessel mimic respectively, and the top and bottom are the anterior and posterior wall sides respectively. This is the same orientation as the experimental chapter for the PV grafts (chapter 3). The colour distribution in the flow maps (velocity and vorticity) is based on a scale from dark blue to dark red for the minimum to maximum value respectively. Vectors are used in in-plane velocity maps to show the direction of the vortices.

5.3.1 Comparison with flow maps from the experimental results

Figure 5.11 - Figure 5.14 illustrate comparisons of the in-plane velocity maps between the CFD and vector Doppler results, for the 20° 40° 60° and 80° models respectively. These comparisons are from cross-flow plane 1, just after the graft anastomosis, where the flow had to readapt itself, using a flow rate of 360 mL·min^{-1}. Figure 5.15 provides a close up of the posterior near wall location of vector Doppler spiral graft maps from Figure 5.11, Figure 5.13 and Figure 5.14. This was considered necessary because the weak second spiral in this location was not visible with the normal scale.

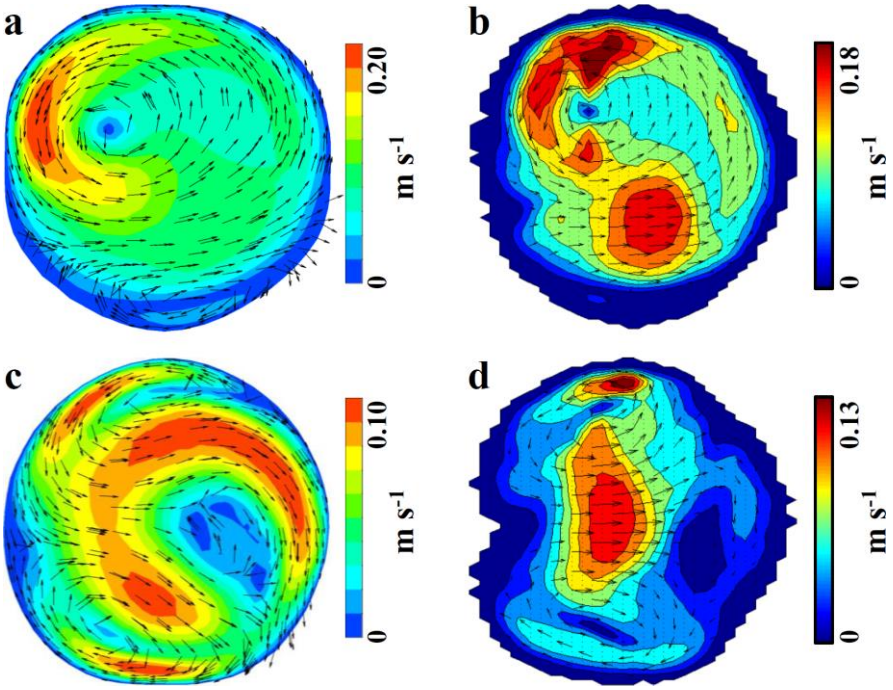

Figure 5.11: Comparison of in-plane velocity maps between CFD (left column) and vector Doppler (right column) for the 20° spiral (a and b) and control (c and d) PV models. The wall sides of each map correspond to the anastomotic locations as: left = toe, right = floor, top = anterior and bottom = posterior.

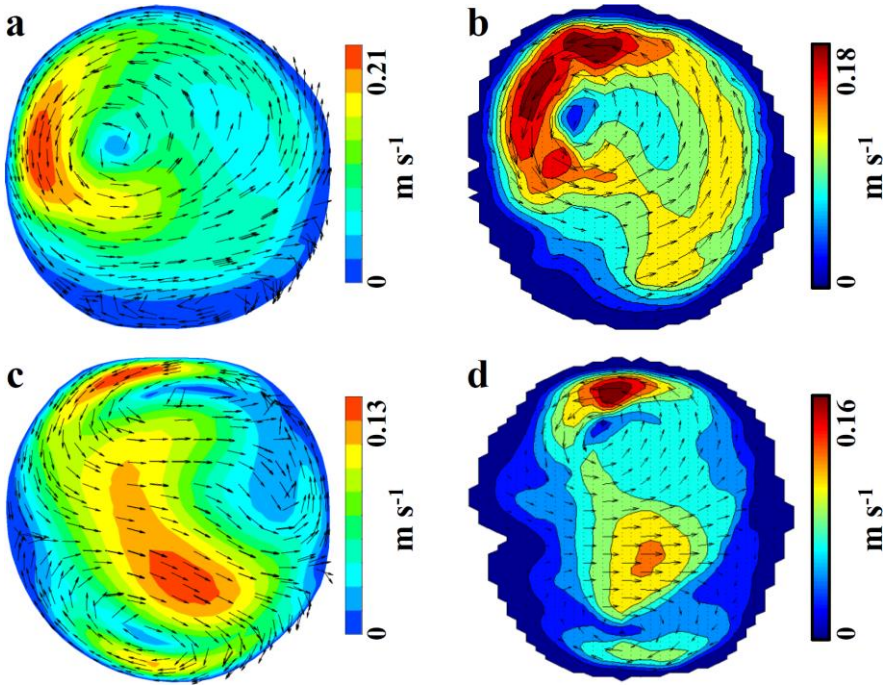

Figure 5.12: Comparison of in-plane velocity maps between CFD (left column) and vector Doppler (right column) for the 40° spiral (a and b) and control (c and d) PV models. The wall sides of each map correspond to the anastomotic locations as: left = toe, right = floor, top = anterior and bottom = posterior.

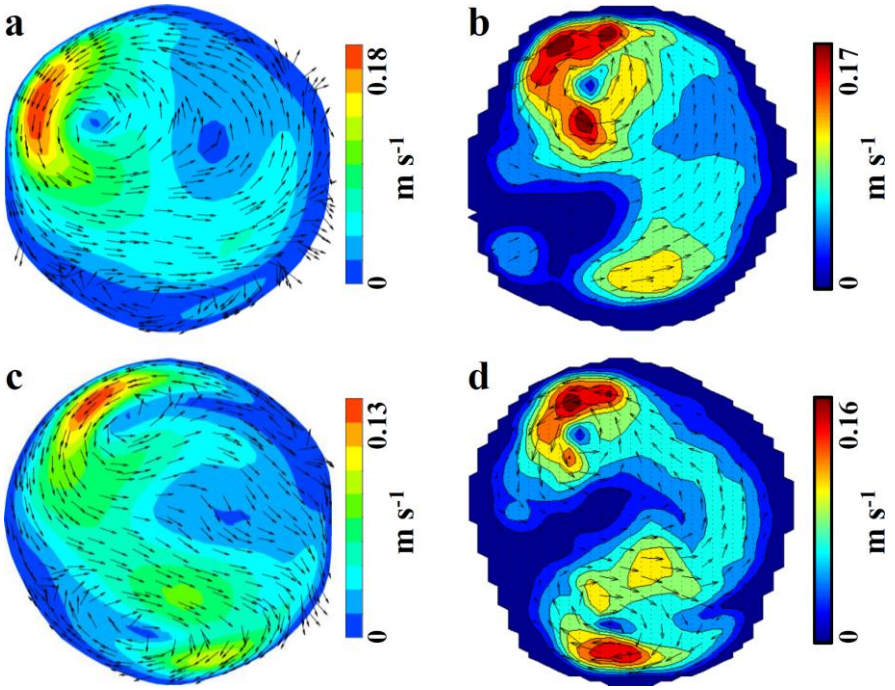

Figure 5.13: Comparison of in-plane velocity maps between CFD (left column) and vector Doppler (right column) for the 60° spiral (a and b) and control (c and d) PV models. The wall sides of each map correspond to the anastomotic locations as: left = toe, right = floor, top = anterior and bottom = posterior.

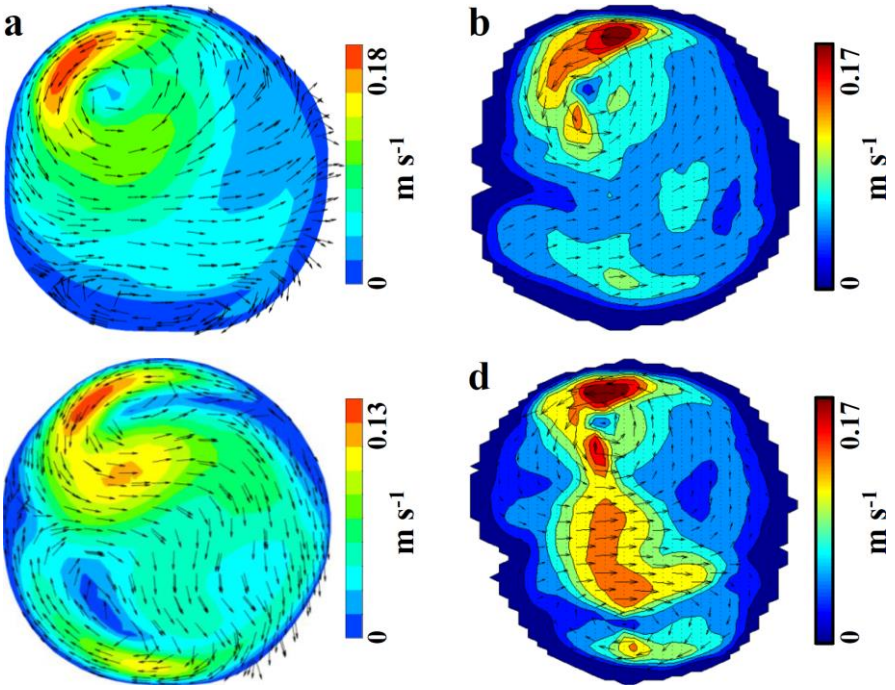

Figure 5.14: Comparison of in-plane velocity maps between CFD (left column) and vector Doppler (right column) for the 80° spiral (a and b) and control (c and d) PV models. The wall sides of each map correspond to the anastomotic locations as: left = toe, right = floor, top = anterior and bottom = posterior.

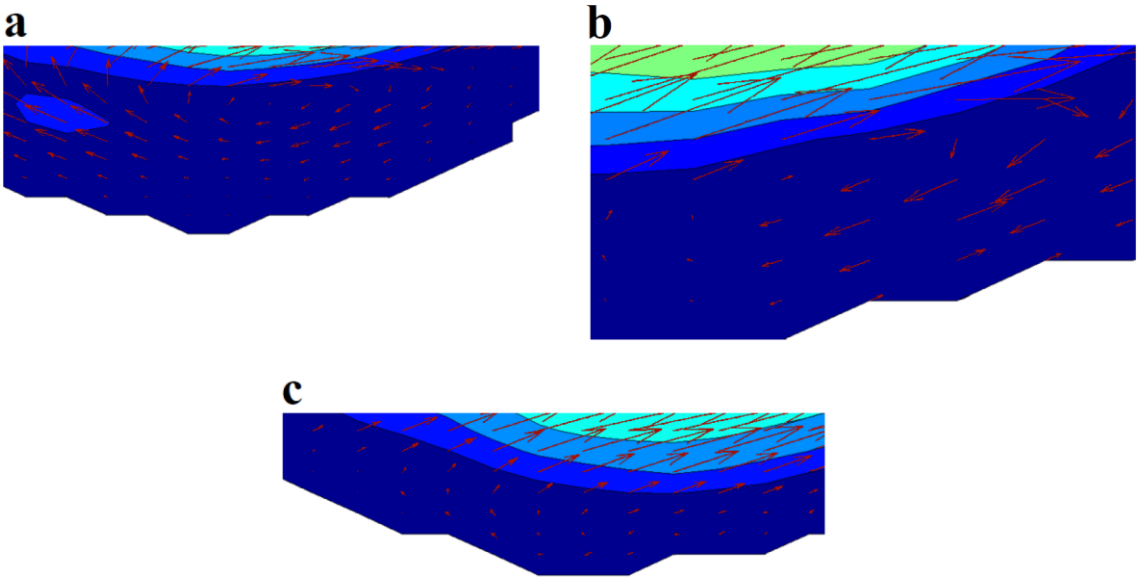

Figure 5.15: Close up of the posterior near wall location of vector Doppler spiral graft maps in Figure 5.11, Figure 5.13 and Figure 5.14; from a - c respectively. A weak spiral can be seen, which was not visible with the normal scale.

5.3.2 Flow maps in the outflow of spiral and control PV grafts

Figure 5.16 - Figure 5.19 demonstrate in-plane velocity, axial vorticity ω_Z and axial velocity maps (from left to right), for the cross-flow planes 1, 2, 3 and 4 respectively. The first and third rows of each figure show flow maps from the spiral and control model for Reynolds number 620 and the second and forth rows, for Reynolds number 935. In vorticity maps a black contour line highlights regions of zero vorticity that separate the regions of positive and negative vorticity.

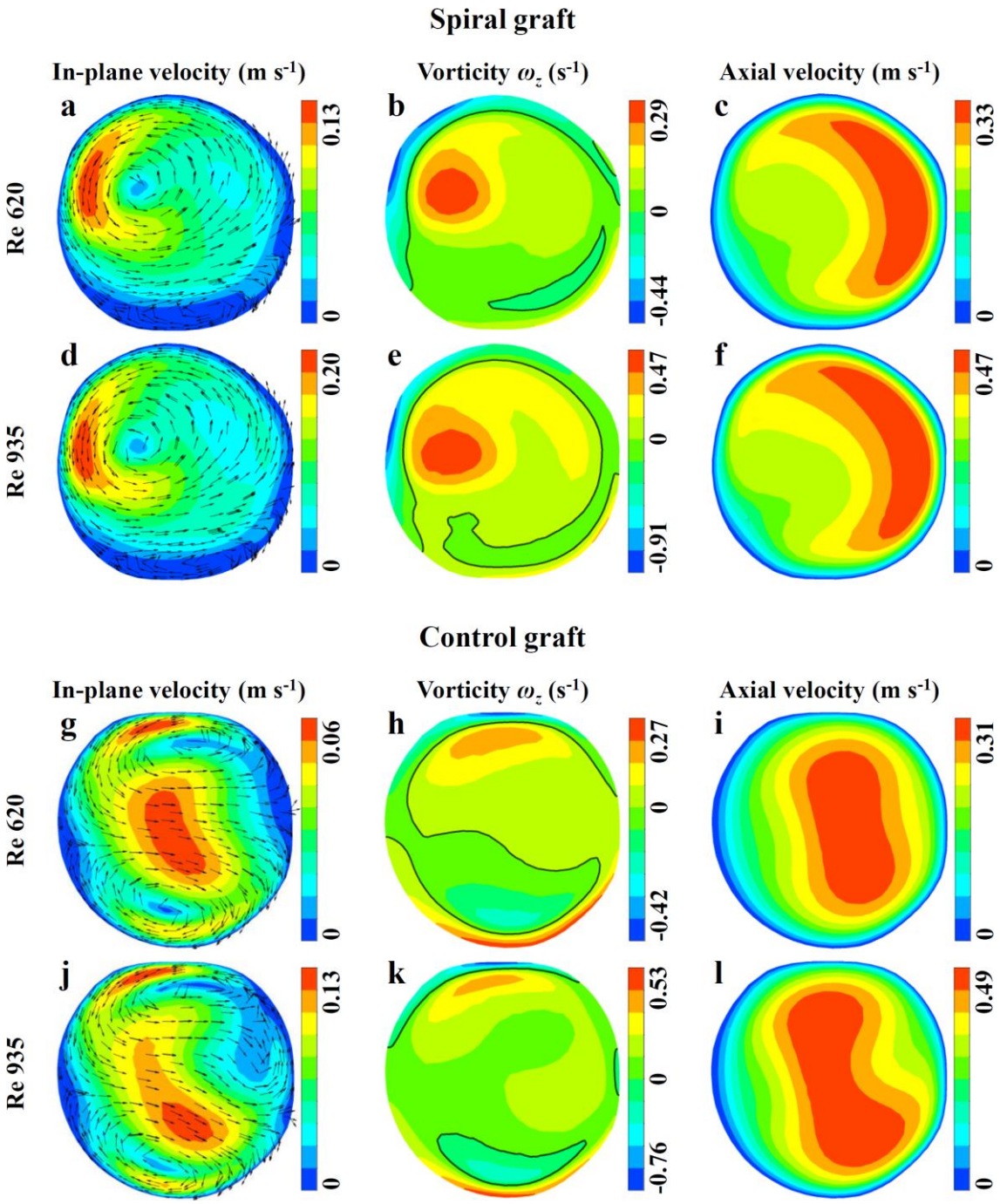

Figure 5.16: In-plane velocity, axial vorticity ω_z and axial velocity from the spiral and non-spiral PV models in cross-flow plane 1; angle of anastomosis 40°. The zero vorticity contour line is coloured black. The orientation of each map in relation to the anastomotic locations is: left side = toe and right side = floor.

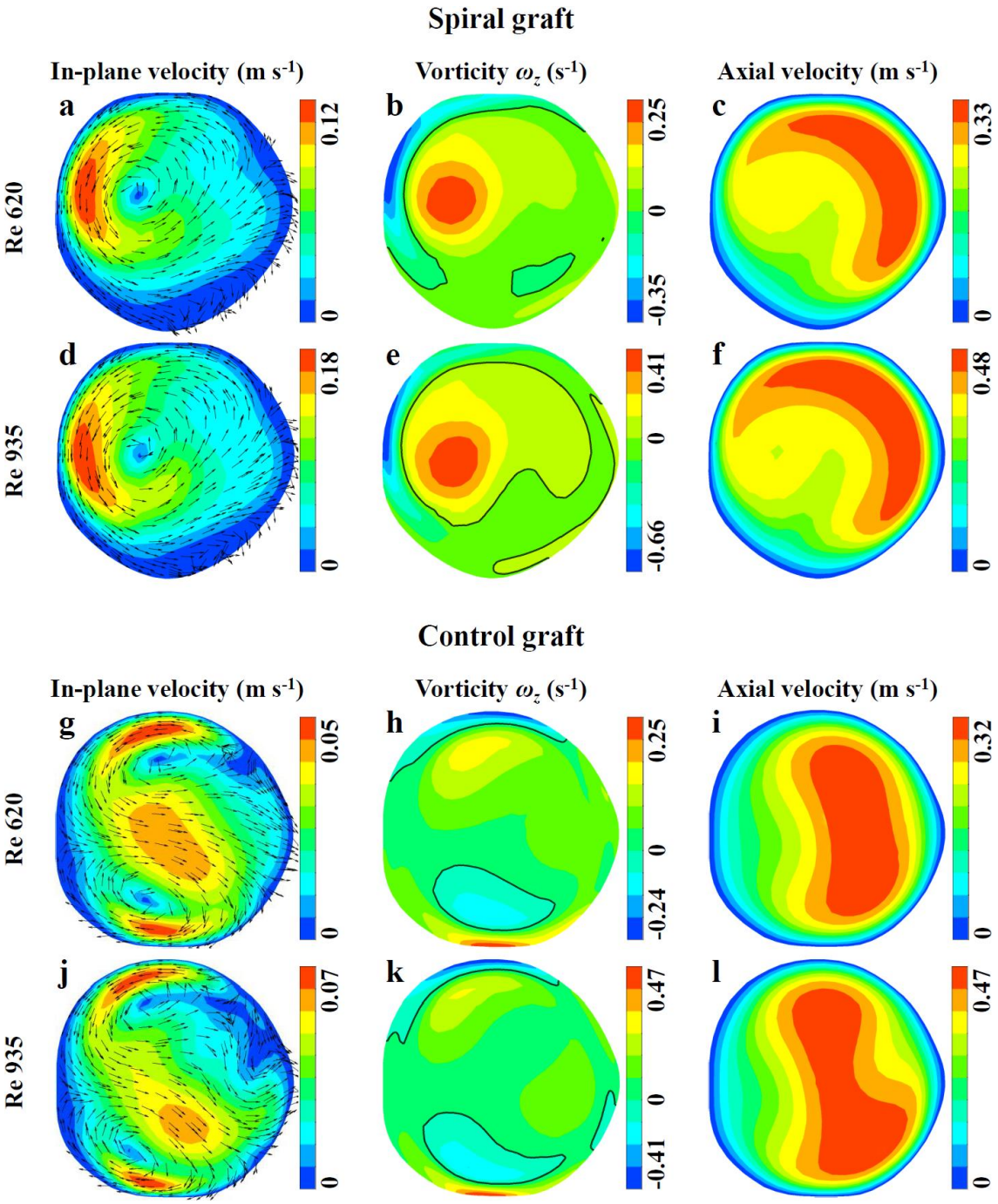

Figure 5.17: In-plane velocity, axial vorticity ω_z and axial velocity from the spiral and non-spiral PV models in cross-flow plane 2; angle of anastomosis 40°. The zero vorticity contour line is coloured black. The orientation of each map in relation to the anastomotic locations is: left side = toe and right side = floor.

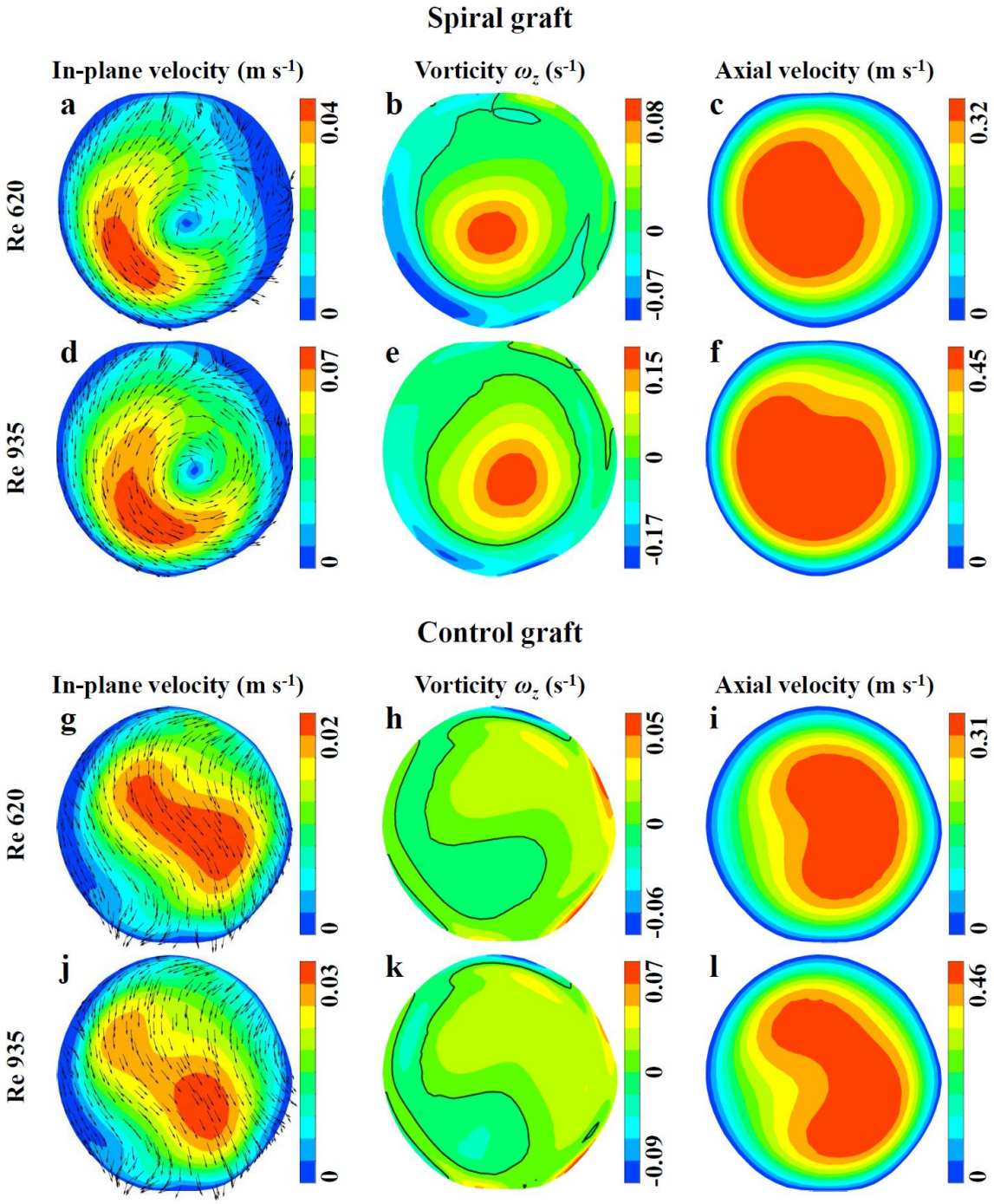

Figure 5.18: In-plane velocity, axial vorticity ω_z and axial velocity from the spiral and non-spiral PV models in cross-flow plane 3; angle of anastomosis 40°. The zero vorticity contour line is coloured black. The orientation of each map in relation to the anastomotic locations is: left side = toe and right side = floor.

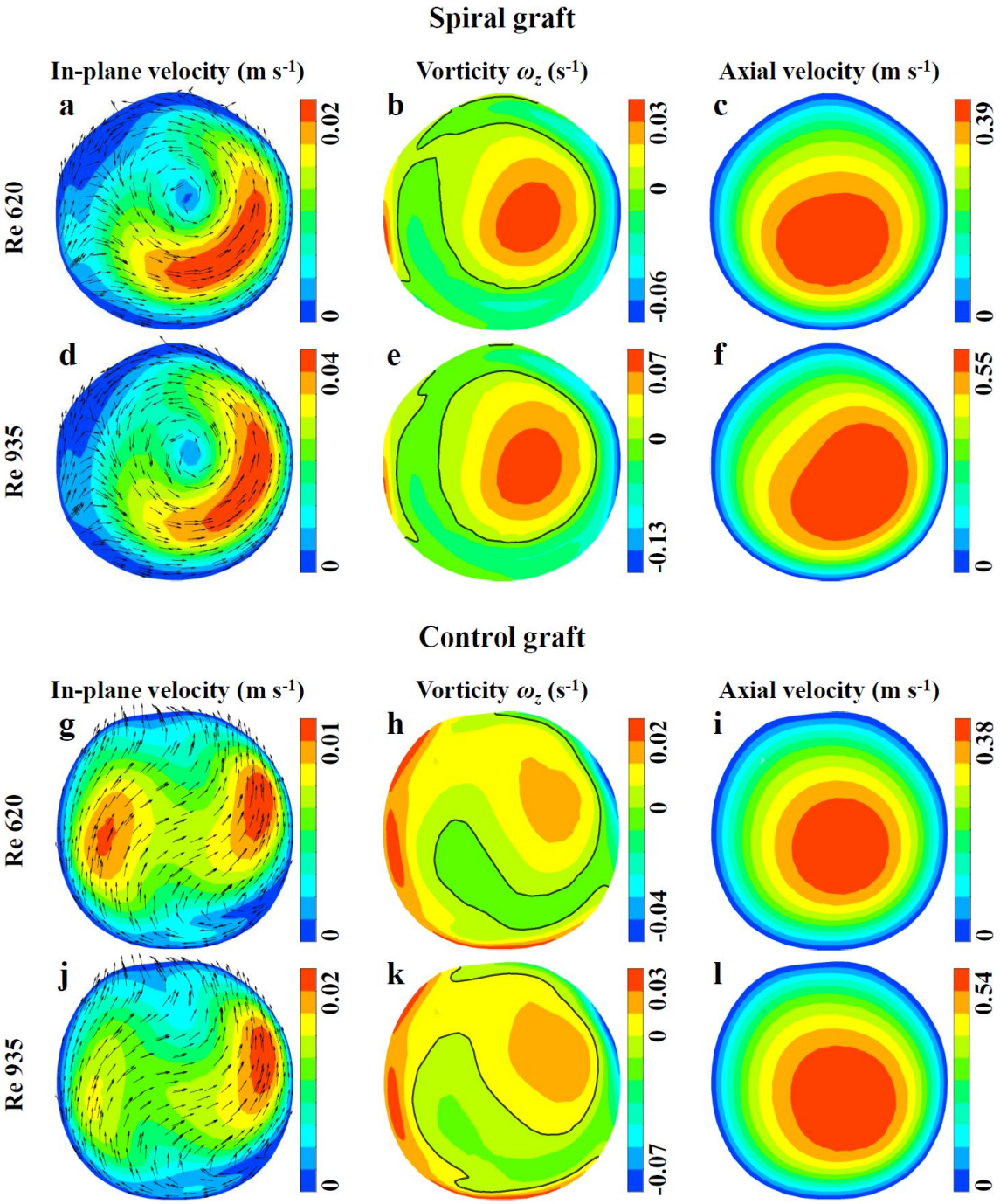

Figure 5.19: In-plane velocity, axial vorticity ω_z and axial velocity from the spiral and non-spiral PV models in cross-flow plane 4; angle of anastomosis 40°. The zero vorticity contour line is coloured black. The orientation of each map in relation to the anastomotic locations is: left side = toe and right side = floor.

5.3.3 Peak in-plane velocity and circulation

Figure 5.20 and Figure 5.21 show the progression of peak in-plane velocity and circulation respectively for the spiral and non-spiral models. Data from cross-flow planes 1 to 4 and for the four applied angles of anastomosis are presented. The values were consistently higher for the spiral models. The differences between the two products decreased with increasing angle.

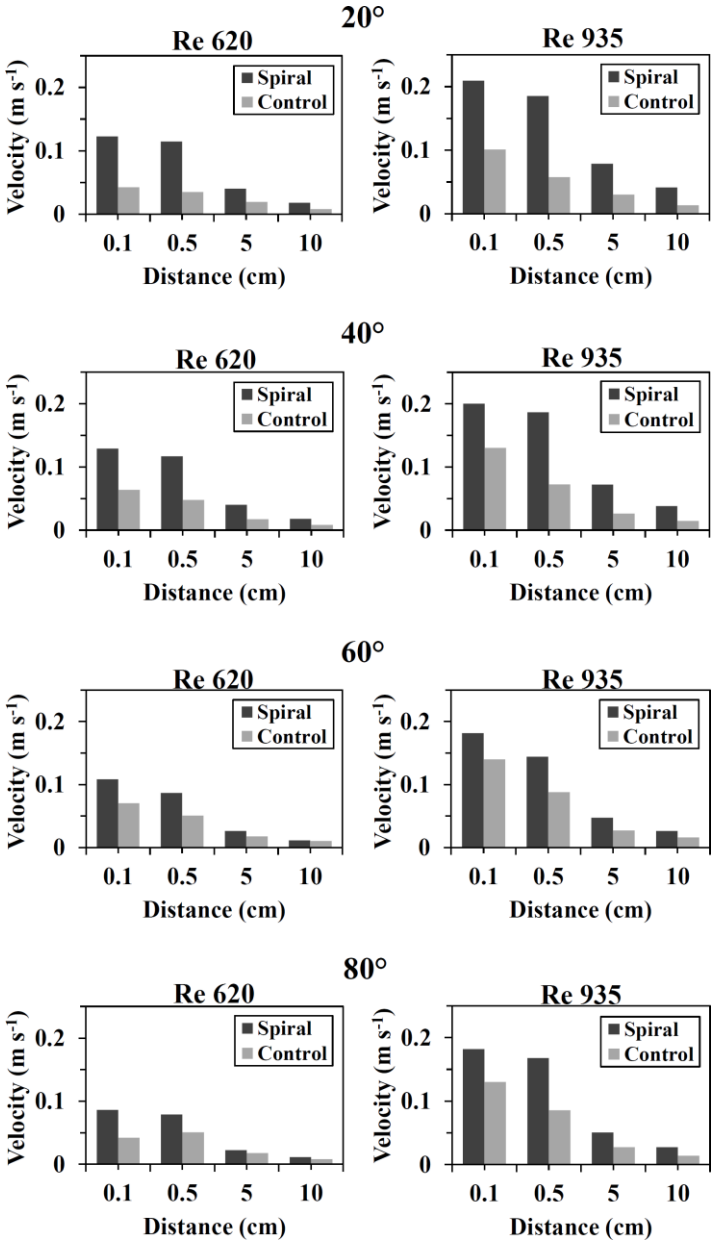

Figure 5.20: Progression of peak in-plane velocity at the outflow of the spiral and control PV models. The distance corresponds to cross-flow planes downstream from the anastomosis. Data from the four applies angles of anastomosis are shown.

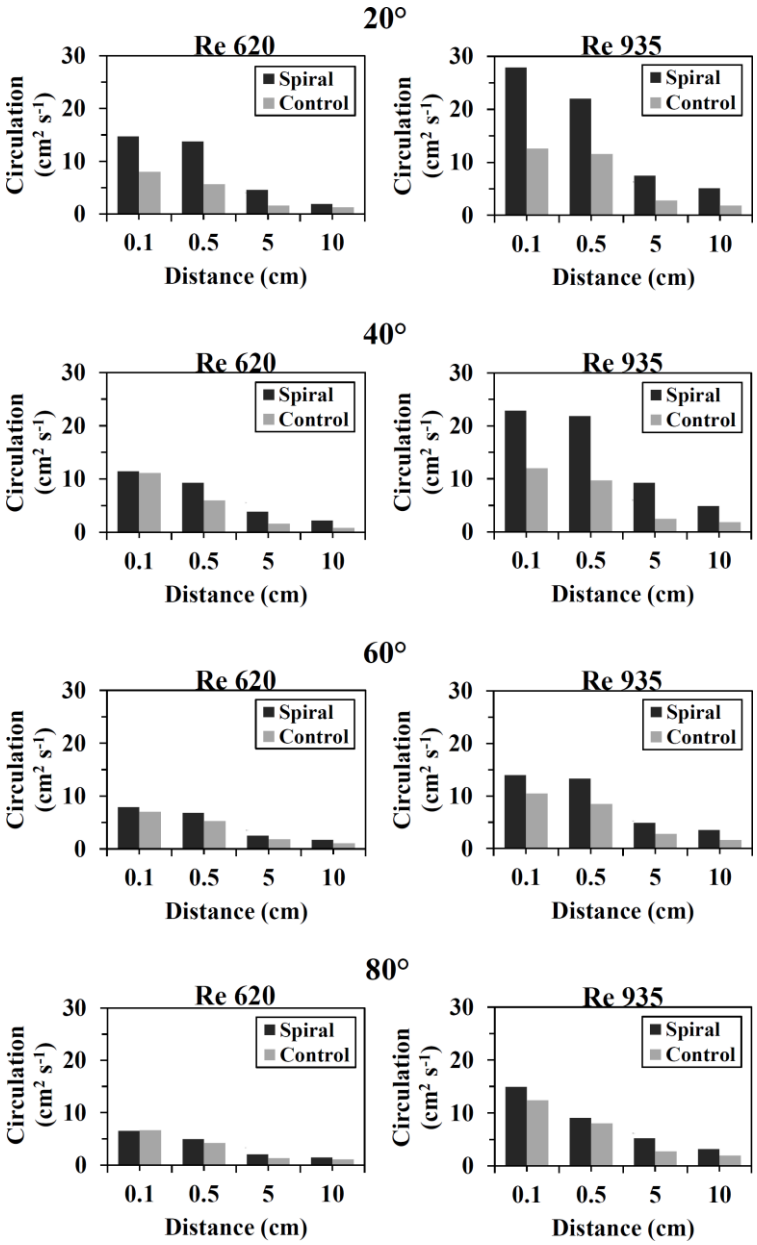

Figure 5.21: Progression of circulation at the outflow of the spiral and control PV models. The distance corresponds to cross-flow planes downstream from the anastomosis. Data from the four applies angles of anastomosis are shown.

5.3.4 Helicity and pressure drop

Figure 5.22 presents a comparison of helicity and Figure 5.23 presents a comparison of pressure drop between the spiral and control models. Data for both applied Reynolds numbers and the four applied angles of connection are shown. Both helicity and pressure drop were higher for the spiral graft models. The comparative differences decreased with increasing angle of anastomosis.

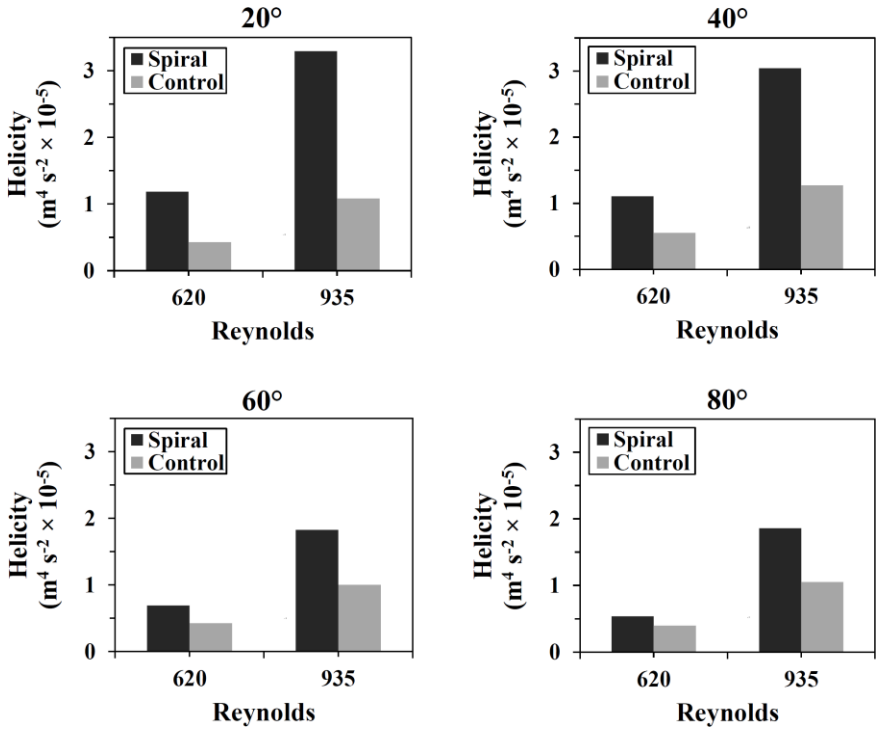

Figure 5.22: Comparison of helicity in the volume between cross-flow plane 1 and 4 for the spiral and control PV models, under both applied Reynolds numbers and for all applied angles of anastomosis.

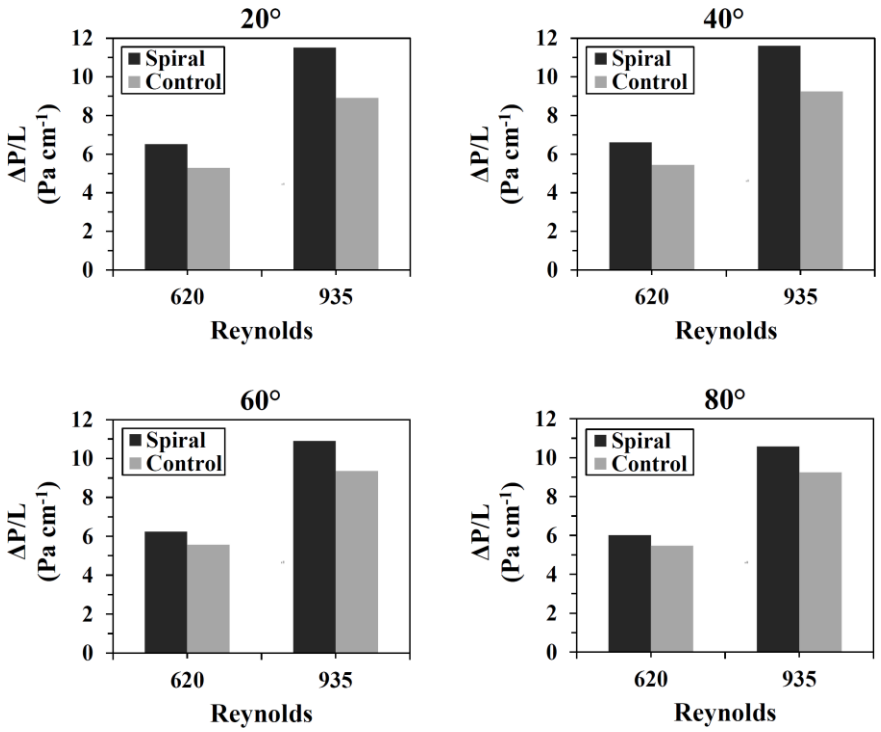

Figure 5.23: Comparison of pressure drop over length from the graft inlet to cross-flow plane 4 of the spiral and control PV models, under both applied Reynolds numbers and for all applied angles of anastomosis.

5.3.5 Wall shear stress

Figure 5.24 - Figure 5.27 illustrate a comparison of WSS at the proximal and distal floor and toe wall sides for the four pairs of models, for Reynolds number 935. Due to the observed fluctuation in the WSS trends, polylines were used to show their averaged profiles and increase clarification in the charts. These fluctuations were related to the surface of the walls.

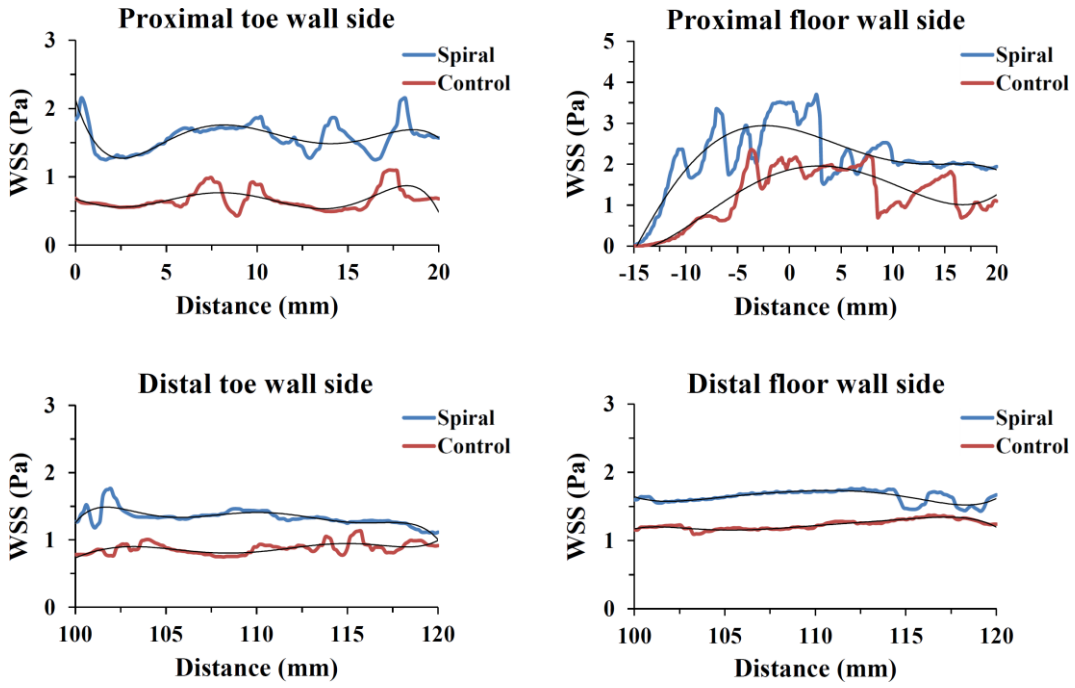

Figure 5.24: Wall shear stress at the four examined locations of the vessel mimic for both types of PV grafts at 20° angle of anastomosis, for Reynolds number 935. Polylines are used to show the averaged profile of each trend and increase the clarification of the charts.

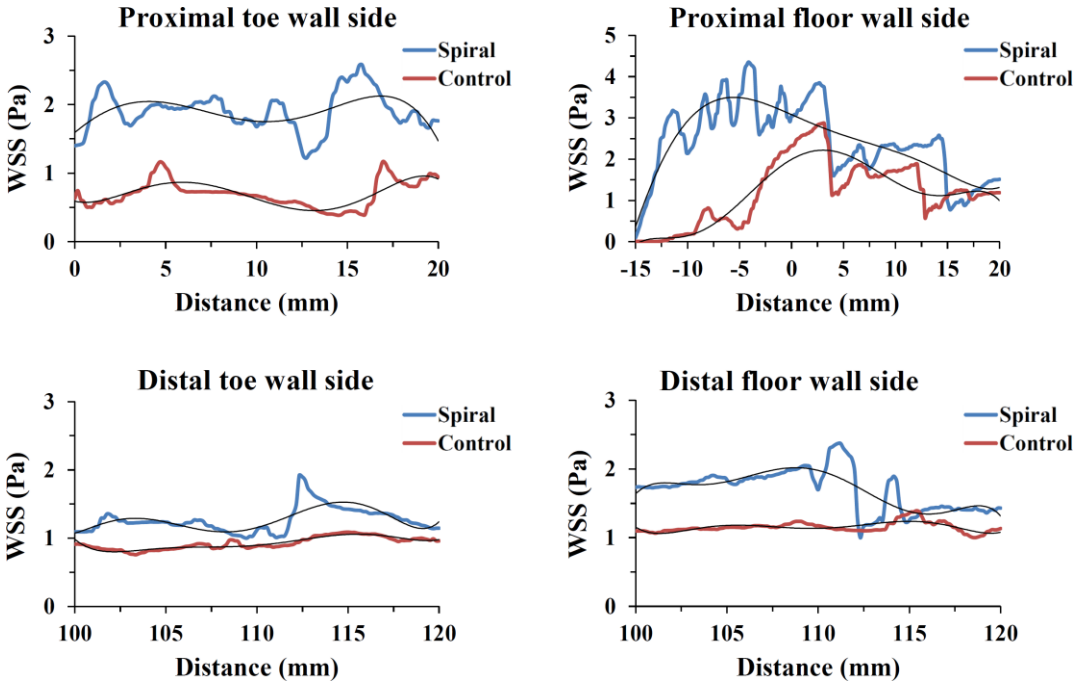

Figure 5.25: Wall shear stress at the four examined locations of the vessel mimic for both types of PV grafts at 40° angle of anastomosis, for Reynolds number 935. Polylines are used to show the averaged profile of each trend and increase the clarification of the charts.

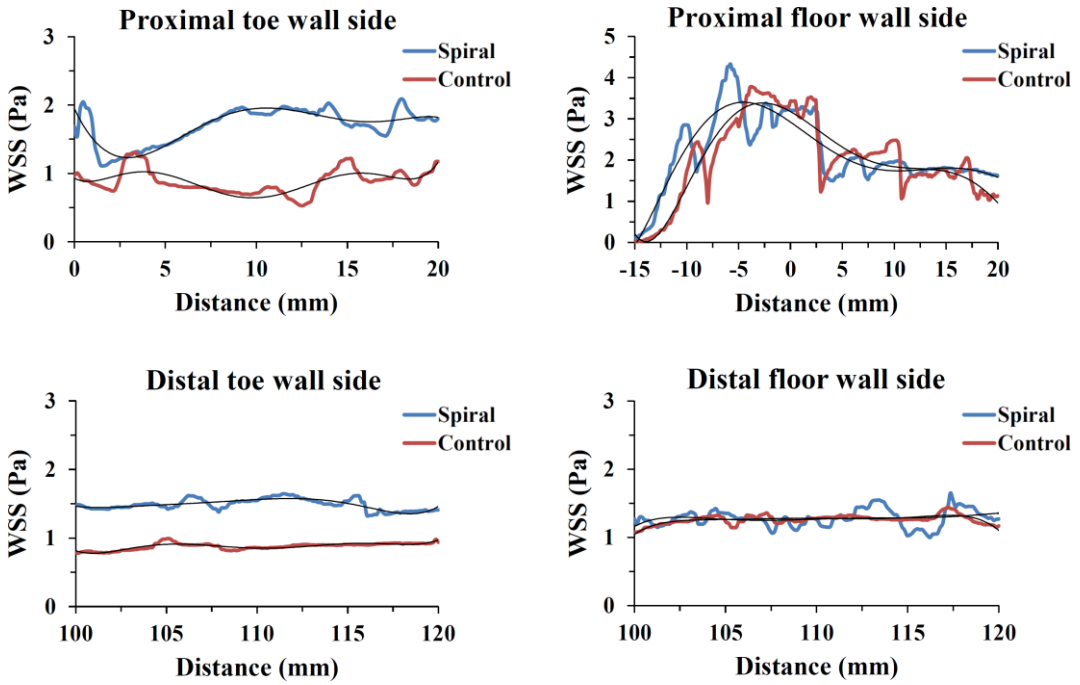

Figure 5.26: Wall shear stress at the four examined locations of the vessel mimic for both types of PV grafts at 60° angle of anastomosis, for Reynolds number 935. Polylines are used to show the averaged profile of each trend and increase the clarification of the charts.

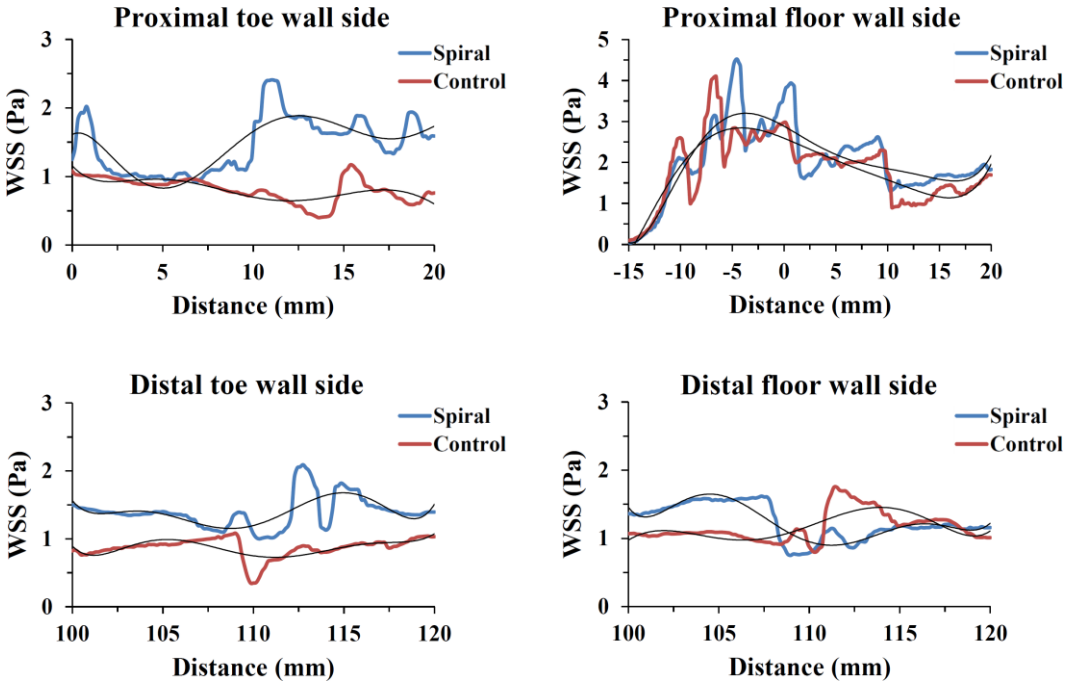

Figure 5.27: Wall shear stress at the four examined locations of the vessel mimic for both types of PV grafts at 80° angle of anastomosis, for Reynolds number 935. Polylines are used to show the averaged profile of each trend and increase the clarification of the charts.

5.3.6 Results from simulations with corrected viscosity

Comparison of flow maps in the outflow of spiral and control PV grafts

In-plane velocity, axial vorticity and axial velocity maps from the simulations with corrected viscosity of 3.5 mPa·s are presented in Figure 5.28 - Figure 5.31, for cross-flow planes 1 to 4 respectively. The first and third rows of each figure show data from Reynolds number 620 and the second and fourth rows data from Reynolds number 935 from the spiral and non-spiral model respectively. In vorticity maps a black contour line highlights regions of zero vorticity that separate the regions of positive and negative vorticity.

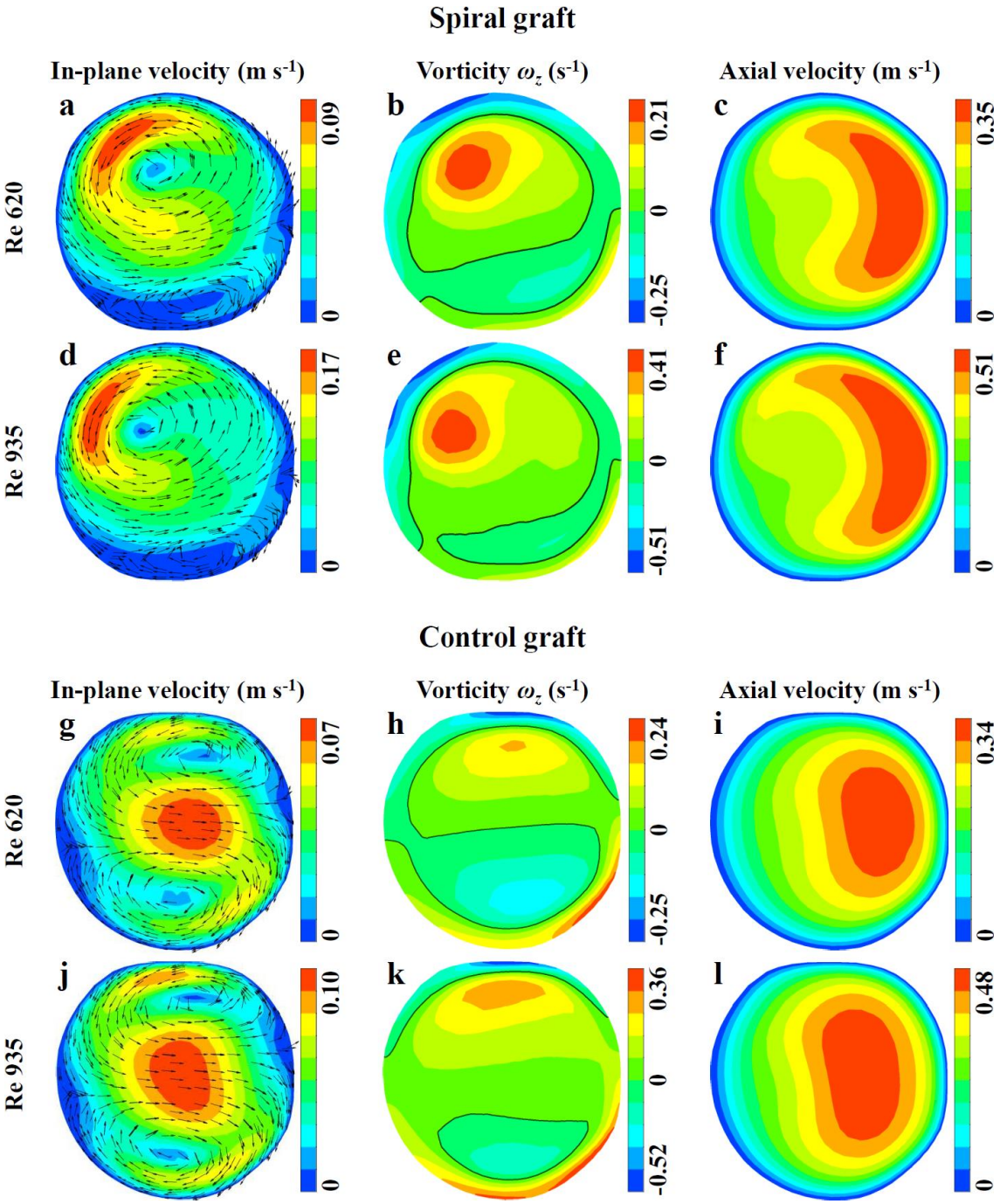

Figure 5.28: In-plane velocity, axial vorticity ω_z and axial velocity from the spiral and non-spiral PV models for the simulations with corrected viscosity in cross-flow plane 1; angle of anastomosis 40°. The zero vorticity contour line is coloured black. The orientation of each map in relation to the anastomotic locations is: left side = toe and right side = floor.

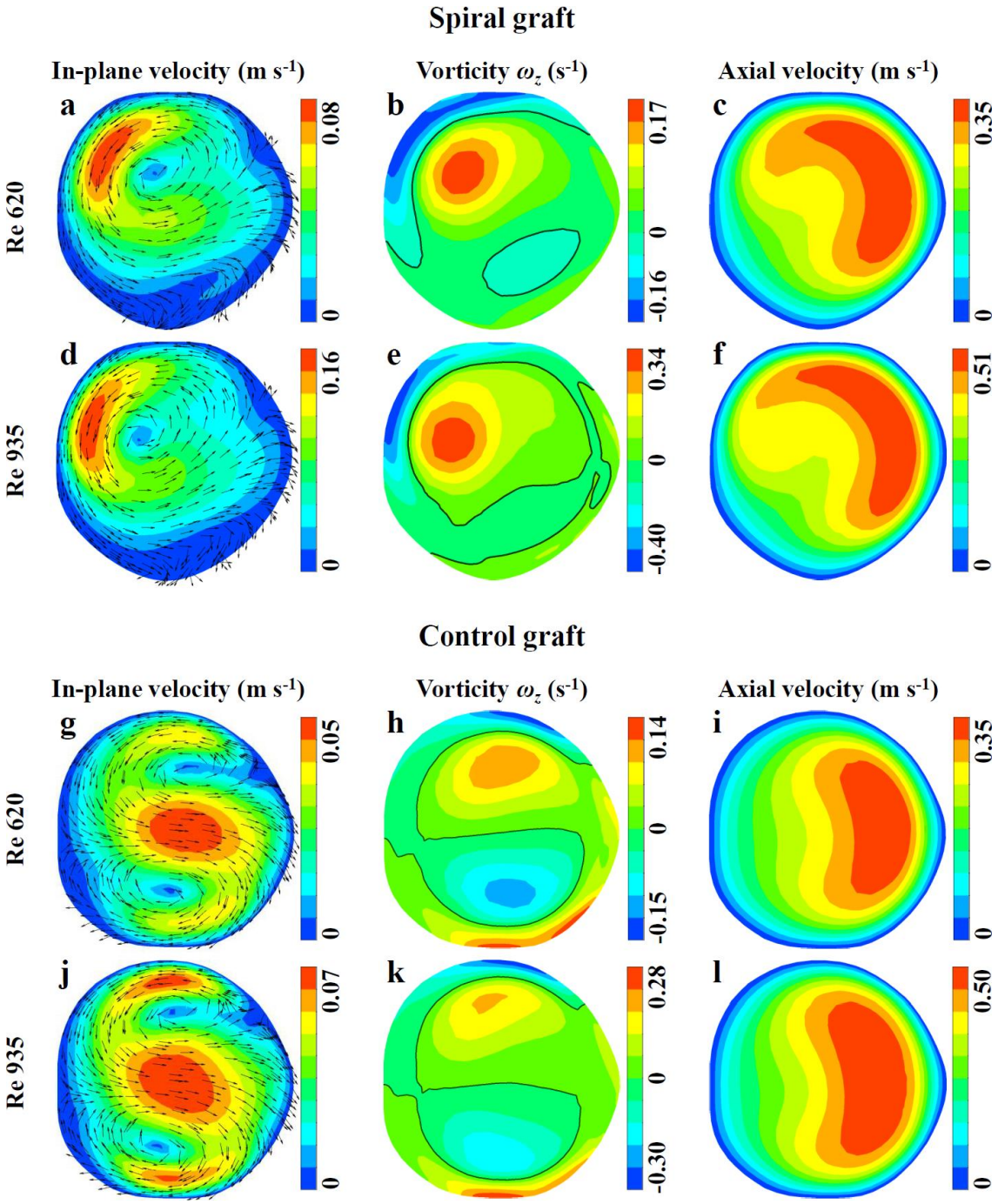

Figure 5.29: In-plane velocity, axial vorticity ω_z and axial velocity from the spiral and non-spiral PV models for the simulations with corrected viscosity in cross-flow plane 2; angle of anastomosis 40°.The zero vorticity contour line is coloured black. The orientation of each map in relation to the anastomotic locations is: left side = toe and right side = floor.

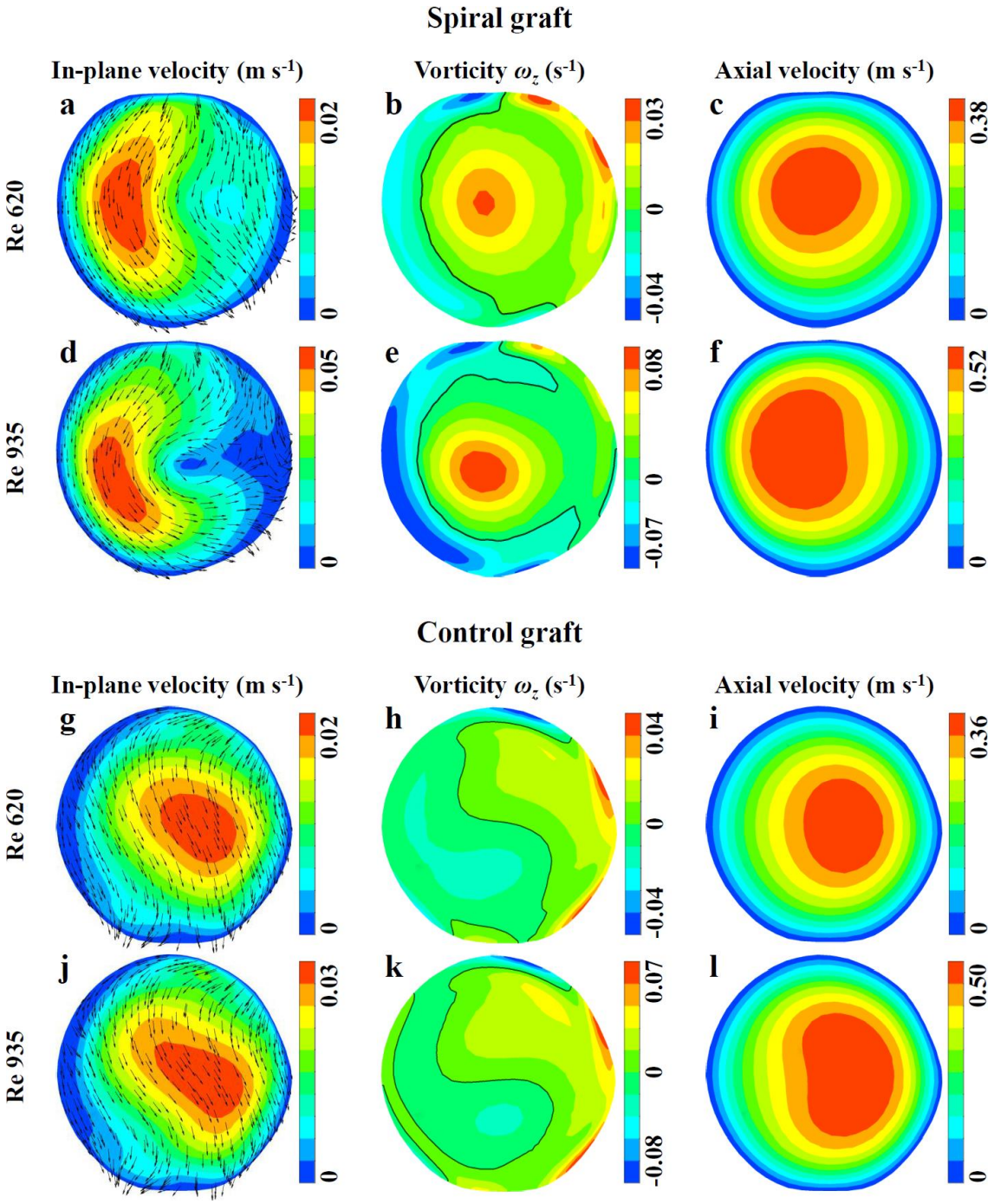

Figure 5.30: In-plane velocity, axial vorticity ω_z and axial velocity from the spiral and non-spiral PV models for the simulations with corrected viscosity in cross-flow plane 3; angle of anastomosis 40°. The zero vorticity contour line is coloured black. The orientation of each map in relation to the anastomotic locations is: left side = toe and right side = floor.

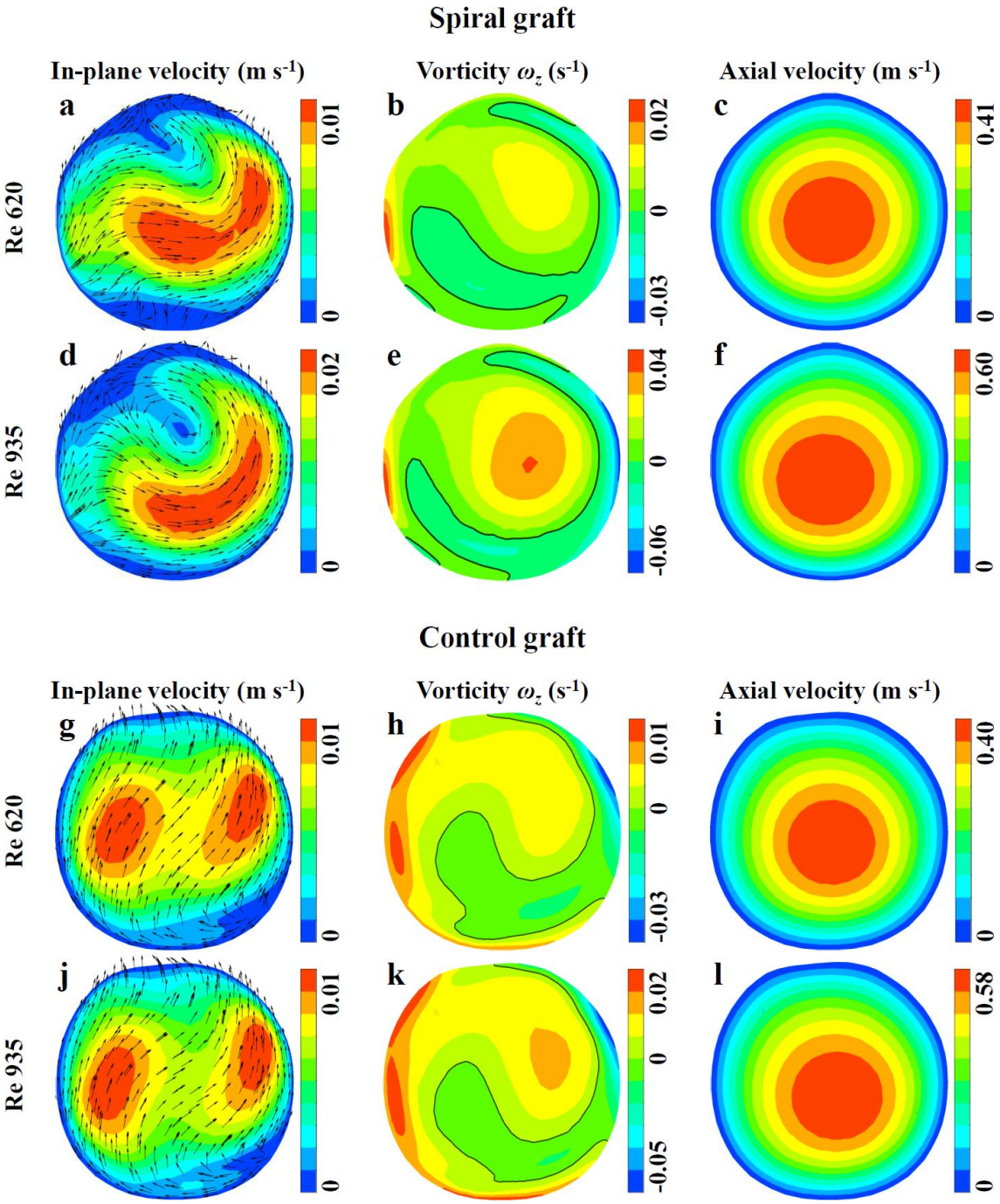

Figure 5.31: In-plane velocity, axial vorticity ω_z and axial velocity from the spiral and non-spiral PV models for the simulations with corrected viscosity in cross-flow plane 4; angle of anastomosis 40°. The zero vorticity contour line is coloured black. The orientation of each map in relation to the anastomotic locations is: left side = toe and right side = floor.

Quantitative results

The progression of peak in-plane velocity and circulation in relation to the distance from the anastomosis using corrected viscosity value are shown in Figure 5.32. The data correspond to both applied Reynolds numbers. The results were increased for the spiral model.

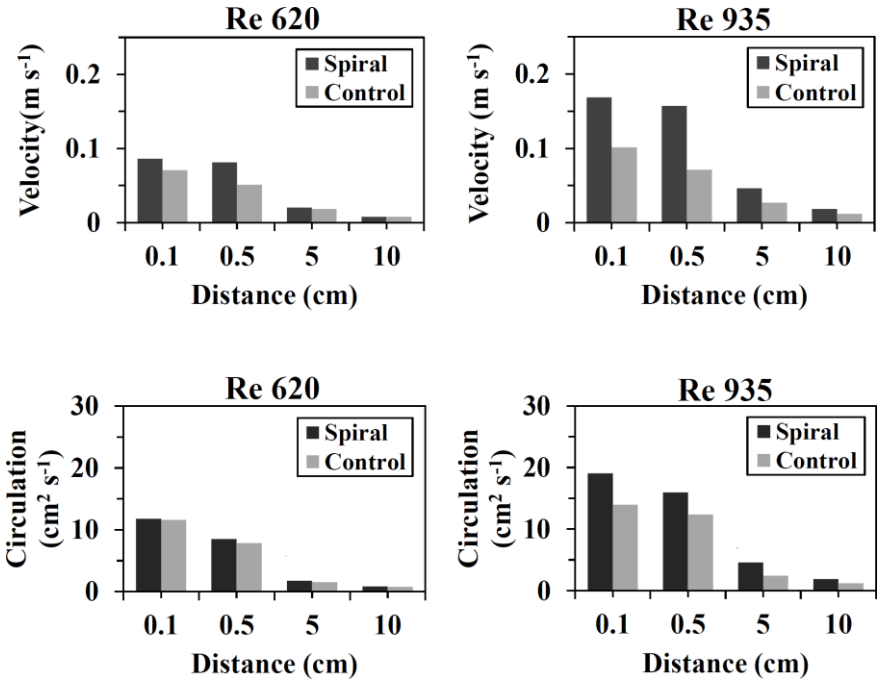

Figure 5.32: Progression of peak in-plane velocity (first row) and circulation (second row) of the 40° spiral and control PV models, from the simulations with corrected viscosity. The distance corresponds to cross-flow planes downstream from the anastomosis.

Figure 5.33 shows a comparison of helicity across the vessel mimic and a comparison of pressure drop from the inlet of the graft to the distal vessel mimic, for the simulations with corrected viscosity. These results are from both applied Reynolds numbers and reveal increased magnitudes for the spiral model.

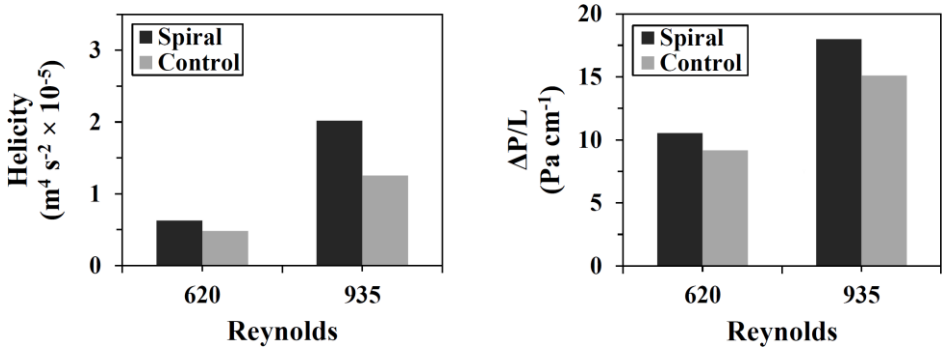

Figure 5.33: Comparison of helicity in the volume between cross flow plane 1 and 4, and pressure drop over length from the graft inlet to plane 5, for the spiral and control 40° PV models using corrected viscosity.

Figure 5.34 presents results of WSS at the proximal and distal wall examined locations, for the simulations with corrected viscosity value and Reynolds number 935. There was increased fluctuation in the WSS gradient over distance. For this reason, polylines were used to indicate the averaged trends of the data in each chart.

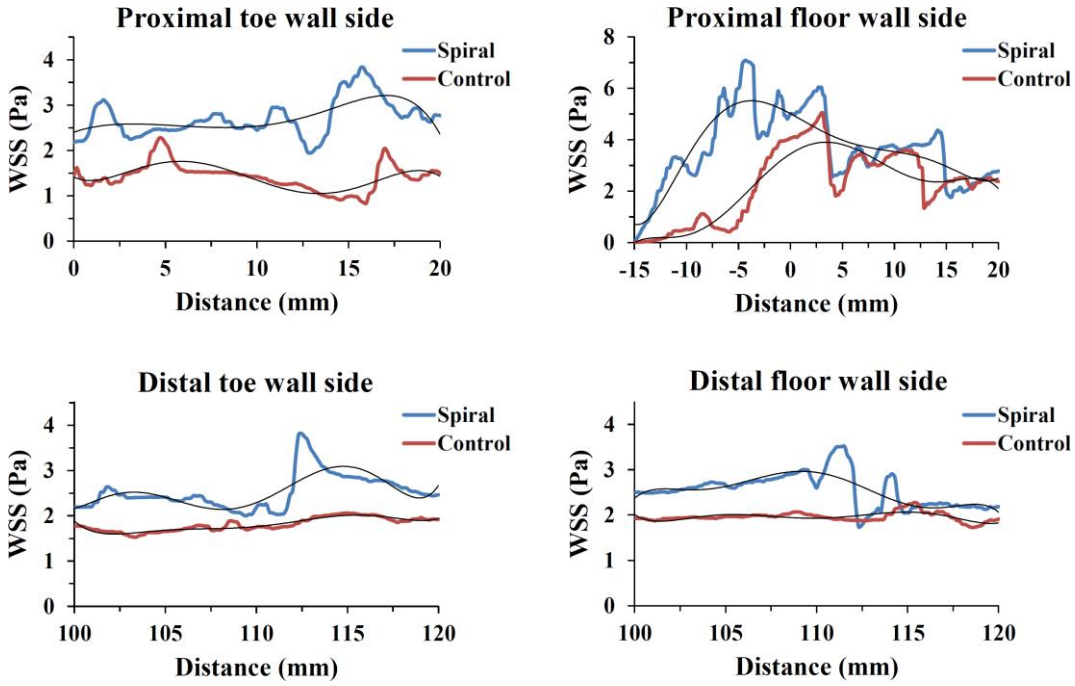

Figure 5.34: Wall shear stress at the four examined locations of the vessel mimic for both types of PV grafts at 40° angle of anastomosis, from the simulations with corrected viscosity and Reynolds number 935. Polylines are used to show the averaged profile of each trend and increase the clarification of the charts.

5.4 Discussion

Flow rates of 240 and 360 mL·min^{-1} were applied to mimic the corresponding PV graft flow experiments in chapter 3. The respective Reynolds numbers that these flow rates produced across the vessel mimic in this numerical study were calculated to be 620 and 935. The corresponding Reynolds numbers in the experimental approach were estimated to be 570 and 850. The main reason for this difference was the decreased diameter of the computational volume meshes in relation to the actual models. The actual diameter across the vessel mimic was 5.4 mm (section 2.2.2, page 36) and that of the computational mesh was 5 mm. The shrinkage of the models was related to the CT scanning, and post process segmentation and smoothing with Amira. During segmentation the intensity threshold value was chosen so as to maximise the diameter of the extracted lumen geometry.

The comparison of experimental and CFD in-plane velocity maps in Figure 5.11 - Figure 5.14 showed as striking similarity between the main vortical structures. In the outflow of the spiral graft there was a main spiral and a second very small spiral. The centre of the main spiral was close to the toe and anterior wall sides, whilst the small vortex was located close to the posterior side. The vector Doppler technique was hardly able to detect the small spiral as shown with the close up in Figure 5.15. In the outflow of the control graft the main observation was a Dean flow pattern. A third recirculation can be seen in both the CFD and vector Doppler maps for the 20° model. In all comparisons between the experimental and computational maps, there were differences in the distribution of velocity magnitudes and the maximum detected velocities. It is possible that these differences were associated with variations between the two techniques, which are discussed in section 7.9, page 175.

The general observation from the in-plane velocity and axial vorticity maps of the spiral, non-planar graft model was a single-spiral flow (Figure 5.16 - Figure 5.19). In cross-flow plane 1 there was a second smaller helix close to the posterior wall side, which dissipated after plane 2. This small helix was associated with a low near wall velocity gradient that could be considered a flow stagnation point. In planes 3 and 4 there was some near wall flow disturbance associated with low tangential velocities.

The axial velocity maps showed a crescent form in cross-flow planes 1 and 2. In plane 3 and particularly plane 4 the shape of the axial velocity was closer to that of concentric circles. These structures were close to the wall side where the peak in-plane velocity was seen. The axial velocity observations in distal planes implied transition to a more parabolic flow profile and reduced intensity of the spiral component of flow, as a result of the viscous effect of the simulated blood. Solutions of a similar nature have been presented in the outflow of non-planar anastomotic models by Doorly and Sherwin (2009) and Sherwin et al. (2000). These flow patterns verified that the PV spiral, non-planar graft could produce a dominant spiral, which reduced flow separation and stagnation, and introduced strong secondary flow phenomena, flow stability and coherence downstream from its outflow (Caro et al. 2005; Stonebridge 2011).

The in-plane velocity and axial vorticity maps at the proximal cross-flow planes 1 and 2 of the control model revealed a Dean flow pattern (Figure 5.16 - Figure 5.17). Stagnation points were observed at the floor and toe wall sides. The axial velocity in these planes had a centralised 'I' or crescent like shape. In distal planes 3 and 4 (Figure 5.18 - Figure 5.19) the in-plane maps revealed a dissipated double-spiral flow with no complete recirculation cell and low velocity gradient. The axial velocity maps in plane 3 showed that a parabolic profile started to develop, a process that was clearly seen in plane 4 with the concentric circular structures.

In addition, the vorticity maps could clearly locate the centre of each spiral in all cross-flow planes of both models (Figure 5.16 - Figure 5.19). The regions of counter vorticity near the wall were associated with the shearing process of the fluid particles due to the no-slip wall boundary condition (Cookson et al. 2009; Yamamoto et al. 2002; Zabielski and Mestel 1998).

Considering the results discussed in the previous three paragraphs in relation to the corresponding flow maps from the vector Doppler approach (Figure 3.5 - Figure 3.8); the main characteristics of spiral flow patterns in the outflow of the PV grafts, such as the number of vortices, their direction and centre of rotation were in close agreement. This agreement was reduced in the distal cross-flow maps 3 and 4 of the control model, where the double-spiral flow was dissipated for the CFD data.

The peak in-plane velocity comparison (Figure 5.20) showed consistently higher values for the spiral device under all applied conditions. This difference was more than 50% for anastomotic angles of 20° and 40°. The magnitude of these peak velocities for the spiral graft decreased with the increase of angle of connection. The peak velocities from the control device did not follow a specific trend with the change of angle. The comparison of circulation (Figure 5.21) revealed higher magnitudes for the spiral device. The differences between the spiral and non-spiral models decreased with increasing anastomotic angle and the differences were highest for Reynolds number 935. Circulation was higher for the control graft at the 80° models, Reynolds number 620, cross-flow plane 1.

The general conclusion from the peak velocity and circulation comparisons was that the spiral device was associated with increased values in comparison to the control and their differences decreased with increasing angle of anastomosis. These trends agreed with the corresponding results from the experimental analysis of the PV grafts (chapter 3: Figure 3.9 - Figure 3.12 and Figure 3.13 - Figure 3.16).

Helicity (Figure 5.22) was significantly higher for the spiral device. The difference between the two products decreased with increasing angle of connection. This was mainly associated with decrease of helicity generated from the spiral graft at high angles. The helicity generated from the control graft was hardly affected by the angle of connection.

The quantitative data of peak in-plane velocity, circulation and helicity showed enhanced secondary flow motions for the spiral device, as a result of the introduction of a single-spiral and minimisation of flow separation. This indicated increased in-plane mixing in the outflow of the spiral graft, which is believed to protect the host vessel from stenosis and thrombosis (Caro et al. 2005).

The pressure drop (Figure 5.23) was found to be higher for the spiral graft in comparison to the non-spiral. Differences were at a maximal for the 20° pair of models and then decreased with increasing angle of connection. More specifically, for the 20° models, the difference in pressure drop per centimetre of distance was approximately 1.5 and 2.5 Pa for Reynolds number 620 and 935 respectively. A pressure drop in

implanted and native vessels is considered a risk factor for the development of neo-intimal hyperplasia and thrombosis (Cookson et al. 2009; Cookson et al. 2010). However, the physiologic pressure relative to atmospheric pressure at the proximal femoral artery is 80-140 mmHg and at the distal femoral artery 80-150 mmHg in upright position (Caro et al. 2012). A pressure of 2.5 Pa is equal to approximately 0.019 mmHg. Taking this into context the detected difference in pressure drop was very small and could be considered negligible.

The WSS was assessed for both vascular-graft models (Figure 5.24 - Figure 5.27). For the 20° models, the WSS was consistently 20-50% higher for the spiral graft (Figure 5.24). Similarly for the 40° models, the WSS for the spiral model was consistently higher, although this difference decreased in the distal floor and toe (Figure 5.25). For the 60° models of anastomosis, there was 30-50% greater WSS for the spiral device in both toe wall side locations, but no difference existed between the models in the floor wall side locations (Figure 5.26). For the 80° models, WSS was similar for both grafts in the first 10 mm proximal of the toe but about 50% higher for the spiral prosthesis after that (Figure 5.27). Further, in the distal toe region the WSS was still greater for the spiral product. In relation to the floor wall locations, there were no clear differences in the charts of the spiral and non-spiral models.

The presented WSS results were from Reynolds number 935. The WSS results from Reynolds number 620 were lesser in magnitude than those of Reynolds number 935; however, the overall trends in both cases were almost identical. As a result only WSS data for Reynolds number 935 were presented.

The results discussed so far indicate that the single-spiral in the outflow of the spiral graft was associated with stronger secondary flow motions and increased WSS. On the contrary, the flow patterns from the control models showed stagnation points in the floor and toe proximal walls as a result of Dean flow profiles. The decreased WSS magnitude of the control models in these locations verified that these stagnation points were subjected to low WSS. This may be associated with the histopathologic observation that the greatest degree of neo-intimal hyperplasia in the host artery is developed along the floor of the outflow anastomosis and along the wall sides of the toe and heel of the anastomosis. The influence of local haemodynamics in the formation of

neo-intimal hyperplasia is considered significant (Keynton et al. 2001; Sottiurai et al. 1989). Increased WSS in normal vessels is generally considered to protect endothelial function because plaque is primarily developed in areas subjected to low and oscillatory WSS (Slager et al. 2005a; Slager et al. 2005b). A complete characterisation of WSS would not only require measurements of WSS magnitude but also its oscillatory index and gradient (Hardman et al. 2013). This would require a transient numerical approach based on the physiologic pulsatile cardiac cycle. The observations of this study may explain the promising clinical results of the PV spiral graft that were presented by Stonebridge et al. (2012). It could be hypothesised that the PV spiral graft not only increases the WSS but also decreases its oscillatory index and gradient through the generation of a stabilised single-spiral that reduces stagnation points.

The flow maps from the 20°, 60° and 80° spiral and control graft models were similar to those presented for the 40° models. The main difference was that a third spiral existed in the proximal outflow of the 20° control model as shown in Figure 5.11. Localised flow pattern disturbances were observed for both models for the maximal 80° angle of anastomosis.

During the MRI based image-guided surface rendering, reduced amounts of gadolinium were used in the solution that filled the lumen of the vascular-graft model. This increased the signal intensity difference between the lumen and the PVA-c wall, enabling segmentation between their boundary. However, the surface of the geometry extracted from the MRI data had a very intense zigzag shape. Another disadvantage of reducing the concentration of gadolinium was that it resulted in poor contrast between the lumen and the wall of the graft. This had a detrimental effect in the quality of the groove from the spiral ridge. On the contrary, CT provided clear intensity differences between the pixels from the lumen and the pixels from the vascular-graft wall and therefore it was better suited for this project.

5.4.1 Analysing the results from simulations with corrected viscosity

The main flow pattern characteristics in cross-flow planes 1 and 2 of the simulations with corrected viscosity (Figure 5.28 and Figure 5.29) remained relatively similar for both models, in comparison to the simulations with the lower value of viscosity (Figure

5.16 and Figure 5.17). For the spiral model there was a dominant main spiral beside a second small spiral. This small spiral was associated with low near wall velocity gradient and flow stagnation at the floor wall side. For the control model, a Dean flow pattern was seen in the outflow resulting in stagnation points at the toe and floor wall sides. The two spirals of the Dean flow were more uniform and centralised in the lumen area in comparison to the simulations with the lower viscosity. In relation to the axial velocity maps, the spiral graft model still exhibited a crescent formation. Crescent like structures were also observed for the non-spiral model, but they were not as distinct as those for the spiral. The same observation has been noted by Sherwin et al. (2000).

Moving to cross-flow planes 3 and 4 (Figure 5.30 and Figure 5.31) of the spiral model, there were decreased secondary flow motions with no clear spiral pattern for Reynolds number 620 and a weak single-spiral for Reynolds number 935. The relevant control model patterns revealed highly reduced secondary flow motions with no specific spiral structure. In relation to the axial velocity in these planes, the circular concentric formations observed for both models indicate the development of parabolic flow as a result of the viscous effect.

Comparing the vorticity maps of the corrected and reduced vorticity simulations in all cross-flow planes, differences can be seen in the location of the boundary between the positive and negative regions of vorticity. Although the main characteristics such as the core of each vortex, remained unchanged.

The peak in-plane velocity and circulation for the simulations with corrected viscosity remained higher for the spiral model in comparison to the non-spiral (Figure 5.32). In comparison to the data from the reduced viscosity simulations, the peak velocity and circulation differences were generally reduced. Particularly in distal planes 3 and 4 for Reynolds number 620 the differences in peak velocity were negligible. Moreover, for Reynolds number 620 the differences in all circulation comparisons were almost negligible. The scale of all peak velocity and circulation magnitudes for the corrected viscosity simulations was decreased showing reduced intensity of secondary flow motions.

Helicity and pressure drop remained higher for the spiral compared to the non-spiral model in the simulations with corrected viscosity (Figure 5.33), but their differences were less than those from the simulations with reduced viscosity. The magnitudes of helicity were decreased and the magnitudes of pressure drop were increased due to the effects of enhanced viscous forces.

The trends of WSS in the four examined locations of the simulations with corrected viscosity and Reynolds number 935 (Figure 5.34) remained similar to the relevant WSS trends from the simulations with decreased viscosity (Figure 5.25). The main difference was the increase in the scale of their magnitudes due to the increased viscous phenomena. WSS data for Reynolds number 620 was not presented, as previously explained in this section for the simulation with decreased viscosity.

5.5 Conclusions

The main observation of these simulations was a single-spiral flow pattern in the outflow of the spiral, non-planar model and a Dean flow pattern in the outflow of the control, planar model. The single-spiral revealed fewer stagnation points, separation and instability in comparison to Dean flow. The spiral graft was associated with increased in-plane velocity, circulation, helicity and WSS. These quantitative parameters showed enhanced secondary flow phenomena and in-plane mixing, which are considered atheroprotective. The spiral graft also created an increased pressure drop, which although not desirable in vascular implants was negligible in comparison to the control graft. The computational results were in agreement with those from the ultrasound study.

The in-plane flow patterns from the simulations with corrected blood viscosity demonstrated little or no changes in the proximal graft outflow and increased changes in the distal graft outflow, related to a dissipation of secondary flow phenomena. The quantitative comparisons of peak in-plane velocity, circulation, helicity, pressure drop and WSS between the spiral and non-spiral models showed greater values for the former model. However, the quantitative differences and propagation of secondary flow phenomena were reduced for the simulations with corrected viscosity compared to those

with low viscosity, because of the higher viscous forces. Viscosity is an important parameter of blood rheology and although differences were expected, the main characteristics in the outflow of the grafts remained constant.

These results verify the ability of the PV spiral graft to generate enhanced secondary flow phenomena, which may prevent the development of neo-intimal hyperplasia and thrombosis in the outflow anastomosis and the progression of PAD downstream in the arterial tree. This could result in improved PV graft patency rates in patients.

Chapter 6

Computational assessments of arteriovenous prosthetic grafts

6.1 Introduction

The AV spiral and control vascular-graft models, positioned in the loop surgical configuration and experimentally assessed in chapter 4 of this thesis, were subjected to numerical simulations. The simulations were acquired using a CT based image-guided modelling method. Velocity, vorticity and circulation assessments were applied using the same approach as that of the experimental study to allow for comparison. The computational simulations provide 3D information of a flow field. Predictions of WSS, helicity and pressure loss were acquired and comparisons between the spiral and control models were assessed, permitting vascular haemodynamics in relation to neo-intimal hyperplasia and thrombosis to be further investigated. The aim of this chapter is to present the CFD simulations of the AV looped models.

6.2 Methods

The CFD methodology of the AV models was based on the final CFD methodology of the PV models.

6.2.1 CT scanning of the AV vascular-graft models

The spiral and non-spiral AV looped models were positioned in the tank that was used during the experimental approach, to maintain an identical geometry and to facilitate the CT scanning. The scanning settings were the same as those applied for the PV models (section ‘Computed tomography’, page 103).

6.2.2 Surface mesh

The CT DICOM files were loaded into Amira for visualisation, segmentation and surface rendering. The wall boundary of the vascular-graft lumen was selected choosing the appropriate intensity threshold in the CT DICOM images, in order to extract the geometry of the lumen.

The transverse, sagittal and coronal view of the AV spiral vascular-graft model connected in the loop surgical configuration is shown in Figure 6.1. The bright grey-scale shades correspond to high intensities and the dark grey-scale shades to low intensities. The high signal intensity difference between the pixels of the lumen and those of the vascular-graft wall ensured that there was no difficulty in defining the boundary between the lumen and the vascular-graft wall, which is shown with a green line in Figure 6.1. The criterion for selecting the optimum segmentation intensity threshold was to ensure the diameter of the extracted lumen geometry matched that of the actual lumen diameter as closely as possible. The same intensity threshold was chosen for both the spiral and non-spiral models.

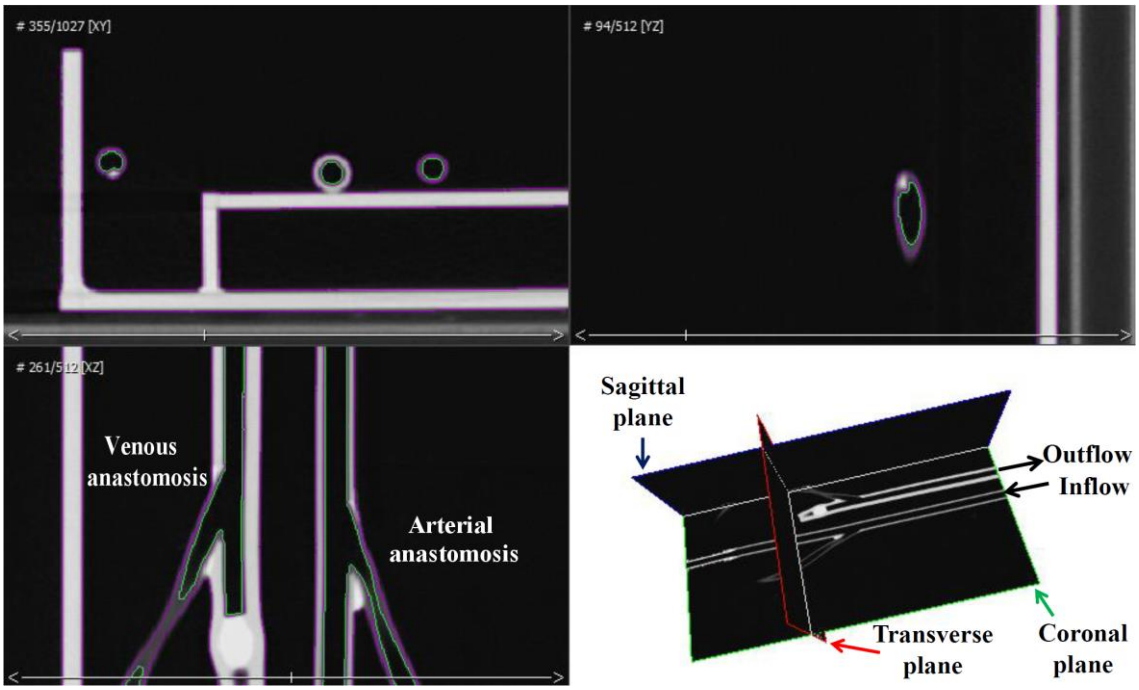

Figure 6.1: CT images from the AV spiral vascular-graft model. Top left: transverse plane; top right: sagittal plane; bottom left: coronal plane. The ridged cross sectional internal geometry of the spiral graft can be seen in the transverse and sagittal views. The green line in the boundary of the lumen defines the segmented region.

An example of the segmented surface mesh from the AV spiral model is shown in Figure 6.2. The surface mesh had a zigzag shape and thus limited smoothing was applied to reduce this phenomenon. This had minimal effect on the extracted geometry and particularly on the groove from the spiral ridge. The final surface meshes from the spiral and control AV vascular-graft models were saved as a triangulated mesh file in STL format.

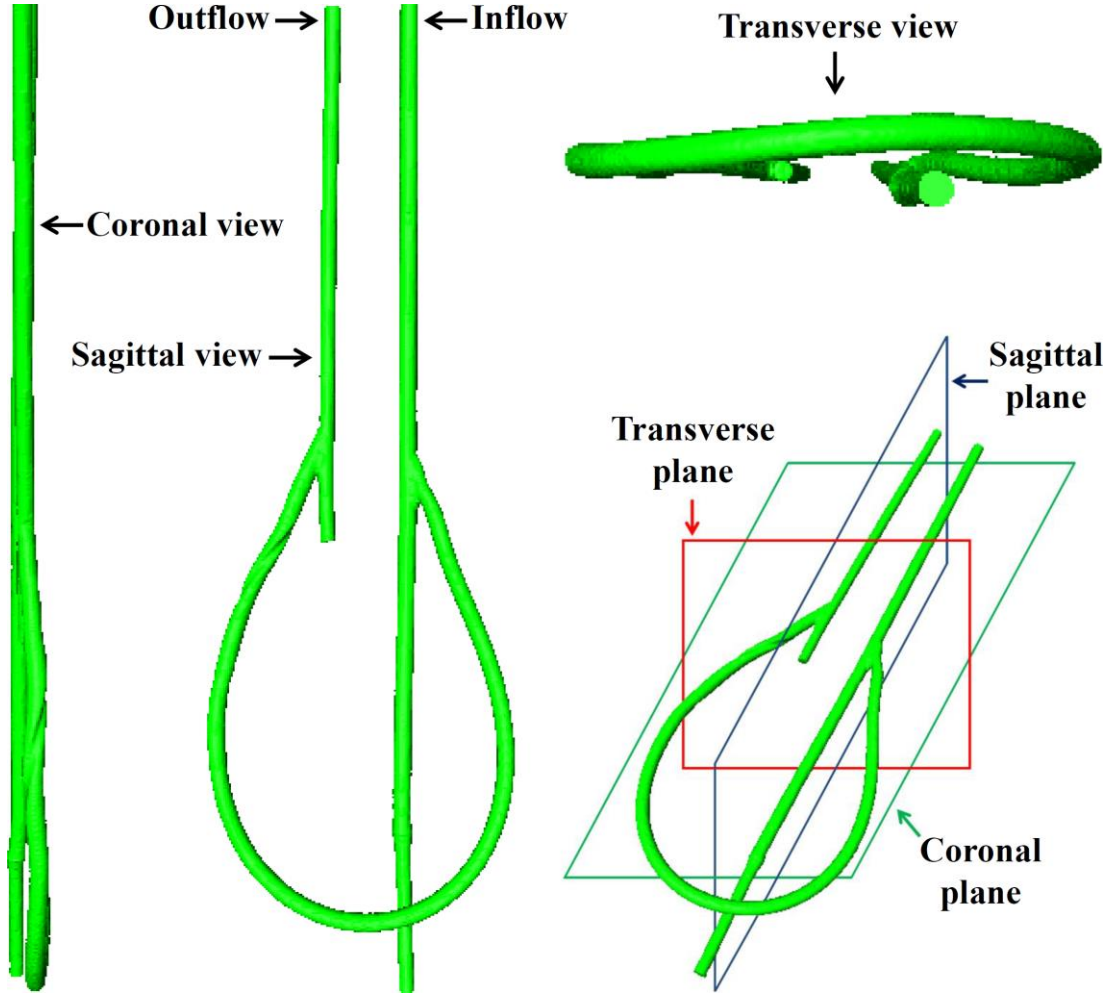

Figure 6.2: Extracted lumen geometry from the AV spiral vascular-graft model based on CT imaging data. The groove from the spiral ridge can be seen at the outflow of the graft.

6.2.3 Volume mesh

The STL files from the spiral and control model were loaded into ICEM CFX (ANSYS) to generate their volume meshes. In order to ensure a fine near wall flow simulation, each volume mesh was composed of 10 layers of prismatic cells at the wall boundary and tetrahedral cells at the centre (ANSYS 2011; Cheng et al. 2010; Cheng et al. 2013). The optimum number of mesh elements was determined by mesh independence tests. These tests were conducted using the maximum applied Reynolds number (Tan et al. 2008) and were based on the change in maximum velocity and maximum WSS in each model. Table 6.1 presents the results from the spiral model and Table 6.2 from the non-spiral model. The criteria for choosing the optimal volume mesh was to have less than 4%

difference in maximum velocity and maximum WSS from the previous and proceeding volume meshes (Cheng et al. 2010; Wood et al. 2006). Mesh number 2 was the optimum choice for both models.

Table 6.1: Mesh independence test results from the comparison of maximum WSS and maximum velocity between three different meshes of the spiral AV model.

Mesh number	Elements	Nodes	Maximum velocity (m s^{-1})	Difference (%)	Maximum WSS (Pa)	Difference (%)
1	4785142	1696337	0.521		5.963	
				0.687		0.778
2	6380181	2171275	0.525		5.917	
				0.521		3.049
3	8157805	2677537	0.522		5.742	

Table 6.2: Mesh independence test results from the comparison of maximum WSS and maximum velocity between three different meshes of the non-spiral AV model.

Mesh number	Elements	Nodes	Maximum velocity (m s^{-1})	Difference (%)	Maximum WSS (Pa)	Difference (%)
1	4347772	1539478	0.516		5.006	
				0.369		1.725
2	5836160	1978732	0.514		5.094	
				0.027		2.358
3	7437279	2439385	0.514		5.217	

Figure 6.3 shows examples from the tested volume meshes in

the cross-section view of the outflow of spiral and non-spiral models. Numbers 1 – 3 in Figure 6.3 correspond to mesh numbers 1 – 3 in Table 6.1 and Table 6.2. During the mesh optimisation, the only parameters that were changed from one volume mesh to a finer were the minimum and maximum size of elements, but their ratio was kept steady (minimum size / maximum size = 0.6) (ANSYS 2011). Therefore, for the increase of number of elements in a volume mesh the minimum and maximum size of elements were decreased proportionally, resulting in proportional decrease of all mesh elements as shown in Figure 6.3. The smallest elements were always the cells in the first prismatic layer at the wall boundary and the largest the tetrahedral cells in the core of the volume mesh.

The meshing settings of volume mesh numbers 1, 2 and 3 for the spiral model had identical parameters with the corresponding mesh numbers 1, 2 and 3 for the control model, thus allowing accurate computational comparison (Table 6.1, Table 6.2, Figure 6.3). Each volume mesh was smoothed using a conservative approach and then tested for integrity.

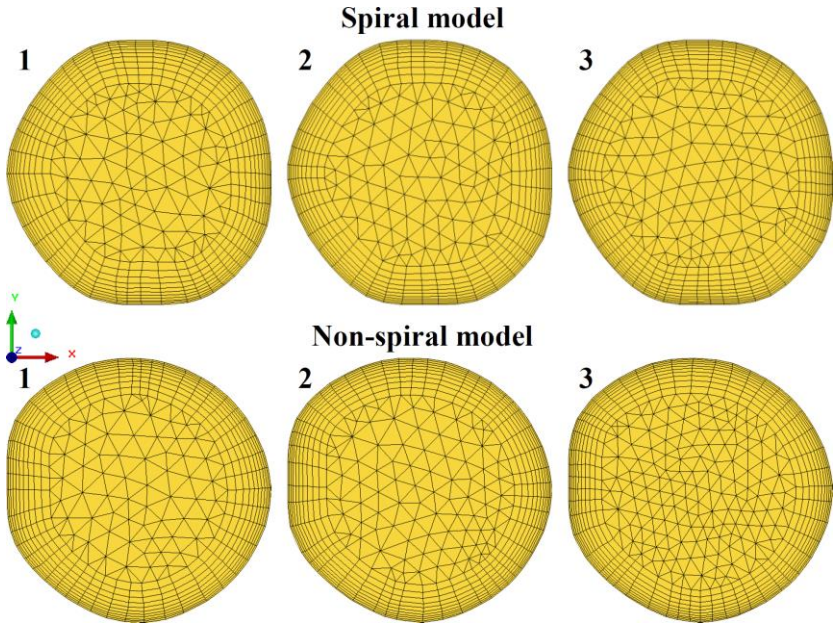

Figure 6.3: Cross-section view of the volume mesh in the outflow of the spiral and non-spiral model. Mesh numbers 1 – 3 correspond to mesh numbers 1 – 3 in Table 6.1 and Table 6.2.

6.2.4 Wall boundary layer thickness

For the boundary layer thickness calculation, the origin of the flow was assumed to be immediately after the outflow anastomosis, which was the beginning of the region of interest for this study and where the flow had to readapt itself. This assumed origin of flow lies at 0 mm of Figure 6.4. The wall boundary layer thickness was assessed in the cross-flow plane at 4 mm downstream from the assumed origin of flow as shown in Figure 6.4, using Equation 5.1 and Equation 5.2. The wall boundary layer thickness was 0.682 mm for the spiral model and 0.685 mm for the non-spiral model. Axial velocity profiles were extracted from the floor-toe and anterior-posterior perpendicular lines, which are shown in the bottom left diagram of Figure 6.4. The extracted axial velocity profiles are presented in Figure 6.5 for the spiral model and Figure 6.6 for the control

model. The agreement between the theoretical wall boundary layer thicknesses and those presented in Figure 6.5 and Figure 6.6, verifies the ability of the applied volume meshes to solve the flow field within the vascular-graft models.

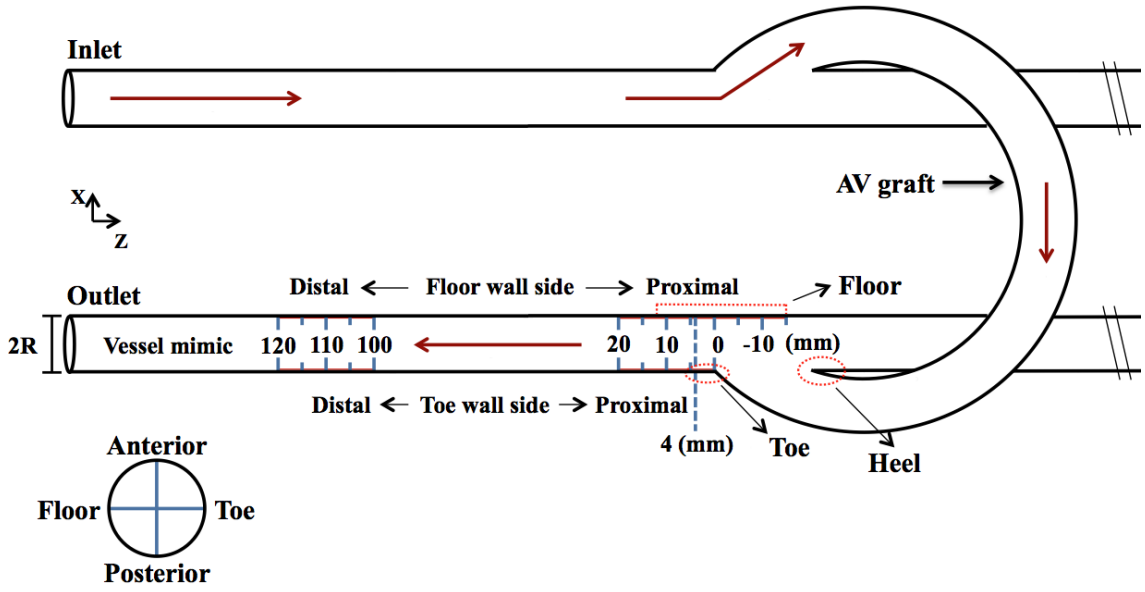

Figure 6.4: Top: schematic diagram of the AV vascular-graft model in looped configuration. The wall boundary layer thickness was tested in the cross-flow plane 4 mm downstream from the graft outflow. The measured regions downstream from the graft outflow (-15 to 20 and 100 to 120 mm) indicate locations where WSS was examined. Bottom left: schematic diagram of a cross-sectional view of the vessel mimic and the perpendicular line locations where the wall boundary layer thickness was tested.

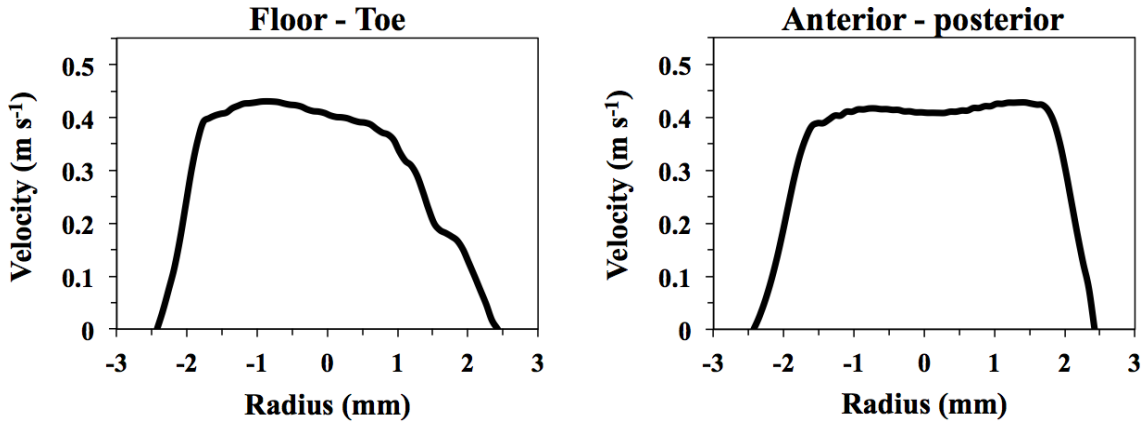

Figure 6.5: Axial velocity profiles from the spiral model in the cross-flow view 4 mm distal from the graft outflow as shown in Figure 6.4. The profile on the left is from the diametric line between the floor and toe wall sides of the vessel mimic; the profile on the right is from the diametric line between the anterior and posterior wall sides of the vessel mimic (Figure 6.4 left bottom diagram).

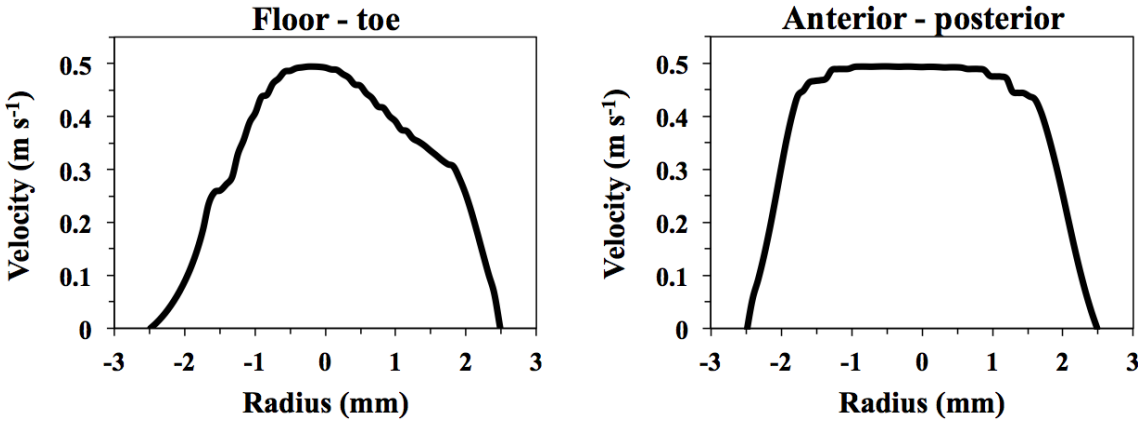

Figure 6.6: Axial velocity profiles from the control model in the cross-flow view 4 mm distal from the graft outflow as shown in Figure 6.4. The profile on the left is from the diametric line between the floor and toe wall sides of the vessel mimic; the profile on the right is from the diametric line between the anterior and posterior wall sides of the vessel mimic (Figure 6.4 left bottom diagram).

6.2.5 Model properties and boundary conditions

The physical parameters for the simulations of the AV vascular-graft models were the same to those described in the first paragraph of section 5.2.5 (page 114) for the PV models. Furthermore, these parameters simulated the experimental flow conditions that were applied in the AV models in chapter 4.

6.2.6 Analysis of results

The applied flow rates of 240 and 360 mL·min^{-1} produced Reynolds numbers of 600 and 900 respectively within the vessel mimic section. Reynolds numbers were calculated for cross-flow areas 0, 5 and 10 cm downstream of the vessel mimic anastomosis for both models and then averaged. Within each area, small variations in diameter and axial velocity resulted in small differences of the Reynolds numbers.

The flow patterns were examined in cross-flow planes 1, 2, 3, 4 and 5 which were located 0.1, 0.5, 2, 5 and 10 cm distal from the graft outflow of each AV vascular-graft model. These locations were the same as those examined in the experimental study (chapter 4), thus allowing for a comparison between the experimental and computational approaches. In each cross-flow plane of the spiral and control AV

models, the in-plane velocity, axial velocity and vorticity maps were extracted and the peak in-plane velocity and circulation were calculated.

The WSS was detected in the centreline of the floor and toe wall sides of both AV models, as presented in Figure 6.4. In the floor centreline the analysis included a region in the proximal (-15 to 20 mm) and a region in the distal (100 to 120 mm) graft outflow anastomosis. Similarly, proximal (0 to 20 mm) and distal (100 to 120 mm) toe centreline regions were analysed. The four regions tested from the spiral model were compared with the corresponding regions tested from the non-spiral model. It is believed that local haemodynamics play a significant role in development of neo-intimal hyperplasia and thrombosis in the outflow anastomosis of an AV graft and the first 2-5 cm distal from it (Haruguchi and Teraoka 2003), but also downstream in the host vein (Doelman et al. 2005).

Pressure drops were detected within the spiral and control AV models and then compared. More specifically, they were detected from the inlet of the grafts to the distal side of the vein mimic segments in cross-flow plane 5 (10 cm distal the anastomosis). The length of the grafted region was not identical for the spiral and control AV grafts, because of the 3D helical shape of the spiral inducer segment of the spiral device. Therefore, it was considered appropriate to calculate the pressure drop in relation to the length of the examined region as showed in Equation 5.3 (page 117).

The intensity of secondary flow phenomena in the outflow of both AV grafts was quantified by helicity (see Equation 5.5, page 117) (Grigioni et al. 2005; Hardman et al. 2013; Morbiducci et al, 2007; Zhan et al. 2010). The region tested for helicity included the vessel mimic volume from cross-flow plane 1 (0 cm) to cross-flow plane 5 (10 cm).

6.3 Results

If *w* is the axial component of velocity then in-plane velocity in this chapter is defined by the *v* and *u* velocity components and is the same as in-plane velocity v_{xy} in the experimental methodology. In the flow maps the orientation is such that the left and right sides are the floor and toe wall sides of the vessel mimic respectively, and the top

and bottom are the anterior and posterior wall sides respectively. This is the same orientation with that of the AV ultrasound chapter 4. The colour distribution in all flow maps is based on a scale from dark blue to dark red for the minimum to maximum value respectively. Vectors are used in in-plane velocity maps to show the direction of the vortices.

6.3.1 Comparison with flow maps from the experimental approach

A comparison of in-plane velocity between the CFD and vector Doppler results is illustrated in Figure 6.7 for both the spiral and control models. The comparison is from the first examined cross-flow plane at 0.1 mm distal from the anastomosis, where the flow had to readapt itself, and for peak CFD applied flow rate (360 mL·min^{-1}).

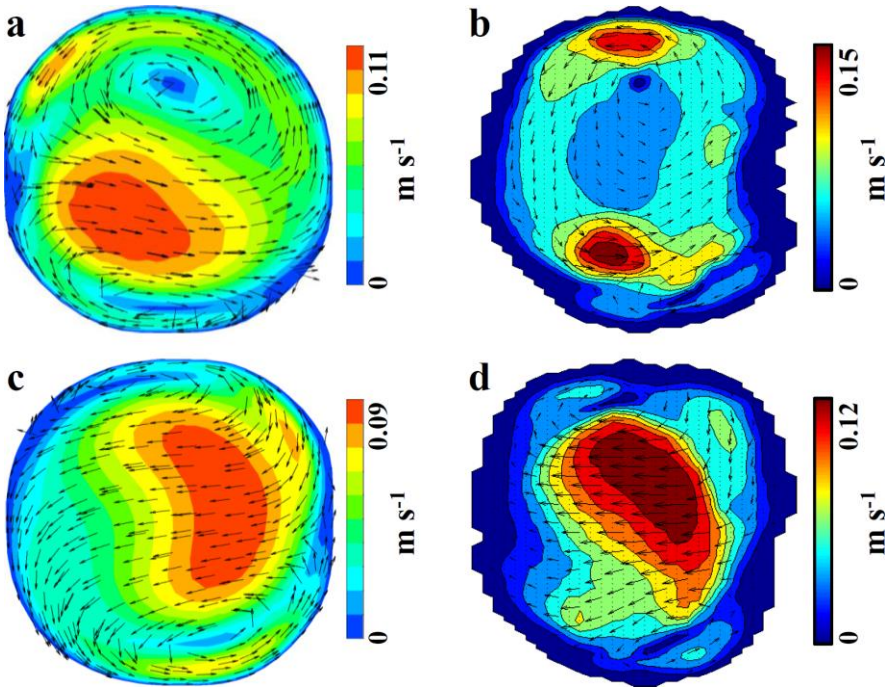

Figure 6.7: Comparison of in-plane velocity maps between CFD (left column) and vector Doppler (right column) for the looped spiral (a and b) and control (c and d) AV models. The wall sides of each map correspond to the anastomotic locations as: left = floor, right = toe, top = anterior, and bottom = posterior.

6.3.2 Flow maps in the outflow of spiral and control AV grafts

The progression of in-plane velocity, axial vorticity ω_Z and axial velocity maps from cross-flow plane 1 to 4, is demonstrated in Figure 6.8 - Figure 6.11 respectively. Each

figure shows results from both applied Reynolds numbers and both types of models to allow comparison. In vorticity maps a black contour line highlights regions of zero vorticity that separate the regions of positive and negative vorticity.

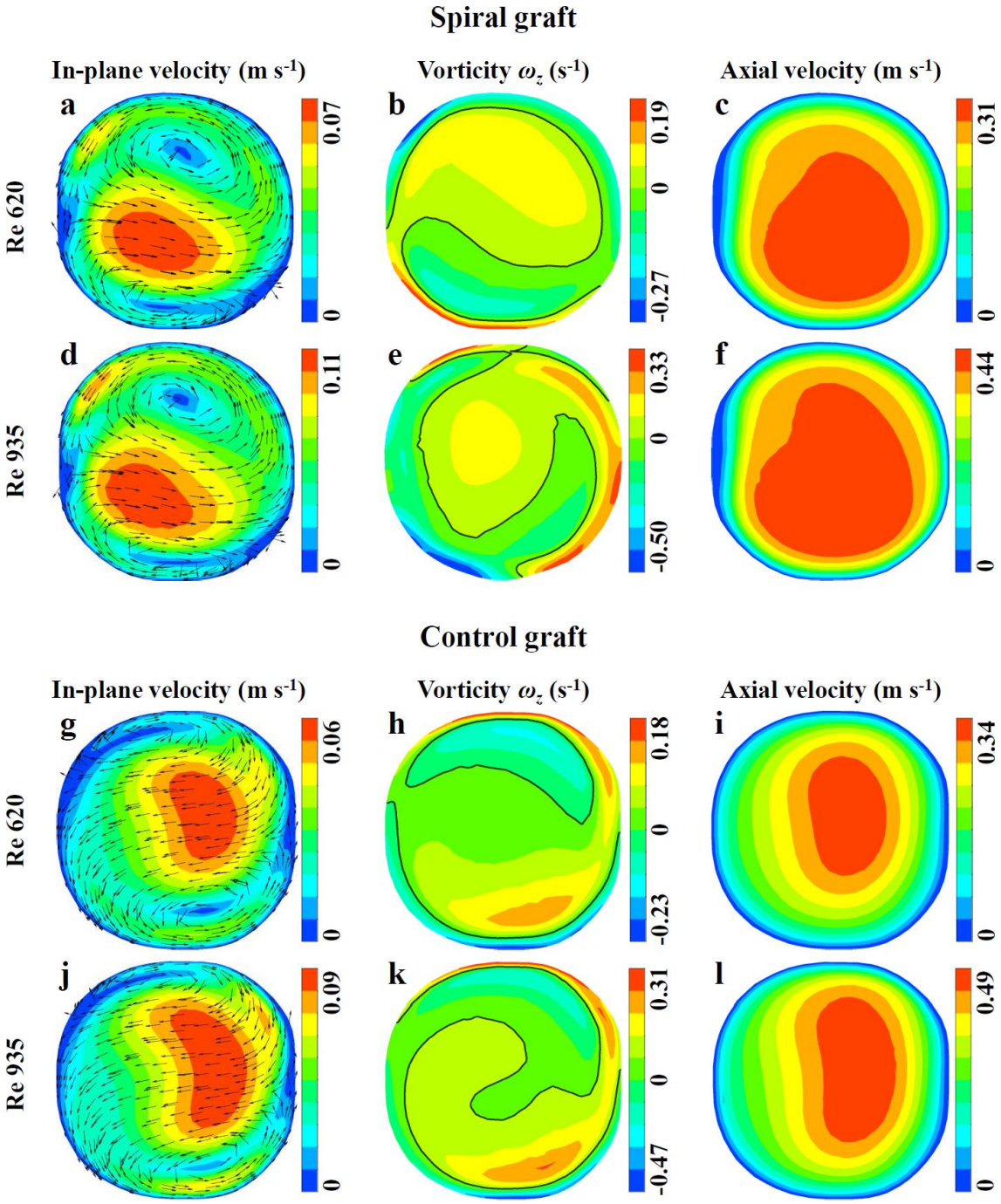

Figure 6.8: In-plane velocity, axial vorticity ω_z and axial velocity from the looped spiral and control AV models in cross-flow plane 1. The zero vorticity contour line is coloured black. The orientation of each map in relation to the anastomotic locations is: left side = floor and right side = toe.

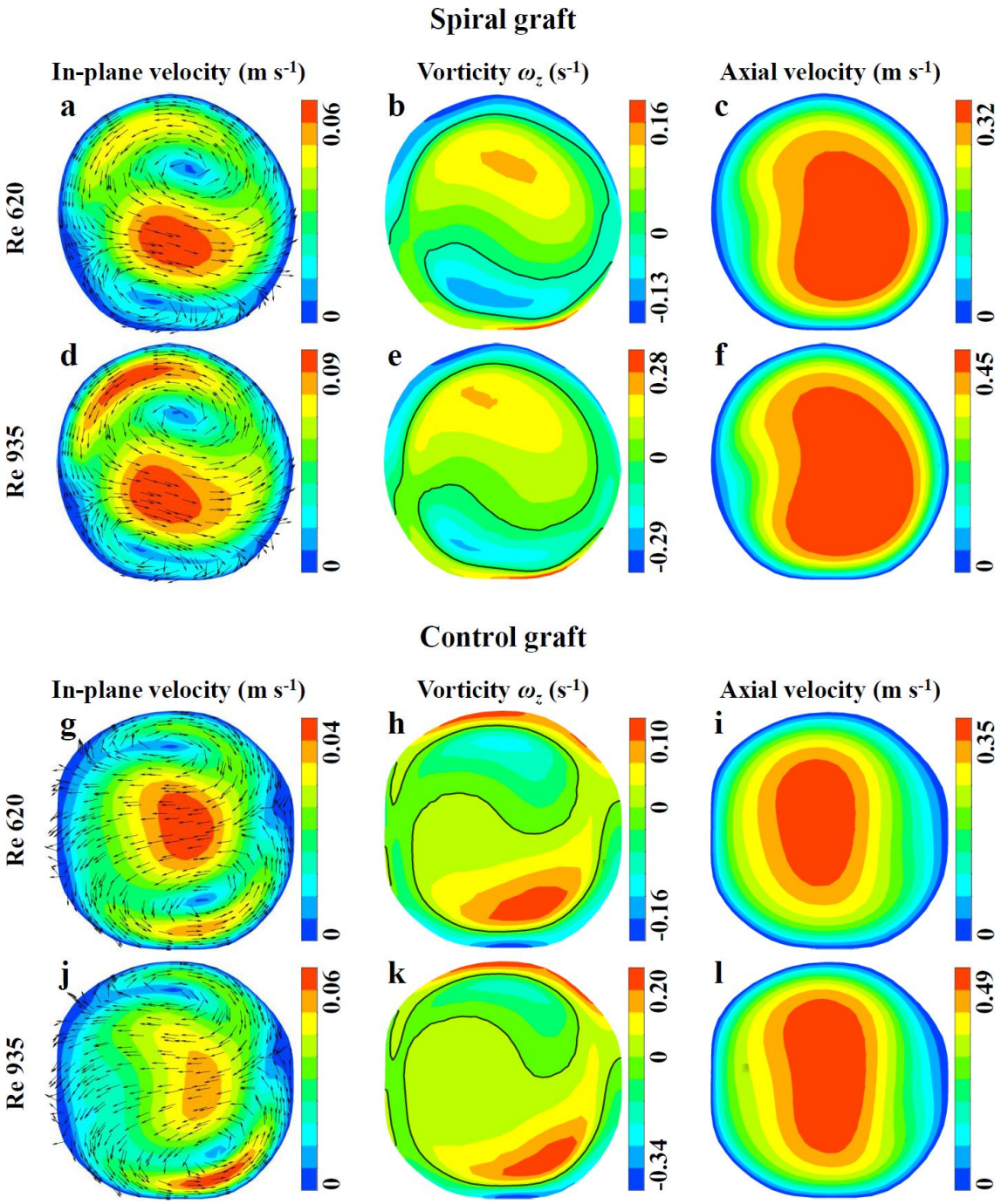

Figure 6.9: In-plane velocity, axial vorticity ω_z and axial velocity from the looped spiral and control AV models in cross-flow plane 2. The zero vorticity contour line is coloured black. The orientation of each map in relation to the anastomotic locations is: left side = floor and right side = toe.

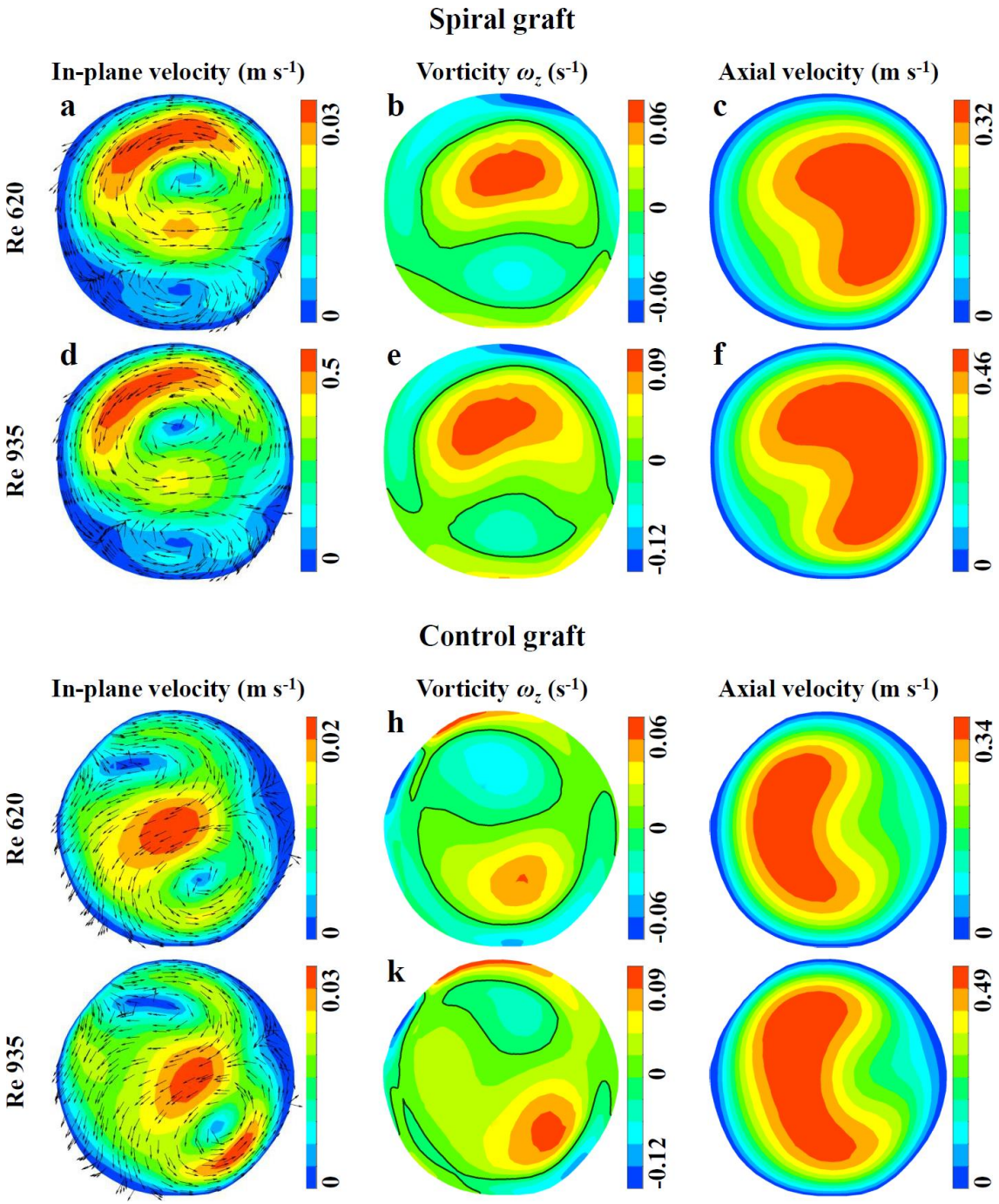

Figure 6.10: In-plane velocity, axial vorticity ω_z and axial velocity from the looped spiral and control AV models in cross-flow plane 3. The zero vorticity contour line is coloured black. The orientation of each map in relation to the anastomotic locations is: left side = floor and right side = toe.

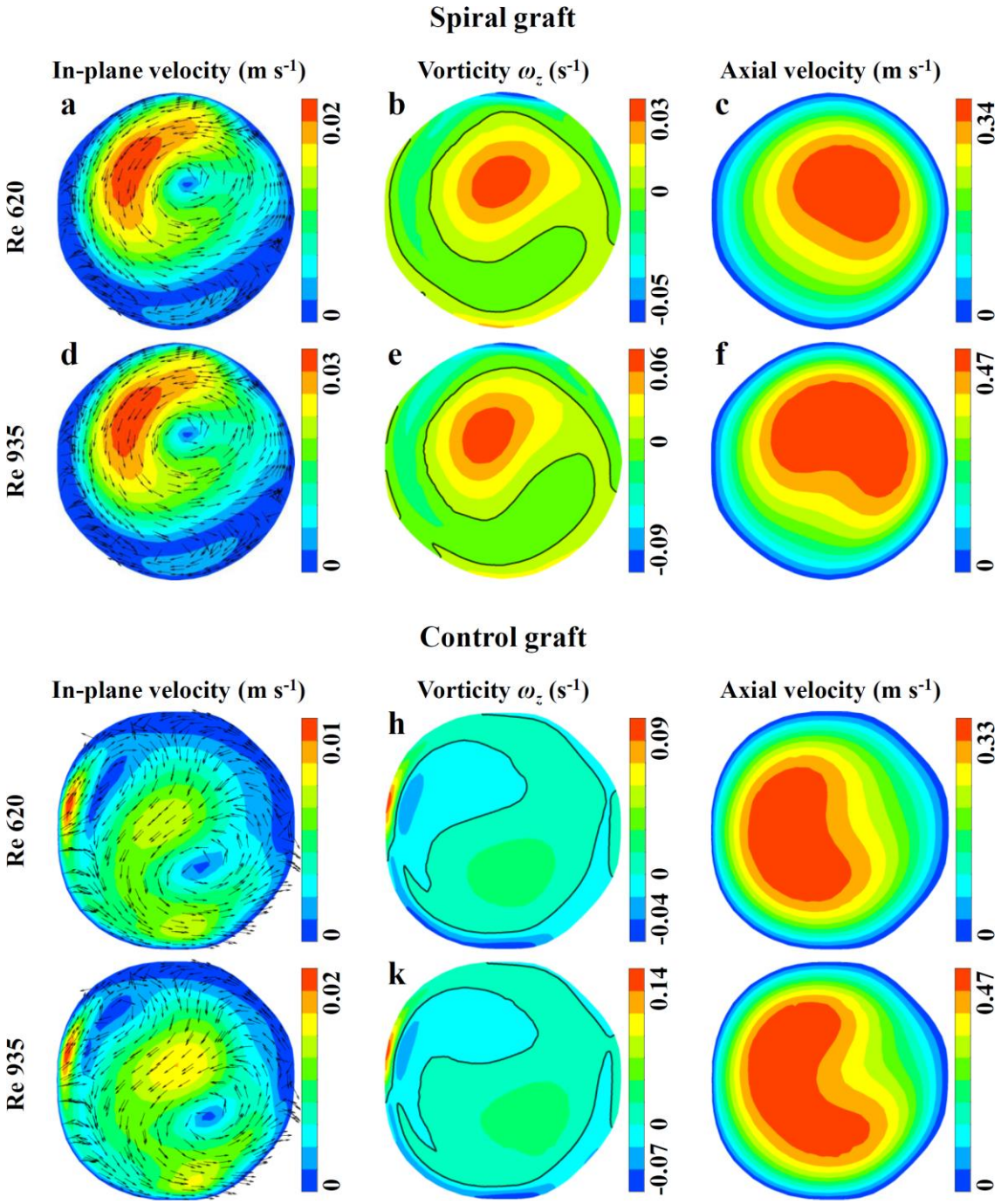

Figure 6.11: In-plane velocity, axial vorticity ω_z and axial velocity from the looped spiral and control AV models in cross-flow plane 4. The zero vorticity contour line is coloured black. The orientation of each map in relation to the anastomotic locations is: left side = floor and right side = toe.

6.3.3 Quantitative results

Figure 6.12 shows the progression of peak in-plane velocity and circulation, from cross-flow plane 1 to 5, for the spiral and control models. Both in-plane velocity and circulation were constantly higher for the spiral vascular-graft model.

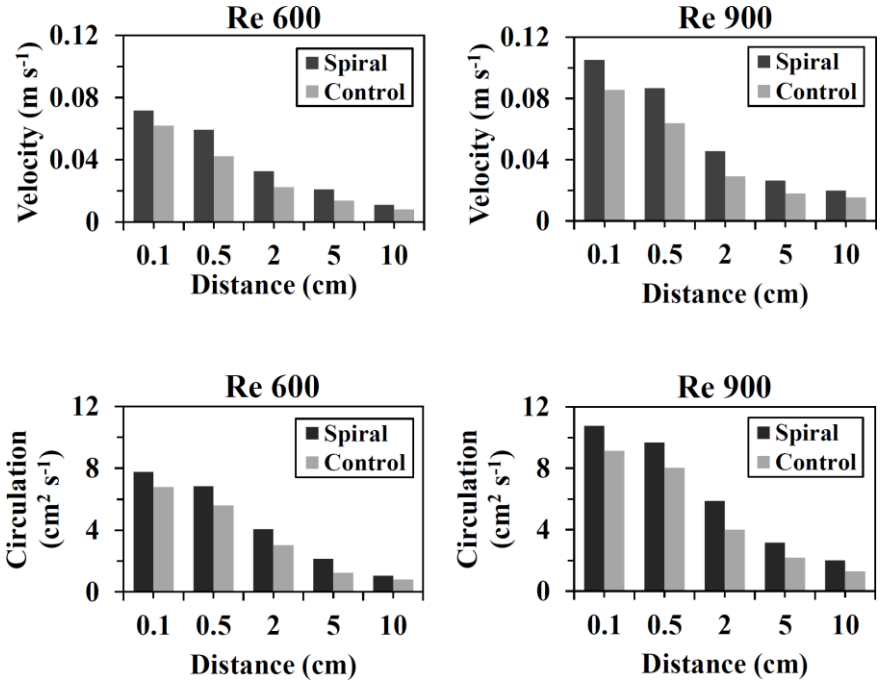

Figure 6.12: Progression of peak in-plane velocity (first row) and circulation (second row) of the spiral and control looped AV models. The distance corresponds to cross-flow planes downstream from the outflow anastomosis.

Figure 6.13 presents a comparison of helicity in the volume between cross flow plane 1 and 5 and pressure drop from the inlet of each graft to plane 5, for both applied Reynolds numbers. Increased values were found for the spiral model in all cases.

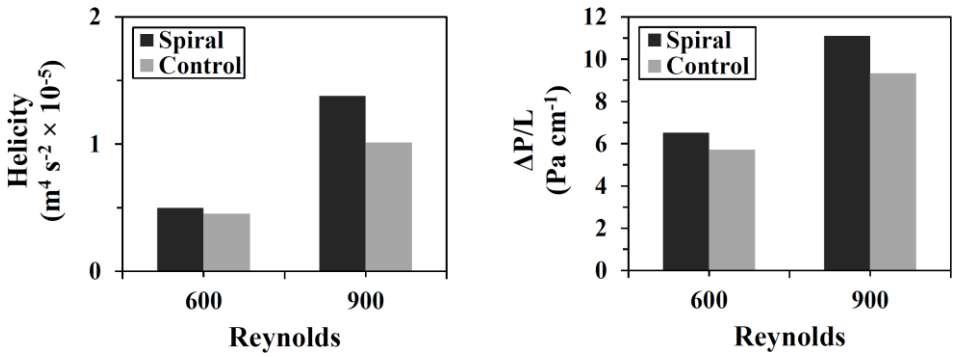

Figure 6.13: Comparison of helicity in the volume between cross-flow plane 1 and 5, and pressure drop over length from the graft inlet to plane 5, for both types of looped AV models, under both applied Reynolds numbers.

The results from WSS comparisons at the centreline of the proximal and distal floor and toe wall sides are shown in Figure 6.14, for Reynolds number 900. Polylines were used to show the averaged progression of each trend, due to increased fluctuations related to the surface of the walls.

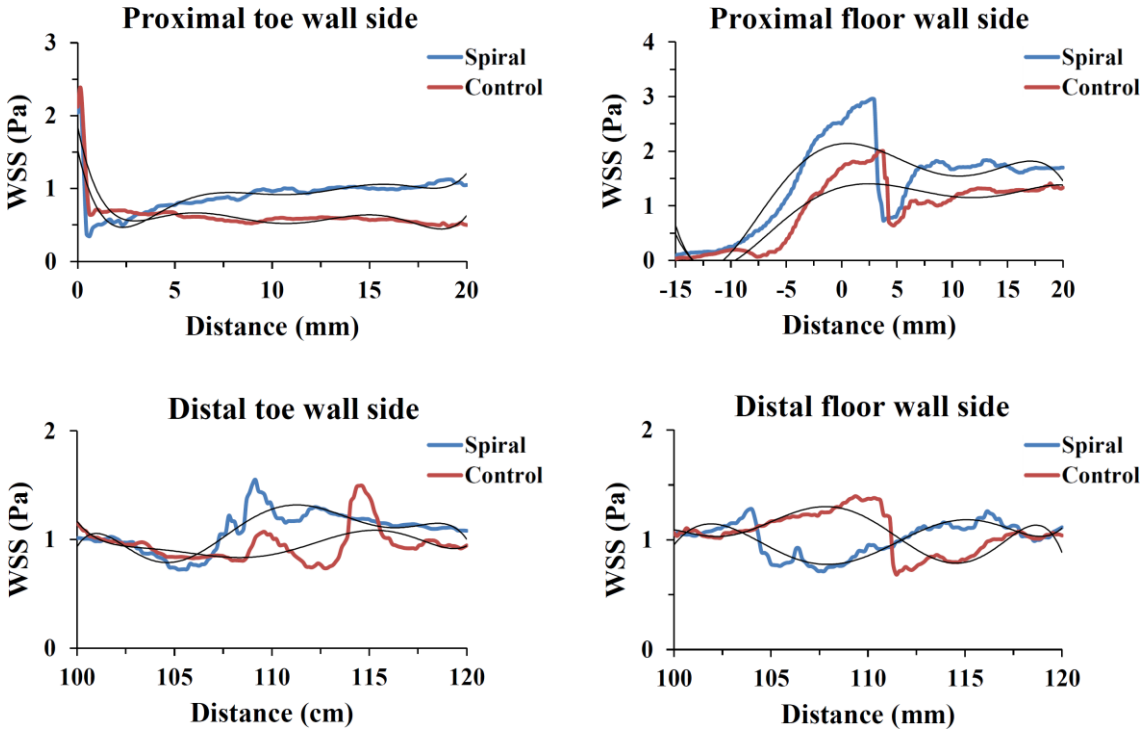

Figure 6.14: Wall shear stress at the four examined locations of the venous mimic for both types of looped AV grafts, for Reynolds number 900. Polylines are used to show the averaged profile of each trend and increase the clarification of the charts.

6.4 Discussion

The applied flow rates were 240 and 360 mL·min^{-1} to mimic the related flow conditions in the experimental work. The resulted Reynolds numbers within the host venous mimic were 600 and 900 respectively. The corresponding estimated Reynolds numbers in the flow phantoms were 570 and 850. This difference is mainly associated with the decreased lumen diameter in the computational models. The actual diameter of the PVA-c venous mimic was 5.4 mm (section 2.2.2, page 36), while that of the volume mesh in this region was 5 mm. This decrease was related to CT scanning, and surface rendering with Amira. The corresponding Reynolds numbers in the numerical PV grafts study (chapter 5) were 620 and 940. This difference was based on the slightly smaller axial velocities, which were detected in the examined cross-flow planes for the AV models. More specifically, during the AV simulations the average axial velocity at these planes was 0.008 m·s^{-1} slower at flow rate 240 mL·min^{-1} and 0.013 m·s^{-1} slower at flow rate 360 mL·min^{-1}, in comparison to the PV simulations. The average diameter of the examined cross-flow planes was almost identical between the PV and AV models.

Figure 6.7 revealed similar flow patterns between the computational and experimental in-plane velocity maps. The double-spiral flow seen for the spiral model, consisted of a dominant recirculating cell and a smaller spiral near the posterior wall. A double-spiral flow was also seen for the control model with the centres of the spirals near to the posterior and anterior walls. There was good agreement on the number of vortices, location of their centres and flow direction between the experimental and computational approaches, although there were differences in the gradient and peak values of velocity. The reasons for these differences are described in section 7.9, page 175.

Two spirals were detected in all cross-flow planes and for both Reynolds numbers downstream from the outflow of the spiral AV graft (Figure 6.8 - Figure 6.11). These vortical structures were composed of a dominant recirculation cell and a second smaller vortex near the posterior wall of the maps. The small spiral decreased in size from cross-flow plane 1 to 4 where it had almost dissipated, whilst the main spiral increased through these planes and its centre moved closer to the centre of the lumen. The existence of two spirals resulted in stagnation points at the floor and toe wall sides of

planes 1 - 3. A greater region of low near wall in-plane velocity was seen in plane 4. In comparison the relevant experimental vortical structures were very similar in planes 1 - 3 (Figure 4.3 - Figure 4.5), whilst in plane 4 the second spiral had totally dissipated but it was still present in the computational simulation (Figure 4.6). In relation to the axial velocity maps of the spiral AV model in this chapter, a large bulk was seen in the centre of the lumen in planes 1 and 2, and crescent structures in plane 3. In plane 4 there was a circular formation for low Reynolds numbers and a crescent formation for high Reynolds numbers. The dissipation of the crescent formations in the axial velocity maps in plane 4 indicated low intensity of the rotational phenomena.

A double-spiral flow was detected for both Reynolds numbers and all cross-flow planes in the outflow of the control AV graft (Figure 6.8 - Figure 6.11). In planes 1 and 2 the size of the spirals was similar, showing symmetric flow between the top and bottom semicircles of the maps. Between planes 3 and 4 the spiral axes of rotation was translated in a counter clockwise direction. The double spiral resulted in stagnation points at the floor and toe walls in planes 1 and 2, and toe wall in plane 3. A greater region of low near wall in-plane velocity was observed in plane 4. In comparison, a double-spiral pattern was also detected for the experimental control AV model as discussed in chapter 4; nevertheless, the experimental in-plane velocity maps revealed symmetric Dean flow for all planes at low Reynolds numbers and not only in planes 1 and 2 as in the computational results. In relation to the axial velocity maps of the control AV model in this chapter, a centralised oval shape was presented in planes 1 and 2 and crescent formations in planes 3 and 4.

The core of each vortex was clearly identified with the axial vorticity maps (Figure 6.8 - Figure 6.11). The regions of counter vorticity near the wall were related to shearing forces of the fluid particles due to the non-slip wall boundary conditions (Cookson et al. 2009; Yamamoto et al. 2002; Zabielski and Mestel 1998).

The presented flow maps were from cross-flow planes 1 - 4 to allow comparison with the corresponding experimental data (Figure 4.3 - Figure 4.6). Flow maps from plane 5 were not presented because the secondary flow phenomena had dissipated, showing no recirculation cell in the in-plane velocity maps and centralised circular structures in the axial velocity maps for both the spiral and control models. Although plane 5 was

included in the quantitative CFD data, in order to show the distal propagation and decline of rotational phenomena.

The magnitudes of peak in-plane velocity and circulation were constantly higher for the spiral model (Figure 6.12). The difference between the two models increased with increasing Reynolds number and decreased with increasing distance from the anastomosis. These trends agreed with the corresponding results from the vector Doppler quantitative analysis (Figure 4.7 and Figure 4.9).

The magnitude of helicity was also higher for the spiral graft outflow in comparison to the control graft outflow and their difference increased for Reynolds number 900 (Figure 6.13).

The increased in-plane velocity, circulation and helicity in the outflow of the spiral prosthesis indicated enhanced secondary flow motions and increased in-plane mixing in relation to the control comparator. In-plane mixing in the outflow of an AV graft has been noted to protect endothelial behaviour and restrict the development of neo-intimal hyperplasia and thrombosis (Caro et al. 2005; Huijbregts et al. 2007).

Figure 6.13 showed increased pressure losses for the spiral model. The difference between the two grafts increased with increasing Reynolds numbers. For instance this difference was 2 Pa for Reynolds number 900. The physiologic mean arterial pressure in the upper extremities, relative to atmospheric pressure, varies from 80-90 mmHg in the shoulder to 80-130 mmHg in the hand in upright position (Caro et al. 2012). Pressure of 2 Pa is equal to 0.015 mmHg. This implies that the difference between the control and spiral models was negligible. Excessive pressure loss in medical applications results in reduced blood circulation and therefore is not desirable (Cookson et al. 2009; Cookson et al. 2010).

The WSS was examined in the floor and toe wall centrelines because neo-intimal hyperplasia is primarily developed in these regions of an AV graft outflow anastomosis (Haruguchi and Teraoka 2003). The WSS in the proximal toe and floor regions was higher by about 0.5 and $0.5 - 1$ Pa respectively, for the spiral model (Figure 6.14). There was no clear difference in the distal floor and toe wall comparisons. It is believed that atherosclerotic lesions in physiologic vessels are mainly developed in regions of

low and oscillating WSS (Cecchi et al. 2011; Ridger et al. 2008). The presented WSS results were from Reynolds number 900. The WSS results from Reynolds number 600 were lesser in magnitude than those of Reynolds number 900; however the overall trends in both cases were almost identical and it was considered unnecessary to present WSS data from both Reynolds numbers.

The flow patterns in planes 1 - 3 showed stagnation points at the floor and toe sides of both grafts, as a result of double helix in their outflows. The double-spiral in the outflow of the control model was associated with decreased quantitative data in comparison to the spiral model. It was symmetric in its position between the floor and toe centreline, which may explain the reduced WSS. The double-spiral in the outflow of the spiral device was related to a dominant helix and a secondary smaller recirculation. It was associated with enhanced secondary flow motions and disrupted the floor-toe axis of symmetry, which may explain the increased WSS. The dominant recirculation in the outflow of the spiral model, occupies the biggest part of the lumen. It can be hypothesised that this protects a significant part of the vessel wall and may result in improved patency rates.

6.5 Conclusions

A double-spiral flow pattern, symmetric in its position between the floor and toe centreline, was detected in the proximal non-spiral, planar graft outflow and a non-symmetric double-spiral flow pattern in its distal outflow. A dominant and a secondary smaller spiral were observed in the outflow of the spiral, non-planar graft showing reduced flow separation. Stagnation points were seen at the floor and toe walls of both host venous mimics as a result of the existence of the two spirals. The flow maps were in good agreement with the relevant experimental maps in the proximal graft outflows, but differences were found in the distal graft outflows.

The quantitative comparisons of peak in-plane velocity, circulation and helicity showed increased values for the spiral prosthesis, indicating stronger secondary flow phenomena and in-plane mixing. These trends of in-plane velocity and circulation, verified those detected in the ultrasound study. High WSS, which is believed

atheroprotective in normal vessels, was found in the outflow of the spiral graft. Pressure drop was higher within the spiral model but its difference from the non-spiral was negligible.

The ability of the spiral AV graft to induce enhanced secondary flow motions may protect the host from neo-intimal hyperplasia and thrombosis and could result in increased patency rates.

Chapter 7

Discussing the experimental and computational assessments on vascular grafts

7.1 Introduction

The vortical structures induces by spiral and non-spiral PV and AV clinical grafts were assessed experimentally in chapters 3 and 4 and computationally in chapters 5 and 6 respectively. The aim of this chapter is to link these experimental and/or computational chapters and to discuss the challenges and limitations experienced whilst performing this work.

7.2 Flow waveforms

The results presented were based in steady flow waveforms. The physiologic flow waveforms are pulsatile. In the case of a PV graft in the lower extremities, intense flow fluctuation with reverse flow during part of the diastolic cardiac phase is observed (e.g. from 1700 $mL \cdot min^{-1}$ to -800 $mL \cdot min^{-1}$ in the distal superficial femoral artery). In the case of an AV graft in the upper extremities, moderate flow fluctuations are observed (e.g. from 850 to 1200 $mL \cdot min^{-1}$ in a successful proximal AV graft outflow) (Armstrong and Bandyk 2010; Lee et al. 2005). The blood's pulsatile flow affects the formation of vortical structures and consequently the formation of neo-intimal hyperplasia and

thrombosis in vessels. A pulsatile flow field is complex and difficult to understand so the prior examination of steady flow is common practice in experimental and numerical vascular flow studies (Blake 2008; Siggers and Waters 2005, 2008; Varghese et al. 2007a, 2007b).

The application of physiologic waveforms in the developed flow phantoms was not possible because the pulsation produced abnormal expansion of the vessel mimicking tubing and waveform damping. A pulsatile simulation requires a solid TMM to prevent excessive wall motions of the vessel mimic. Such phantoms can be manufactured based on agar or konjac and carrageenan gels (Dineley et al. 2006; Meagher et al. 2007).

7.3 Geometry of the vascular-graft models

The vascular-graft models were developed with ideal geometries. More specifically, the models were planar in order to standardise the flow field, with the exception of the spiral ridge segment of the spiral grafts which was non-planar. There was no bi-directional run-off in the host mimic vessels, which is a common physiologic situation. The graft-vessel mimic anastomoses were finalised after a number of tries and under directions from consultant vascular surgeons, to ensure their quality and similarity with clinical practice. During the experimentation it became clear that the quality of the anastomosis and the graft position affected the vortical structures in their outflow. These could be critical factors in patients where the anastomosis can vary from surgeon to surgeon and the position of the graft in the body is not standardised. The effect of graft position is hard to control and could be either beneficial or detrimental to the quality of induced secondary flow motions in the outflow of both spiral and conventional grafts.

The number of spirals, or flow separation, and the related stagnation points in a cross-flow plane, were increased for the spiral and non-spiral AV graft models in comparison to their corresponding PV graft models. Moreover, the quantitative data from the AV models showed decreased magnitude in comparison to the relevant PV models. It can be postulated that the complexity of secondary flow motions in the outflow of the AV grafts was associated with the complicated geometry of their models. This supports the

belief that the secondary flow motions in the host vessel are influenced by the graft geometry.

7.4 Vorticity, circulation and colour Doppler

Vorticity maps were successfully generated from conventional colour Doppler data, to visualise the shearing phenomena in 2D cross-flow planes of vascular graft run-offs. This study was the first to calculate whole area vorticity from conventional colour Doppler data. A similar approach was presented by Mehregan et al. (2014) to quantify the formation of intraventricular eddies during left ventricular filling. They proposed a core vorticity technique where the centre of each vortex was colour mapped in red and blue hues in relation to vortex direction. Vorticity maps provide further understanding of helical flow fields in vessels and an option to quantify these fields using parameters from fluid dynamics such as circulation.

Circulation was computed from the area integral of each vorticity map. The area of a vorticity map, which was based on the corresponding areas of the left and right steered colour Doppler images, can be affected by settings such as the PRF, gain and wall filter. Potential overestimation or underestimation of the area of the examined flow can induce errors in the calculated circulation highlighting the strong operator dependence of colour Doppler. It is important that velocity information is recorded from the actual flow region and not the surrounding vessel or vessel mimic wall.

7.5 Computational prediction of wall shear stress

The WSS trends in chapters 5 and 6 showed increase fluctuation of the WSS magnitude across the examined wall boundary locations. This was related to the wall surfaces which were not totally smooth due to the acquisition of the lumen geometries by an image-guided approach. Similar WSS analyses in geometries made with CAD software resulted in volume mesh with a smooth external surface capable of producing WSS

trends free of such fluctuations across the wall boundary (O'Brien et al. 2005; O'Callaghan et al. 2006; Paul and Larman 2009).

The magnitude of WSS in vessels is affected by their diameter and geometry. Non-planarity, bending and branching produce secondary flow motions that induce WSS gradients. In addition, the pulsatile blood flow introduces WSS oscillation. Table 7.1 provides an indication of the magnitude of WSS in vessels assuming Hagen-Poiseuille flow (Caro et al. 2012). The WSS measurements performed in this project showed either increased magnitudes for spiral models or similar magnitudes between spiral and non-spiral models. In the first case the differences were in the range of 0.5-1 Pa. Based on the WSS indications of Table 7.1 it can be noted that the WSS differences in this work were significant. Increased WSS is commonly considered atheroprotective, which supports the haemodynamic advantage of a spiral graft. However, the exact clinical impact of increased WSS in the outflow of spiral grafts would require further studies in relation to WSS oscillations and gradients. The mechanism between WSS and venous endothelial behaviour in an AV graft outflow may be more complicated than that in a bypass PV graft outflow, because the host vein is subjected in abnormally high flow rates.

Table 7.1: Wall shear stress for blood vessels assuming parabolic flow.

Vessel	WSS (Pa)
Ascending aorta	0.43
Abdominal aorta	0.53
Femoral artery	0.80
Arteriole	4.8
Capillary	3.7
Venule	3.0
Inferior vena cava	0.64
Main pulmonary artery	0.28

7.6 Computational prediction of pressure drop

The pressure drop in a tube with flow rate Q, length L, dynamic viscosity μ, and radius r can be described by Equation 7.1 (Nichols and O'Rourke 2005).

$$\Delta P = \frac{8L\mu Q}{\pi r^4} \quad \textbf{7.1}$$

In the comparisons between spiral and non-spiral vascular graft models the dynamic viscosity and flow rates were steady. The length and radius were generally the same apart from the distal end of the grafts which varied due to the spiral inducer segment of the spiral device. The spiral ridge created a 3D helical shape that increased the length of the spiral graft. Additionally, the spiral ridge decreased the inside diameter or radius of the lumen. Equation 7.1 shows that the length *L* is proportional and the radius *r* is inversely proportional to pressure drop, explaining the increased pressure drop in the outflow of the spiral grafts.

The pressure drop in the PV spiral models decreased with increasing angle (θ) of anastomosis (Figure 5.23). The same trend was observed for the parameters of in-plane velocity (Figure 5.20), circulation (Figure 5.21) and helicity (Figure 5.22) which show the intensity of secondary flow motions. This indicates that the pressure drop was reduced with a reduction in the intensity of spiral flow. Cookson et al. (2009) have reported that the pressure drop in helical tubes is proportional to an increase in helical radius, due to the relevant increase in the length of the tube and the energy required to drive the stronger vortical structures. The latter observation from Cookson et al. (2009) may explain the relationship between pressure loss and intensity of spiral flow in this study.

7.7 Flow maps

The flow maps between the spiral and corresponding control grafts were not scaled based on a common peak value. In many cases, particularly of the velocity magnitude maps, the peak value from the spiral graft was significantly higher than that of the non-spiral. Such a scale would restrict the illustration of the flow gradient and the characteristics of secondary flow motions, which was the main aim of the flow maps.

7.8 Mixing and wall shear stress in vessels

WSS is defined as the viscous drag of blood on the arterial wall and is known to be an important parameter in the formation of atherosclerlsosis, neo-intimal hyperplasia and thrombosis in native and implanted vessels (Caro 2009; Caro et al. 1969; Keynton et al. 2001; Wentzel et al. 2001). It is commonly believed that regions of the vessels subjected to low and oscillatory WSS are associated with the development of the aforementioned diseases, while high WSS with reduced oscillatory index and gradient is considered atheroprotective (Caro 2009; Cecchi et al. 2011; Ridger et al. 2008; Slager et al., 2005; Slager et al. 2005). Nevertheless, a recent review on the relation of atherosclerosis and low/oscillatory WSS noted that this theory is less robust than widely assumed, suggesting that long-term *in-vivo* studies are required to improve our understanding of the blood flow impact on atherogenesis (Peiffer et al. 2013).

The relationship between WSS and flow mixing with spiral flow has been studied by several authors. In 1996 Caro et al. found that single-spiral flow is associated with a uniform near-wall velocity gradient leading him to hypothesise that this induces uniform wall shear and greater mixing. Ten years later Caro et al. (2005) presented experimental and computational results that supported his hypothesis. The increased in-plane mixing, as a result of helical flow, was verified with numerical flow simulations by Cookson et al. (2009). Zhan et al. (2010) showed that single-spiral flow generates less platelets adhesion to the inner surface of a tube in comparison to parabolic flow, due to increased WSS and in-plane mixing. They concluded that single-spiral flow in small-caliber arterial grafts has no adverse affect on platelet activation and may suppress the formation of acute thrombus and improve patency rates. In 2008 Zhang et al. compared a spiral vascular graft and a conventional vascular graft using CFD. The grafts were examined in a straight configuration with no host vessels connected in their proximal and distal ends. Single-spiral flow was found in the former and Hagen-Poiseuille flow in the latter prosthesis. The single helical flow was related to highly increased wall shear rate and near-wall velocity. The authors speculated that single helical flow could reduce neo-intimal hyperplasia and acute thrombus formation and thereby improve graft patency. Paul and Larman (2009) compared single-spiral and parabolic flow in the post-stenotic region of a stenosed model using CFD and found

increased longitudinal and perpendicular velocity for the spiral flow. Moreover the turbulent kinetic energy was decreased for the single-spiral and a rotational stability was induced in the forward flow. The relation of single-spiral flow with reduced turbulence and flow coherence in a stenosed conduit was also noted by Stonebridge et al. (2004). Increased turbulent kinetic energy in a post-stenotic region is considered detrimental for endothelial function (Ku 1997).

The non-planarity in a curved tube or curved like geometries, such as an end-to-side anastomosis, can significantly influence the flow. The torsion of a non-planar tube breaks the symmetric Dean vortex profile, which is observed in a planar curved geometry, by making either one of the two vortices more dominant or by completely obliterating one of the vortices (Doorly and Sherwin 2009; Zabielski and Mestel 1998).

Planar and non-planar anastomotic models have been previously studied with experimental (based on MRI imaging) and computational methods using low Reynolds numbers (< 570) by Doorly et al. (2002), Papaharilaou et al. (2002) and Sherwin et al. (2000). These models, which were similar to the conventional and spiral graft models discussed in this thesis, exhibited Dean flow in the outflow of the planar model, related to a centreline plane of symmetry and stagnation points in the toe and floor wall sides as shown in Figure 7.1. Two recirculation cells were reported in the proximal outflow of the non-planar model composed of a dominant and a second smaller spiral. In the distal outflow they were coalesced into a single recirculation. Their work supported the belief that a non-planar helical graft may break the potential symmetric flow, reduce stagnation points and increase flow mixing. In addition, they presented results of reduced WSS magnitudes and oscillations for the non-planar geometry in the floor of end-to-side anastomoses, to support their hypothesis that increased and oscillatory WSS at this location, where the blood impinges abnormally at the wall of the host vessel, may be detrimental for the endothelium.

The results by Doorly et al. (2002), Papaharilaou et al. (2002) and Sherwin et al. (2000) about flow patterns, separation, stagnation and mixing in the outflow of non-planar and planar anastomosis, were in agreement with the experimental and computational results from the spiral and non-spiral vascular-graft models in this project for Reynolds

numbers smaller than 1000. On the contrary, their results regarding WSS at the floor of the anastomosis contradicted those found in this study.

The experimental and computational results showed that spiral grafts were able to induce single-spiral or double-spiral flow that consisted of a dominant and a secondary small spiral. These patterns were related to increased flow mixing, WSS and reduced flow separation and stagnation when compared to flow patterns from non-spiral grafts. These results, and the studies of the aforementioned paragraphs, support the hypothesis that spiral grafts may protect from neo-intimal hyperplasia in the anastomosis and development of stenosis downstream the vascular tree.

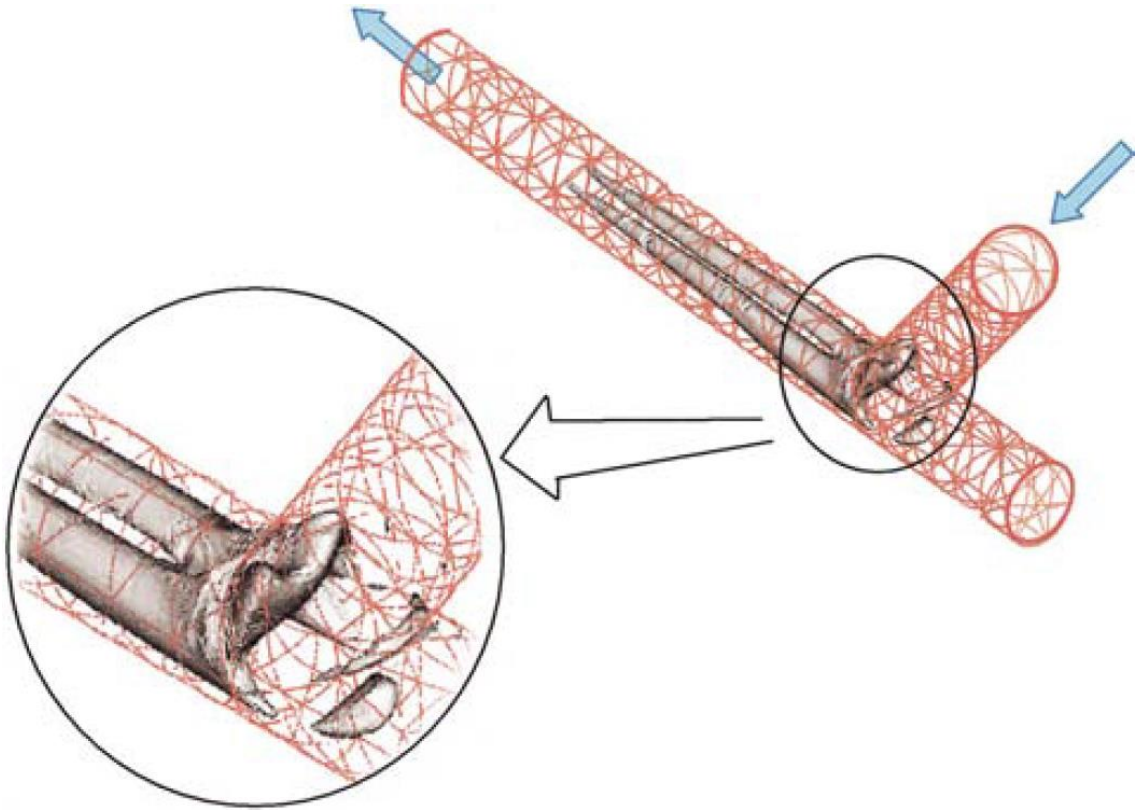

Figure 7.1: Dean flow structure in a planar anastomotic model using steady flow at Re 250. A centreline plane of symmetry and stagnation points in the toe and floor wall sides can be seen [republished with permission of Taylor & Francis Group (www.tandfonline.com), from Doorly et al. 2002].

7.9 Limitations of the experimental and computational methods

This study was subjected to limitations related to both the experimental and computational techniques.

7.9.1 Doppler high-pass filter

The high pass Doppler filter is an important tool that removes clutter signal from tissue or tissue mimic motion. This cut-off filter is based on a frequency threshold, which leaves out of the image Doppler frequency shifts from slowly moving flow. In a region where flow velocities vary from very small to large magnitudes, setting a low frequency threshold allows signal from low velocities to be detected but this induces aliasing in the peak velocities. Conversely, increasing the threshold stops aliasing but removes the information from low flow velocities.

In the proximal outflow of a vascular graft the blood impinges at the host vessel generating non-uniform secondary flow motions. The tangential cross-flow velocities vary from very low magnitudes in flow stagnation points to high magnitudes in the spirals. During the ultrasound data collection from the proximal graft outflow region, the elimination of aliasing was in some cases associated with loss of information from low frequency shifts. A characteristic example was the control graft Figure 3.5, page 69 (Reynolds number 570) and Figure 3.6, page 70 (Reynolds number 570 and 1140), where the left (toe) side of each flow map had an incomplete circular shape in the region of the flow stagnation due to loss of low velocity data. This lack of velocity data information inevitably affected the calculated circulation as it was dependent on the area of the respective vorticity map.

A second example of colour Doppler reduced sensitivity in low frequency shifts was the barely visible second vortex in the spiral graft outflow of Figure 5.11b - Figure 5.14b (page 119 – page 120) in the bottom or posterior side of the maps. These small vortices were detectable in three of these figures as shown in the close up of Figure 5.15 (page 121).

7.9.2 Vector Doppler accuracy

In section 2.5 (page 48), the accuracy of the applied vector Doppler technique was tested using a rotating phantom spinning with known velocity. The technique was found to be accurate in regions where the mean Doppler frequency was above the cut-off Doppler filter for both the right and left beam projections. However, in regions where the mean Doppler frequency shift was under the high pass filter for at least one of the steered beams, the velocity magnitude error could be as much as 22% and the velocity direction error as much as 14.5%. These errors could increase to 64.9% and 15.7% respectively, when the detected frequencies were under the cut-off filter for both oblique projections. The reduced accuracy of the vector Doppler technique, in areas with frequency shifts under the cut-off filter, could produce localised vorticity errors up to 31.4%. Although these errors only affect a small area of the examined cross-flow section, they need to be considered.

Some of the presented vector Doppler velocity magnitude maps showed peak values at the top (anterior) and bottom (posterior) part of the maps. In section 2.5 (page 48) it was noted that these locations are associated with velocity magnitude overestimation. It is possible that the observation of peak values in the anterior and posterior locations of experimental velocity magnitude maps was related to overestimation. This potential source of error can easily be seen in velocity magnitude maps of single rather than multiple-spiral patterns, because the flow is more organised; e.g. Figure 3.7d-f (page 71), Figure 3.8d-f (page 72), Figure 4.5d-f (page 93), Figure 4.6d-f (page 94).

7.9.3 Viscosity

The viscosity of the applied BMF was 1.7 mPa·s and thus the same viscosity was simulated in all numerical studies, with the exception of the small substudy where the viscosity was corrected to 3.5 mPa·s. It was shown that the decreased viscosity enhanced the intensity of secondary flow motions and their distance of propagation downstream in the vessel mimic. However, both applied viscosities showed similar vortical structures at the proximal graft outflows and increased quantitative values for the spiral graft.

On the other hand, the Reynolds number is an important parameter in the development of rotational phenomena in a tube as it is proportional to the flow rate and diameter of the examined cross-section plane and inversely proportional to viscosity (see Equation 1.6, page 26). The application of a BMF with low viscosity enabled peak systolic Reynolds numbers to be obtained. With a higher viscosity BMF the application of increased Reynolds numbers requires increased flow rates, which can induce problems such as air bubbles in the flow circulation and rupture of the anastomosis.

7.9.4 Spatial resolution

The spatial resolution of Doppler ultrasound is limited to approximately 0.5 mm. The spatial resolution of CFD can be reduced to 0.02 mm at the wall boundary region where the volume mesh is composed of very small volume cells (Hoskins 2010). Smoothing in ultrasound imaging is known to reduce spatial resolution (ATL Ultrasound 2000) and therefore was kept low to minimise this effect.

The volume mesh of the numerical simulation of each vascular-graft model was based on CT scanning and geometry segmentation. The CT slice thickness was 0.6 mm with a slice-to-slice increment of 0.3 mm and the isotropic resolution was $0.33 \times 0.33\ mm^2$. Although this spatial resolution is considered high for medical imaging, it can still affect the geometry of the models especially that of the spiral inducer ridge which is less than 1.5 mm in height.

The segmentation with Amira was based on the different pixel intensities between the vascular-graft model wall and its lumen. The pixels in this interface had varying but similar intensities and as a consequence the surface of the segmented geometry was zigzagged. Smoothing was necessary to reduce this effect. The smoothing further distorted the groove from the spiral inducer ridge and decreased the diameter of the segmented lumen. The diameter was also affected by the limitations of CT resolution and the Amira segmentation process. As a result the diameter of the vessel mimic region was 5 mm instead of 5.4 mm.

7.9.5 Model positioning and data collection planes

The positioning of each vascular-graft model in the acrylic tank was standardised to allow accurate repositioning. Nonetheless, it is likely that very small differences existed between the position of each model during ultrasound data collection and the CT scanning. Similarly very small variations could be assumed between the examined ultrasound scanning planes and the CFD cross-flow planes.

7.9.6 Computational flow analysis

An established methodology was used to create the volume mesh and a conservative laminar model was used to solve the governing Navier-Stokes equations of flow. The Reynolds numbers were kept under 1000 for increased reliability of the results. Even so, it is possible that the numerical simulation introduced some errors when solving the 3D flow field.

7.9.7 Summary

This section described limitations and differences in the applied experimental and numerical approaches. These limitations and differences affected to some extent the results from both approaches and consequently their comparison. As a result it was considered appropriate to compare the trends of peak in-plane velocity and circulation between the experimental and numerical studies and not their actual magnitudes.

7.10 Industrial application of the experimental methodology

Spiral grafts are manufactured from an ePTFE tube. The graft is housed in an appropriate tooling which acts as a mould for the formation of the spiral inducer ridge when injected with Chronoflex 80® polyurethane. A different tooling is used for each type of spiral graft. The main geometric features of this tooling are the ridged cross sectional profile parameters and helical pitch of the spiral flow inducer. These features were previously optimised by Vascular Flow Technologies Ltd.

The implementation of optimal design configurations was found to be challenging and adjustments were made to allow adaptation of spiral flow technology in grafts. Necessary preclinical tests were conducted to demonstrate that these adjustments did not significantly affect the ability of the graft to produce single-spiral flow.

Spiral grafts have been manufactured for Vascular Flow Technologies by two separate companies over time. The transfer from one company to the other happened during the computational phase of this project. New tooling was required and it was considered appropriate to attempt to bring the geometrical features of spiral grafts closer to the optimal design. The manufacturing transfer and tooling iteration required authorisation of the new product by the companies Notified Body (Intertie) to comply with the requirements of the European Medical Device Directive (MMD 92/42/EEC), the United States Food and Drug Administration Quality System Regulation (QSR 21 CRF Part 820) and the companies own quality system which is certified to ISO 13485:2003.

The new PV (6 and 8 mm inner diameter) and AV (6 mm inner diameter) spiral grafts were made by a new generation ePTFE material and were successfully tested using the experimental methodology of this thesis. The new products were able to generate a more centralised single spiral flow with more uniform velocity magnitude dispersion than the old grafts. The in-plane velocity and circulation were higher for the new devices verifying their ability to induce stronger single spiral flow. The consistency of the new prostheses was examined with an iteration process.

7.11 Conclusions

The development of the vascular-graft models was based on assumptions that provided a standardised environment for steady flow experiments.

Vorticity mapping is a new concept in medical ultrasound imaging and provides further characterisation of rotational flow. The evolving understanding of the clinical impact of vortices on the cardiovascular system could make 2D vector Doppler, vorticity and extracted parameters such as circulation, important and low cost tools for use in clinical diagnosis.

The increased mixing and WSS of a single-spiral in the outflow of a spiral graft correlates well with previous studies in the field. Single-spiral flow may be a biomarker related to advanced local haemodynamics that inhibit atherogenesis.

The experimental and computational simulations of this project were subjected to limitations. However, the close agreement of their results showed that they were both appropriate methods for characterising vortical structures.

The application of this experimental methodology in industry highlighted its recognition as a tool to visualise and quantify flow patterns induced by vascular implants.

Chapter 8

Conclusions and future work

8.1 Conclusions

The in-house PV and AV vascular-graft flow phantoms proved to be appropriate testing models for graft assessments using ultrasound. The developed dual-beam vector Doppler methodology provided 2D velocity and vorticity maps to enable visualisation of the cross-flow rotational phenomena and hence permitting quantification by comparison of velocity and circulation. The accuracy of 2D velocity and vorticity mapping was high when the Doppler frequency shifts were above the cut-off colour filter for both steered beams. Errors were increased when the Doppler frequency shifts were under the cut-off filter for at least one of the oblique projections.

Chapter 3 presented the ultrasound results for the PV vascular-graft models. The main observation was a single-spiral flow pattern in the outflow of the spiral prosthesis and a symmetric double- or triple-spiral flow pattern in the outflow of the non-spiral prosthesis. Reduced flow stagnation points, instability and separation were shown for the former device. The peak tangential velocity and circulation was higher for the spiral product indicating increased in-plane mixing.

Chapter 5 described an image-guided modelling comparison of the PV models. The patterns of the flow maps and the trends of peak tangential velocity and circulation from the computational approach were in agreement with those from the experimental approach. With the computational study the secondary flow motions were further characterised using helicity and WSS. Both were found higher for the spiral graft

suggesting advanced haemodynamics. In addition, increased pressure loss was detected for the spiral device in comparison to the conventional graft; however this difference was considered negligible.

Chapter 4 studied secondary flow phenomena in the outflow of spiral and conventional AV vascular-graft models. The spiral graft induced a double-spiral pattern composed of a dominant and a smaller vortex in the proximal graft outflow and a single-spiral in the distal outflow. On the contrary, between one and four rotational cells were seen in the outflow of the conventional graft, depending on surgical configuration of the model, Reynolds number and distance from the anastomosis. The multiple-spiral structures were associated with increased flow stagnation, separation and instability showing the beneficial effect of the spiral graft. Increased tangential velocity and circulation was detected in the outflow of the spiral graft showing enhanced in-plane mixing.

The AV models were subjected to CFD simulations in chapter 6. Flow patterns from the computational analysis agreed with those of the experimental approach in the proximal grafts outflow, but differences were observed in the examined distal cross-flow planes. The CFD trends of tangential velocity and circulation verified those from the experimental results. Increased helicity was found with the spiral graft, verifying the enhanced secondary flow motions and in-plane mixing also found in the experimental analysis. WSS was either higher for the spiral graft or the same for both devices suggesting advanced haemodynamics for the former product. The pressure drop was higher for the spiral device but the difference between it and the control was considered negligible.

The aims of this thesis (section 1.8, page 28) were well addressed in chapters 3 - 6. The spiral grafts were associated with advanced haemodynamics in comparison to conventional grafts. These haemodynamics may be beneficial for endothelial behaviour preventing the development of neo-intimal hyperplasia and thrombosis in the graft outflow anastomosis and downstream the host vessel, which would result in improved clinical patency rates.

8.2 Future work

Future work related to this thesis should be based on a blood mimic with a dynamic viscosity of between 3.4 – 4 mPa·s. Numerical studies have suggested that the assumption that blood is a Newtonian fluid can significantly affect the flow phenomena (O'Callaghan et al. 2006; Tu and Deville 1996). Future development of flow phantom materials may allow the simulation of non-Newtonian viscous behaviour of blood, thus minimising errors related to rheological properties.

Another design development to be considered is the assessment of vascular-graft models with bi-directional runoff in order to determine how this would affect flow patterns downstream from the distal anastomosis.

The most obvious extend of this study is the application of pulsatile flow, especially in the PV grafts where the flow rate not only varies in magnitude but also in direction. The pulsatile flow could be combined with the application of turbulent models in CFD to reach physiologic Reynolds numbers.

It would be interesting to apply the vector Doppler technique in a cohort of patients with spiral grafts *in situ* to assess the ability of the device to induce a stabilised single spiral *in-vivo.* This could be extended further in a cohort of patients with conventional graft for comparison.

Another possible and highly demanding study would be the testing of flow produced by spiral and non-spiral grafts in a vascular biological model involving living cells.

Appendix A

Supplementary experimental data

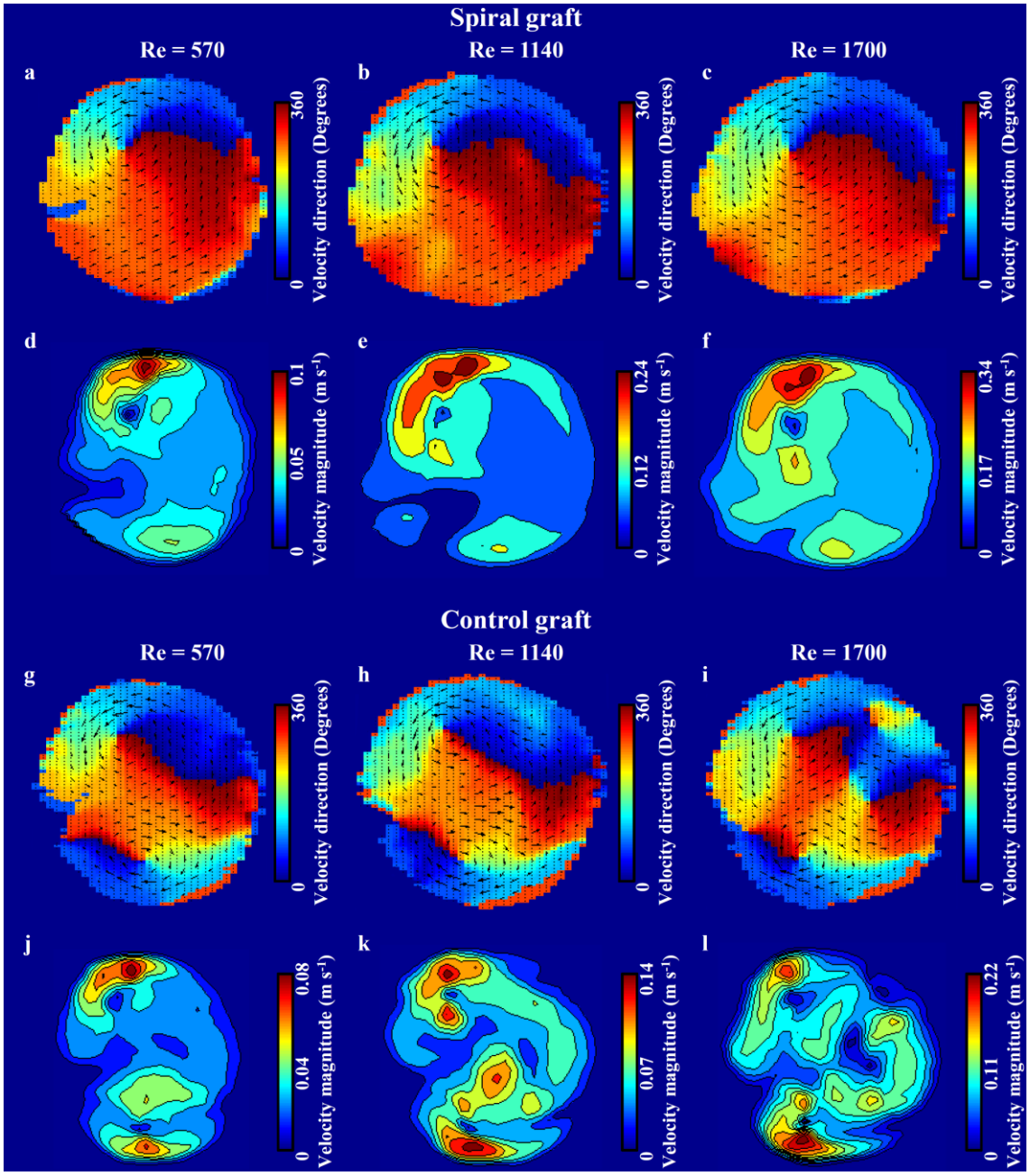

Figure A.1: Direction (first and third rows) and magnitude (second and forth rows) velocity maps for the spiral and control grafts. Scan plane 1, angle θ = 60° (republished with permission of ELSEVIER, from Kokkalis et al. 2013).

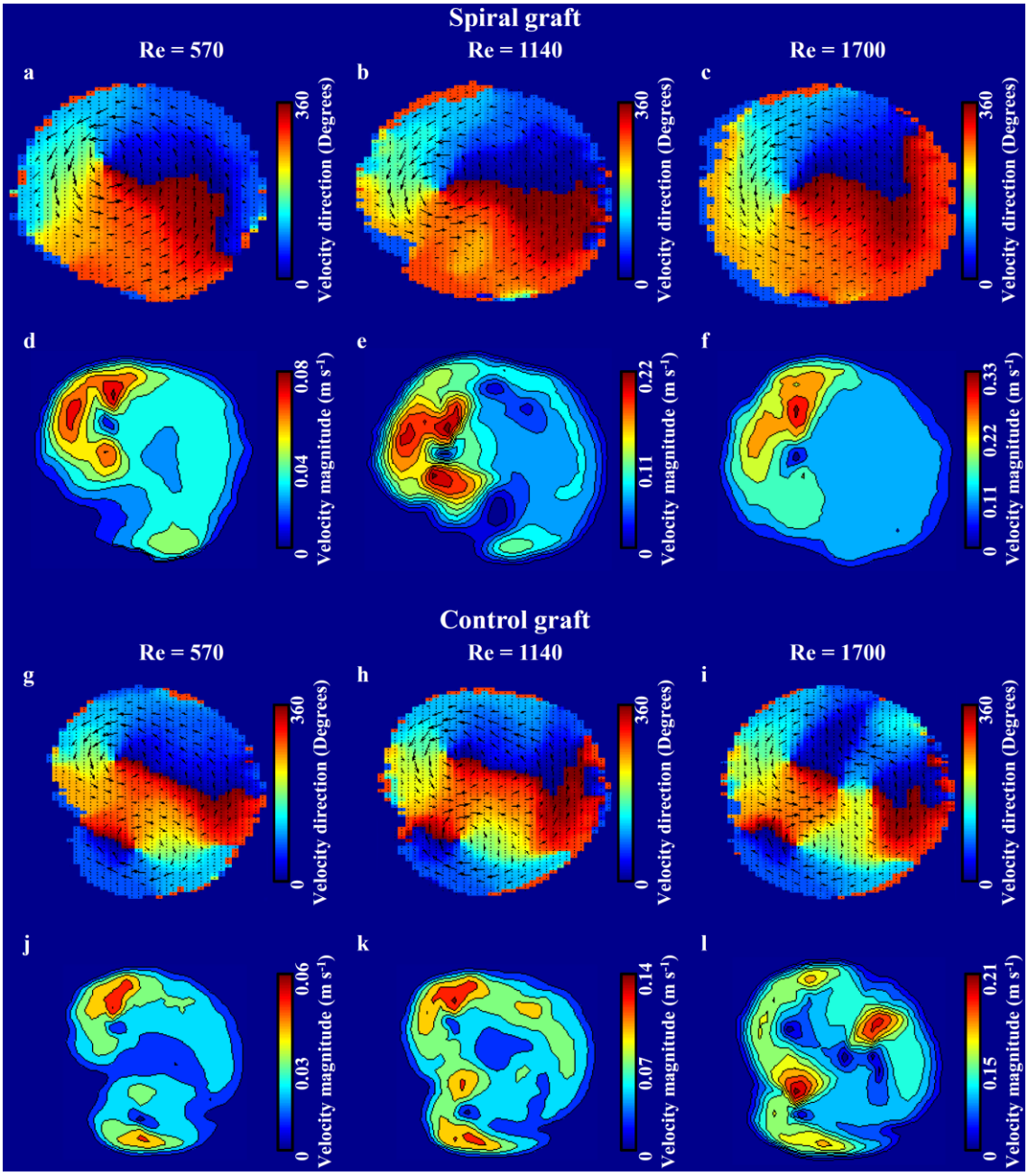

Figure A.2: Direction (first and third rows) and magnitude (second and forth rows) velocity maps for the spiral and control grafts. Scan plane 2, angle θ = 60° (republished with permission of ELSEVIER, from Kokkalis et al. 2013).

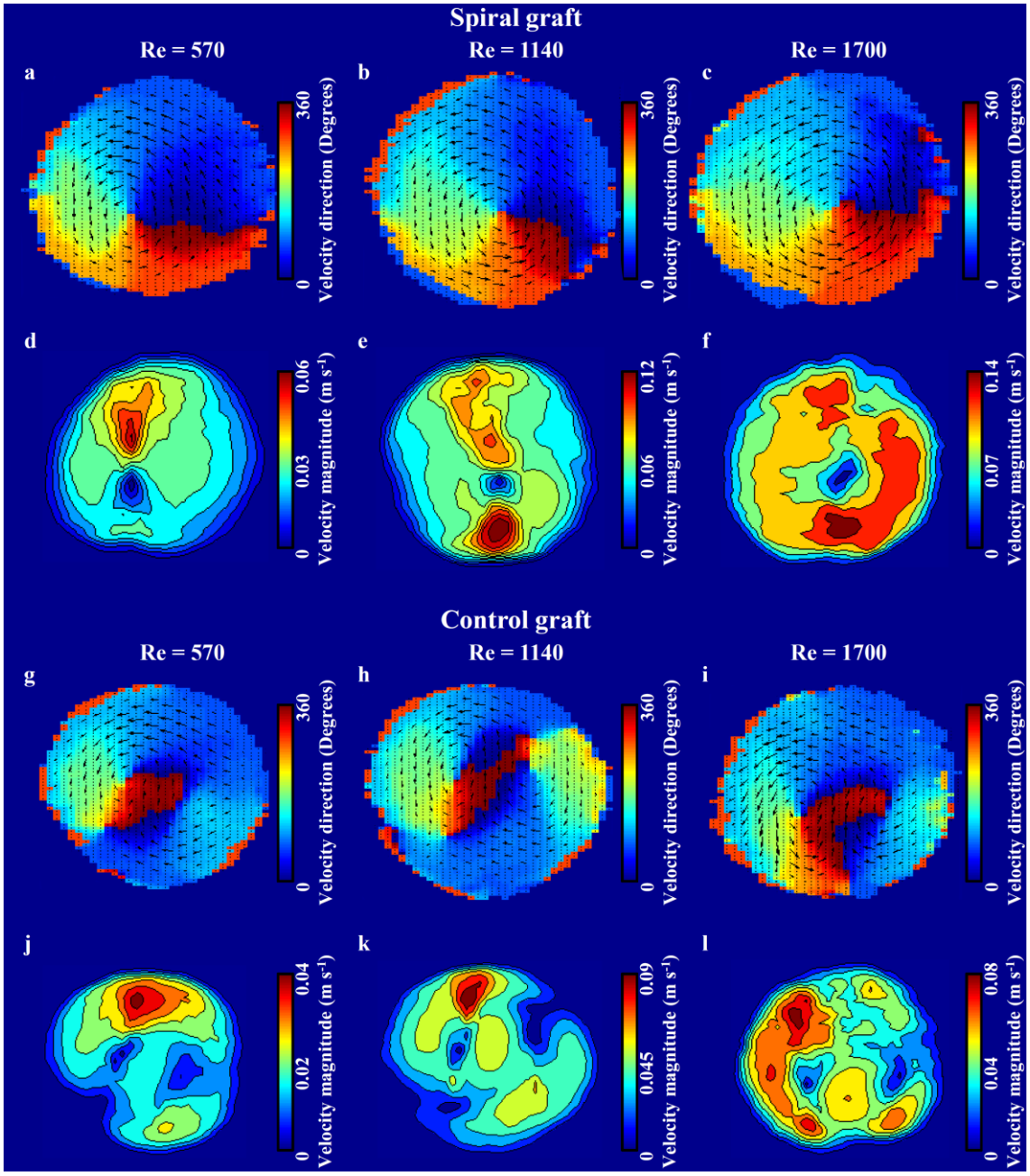

Figure A.3: Direction (first and third rows) and magnitude (second and forth rows) velocity maps for the spiral and control grafts. Scan plane 3, angle θ = 60° (republished with permission of ELSEVIER, from Kokkalis et al. 2013).

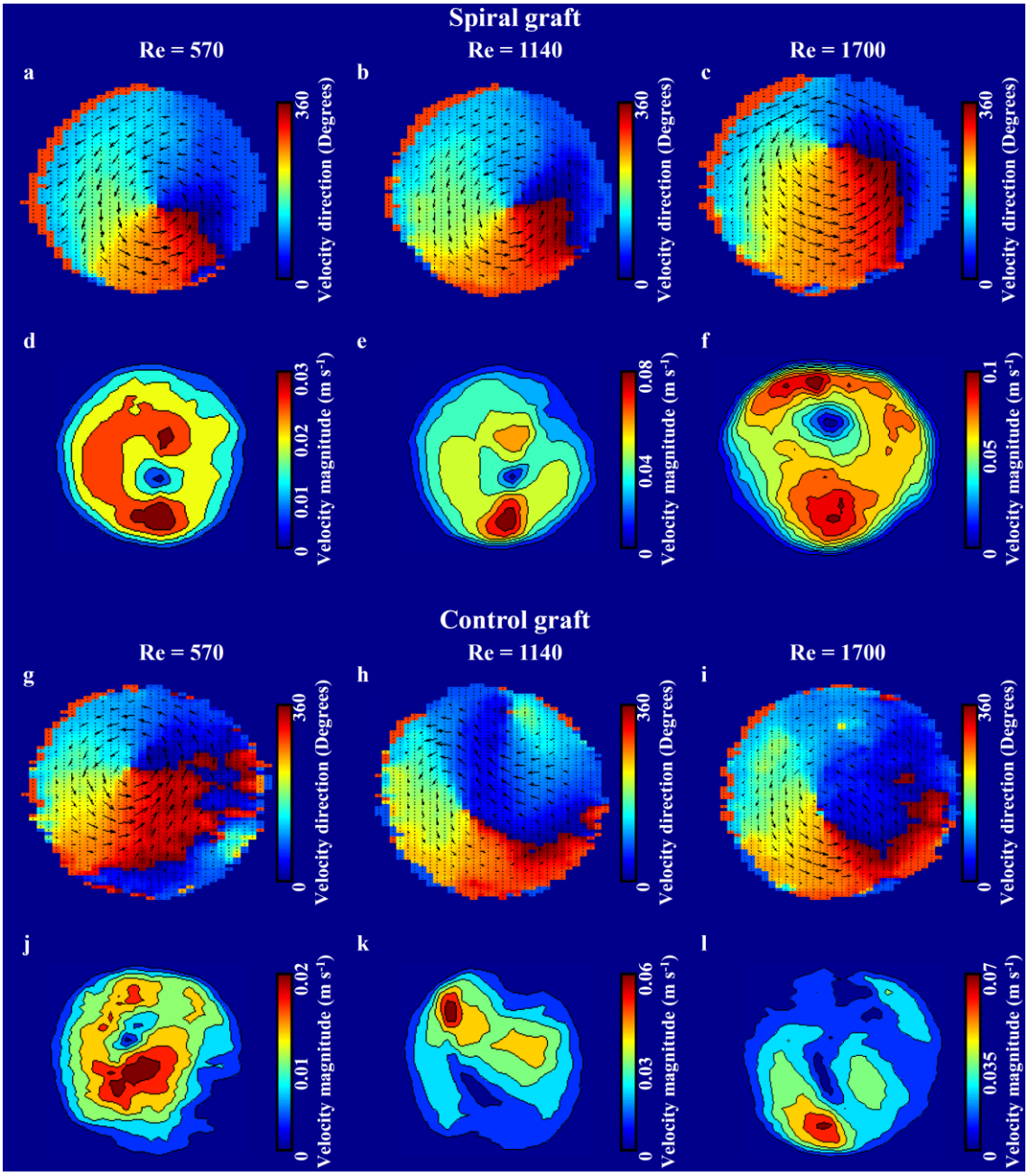

Figure A.4: Direction (first and third rows) and magnitude (second and forth rows) velocity maps for the spiral and control grafts. Scan plane 4, angle θ = 60 (republished with permission of ELSEVIER, from Kokkalis et al. 2013).

Appendix B

Publications

C.1 Papers and conference proceedings

Kokkalis, E., Cookson, A. N., Stonebridge, P. A., Corner, G.A., Houston, J. G., Hoskins, P. R., Comparison of vortical structures induced by arteriovenous grafts using vector Doppler ultrasound, *Ultrasound in Medicine and Biology* (in press).

Kokkalis, E., Hoskins, P. R., Corner, G. A., Stonebridge, P. A., Doull, A. J., Houston, J. G. (2013), Secondary flow in peripheral vascular prosthetic grafts using vector Doppler imaging, *Ultrasound in Medicine and Biology*; 39(12):2295-2307.

Kokkalis, E., Hoskins, P. R., Corner, G. A., Doull, A. J., Stonebridge, P. A., Houston, J. G. (2013), Hemodynamic differences in the outflow of access vascular grafts, *The Journal of Vascular access*, 14(1):47.

Kokkalis, E., Hoskins, P. R., Corner, G. A., Stonebridge, P. A., Doull, A. J., Melzer, A., Houston, J. G. (2012), Vector Doppler Imaging and Secondary Flow Patterns in Vascular Prostheses, *IEEE International Ultrasonics Symposium*; 1894-7.

C.2 Presentations in peer review conferences

Matthew, S., Webb, A., **Kokkalis, E.**, Dunn, M. H., Houston, J. G. (2014), Re-introducing spiral flow in a vascular access graft using a spiral inducing stent, *American Society of Nephrology*, November, 11-16, Philadelphia, USA

Matthew, S., Webb, A., **Kokkalis, E.**, Dunn, M. H., Houston, J. G. (2014), Improving central vein blood flow parameters in central vein catheter dialysis, *American Society of Nephrology*, November, 11-16, Philadelphia, USA

Kokkalis, E., Hoskins, P. R., Valluri, P., Corner, G. A., Duce, S. L., Houston, J. G. (2014), Computational comparison of a spiral and a non-spiral peripheral bypass graft, *World Congress of Biomechanics*, July, 6-11, Boston, USA.

Kokkalis, E., Hoskins, P. R., Corner, G. A., Doull, A. J., Stonebridge, P. A., Houston, J. G. (2013), Hemodynamic Differences in the Outflow of Access Vascular Grafts, *Vascular Access Society International Congress*, April, 25-27, Prague, Czech Republic (best poster award).

Kokkalis, E, Hoskins, P. R., Corner, G. A., Stonebridge, P. A., Doull, A. J., Houston, J. G. (2012), Vector Doppler maps and helical flow in the outflow of vascular prostheses, *British Medical Ultrasound Society*, December, 10-12, Telford, UK.

Kokkalis, E, Hoskins, P. R., Corner, G. A., Stonebridge, P. A., Doull, A. J., Melzer, A., Houston, J. G. (2012), Vector Doppler Imaging and Secondary Flow Patterns in Vascular Prostheses, *IEEE International Ultrasound Symposium*, October, 7-10, Dresden, Germany.

Kokkalis, E, Hoskins, P. R., Corner, G. A., Stonebridge, P. A., Melzer, A., Houston, J. G. (2012), Secondary flow motions in spiral and non-spiral vascular prostheses using ultrasound flow phantoms, *IPEM Medical Physics and Engineering Conference*, September, 10-12, Oxford, UK.

Rube, M. A., **E Kokkalis**, Immel, E., Guerguieva, M., Eisma, R., Melzer, A. (2012), Training and Testing Environment for MR-guided Vascular Interventions, *International Society of Magnetic Resonance in Medicine*, May, 5-11, Melbourne, Australia.

References

Abdulhannan, P., Russell, D. A., & Homer-Vanniasinkam, S. (2012). Peripheral arterial disease: a literature review. *British Medical Bulletin*, *104*, 21–39.

Akoh, J. A. (2009). Prosthetic arteriovenous grafts for hemodialysis. *The Journal of Vascular Access*, *10*(3), 137–47.

ANSYS. (2011). ANSYS ICEM CFD Tutorial Manual. Canonsburg, PA, USA: ANSYS.

Armstrong, P. A., & Bandyk, D. F. (2010). Duplex scanning for lower extremity arterial disease. In A. F. Aburahman & J. J. Bergan (Eds.), *Noninvasive peripheral arterial diagnosis*. Springer London.

ATL Ultrasound. (2000). *HDI 5000 Ultrasound System - Reference Manual* (p. 438). Bothell, USA.

ATS. (2011). Model 707 Doppler Test Fluid. Retrieved August 23, 2011, from http://www.atslaboratories-phantoms.com/images/707data2012.pdf

Belch, J. J. F., Topol, E. J., Agnelli, G., Bertrand, M., Califf, R. M., Clement, D. L., Creager, M. A., Easton, J. D., Gavin, J. R., Greenland, P., Hankey, G., Hanrath, P., Hirsch, A. T., Meyer, J., Smith, S. C., Sullivan, F., & Weber, M. A. (2003). Critical issues in peripheral arterial disease detection and management: a call to action. *Archives of Internal Medicine*, *163*(8), 884–92.

Belian, A., Chkhetiani, O., Golbraikh, E., & Moiseev, S. (1998). Helical turbulence: turbulent viscosity and instability of the second moments. *Physica A*, *258*(1-2), 55–68.

Bird, R. B., Stewart, W. E., & Lightfoot, E. N. (2002). *Transport Phenomena* (2nd ed., p. 895). Toronto: John Wiley & Sons, Inc.

Blake, J. R. (2006). xiftoolbox v0.4.3. MATLAB File Exchange. Retrieved from http://www.mathworks.co.uk/matlabcentral/fileexchange/9294-readxif-xiftoolbox/all_files

Blake, J. R. (2008). *On the assessment of blood velocity and wall shear rate in arteries with Doppler ultrasound: a validation study*. The University of Edinburgh.

Blake, J. R., Easson, W. J., & Hoskins, P. R. (2009). A dual-phantom system for validation of velocity measurements in stenosis models under steady flow. *Ultrasound in Medicine & Biology*, *35*(9), 1510–24.

Brown, P. W., & Mitchell, D. C. (2014). Central venous and dialysis. In J. D. Beard, P. A. Gaines, & I. Loftus (Eds.), *Vascular and Endovascular Surgery* (5th ed., pp. 279–297). London: Saunders Ltd.

Buckberg, G. D. (2002). Basic science review: The helix and the heart. *The Journal of Thoracic and Cardiovascular Surgery*, *124*(5), 863–883.

Caro, C. G. (2009). Discovery of the role of wall shear in atherosclerosis. *Arteriosclerosis, Thrombosis, and Vascular Biology*, *29*(2), 158–61.

Caro, C. G., Cheshire, N. J., & Watkins, N. (2005). Preliminary comparative study of small amplitude helical and conventional ePTFE arteriovenous shunts in pigs. *Journal of the Royal Society Interface*, *2*(3), 261–6.

Caro, C. G., Doorly, D. J., Tarnawski, M., Scott, K. T., Long, Q., & Dumoulin, C. L. (1996). Non-Planar Curvature and Branching of Arteries and Non-Planar-Type Flow. *Proceedings of the Royal Society*, *452*(1944), 185–197.

Caro, C. G., Fitz-Gerald, J. M., & Schroter, R. C. (1969). Arterial wall shear and distribution of early atheroma in man. *Nature*, *223*, 1159–60.

Caro, C. G., Pedley, T. J., Schroter, R. C., & Seed, W. A. (2012). The systemic arteries. In *The Mechanics of the Circulation*. Cambridge: Cambridge University Press.

Cecchi, E., Giglioli, C., Valente, S., Lazzeri, C., Gensini, G. F., Abbate, R., & Mannini, L. (2011). Role of hemodynamic shear stress in cardiovascular disease. *Atherosclerosis*, *214*(2), 249–56.

Chen, Z., Fan, Y., Deng, X., & Xu, Z. (2009). Swirling flow can suppress flow disturbances in endovascular stents: a numerical study. *ASAIO Journal (American Society for Artificial Internal Organs : 1992)*, *55*(6), 543–9.

Cheng, Z., Riga, C., Chan, J., Hamady, M., Wood, N. B., Cheshire, N. J. W., Xu, Y., & Gibbs, R. G. J. (2013). Initial findings and potential applicability of computational simulation of the aorta in acute type B dissection. *Journal of Vascular Surgery*, *57*(2 Supplement), 35S–43S.

Cheng, Z., Tan, F. P. P., Riga, C. V, Bicknell, C. D., Hamady, M. S., Gibbs, R. G. J., Wood, N. B., & Xu, X. Y. (2010). Analysis of flow patterns in a patient-specific aortic dissection model. *Journal of Biomechanical Engineering*, *132*(5), 051007–1 – 051007–9.

Chu, K. C., & Rutt, B. K. (1997). Polyvinyl alcohol cryogel: an ideal phantom material for MR studies of arterial flow and elasticity. *Magnetic Resonance in Medicine*, *37*(2), 314–9.

Cimino, S., Pedrizzetti, G., Tonti, G., Canali, E., Petronilli, V., De Luca, L., L., Iacoboni, C., & Agati, L. (2012). In vivo analysis of intraventricular fluid dynamics in healthy hearts. *European Journal of Mechanics - B/Fluids*, *35*, 40–46.

Cookson, A. N., Doorly, D. J., & Sherwin, S. J. (2009). Mixing through stirring of steady flow in small amplitude helical tubes. *Annals of Biomedical Engineering*, *37*(4), 710–21.

Cookson, A. N., Doorly, D. J., & Sherwin, S. J. (2010). Using coordinate transformation of Navier–Stokes equations to solve flow in multiple helical geometries. *Journal of Computational and Applied Mathematics*, *234*(7), 2069–2079.

Daenens, K., Schepers, S., Fourneau, I., Houthoofd, S., & Nevelsteen, A. (2009). Heparin-bonded ePTFE grafts compared with vein grafts in femoropopliteal and femorocrural bypasses: 1- and 2-year results. *Journal of Vascular Surgery*, *49*(5), 1210–6.

Deane, C. R., & Goss, D. E. (2011). Peripheral arteries. In P. Allan, G. Baxter, & M. Weston (Eds.), *Clinical Ultrasound* (Third., pp. 1197–1226). Elsevier.

Diehm, N., Baumgartner, I., Jaff, M., Do, D.-D., Minar, E., Schmidli, J., Diehm, C., Biamino, G., Vermassen, F., Scheinert, D., van Sambeek, M., & Schillinger, M. (2007). A call for uniform reporting standards in studies assessing endovascular treatment for chronic ischaemia of lower limb arteries. *European Heart Journal*, *28*(7), 798–805.

Dineley, J., Meagher, S., Poepping, T. L., McDicken, W. N., & Hoskins, P. R. (2006). Design and characterisation of a wall motion phantom. *Ultrasound in Medicine & Biology*, *32*(9), 1349–57.

Ding, Z., Fan, Y., Deng, X., Zhan, F., & Kang, H. (2010). Effect of swirling flow on the uptakes of native and oxidized LDLs in a straight segment of the rabbit thoracic aorta. *Experimental Biology and Medicine (Maywood)*, *235*(4), 506–13.

Doelman, C., Duijm, L. E. M., Liem, Y. S., Froger, C. L., Tielbeek, A. V, Donkers-van Rossum, A. B., Cuypers, P. W. M., Douwes-Draaijer, P., Buth, J., & van den Bosch, H. C. M. (2005). Stenosis detection in failing hemodialysis access fistulas and grafts: comparison of color Doppler ultrasonography, contrast-enhanced magnetic resonance angiography, and digital subtraction angiography. *Journal of Vascular Surgery*, *42*(4), 739–46.

Doorly, D. J., Sherwin, S. J., Franke, P. T., & Peiró, J. (2002). Vortical flow structure identification and flow transport in arteries. *Computer Methods in Biomechanics and Biomedical Engineering*, *5*(3), 261–73.

Doorly, D., & Sherwin, S. (2009). Geometry and Flow. In L. Formaggia, A. Quarteroni, & A. Veneziani (Eds.), *Cardiovascular Mathematics* (pp. 177–209). Springer Milan.

Duck, F. A. (1990). *Physical properties of tissue*. London: Academic Press.

Ethier, C. R., Prakash, S., Steinman, D. A., Leask, R. L., Couch, G. G., & Ojha, M. (2000). Steady flow separation patterns in a 45 degree junction. *Journal of Fluid Mechanics*, *411*, 1–38.

Evans, D. H., Jensen, J. A., & Nielsen, M. B. (2011). Ultrasonic colour Doppler imaging. *Interface Focus*, *1*(4), 490–502.

Fei, D.-Y., Fu, C.-T., Brewer, W. H., & Kraft, K. A. (1994). Angle independent Doppler colour imaging: determination of accuracy and a method of display. *Ultrasound in Medicine & Biology*, *20*(2), 147–155.

Fisher, R. K., How, T. V., Bakran, A., Brennan, J. A., & Harris, P. L. (2004). Outflow distribution at the distal anastomosis of infrainguinal bypass grafts. *Journal of Biomechanics*, *37*(3), 417–420.

Fox, M. D. (1978). Multiple Crossed-Beam Ultrasound Doppler Velocimetry. *IEEE Transactions on Sonics and ultrasonics1*, *2*(SU-25), 281–286.

Fox, M. D., & Gardiner, W. M. (1988). Three-Dimensional Doppler Velocimetry of Flow Jets. *IEEE Transactions on Biomedical Engineering*, *35*(10), 834–841.

Frazin, L. J., Lanza, G., Vonesh, M., Khasho, F., Spitzzeri, C., McGee, S., Mehlman, D., Chandran, K. B., Talano, J., & McPherson, D. (1990). Functional Chiral Asymmetry in Descending Thoracic Aorta. *Circulation*, *82*(6), 1985–94.

Frazin, L. J., Vonesh, M. J., Chandran, K. B., Shipkowitz, T., Yaacoub, A. S., & McPherson, D. D. (1996). Confirmation and Initial Documentation of Thoracic and Abdominal Aortic Helical Flow. *American Society for Arteficial Internal Organs*, *49*, 951–956.

Gallo, D., Steinman, D. A., Bijari, P. B., & Morbiducci, U. (2012). Helical flow in carotid bifurcation as surrogate marker of exposure to disturbed shear. *Journal of Biomechanics*, *45*(14), 2398–2404.

Garcia, D., Del Alamo, J. C., Tanne, D., Yotti, R., Cortina, C., Bertrand, E., Antoranz, J. C., Perez-David, E., Rieu, R., Fernandez-Aviles, F., & Bermejo, J. (2010). Two-dimensional intraventricular flow mapping by digital processing conventional color-Doppler echocardiography images. *IEEE Transactions on Medical Imaging*, *29*(10), 1701–13.

Gessaroli, M., & Massini, S. (2012). Improved Primary Patency Rate of Hemodialysis Arterovenous Grafts Associated With Modified Stretch e-PTFE Vascular Grafts (Gore) by Compliant ePTFE Cuff. *Surgery: Current Research*, *02*(03), 3–5.

Gibbs, V., Cole, D., & Sassano, A. (2009). *Ultrasound Physics and Technology. How, Why and When* (p. 144). Elsevier.

Greenleaf, J. F., Duck, F. A., Samayoa, W. F., & Johnson, S. A. (1974). Ultrasonic Data Acquisition and Processing System for Atherosclerotic Tissue Characterization. *IEEE Ultrasonics Symposium*, 738–743.

Grigioni, M., Daniele, C., Morbiducci, U., Del Gaudio, C., D'Avenio, G., Balducci, A., & Barbaro, V. (2005). A mathematical description of blood spiral flow in vessels: application to a numerical study of flow in arterial bending. *Journal of Biomechanics*, *38*(7), 1375–86.

Hammer, S. J. (2008). *Engineering a 3D ultrasound system for image-guided vascular modelling*. University of Edinburgh.

Hansen, P. M., Pedersen, M. M., Hansen, K. L., Nielsen, M. B., & Jensen, J. A. (2011). Examples of Vector Velocity Imaging. *IFMBE Proceedings*, *34*, 77–80.

Hardman, D., Semple, S. I., Richards, J. M. J., & Hoskins, P. R. (2013). Comparison of patient-specific inlet boundary conditions in the numerical modelling of blood flow in abdominal aortic aneurysm disease. *International Journal for Numerical Methods in Biomedical Engineering*, *29*(December 2012), 165–178.

Harloff, A., Albrecht, F., Spreer, J., Stalder, A. F., Bock, J., Frydrychowicz, A., Schollhorn, J., Hetzel, A., Schumacher, M., Hennig, J., & Markl, M. (2009). 3D blood flow characteristics in the carotid artery bifurcation assessed by flow-sensitive 4D MRI at 3T. *Magnetic Resonance in Medicine*, *61*(1), 65–74.

Harloff, A., Simon, J., Brendecke, S., Assefa, D., Helbing, T., Frydrychowicz, A., Weber, J., Olschewski, M., Strecker, C., Hennig, J., Weiller, C., & Markl, M. (2010). Complex plaques in the proximal descending aorta: an underestimated embolic source of stroke. *Stroke*, *41*(6), 1145–50.

Haruguchi, H., & Teraoka, S. (2003). Intimal hyperplasia and hemodynamic factors in arterial bypass and arteriovenous grafts: a review. *Journal of Artificial Organs*, *6*(4), 227–35.

Hong, G.-R., Pedrizzetti, G., Tonti, G., Li, P., Wei, Z., Kim, J. K., Baweja, A., Liu, S., Chung, N., Houle, H., Narula, J., & Vannan, M. A. (2008). Characterization and quantification of vortex flow in the human left ventricle by contrast echocardiography using vector particle image velocimetry. *JACC. Cardiovascular Imaging*, *1*(6), 705–17.

Hoskins, P. (2010). Principles of Doppler ultrasound. In P. Hoskins, K. Martin, & A. Thrush (Eds.), *Diagnostic Ultrasound Physics and Equipment* (Second., pp. 84–95). Cambridge University Press.

Hoskins, P. R. (1994). *Review of the Design and Use of Flow Phantoms In Hoskins, P R, Evans, J A and Sheriff, S (Eds) Testing of Doppler Ultrasound Equipment* (pp. 12 – 29). York: IPEM.

Hoskins, P. R. (1997). Peak velocity estimation in arterial stenosis models using colour vector Doppler. *Ultrasound in Medicine & Biology*, *23*(6), 889–897.

Hoskins, P. R. (1999). A comparison of single- and dual-beam methods for maximum velocity estimation, *25*(4), 583–592.

Hoskins, P. R. (2007). Physical properties of tissues relevant to arterial ultrasound imaging and blood velocity measurement. *Ultrasound in Medicine & biology2*, *33*, 1527–1539.

Hoskins, P. R. (2008). Simulation and validation of arterial ultrasound imaging and blood flow. *Ultrasound in Medicine & Biology*, *34*(5), 693–717.

Hoskins, P. R. (2010). Haemodynamics and blood flow measured using ultrasound imaging. *Journal of Engineering in Medicine*, *224*(2), 255–271.

Hoskins, P. R. (2011). Estimation of blood velocity , volumetric flow and wall shear rate using Doppler ultrasound. *Ultrasound*, *19*, 120–129.

Hoskins, P. R., Fleming, A., Stonebridge, P. A., Allan, P. L., & Cameron, D. (1994). Scan-plane vector maps and secondary flow motions in arteries. *European Journal of Ultrasound*, *I*, 159–169.

Hoskins, P. R., & Hardman, D. (2009). Three-dimensional imaging and computational modelling for estimation of wall stresses in arteries. *The British Journal of Radiology*, *82*, S3–17.

Houston, J. G., Bhat, R., Ross, R., & Stonebridge, P. a. (2007). Long-term results after placement of aortic bifurcation self-expanding stents: 10 year mortality, stent restenosis, and distal disease progression. *Cardiovascular and Interventional Radiology*, *30*(1), 42–7.

Houston, J. G., Gandy, S. J., Milne, W., Dick, J. B. C., Belch, J. J. F., & Stonebridge, P. a. (2004). Spiral laminar flow in the abdominal aorta: a predictor of renal impairment deterioration in patients with renal artery stenosis? *Nephrology, Dialysis, Transplantation : Official Publication of the European Dialysis and Transplant Association - European Renal Association*, *19*(7), 1786–91.

Houston, J. G., Gandy, S. J., Sheppard, D. G., Dick, J. B., Belch, J. J. F., & Stonebridge, P. a. (2003). Two-dimensional flow quantitative MRI of aortic arch blood flow patterns: Effect of age, sex, and presence of carotid atheromatous disease on prevalence of spiral blood flow. *Journal of Magnetic Resonance Imaging : JMRI*, *18*(2), 169–74.

How, T. V, Fisher, R. K., Brennan, J. A, & Harris, P. L. (2006). Swirling flow pattern in a non-planar model of an interposition vein cuff anastomosis. *Medical Engineering & Physics*, *28*(1), 27–35.

Huijbregts, H. J. T. A. M., Blankestijn, P. J., Caro, C. G., Cheshire, N. J. W., Hoedt, M. T. C., Tutein Nolthenius, R. P., & Moll, F. L. (2007). A Helical PTFE Arteriovenous Access Graft to Swirl Flow Across the Distal Anastomosis: Results of a Preliminary Clinical Study. *European Journal of Vascular and Endovascular Surgery*, *33*(4), 472–5.

IEC 61685. (2001). *Ultrasonics - Flow measurement systems: Flow test objects. International Electrotechnical Commission*. Geneva, Switzerland.

Inston, N., & Hofmann, W. (2013). Early experience with the SLF (Spiral Laminar Flow) AV access graft. *The Journal of Vascular Access*, *14*(1), 43.

ISO 13485. (2003). *Medical devices - Quality management systems - Requirements for regulatory purposes* (p. 57). Geneva, Switzerland.

ISO 5840. (2005). *Cardiovascular implants - Cardiac valve prostheses* (p. 84). Geneva, Switzerland.

Jahrome, O., Hoefer, I., Houston, G., Stonebridge, P., Blankestijn, P., Moll, F., & de Borst, G. (2011). Hemodynamic effects of spiral ePTFE prosthesis compared with standard arteriovenous graft in a carotid to jugular vein porcine model. *The Journal of Vascular Access*, *12*(3), 224–30.

Jensen, J. a, & Munk, P. (1998). A new method for estimation of velocity vectors. *IEEE Transactions on Ultrasonics, Ferroelectrics, and Frequency Control*, *45*(3), 837–51.

Jung, B., Markl, M., Föll, D., & Hennig, J. (2006). Investigating myocardial motion by MRI using tissue phase mapping. *European Journal of Cardio-Thoracic Surgery*, *29S*, S150–7.

Kanjwal, M. K., Cooper, C., & Bashir, R. (2004). Peripheral arterial disease - the silent killer. *JK - Practitioner*, *11*(4), 225–232.

Karino, T., Goldsmith, H., Motomiya, S., & Sohara, Y. (1987). Flow patterns in vessels of simple and complex geometries. *Ann N Y Acad Sci*, *516*(422-441).

Keynton, R. S., Evancho, M. M., Sims, R. L., Rodway, N. V., Gobin, A., & Rittgers, S. E. (2001). Intimal Hyperplasia and Wall Shear in Arterial Bypass Graft Distal Anastomoses: An In Vivo Model Study. *Journal of Biomechanical Engineering*, *123*(5), 464–73.

Kilner, P. J., Yang, G. Z., Mohiaddin, R. H., Firmin, D. N., & Longmore, D. B. (1993). Helical and retrograde secondary flow patterns in the aortic arch studied by three-directional magnetic resonance velocity mapping. *Circulation*, *88*(5 Pt 1), 2235–47.

Kim, Y.-H., Kim, J.-E., Ito, Y., Shih, A. M., Brott, B., & Anayiotos, A. (2008). Hemodynamic analysis of a compliant femoral artery bifurcation model using a

fluid structure interaction framework. *Annals of Biomedical Engineering*, *36*(11), 1753–63.

King, D. M., Moran, C. M., McNamara, J. D., Fagan, A. J., & Browne, J. E. (2011). Development of a Vessel-Mimicking Material for use in Anatomically Realistic Doppler Flow Phantoms. *Ultrasound in Medicine & Biology*, *37*(5), 813–826.

Kocica, M. J., Corno, A. F., Carreras-Costa, F., Ballester-Rodes, M., Moghbel, M. C., Cueva, C. N. C., Lackovic, V., Kanjuh, V., & Torrent-Guasp, F. (2006). The helical ventricular myocardial band: global, three-dimensional, functional architecture of the ventricular myocardium. *European Journal of Cardio-Thoracic Surgery : Official Journal of the European Association for Cardio-Thoracic Surgery*, *29 Suppl 1*, S21–S40.

Kokkalis, E., Hoskins, P., Corner, G., Doull, A., Stonebridge, P., & Houston, J. (2013). Hemodynamic differences in the outflow of access vascular grafts. *The Journal of Vascular Access*, *14*(1), 47.

Kokkalis, E., Hoskins, P. R., Corner, G. A., Stonebridge, P. A., Doull, A. J., & Houston, J. G. (2013). Secondary flow in peripheral vascular prosthetic grafts using vector Doppler imaging. *Ultrasound in Medicine & Biology*, *39*(12), 2295–307.

Ku, D. N. (1997). Blood Flow in Arteries. *Annual Review of Fluid Mechanics*, *29*(1), 399–434.

Ku, D. N., & Giddens, D. P. (1983). Pulsatile flow in a model carotid bifurcation. *Arteriosclerosis, Thrombosis, and Vascular Biology*, *3*(1), 31–39.

Lee, S.-W., Fischer, P. F., Loth, F., Royston, T. J., Grogan, J. K., & Bassiouny, H. S. (2005). Flow-induced vein-wall vibration in an arteriovenous graft. *Journal of Fluids and Structures*, *20*(6), 837–852.

Liu, X., Fan, Y., & Deng, X. (2010). Effect of spiral flow on the transport of oxygen in the aorta: a numerical study. *Annals of Biomedical Engineering*, *38*(3), 917–26.

Liu, X., Pu, F., Fan, Y., Deng, X., Li, D., & Li, S. (2009). A numerical study on the flow of blood and the transport of LDL in the human aorta: the physiological significance of the helical flow in the aortic arch. *American Journal of Physiology Heart and Circulatory Physiology*, *297*(1), H163–70.

Malek, A. M., Alper, S. L., & Izuno, S. (1999). Hemodynamic Shear Stress and Its Role in Atherosclerosis. *The Journal of the American Medical Association*, *282*(21), 2035–2042.

Maniatis, T. A., Cobbold, R. S. C., & Wayne, K. (1994). Flow imaging in an end to side anastomosis model using two-dimensional velocity vectors. *Ultrsound in Medicine & Biology*, *20*(6), 559–569.

Marie, Y., Guy, A., Tullett, K., Krishnan, H., Jones, R., & Inston, N. (2014). Patterns of Blood Flow as a Predictor of Maturation of Arteriovenous Fistula for Haemodialysis. *The Journal of Vascular Access*, *15*(3), 169–74.

Markl, M., Draney, M. T., Miller, D. C., Levin, J. M., Williamson, E. E., Pelc, N. J., Liang, D. H., & Herfkens, R. J. (2005). Time-resolved three-dimensional magnetic resonance velocity mapping of aortic flow in healthy volunteers and patients after valve-sparing aortic root replacement. *The Journal of Thoracic and Cardiovascular Surgery*, *130*(2), 456–63.

Marshall, I., Zhao, S., Papathanasopoulou, P., Hoskins, P., & Xu, Y. (2004). MRI and CFD studies of pulsatile flow in healthy and stenosed carotid bifurcation models. *Journal of Biomechanics*, *37*(5), 679–87.

Martin, K. (2010). Introduction to B-mode imaging. In P. Hoskins, K. Martin, & A. Thrush (Eds.), *Diagnostic Ultrasound Physics and Equipment* (Second., pp. 1–3). Cambridge University Press.

Martin, K., & Ramnarine, K. (2010). Physics. In P. Hoskins, K. Martin, & A. Thrush (Eds.), *Diagnostic Ultrasound Physics and Equipment* (Second., pp. 4–22). Cambridge University Press.

Maulik, D. (2005). Physical Principles of Doppler Ultrasonography. In *Doppler Ultrasound in Obstetrics and Gynecology* (pp. 9–17). Springer.

McDicken, W., & Anderson, T. (2011). Basic physics of medical ultrasound. In P. Allan, G. Baxter, & M. Weston (Eds.), *Clinical Ultrasound* (Third., pp. 3–15). Elsevier.

McDonald, D. A. (1960). *Blood Flow in Arteries*. (E. Arnold, Ed.) (1th ed., p. 328).

Meagher, S., Poepping, T. L., Ramnarine, K. V, Black, R. A., & Hoskins, P. R. (2007). Anatomical flow phantoms of the nonplanar carotid bifurcation, part II: experimental validation with Doppler ultrasound. *Ultrasound in Medicine & Biology*, *33*(2), 303–10.

Mehregan, F., Tournoux, F., Muth, S., Pibarot, P., Rieu, R., Cloutier, G., & Garcia, D. (2014). Doppler vortography: a color Doppler approach to quantification of intraventricular blood flow vortices. *Ultrasound in Medicine & Biology*, *40*(1), 210–21.

Mickley, V. (2004). Stenosis and thrombosis in haemodialysis fistulae and grafts: the surgeon's point of view. *Nephrology Dialysis Transplantation*, *19*(2), 309–311.

Morbiducci, U., Ponzini, R., Grigioni, M., & Redaelli, A. (2007). Helical flow as fluid dynamic signature for atherogenesis risk in aortocoronary bypass. A numeric study. *Journal of Biomechanics*, *40*(3), 519–34.

Morris, L., Delassus, P., Callanan, a., Walsh, M., Wallis, F., Grace, P., & McGloughlin, T. (2005). 3-D Numerical Simulation of Blood Flow Through Models of the Human Aorta. *Journal of Biomechanical Engineering*, *127*(5), 767.

Morrison, F. A. (2013). *An introduction to fluid mechanics* (p. 927). New York: Cambridge University Press.

Nichols, W. W., & O'Rourke, M. F. (2005). *McDonald's Blood Flow in Arteries* (Hodder Arn., p. 607). London.

Norgren, L., Hiatt, W. R., Dormandy, J. a, Nehler, M. R., Harris, K. a, & Fowkes, F. G. R. (2007). Inter-Society Consensus for the Management of Peripheral Arterial Disease (TASC II). *Journal of Vascular Surgery*, *45*(1), S5–S67.

O'Brien, T. P., Grace, P., Walsh, M., Burke, P., & McGloughlin, T. (2005). Computational investigations of a new prosthetic femoral-popliteal bypass graft design. *Journal of Vascular Surgery*, *42*(6), 1169–75.

O'Callaghan, S., Walsh, M., & McGloughlin, T. (2006). Numerical modelling of Newtonian and non-Newtonian representation of blood in a distal end-to-side vascular bypass graft anastomosis. *Medical Engineering & Physics*, *28*(1), 70–4.

Ohtsuki, S., & Tanaka, M. (2006). The Flow Velocity Distribution from the Doppler Information on a Plane in Three-Dimensional Flow. *Journal of Visualization*, *9*(1), 69–82.

Ouriel, K. (2001). Peripheral arterial disease. *Lancet*, *358*(9289), 1257–64.

Papaharilaou, Y., Doorly, D. J., & Sherwin, S. J. (2002). The influence of out-of-plane geometry on pulsatile flow within a distal end-to-side anastomosis. *Journal of Biomechanics*, *35*(9), 1225–39.

Paul, M. C., & Larman, A. (2009). Investigation of spiral blood flow in a model of arterial stenosis. *Medical Engineering & Physics*, *31*(9), 1195–203.

Peach, G., Griffin, M., Thompson, M. M., & Hinchliffe, R. J. (2012). Diagnosis and management of peripheral arterial. *British Medical Journal*, *345*(e5208), 1–8.

Pedersen, M. M., Pihl, M. J., Hansen, J. M., Hansen, P. M., Haugaard, P., Nielsen, M. B., & Jensen, J. A. (2011). Arterial secondary blood flow patterns visualized with vector flow ultrasound. *IEEE International Ultrasonics Symposium*, 1242–1245.

Pedersen, M. M., Pihl, M. J., Haugaard, P., Hansen, J. M., Hansen, K. L., Nielsen, M. B., & Jensen, J. A. (2012). Comparison of real-time in vivo spectral and vector velocity estimation. *Ultrasound in Medicine & Biology*, *38*(1), 145–51.

Pedley, T. (1980). *The fluid mechanics of large blood vessels*. (G. Batchelor & J. Miles, Eds.) (p. 446). Cambridge: Cambridge University Press.

Peiffer, V., Sherwin, S. J., & Weinberg, P. D. (2013). Does low and oscillatory wall shear stress correlate spatially with early atherosclerosis? A systematic review. *Cardiovascular Research*, *99*(2), 242–50.

Picot, P. A., Rickey, D. W., Mitchell, R., Rankin, R. N., & Fenster, A. (1993). Three-dimensional colour Doppler imaging. *Ultrasound in Medicine & Biology*, *19*(2), 95–104.

Poepping, T. L., Nikolov, H. N., Thorne, M. L., & Holdsworth, D. W. (2004). A thin-walled carotid vessel phantom for Doppler ultrasound flow studies. *Ultrasound in Medicine & Biology*, *30*(8), 1067–78.

Prakash, S., & Ethier, C. R. (2001). Requirements for Mesh Resolution in 3D Computational Hemodynamics. *Journal of Biomechanical Engineering*, *123*(2), 134–144.

Rayner, H. C., Besarab, A., Brown, W. W., Disney, A., Saito, A., & Pisoni, R. L. (2004). Vascular access results from the Dialysis Outcomes and Practice Patterns Study (DOPPS): Performance against Kidney Disease Outcomes Quality Initiative (K/DOQI) Clinical Practice Guidelines. *Americal Journal of Kidney Diseases*, *44*(S2), 22–26.

Ridger, V., Krams, R., Carpi, A., & Evans, P. C. (2008). Hemodynamic parameters regulating vascular inflammation and atherosclerosis: a brief update. *Biomedicine & Pharmacotherapy*, *62*(8), 536–40.

Rosenthal, S. J., Harrison, L. A., Baxte, K. G., Wetzel, L. H., Cox, G. G., & Batnitzky, S. (1995). Doppler US of helical flow in the portal vein. *RadioGraphics*, *15*, 1103–1111.

Segadal, L., & Matre, K. (1987). Blood velocity distribution in the human ascending aorta. *Circulation*, *76*(1), 90–100.

Sherwin, S. J., Shah, O., Doorly, D. J., Peiro, J., Papaharilaou, Y., Watkins, N., Cara, C. G., & Dumoulin, C. L. (2000). The influence of out-of-plane geometry on the flow within a distal end-to-side anastomosis. *Journal of Biomechanical Engineering*, *122*, 86–95.

Siggers, J. H., & Waters, S. L. (2005). Steady flows in pipes with finite curvature. *Physics of Fluids*, *17*(7), 077102 1–18.

Siggers, J. H., & Waters, S. L. (2008). Unsteady flows in pipes with finite curvature. *Journal of Fluid Mechanics*, *600*, 133–165.

Slager, C., Wentzel, J., Gijsen, F., Schuurbiers, J., van der Wal, A., van der Steen, A., & Serruys, P. (2005). The role of shear stress in the generation of rupture-prone vulnerable plaques. *Nature Clin Pract Cardiovasc Medicine*, *2*(8), 401–407.

Slager, C., Wentzel, J., Gijsen, F., van der Wal, A., Schaar, J., & Serruys, P. (2005). The role of shear stress in the destabilization of vulnarable plaques and related therapeutic implications. *Nature Clin Pract Cardiovasc Medicine*, *2*(9), 456–464.

Sottiurai, V. S., Yao, J. S., Batson, R. C., Sue, S. L., Jones, R., & Nakamura, Y. A. (1989). Distal anastomotic intimal hyperplasia: histopathologic character and biogenesis. *Annals of Vascular Surgery*, *3*(1), 26–33.

Spirou, G. M., Oraevsky, A. A., Vitkin, I. A., & Whelan, W. M. (2005). Optical and acoustic properties at 1064 nm of polyvinyl chloride-plastisol for use as a tissue phantom in biomedical optoacoustics. *Physics in Medicine and Biology*, *50*(14), N141–53.

Stonebridge, P. (2011). Three-dimensional blood flow dynamics: spiral/helical laminar flow. *Methodist Debakey Cardiovascular Journal*, *7*(1), 21–26.

Stonebridge, P. A., & Brophy, C. M. (1991). Spiral laminar flow in arteries? *The Lancet*, *338*, 1360–1360.

Stonebridge, P. A., Buckley, C., Thompson, A., Dick, J., Hunter, G., Chudek, J. A., Houston, J. G., & Belch, J. J. F. (2004). Non spiral and spiral (helical) flow patterns in stenoses. *International Angiology*, *23*(276-283).

Stonebridge, P. A., Hoskins, P. R., Allan, P. L., & Belch, J. F. F. (1996). Spiral laminar flow in vivo. *Clinical Science*, *91*, 17–21.

Stonebridge, P. A., Prescott, R. J., & Ruckley, C. V. (1997). Randomized trial comparing infrainguinal polytetrafluoroethylene bypass grafting with and without vein interposition cuff at the distal anastomosis. The Joint Vascular Research Group. *Journal of Vascular Surgery*, *26*(4), 543–50.

Stonebridge, P. A., Vermassen, F., Dick, J., Belch, J. J. F., & Houston, G. (2012). Spiral laminar flow prosthetic bypass graft: medium-term results from a first-in-man structured registry study. *Annals of Vascular Surgery*, *26*(8), 1093–9.

Tan, F. P. P., Soloperto, G., Bashford, S., Wood, N. B., Thom, S., Hughes, A., & Xu, X. Y. (2008). Analysis of flow disturbance in a stenosed carotid artery bifurcation using two-equation transitional and turbulence models. *Journal of Biomechanical Engineering*, *130*(6), 061008–1 – 061008–12.

Tanaka, M., Sakamoto, T., Sugawara, S., Nakajima, H., Kameyama, T., Katahira, Y., Ohtsuki, S., & Kanai, H. (2010). Spiral systolic blood flow in the ascending aorta and aortic arch analyzed by echo-dynamography. *Journal of Cardiology*, *56*(1), 97–110.

Teirlinck, C. J., Bezemer, R. a, Kollmann, C., Lubbers, J., Hoskins, P. R., Ramnarine, K. V, Fish, P., Fredeldt, K. E., & Schaarschmidt, U. G. (1998). Development of an example flow test object and comparison of five of these test objects, constructed in various laboratories. *Ultrasonics*, *36*(1-5), 653–60.

Tortora, G. J., & Derrickson, B. (2006). *Introduction to the Human Body: The Essentials of Anatomy and Physiology* (7th ed., p. 728). Wiley, John & Sons, Incorporated.

Tricht, I., Wachter, D., Tordoir, J., & Verdonck, P. (2005). Hemodynamics and Complications Encountered with Arteriovenous Fistulas and Grafts as Vascular Access for Hemodialysis: A Review. *Annals of Biomedical Engineering*, *33*(9), 1142–1157.

Tritton, D. J. (2007). *Physical Fluid Dynamics* (2nd ed., p. 544). New York: Oxford University Press.

Tu, C., & Deville, M. (1996). Pulsatile flow of non-Newtonian fluids through arterial stenoses. *Journal of Biomechanics*, *29*(7), 899–908.

Udesen, J., Nielsen, M. B., Nielsen, K. R., & Jensen, J. A. (2007). Examples of in vivo blood vector velocity estimation. *Ultrasound in Medicine & Biology*, *33*(4), 541–8.

Uejima, T., Koike, A., Sawada, H., Aizawa, T., Ohtsuki, S., Tanaka, M., Furukawa, T., & Fraser, A. G. (2010). A new echocardiographic method for identifying vortex flow in the left ventricle: numerical validation. *Ultrasound in Medicine & Biology*, *36*(5), 772–88.

Varghese, S. S., Frankel, S. H., & Fischer, P. F. (2007a). Direct numerical simulation of stenotic flows. Part 1. Steady flow. *Journal of Fluid Mechanics*, *582*, 253–80.

Varghese, S. S., Frankel, S. H., & Fischer, P. F. (2007b). Direct numerical simulation of stenotic flows. Part 2. Pulsatile flow. *Journal of Fluid Mechanics*, *582*, 281–318.

Walsh, M. T., Kavanagh, E. G., O'Brien, T., Grace, P. A., & McGloughlin, T. (2003). On the existence of an optimum end-to-side junctional geometry in peripheral bypass surgery-a computer generated study. *European Journal of Vascular and Endovascular Surgery*, *26*(6), 649–56.

Wentzel, J. J., Krams, R., Schuurbiers, J. C. H., Oomen, J. A., Kloet, J., van der Giessen, W. J., Serruys, P. W., & Slager, C. J. (2001). Relationship Between Neointimal Thickness and Shear Stress After Wallstent Implantation in Human Coronary Arteries. *Circulation*, *103*(13), 1740–1745.

Wood, N. B., Zhao, S. Z., Zambanini, A., Jackson, M., Gedroyc, W., Thom, S. A., Hughes, A. D., & Xu, X. Y. (2006). Curvature and tortuosity of the superficial femoral artery: a possible risk factor for peripheral arterial disease. *Journal of Applied Physiology*, *101*(5), 1412–8.

World Health Organization. (2014). The 10 leading causes of death in the world, 2000 and 2012.

Wu, J.-Z., Ma, H.-Y., & Zhou, M.-D. (2006). *Vorticity and vortex dynamics* (p. 776). Springer Berlin Heidelberg.

Yamamoto, K., Aribowo, A., Hayamizu, Y., Hirose, T., & Kawahara, K. (2002). Visualization of the flow in a helical pipe. *Fluid Dynamics Research*, *30*, 251–267.

Yang, X., Sun, C., Anderson, T., Moran, C. M., Hadoke, P. W. F., Gray, G. A., & Hoskins, P. R. (2013). Assessment of spectral Doppler in preclinical ultrasound using a small-size rotating phantom. *Ultrasound in Medicine & Biology*, *39*(8), 1491–9.

Zabielski, L., & Mestel, A. J. (1998). Steady flow in a helically symmetric pipe. *Journal of Fluid Mechanics*, *370*, 297–320.

Zell, K., Sperl, J. I., Vogel, M. W., Niessner, R., & Haisch, C. (2007). Acoustical properties of selected tissue phantom materials for ultrasound imaging. *Physics in Medicine and Biology*, *52*(20), N475–84.

Zhan, F., Fan, Y., & Deng, X. (2010). Swirling flow created in a glass tube suppressed platelet adhesion to the surface of the tube: its implication in the design of small-caliber arterial grafts. *Thrombosis Research*, *125*(5), 413–8.

Zhang, Z., Fan, Y., Deng, X., Wang, G., Zhang, H., & Guidoin, R. (2008). Simulation of blood flow in a small-diameter vascular graft model with a swirl (spiral) flow guider. *Science in China Series C: Life Sciences*, *51*(10), 913–21.